

**Mathematical modelling of
carbon dioxide dissolution
and reaction processes**

Mark J. Mitchell, B.Sc. M.Sc.

Thesis submitted to The University of Nottingham
for the degree of Doctor of Philosophy

December 2011

Abstract

Carbon dioxide dissolution into water is a ubiquitous chemical process on earth, and having a full understanding of this process is becoming ever more important as we seek to understand the consequences of 250 years of exponentially-increasing anthropogenic CO_2 emissions to the atmosphere since the start of the Industrial Revolution. We examine the dissolution of CO_2 into water in a number of contexts.

First, we analyse what happens to a range of chemical species dissolved in water following an injection of additional CO_2 . We consider the well-mixed problem, and use the method of matched asymptotic expansions to obtain new expressions for the changes in the species' concentrations with time, the new final chemical equilibrium, and the time scales over which this equilibrium is reached, as functions of time, the parameters and the initial condition. These results can be used to help predict the changes in the pH and concentrations of dissolved carbonic species that will occur in the oceans as a result of anthropogenic CO_2 emissions, and in saline aquifer formations after pumping CO_2 deep underground.

Second, we consider what happens deep underground in a saline aquifer when CO_2 has been pumped in, spreads through the pore space, and dissolves into the resident water, when advection, diffusion, and chemical reaction have varying levels of relative importance. We examine the length scales over which the dissolved CO_2 will spread out through an individual pore, ahead of a spreading drop of CO_2 , and the concentrations of the different chemical species within the pore, in the steady-state case.

Finally, some experiments have been carried out to investigate the effect of an injection of gaseous CO_2 on the chemical composition and pH of a saturated limestone aquifer formation. As the CO_2 enters the soil, it dissolves into the water, and we model the changes in the chemical composition of the water/limestone mixture with time.

Acknowledgements

I would like to thank my principal supervisors, Prof. Oliver Jensen and Prof. Andrew Cliffe, of the School of Mathematical Sciences, and Prof. Mercedes Maroto-Valer, of the School of Chemical and Environmental Engineering, for their abundant and invaluable guidance and mathematical expertise over the past four years, without which this piece of work would not have been possible.

I would also like to thank the EPSRC and the Centre for Innovation in Carbon Capture and Storage for funding me, Dr. Steve Bouzalakos and Dr. Giorgio Caramanna, of the School of Chemical and Environmental Engineering, for their help in answering my many questions, Dr. Chris Rochelle, of the British Geological Survey, for giving me access to all the papers he has collected over the years, and hence providing me with many valuable references, and Miss Yang Wei, of the School of Geography, for her collaboration with me for Chapter 4.

Some of the material in Chapter 2 has been published in [1].

Contents

1	Introduction	1
1.1	Why is carbon dioxide dissolution important?	1
1.2	What are the anthropogenic sources of CO ₂ ?	2
1.3	Carbon capture and storage	4
1.4	Saline aquifer storage of CO ₂	5
1.5	The context for mathematical modelling of CCS	7
1.6	The challenges of mathematically modelling CCS	9
1.7	The reactive chemistry	12
1.7.1	The dissolution of CO ₂ into water	12
1.7.2	Reactions between dissolved CO ₂ and water compounds	19
1.7.3	Reactions between dissolved CO ₂ and minerals	23
1.8	Aquifer-scale fluid mechanics of CCS	25
1.9	Pore-scale water transport for CCS	29
1.9.1	Flows far in front of the CO ₂ drop	31
1.9.2	Flows immediately in front of the CO ₂ drop, with no thin film	33
1.10	Reactive transport modelling of CCS	37
1.11	Summary	40
2	The reactive chemistry of CO₂ dissolution in water	45
2.1	The chemical reactions	45

2.2	Mathematical modelling	46
2.2.1	Assumptions	46
2.2.2	Full dimensional model	47
2.2.3	Parameter estimates and initial conditions	49
2.2.4	Predicted impact of CO ₂ (g) injection	51
2.2.5	Dimensionless model	52
2.2.6	The evolution of the system to equilibrium	54
2.3	Asymptotic analysis	57
2.3.1	Timescale 1: $\bar{t} = O(\alpha^{-3/2})$	57
2.3.2	Timescale 2: $\bar{t} = O(\alpha^{-1})$	58
2.3.3	Timescale 3: $\bar{t} = O(\alpha^{-3/4})$	59
2.3.4	Timescale 4: $\bar{t} = O(\alpha^{-1/2})$	61
2.3.5	Timescale 5: $\bar{t} = O(\alpha^{-1/4})$	63
2.3.6	Timescale 6: $\bar{t} = O(\alpha^{1/4})$	65
2.3.7	Plotted expressions	66
2.3.8	Equilibrium concentrations	67
2.3.9	The six timescales	69
2.4	Summary	70
3	Saline aquifer pore space distributions	72
3.1	Model formulation	72
3.2	Nondimensionalisation	75
3.3	Steady-state far-field model simplification	77
3.4	Far-field distribution for a solute ahead of a moving drop in a pore	79
3.5	Coupled chemical distributions when axial diffusion balances reaction	87
3.5.1	Small amplitude approximation: Model 8LF	91
3.5.2	Model 8NF	97

3.5.3	Model 4NF	101
3.5.4	Increasing the amplitude: Model 4NF	101
3.6	Other influences on concentration distributions	107
3.6.1	Advection	107
3.6.2	Density-driven convection	108
3.6.3	Alternative pore space structure	108
3.6.4	Variable thin film width	109
3.6.5	Additional chemical reactions	109
3.6.6	Alternative parameter values or initial conditions	109
3.6.7	Ionic charge	110
3.7	Conclusions	110
4	CO₂ rising through saturated limestone	123
4.1	Experimental set-up	123
4.2	Experimental data	126
4.3	Mathematical modelling	127
4.4	Comparison of mathematical modelling with experimental data	132
4.5	Summary	134
5	Conclusions	136
	References	140

Introduction

1.1 Why is carbon dioxide dissolution important?

Carbon dioxide dissolution into water, and reaction with water, is a ubiquitous natural chemical process on earth, happening in the atmosphere, in oceans, rivers and lakes, in the ground soils, and in processes such as photosynthesis. It also occurs in industrial processes such as the manufacture of carbonated drinks, and deep underground in enhanced oil recovery schemes. Improving our understanding of this process is therefore very important.

Understanding this process has become even more important as a result of 250 years of exponentially-increasing anthropogenic CO₂ emissions to the atmosphere, from power stations, from iron, steel, glass, and cement works, from cars and aeroplanes, from landfill sites, and from human beings. The atmospheric concentration of CO₂ has risen from about 280 parts per million by volume (ppmv) before the Industrial Revolution, to around 380 ppmv today [2], a 36% increase, and is currently increasing by 1.7ppmv [3] (or about 30 Gt [2]), per year.

When carbon dioxide dissolves into water and reacts with the water, carbonic acid is formed from which hydrogen ions then dissociate, increasing acidity. With plentiful water in the atmosphere, an increase in the atmospheric concentration of CO₂ can therefore also increase the acidity of the atmosphere and precipitation. Between one third and one half of anthropogenic CO₂ emitted to the atmosphere dissolves into the oceans, rivers and lakes [4, 5], and the reaction with sea water has already increased ocean acidity by 0.1 pH units since pre-industrial times [2]. Around 20% of anthro-

pogenic CO₂ emissions to the atmosphere are absorbed by the terrestrial biosphere [6], and the reaction between the absorbed CO₂ and soil moisture can alter soil acidity. Therefore, aside from any climate change due to an increased greenhouse effect, anthropogenic CO₂ emissions to the atmosphere can also increase the acidity of land, sea and air. Increasing acidity can critically affect different aspects of these ecosystems. For example, it is believed to depress metabolic rates in jumbo squid [7], depress immune responses of blue mussels [8], and make it harder for juvenile clownfish to distinguish between the smells of predators and non-predators [9], or hear and recognise the sounds of their predators [10], possibly because increasing acidity makes the oceans noisier by reducing the oceans' ability to absorb noise in the auditory range [11]. Associated with the change in acidity is a redistribution of the different dissolved carbonic species – the concentrations of dissolved carbon dioxide and bicarbonate increase, while the concentration of carbonate ions decreases [5], and this also affects the ocean ecosystems. For example, the reduction in carbonate makes it more difficult for marine calcifying organisms (such as corals and some plankton) to form and retain biogenic calcium carbonate [12, 13].

1.2 What are the anthropogenic sources of CO₂?

Emissions of CO₂ to the atmosphere started increasing exponentially shortly after James Watt patented his coal-powered steam engine in 1769, which enabled energy to be efficiently extracted from coal (with CO₂ created as a by-product). This was used to make iron, to make ships, to heat buildings, to power locomotives and other machinery, and to power the water pumps that enabled even more coal to be mined, and started the Industrial Revolution. Worldwide coal production has doubled every 20-30 years ever since [14]. Today, energy-related greenhouse gas emissions are still the most important, accounting for around 70% of all anthropogenic greenhouse gas emissions [15], and the main categories within this are heat supply, electricity generation and transport. Electricity generation is by far the most important single source of CO₂, providing over 27% of all anthropogenic CO₂ emissions by 2004 [15]. This is due to the continued reliance on fossil fuels in power generation – coal currently provides 42% of the world's electricity [16] (including, for example, 94% of South Africa's, and 81% of China's [17]), followed by natural gas with 21%.

Coal is the biggest individual source of electricity as coal-fired plants are safe, easy to build and run, very reliable, not dependent on the weather, and easy to dial up and down. Also, coal is cheap, easy to transport and stockpile safely, and an abundant and widespread resource (it is currently mined in over 50 countries [17]), with the biggest reserves situated in the countries with the biggest and fastest-growing electricity demands (USA, China and India). Coal-fired power generation capacity is therefore continuing to increase rapidly (in 2008, China had 112 GW under construction, India 51 GW and the USA 19 GW [17]).

As well as electricity generation, coal is also vital in making iron, steel, glass, cement and aluminium. Coal has therefore been one of the key drivers in raising and maintaining current standards of living and lengths of life in the West, and is doing the same for other countries which are industrialising. Continuing industrialisation and population growth mean that the total demand for electricity is expected to increase by 77% between 2006 and 2030 [16]. Despite the fact that large increases in the use of renewable and nuclear energy sources in electricity generation are being implemented (total worldwide electricity generation from renewables is expected to double, and total generation from nuclear is expected to increase by 40% over this period [16]), this increase in electricity demand is much larger than renewables and nuclear can provide, and hence fossil fuels will continue to provide the majority of electricity. Coal is expected to nearly double its output from 7.4 trillion kWh in 2006 to 13.6 trillion kWh in 2030, actually increasing its share of world electricity supply from 42% to 43% [16].

The burning of fossil fuels is therefore with us for the foreseeable future, and so ways must be found to reduce the resulting CO₂ emissions. This can be done through improving power station efficiencies, choosing gas-fired power stations in preference to coal, increasing the use of underground coal gasification, and carbon capture and storage (discussed below). Other ways of reducing anthropogenic CO₂ emissions include increasing further the use of renewable and nuclear energy sources, changing energy sources and improving energy efficiencies in transport and buildings [18], reforestation, carbon taxes [19], changing diets [20], population control, and exotic and controversial geo-engineering schemes. These schemes either reflect sunlight back into space (for example by using billions of small mirrors in space, by cloud whitening (spraying seawater into the sky to evaporate and leave behind shiny salt crystals to

brighten the clouds), or by spraying sulphur compounds into the stratosphere), or remove CO₂ from the atmosphere (for example by depositing iron filings in the sea to increase plankton growth ('ocean fertilisation') [21, 22], or by using artificial trees to chemically replicate photosynthesis). A successful reduction in global CO₂ emissions will require the simultaneous implementation of many of these different measures.

1.3 Carbon capture and storage

Carbon capture and storage (CCS) is the process of capturing waste CO₂ from large point sources, such as fossil fuel-burning power plants, iron, steel, glass and cement works, and oil and gas refineries, and permanently storing it away from the atmosphere. A complete CCS scheme comprises three distinct stages, which are: capturing the CO₂ (and isolating it from other waste products); transporting it to the storage site; and depositing it into its place of permanent storage. Each of these stages can be implemented in a number of different ways, which gives a wide variety of potential CCS schemes.

For example, a power plant may capture the CO₂ using post-combustion capture (where CO₂ is extracted from flue gases) [23], pre-combustion capture (where the fossil fuel is converted into CO and H₂, and then partially oxidized to give CO₂ and more H₂, which is used as fuel) [24], oxy-fuel combustion (where fuel is burned in oxygen instead of air, to produce CO₂ and water vapour only) [25], or chemical-looping combustion (where metal oxide particles react with the fuel to produce solid metal particles and a mixture of CO₂ and water vapour) [26]. Transport from the capture site to the storage site may be by pipeline [27] or ship [28], or the transport stage may be eliminated altogether by locating the source of CO₂ and the storage site together [29]. The CO₂ may be stored deep in the oceans [30], or in geological formations such as deep saline aquifers [31], deep-sea sediments [32], depleted oil and gas fields [33], or unmineable coal seams [33]. It may be injected as part of an enhanced oil or gas recovery (EOR or EGR) project [34, 35], it may be injected by itself, or together with water to reduce upward migration [36, 37]. The role of plants [38, 39] and animals [40] in storing carbon, and the potential for sequestration above ground in industrial processes [41], have also been considered. The dominance of coal as a source of CO₂ means that attempting to reduce the emis-

sions of CO₂ to the atmosphere without a serious implementation of CCS would be futile. In fact, Nobuo Tanaka, the head of the International Energy Agency has said that, "The deployment of CCS should be a 'litmus' test for the seriousness of environmental negotiators dealing with climate challenge" [42].

The scale on which CCS must be done is enormous. According to one scenario, which limits the atmospheric concentration of CO₂ to 450 ppmv, CCS is envisaged as accounting for 19% of the energy-related emissions reduction, which will require building or fitting 55 fossil fuel power plants with CCS every year between 2010 and 2050 [43]. However, CCS is still a very young technology – although there are a number of pilot-scale CCS projects in operation (mainly at gas refineries), and many CO₂-EOR schemes currently running, there is not yet a single commercial-scale CCS power plant scheme in operation. This is due to the high costs, technological difficulties, and issues around public perception. There is therefore an urgent need to develop improvements to CCS technologies.

1.4 Saline aquifer storage of CO₂

Depleted oil and gas fields are an obvious choice for CO₂ sequestration, because the oil and gas originally trapped in them demonstrably did not escape for thousands of years, their structure and physical properties have been extensively studied already, models have already been developed to characterize their behaviour, and the infrastructure necessary for CO₂ storage is already largely in place [44]. However, depleted oil and gas fields are unlikely to be able to hold more than 900 Gt CO₂ [44], which provides a maximum of 30 years' capacity at current global anthropogenic CO₂ emission rates of about 30 Gt/year [2].

Deep saline aquifer formations are very large deep porous geological formations saturated with water, and are often rich in different metals. They comprise grains of rock or sand glued together by natural mineral cements. The pore spaces between the rocks are connected, so the aquifer as a whole is permeable and porous, and fluids may flow through. The pore spaces tend to be filled with water, of varying salinity. Pure carbon dioxide is 'supercritical' when its temperature is greater than 31.1°C and its pressure is greater than 72.9 atm (this is known as the 'critical point'), and a saline aquifer's

ambient temperature and pore pressure are normally above these points, making supercriticality the normal phase for injected CO₂. This is the ideal phase, as it gives the CO₂ the density of a liquid and the freedom of movement of a gas. For example, at 35°C and 100 bar, CO₂ has density about 710 kg/m³, and viscosity about 0.06 mPa.s [45] (water has density 1000 kg/m³ and viscosity ~1 mPa.s).

The three main species (undissolved CO₂, water, and water saturated with CO₂) have different densities (for example, one simulation assumes densities of 710 kg/m³, 1050 kg/m³, and 1061 kg/m³ respectively [36]). The CO₂ source pushes the less dense undissolved CO₂ against the denser resident water, which in turn is pushed back, increasing pressure elsewhere in the aquifer. This is not a stable process, but small irregularities in the boundary between the water and the undissolved CO₂ are magnified and grow. This produces fingering instabilities [46], with subsequent overturning by these protruding fingers, causing rolling flows. These can help mix and stir the whole solution, increasing dissolution. The instability of the interface between CO₂ and water caused by the density difference is known as a Rayleigh-Taylor instability [47]. Also, as the CO₂ is buoyant compared to the water, it will also filter upwards through the pore spaces until it reaches an impermeable boundary. The CO₂ can remain above the denser saturated water and form a spreading gravity current below the impermeable boundary [48–51].

Saline aquifers have significantly more storage capacity than oil and gas fields, as well as being more widespread across the globe. Estimates of global storage capacity can vary wildly, as relatively little is known about the behaviour of CO₂ in saline aquifers in comparison with oil and gas fields, but it is believed to be 'very likely' that global storage capacity in deep saline aquifers is significantly above 1000 Gt CO₂, while estimates range up to 200,000 Gt CO₂ [44]. If CCS is to be implemented successfully on the scale thought necessary during the transition to a non-fossil fuel-based economy, it will therefore inevitably include storage in saline aquifers.

There are several different ways in which CO₂ may become trapped in a saline aquifer: (1) by an impermeable caprock overlying the aquifer, or by a series of thinner low-permeability layers, which provides a physical trap ('structural' or 'stratigraphic trapping'); (2) by adsorption onto rock surfaces; (3) by capillary forces in pore spaces ('hydrodynamic trapping'); (4) by dissolving into the resident water, rather than displac-

ing it ('solubility trapping'); and (5) by reacting chemically with the water or the rocks through which it is flowing ('geochemical' or 'mineral trapping'). This type of storage is the slowest process, but results in the most secure form of storage [52].

The likelihood of the large-scale implementation of CCS is another reason why understanding the dissolution of CO₂ in water is extremely important, as saline aquifers and depleted oil and gas fields normally contain water (which is displaced by the injected CO₂), as CO₂ storage may occur in the depths of the oceans or under the oceans in the saturated deep-sea sediments, as CO₂ may be deliberately pumped underground with water to reduce its upward migration, and as the dissolution of CO₂ into water is an important way of increasing storage security.

1.5 The context for mathematical modelling of CCS

As CO₂ is denser than air, if a cloud of CO₂ escapes from the ground into the atmosphere, it will remain at ground level. This can have potentially fatal consequences, as breathing CO₂ at concentrations greater than 8-10% can quickly lead to fainting, vomiting and asphyxiation. This was demonstrated in August 1986 when more than 1700 people, and all animal life within a radius of about 14km, were suffocated to death following a volcanic eruption at Lake Nyos, Cameroon, which emitted a large cloud of concentrated CO₂ [53, 54]. Other potential dangers of CO₂ sequestration include polluting groundwater or other underground resources, and increasing the aquifer pressure, leading to subsidence or absidence at the earth's surface, or increased seismicity (as experienced, for example, in the region of the Rocky Mountain Arsenal well following the injection of waste water [55]) [56].

If many millions of tons of CO₂ are to be pumped deep underground in CCS projects, it is therefore most important that the health, safety and environmental risks are well understood. It is therefore necessary to have a good understanding of what happens to the injected CO₂ and the surrounding aquifer environment, of the chances of leakage, and of the effects throughout the aquifer of the resulting increases in pressure. It is also important to have a good understanding of practical issues, such as the capacities of particular aquifers, the costs, and the most efficient injection methods, as these projects are currently very costly, and the degree to which the costs can be reduced is likely to

determine how many schemes are implemented.

Knowledge about what happens to injected CO₂, and the optimal methods of implementation, can be achieved in several different ways. One such way is the experiences gained from Enhanced Oil Recovery projects already running. CO₂ has been injected into geological formations in order to enhance oil recovery since the early 1970s, and there are currently about 73 such operations in place in the USA alone, injecting about 30 Mt CO₂ per year (of which 10% is anthropogenic) [44]. For example, primary oil recovery at Weyburn, Canada, finished in 1964, and secondary oil recovery, via a conventional water flood, in 2000. Since then, further oil has been recovered using a 'miscible CO₂ flooding' scheme. In this scheme, CO₂ is transported to Weyburn via a pipeline from a coal gasification plant in North Dakota, 320 km away, and then mixed with water (to reduce its mobility and to minimise fingering), and pumped underground some distance from the oil production well. Oil recovery at the production well is enhanced because the injected fluids push the oil towards the well, because CO₂ becomes miscible with oil at the correct conditions, and reduces the oil's viscosity, and because the increased acidity of the carbon dioxide-water mixtures dissolves carbonate minerals in the formation matrix, resulting in a permeability increase [57]. This operation is injecting about 1000 t CO₂ per day, and it is expected that about 20 Mt CO₂ will eventually be stored in this field [44], though calculations indicate that the 2×10^{12} litres of water in this aquifer may be capable of storing up to 100 Mt of dissolved CO₂. Monitoring of the oilfield is extensive, and to date has revealed no evidence of any CO₂ leakage to the surface.

A second source of knowledge is the handful of pilot CCS projects that are already up and running. For example, CO₂ stripped from natural gas at Sleipner, North Sea, has been re-injected into the Utsira sandstone saltwater aquifer at a rate of about 1 Mt CO₂ per year, since October 1996. With a cross-sectional area of over 26,000 km² [29], this aquifer is believed to have a very large storage capacity of 1-10 Gt CO₂, but only about 20 Mt CO₂ will be stored over the lifetime of this project. The injected CO₂ has been regularly imaged using seismic time-lapse reflection surveys, and the surveys show that the caprock is successfully sealing the CO₂ inside the sandstone formation [58]. In addition, many other pilot CO₂ sequestration schemes are in place or planned in many different countries, including USA, China, UK, Canada, Australia, Japan, Germany,

Norway, Italy, Netherlands, Poland, Turkey, and Brazil [44].

CO₂-EOR and pilot CCS projects already in operation therefore provide extensive knowledge about safety and practicality issues, and this knowledge has been thoroughly reviewed (e.g. [44, 52]). In addition to these field experiments, valuable insight can also be provided by laboratory experiments which simulate conditions deep underground (pressure, temperature, mineralogy, pH, etc.). For example, they can be used to examine the effects of injecting large quantities of CO₂ on chemical reaction rates, chemical composition and pH [59], or to investigate which parameters are most critical in the formation of mineral carbonates [60]. However, as it is only relatively recently that CCS has come to be regarded as a viable option in mitigating climate change, relatively few such experiments have been reported.

An equally-important source of knowledge is mathematical modelling and simulation, which can support and enhance the other three sources. Theoretical modelling goes hand-in-hand with experiments to provide explanations for observed phenomena and justify derived rules. It also provides the foundations for simulations – as the aquifers which could potentially store the vast quantities of CO₂ are largely inaccessible (due to their depth), carrying out experiments can be impracticable. Using computer simulation to predict what will happen at a particular aquifer (whether the CO₂ is likely to escape, how far the CO₂ will spread, how the pH will change, how much CO₂ the aquifer will be able to hold, etc.) may therefore be the only way of finding out whether that particular aquifer is suitable. It is therefore most important that the simulations can be done accurately, which requires that the modelling be reliable.

1.6 The challenges of mathematically modelling CCS

Of key importance in CCS is understanding how far from the injection point the injected CO₂ will spread out, and how much will dissolve into the resident water.

Modelling the fate of injected CO₂ is an extremely challenging mathematical task even if dissolution and chemical reaction are ignored. These are moving boundary problems made more difficult by a complex geometry, involving local impediments to flow (such as local low-permeability layers), local aids to flow (such as fault lines or abandoned wells), and a high degree of variability in the physical characteristics (such as depth,

thickness, temperature, pressure, salinity, pH, mineralogy, density, permeability and porosity), even within a single aquifer. Within this complex geometry there are many different forces acting on the injected CO₂, including buoyancy, gravity, pressure gradients, diffusion forces, capillary forces, and mean flows of groundwater through the host rock.

As CO₂ is continuously pumped into an aquifer, it forms a drop in the pore space. The drop is a mass of CO₂ molecules, has the density of a liquid and the viscosity of a gas, and expands and spreads away from the injection point as more CO₂ is pumped in, through the many inter-connected channels in the pore space. The CO₂ molecules can move within the drop, and may leave the drop by dissolving from the edge of the drop into the adjacent resident water. How much CO₂ dissolves from the drop into the water is dependent on many factors, including: how much CO₂ is pumped into the aquifer; the size and shape of the drop the CO₂ forms in the pore; how rapidly the CO₂ can diffuse within this drop; the pH, temperature, pressure, salinity and mineralogy of the resident water; the contact angle between the drop and the pore walls; and how well the dissolved CO₂ can be transported away from the drop. This depends on the relative importance of advection, diffusion and reaction, the existence of local impediments or aids to flow, the pore's diameter and inclination to the horizontal, and the size of the gap between the drop and the pore walls. In addition, these factors can vary temporally as CO₂ dissolves into the water, and spatially across a single aquifer. For example, the pores can be fairly tortuous, and far from a constant angle to the horizontal.

There are complex webs of chemical reactions that take place between the CO₂ that dissolves into the water, the species in the resident water, and the various minerals present in the aquifer, and these reactions should not be ignored while modelling the fluid mechanics as they can affect the aquifer's physical characteristics. For example, the permeability of the host rock may be increased as the water's higher acidity dissolves formation minerals, or decreased as metals form and precipitate out of solution into the pore spaces. Also, the fluid mechanics needs to account for the fact that as CO₂ dissolves into the water, this denser water will sink compared to the water not containing CO₂.

Impurities in the CO₂, either from the initial injection, or through chemical changes that take place as it advances through the aquifer, mean that the fluid's critical point

can change, and the CO₂ could end up changing phase.

Moreover, there are extremely wide ranges of scales. The CO₂ percolates through pore spaces that are normally less than 1 mm wide, but encounters stratigraphic structures that are measured in tens of metres, and ends up moving across distances that can be tens, or even hundreds, of kilometres. Also, the chemical rates of reaction can vary by many orders of magnitude, taking less than one second or many years to reach equilibrium, making any numerical calculations extremely difficult. In addition, it is often the fate of the injected CO₂ over an even longer time period (>1000 yr) that is of interest. Also, the concentrations of the different species vary by orders of magnitude within a single aquifer, and individual species can vary similarly between different aquifers, and over time within one location.

Another big issue is uncertainty, as the environment into which the CO₂ is pumped cannot be observed directly. Knowledge of the aquifer conditions must therefore be obtained by drawing inferences (such as estimating temperatures based on depth), remote imaging, and taking samples, and there can be large uncertainties surrounding parameter estimates. The aquifer may even contain sizeable features, such as fault lines, that are not known about. Furthermore, assessing how well model predictions match up to a particular injection project is also difficult, as monitoring CO₂ injections must be done remotely. It can therefore be hard to judge how well a particular model captures reality.

Section 1.7 contains an overview of the reactive chemistry. The most realistic mathematical modelling of CCS couples together both fluid transport and chemical reactions, which is known as reactive transport modelling. However, solving such systems is very challenging, due to the complexity of the models, and because the solutions must find ways of resolving the wide ranges of temporal and spatial scales. Therefore, one area of focus for CCS is models that exclude all chemical reactions, and instead analyse just the aquifer-scale (Section 1.8) or pore-scale (Section 1.9) fluid flows. Some of the methods of obtaining solutions to reactive transport models are reviewed in Section 1.10.

1.7 The reactive chemistry

The release of vast quantities of CO₂ into the atmosphere, the dissolution of CO₂ into the oceans, and the injection of CO₂ into aquifer formations, immediately results in chemical disequilibria, and therefore the onset of various chemical reactions.

1.7.1 The dissolution of CO₂ into water

The first, and main, reaction that takes place is the dissolution of the CO₂ into the resident water or water solution,



(or $\text{CO}_2(\text{sc}) \rightleftharpoons \text{CO}_2(\text{aq})$ if the undissolved CO₂ is underground and supercritical).

The amount of one substance that will dissolve into a given quantity of another substance is called the solubility. The solubility of a gas in a liquid, S (in mol/litre, or M), increases as pressure increases and decreases as temperature increases (hence water bubbles when boiled). This relationship is given by Henry's Law, $S = k_H P$, where P is the partial pressure of the gas outside the solution (atm), and k_H is the Henry's law constant (in M/atm), which varies with solute, solvent and temperature. The solubility of CO₂ in water has been investigated since the 1880's [61]. For CO₂ in water at 25°C, $k_H = 0.034$ M/atm [62]. At 380 ppm, the atmospheric partial pressure of CO₂ at ground level is 0.00038 atm, and so the solubility of CO₂ in an open glass of water at room conditions is about 1.3×10^{-5} M.

In an injection scenario, suppose the injected gas is pure CO₂, so its partial pressure is the full pressure (and remains at this pressure while CO₂ dissolves into the water), and the aquifer temperature is 25°C. Then Henry's Law with $k_H = 0.034$ M/atm and 1 atm of pressure gives a solubility of 0.034 M. One experimental study found a solubility of CO₂ in water at 25°C and 1 atm of pressure of 0.110 g CO₂ per 100 g seawater [61]. As CO₂ has atomic mass 44 g/mol, 0.11 g is 0.0025 mol, and at about 1000 g/l, 100 g seawater is 0.1 litre, and so this is a solubility of 0.025 M, so there is a small disagreement here. At this study's upper conditions of 25°C and 45 atm, solubilities of 4.110 g CO₂ per 100 g distilled water (=0.9 M) and 3.090 g CO₂ per 100 g synthetic seawater (=0.7 M) were found.

Aquifer temperatures and pressures can go higher than this, and can vary widely, even within a single aquifer. For example, the temperatures in one aquifer were found to vary between 20°C and 60°C [63], and in another study, 80°C and 27 MPa (=266.5 atm) are taken as typical [36]. A comprehensive investigation studied solubilities between 0 and 100°C and between 25 and 700 atm [64, 65]. In the least soluble of these conditions (100°C and 25 atm), solubility was found to be 5.37 cm³ CO₂ at standard temperature and pressure (S.T.P.) per 1 g of water. At S.T.P. (0°C and 1 atm), CO₂ has density 1.977 g/l, so a volume of 5.37 cm³ is a mass of 0.0106 g. With atomic mass 44 g/mol, this is 0.000241 mol. Also, 1 g water is 0.001 litre, and so this is a solubility of 0.24 M. In the most soluble measured combination of conditions (12°C and 300 atm), solubility was 41.07 cm³ CO₂ at S.T.P. per 1 g of water (=1.8 M).

As an alternative approach, one empirical equation that gives the dependence on temperature of an alternative version of Henry's constant for CO₂ in water (valid in the range 0-80°C) is [66]

$$\log_{10} H = 69.4237 - \frac{3796.46}{T} - 21.6694 \log_{10} T + (4.78857 \times 10^{-4} \times T), \quad (1.7.1)$$

where T is Kelvin temperature, and H is Henry's constant in atm/mol fraction. Noting that

$$\text{mol fraction of CO}_2 \text{ in a mixture} = \frac{\text{the concentration of CO}_2 \text{ in the mixture}}{\text{total concentration of the mixture}},$$

dividing through by pressure, and assuming that the total concentration of the mixture is approximately the concentration of water, which, as water has density 1000 g/l (g/l \equiv kg/m³) and atomic mass 18.0106 g/mol, is 55.5 M, gives

$$\frac{1}{H} = \frac{k_H}{55.5 \text{ M}}. \quad (1.7.2)$$

(At 25°C, equation (1.7.1) gives $H = 1628.6$ atm/mol fraction, so (1.7.2) gives $k_H = 0.034$ M/atm, which agrees with the above.) At 100°C (373K) (strictly slightly outside its range of validity), (1.7.1) gives $H = 4974.5$ atm/mol fraction, i.e. k_H decreases to 0.0112 M/atm. With 25 atm of pressure, this gives a solubility of 0.28 M, which agrees with 0.24 M in the previous paragraph. As CO₂ has atomic mass 44 g/mol, $S = 0.28$ M corresponds to a density for the CO₂ within water saturated with CO₂ of 12.32 kg/m³, which matches the widely-used density difference estimate quoted above of about 11 kg/m³ [36]. This suggests that, in aquifer conditions, solubilities are unlikely to go significantly above about 1 M.

A solubility of CO₂ in aquifer water of $S \approx 0.28 \text{ M}$ is over 21,000 times greater than room conditions – the reduction in solubility resulting from the increase in temperature is far outweighed by the increase in solubility resulting from the increase in pressure.

At 11 kg/m^3 , taking an aquifer porosity of 15% [36], a 1 tonne (1000 kg) injection will therefore dissolve into about 614 m^3 of resident aquifer water. If the total annual human output of 30 Gt CO₂ was to be pumped into an aquifer in these conditions, the CO₂ will dissolve into an aquifer volume 100 m deep by about 13 km wide and long. Note this is not the volume of space that would be required to store the undissolved CO₂ – if the undissolved pure CO₂ finger has density 710 kg/m^3 , with an aquifer porosity of 15%, this needs an aquifer volume 100 m deep by only 1.6 km wide and long. The earth's saline aquifers therefore certainly provide a store that could hold a significant proportion of anthropogenic CO₂.

There are substantial density differences between the undissolved CO₂, the water, and the water saturated with CO₂, and these density differences drive the vertical movements of the CO₂. While CO₂ exists in its separate gaseous or supercritical phase, its significantly lower density causes a predominantly upwards, relatively fast, migration, compared to the water. However, when the injected CO₂ dissolves into the slowly moving resident water, this changes to a slow, predominantly downwards migration. Dissolution is therefore one of the trapping mechanisms for CO₂, and a desirable reaction in carbon sequestration. As the groundwater containing dissolved CO₂ migrates downwards and further from the injection point, the ambient temperature is likely to increase, and the pore pressure is likely to decrease, both of which reduce the solubility of CO₂ in water. The dissolved CO₂ may therefore be expelled out of the water back into a free gaseous or supercritical phase.

The rate at which a geochemical reaction happens is dependent on many factors, including temperature, pressure, pH, rate of mixing, salinity, the concentrations of the different chemical species involved (and their distance from chemical equilibrium), the concentrations of other species in the environment which may also react, the presence of catalysts or pH buffers, the reactive surface area, the ionic strength of the solution, and the size of the reaction's activation energy (the minimum energy necessary for the

reaction to occur). Moreover, some of these influences can change as the reaction progresses.

Most of these factors are controlled to be constant in an experimental investigation, leaving only the concentrations of the different chemical species (and their distance from chemical equilibrium). The rate of change of a species can therefore be modelled either as some function of all the concentrations involved, or alternatively just some of the concentrations and a variable denoting the distance from equilibrium (e.g. [67–69]).

The simplest function of concentrations to use is the mass action law, which states that the rate of a chemical reaction is proportional to the product of the concentrations of the reactants. However,

‘Most reactions, unfortunately, are not this simple. If reaction rates are measured experimentally, they are found in general to depend on various powers of the concentration, even sometimes on negative powers, and only rarely on the first power as the statement requires. Presumably this means that reactions take place in steps, some steps being slower than others; each step may follow the "law", but the sum of steps going at different rates does not.’ [70]

It is therefore necessary to distinguish between elementary reactions, which actually occur at the molecular level as written down, and overall reactions, which actually represent the net result of a series of elementary reactions [71]. The mass action law is a good model for elementary reactions, but not necessarily for overall reactions. Generally, experimentation is necessary to determine whether a given reaction follows the mass action law [72].

It is common practice to assume the dissolution reaction (R1) follows the mass action law (e.g. [73]), and so its kinetics can be modelled as follows:

$$-\frac{d[\text{CO}_2(\text{g})]}{dt} = \frac{d[\text{CO}_2(\text{aq})]}{dt} = k_1[\text{CO}_2(\text{g})] - k_{-1}[\text{CO}_2(\text{aq})],$$

where t is time, $[]$ denotes concentration, and k_1 and k_{-1} are appropriate constants of proportionality, called respectively the forwards and reverse rate constants for this reaction. Therefore, at any equilibrium, the ratio of rate constants equals the ratio of equilibrium concentrations, and this ratio, denoted K_1 , is called the equilibrium con-

stant:

$$K_1 \equiv \frac{k_1}{k_{-1}} = \frac{[\text{CO}_2(\text{aq})]_{\text{eq}}}{[\text{CO}_2(\text{g})]_{\text{eq}}}$$

The value of this equilibrium constant varies with many factors, including temperature, pressure, pH and salinity. In well-mixed conditions at room temperature and pressure, 'CO₂ distributes itself approximately equally between its gas phase and aqueous phase' [73], i.e. $K_1 \approx 1$. At sea level, the air has density 1.2 g/l, and atomic mass 29 g/mol, i.e. total concentration 0.041 M. If 380/10⁶ of this is CO₂, this gives CO₂ a concentration in air of 1.57×10^{-5} M, which is indeed close to the concentration dissolved in the open glass of water found above ($K_1 = 0.83$). When authors use this definition of the equilibrium constant, it is therefore taken as being equal to, or just below, 1 (e.g. 0.9 [74]). Therefore, at room temperature and pressure, the dissolution and precipitation rate constants are also approximately equal. Moreover, in well-mixed conditions, such as when aquifer water and CO₂ are adjacent in the same pore space, this reaction is known to be 'rapid' [44], as shown by shaking and opening a can of fizzy drink. In fact, in room conditions, this reaction is sometimes modelled as instantaneous (e.g. [74]).

However, aquifer temperatures and pressures are much higher than room temperature and pressure. If the density of the CO₂ gas bubble is 710 kg/m³ [36], then at atomic mass 44 g/mol, it has concentration 16.1 M. This compares with concentrations found above of about 1 M for the aquifer's dissolved CO₂. So although CO₂ is a lot more soluble in aquifer conditions than in room conditions (i.e. the aquifer water can hold a lot more CO₂ per litre than the glass of water), this increase in concentration for the dissolved phase is far out-weighted by the increase in concentration of the gaseous phase, meaning that the actual ratio of dissolved to undissolved CO₂ concentrations (K_1) decreases. It should be noted that many of the parameter values used in these calculations (such as temperature, pressure, porosity, and density) can vary widely, which gives a wide range of different figures.

To establish whether the dissolution still happens quickly at aquifer temperatures and pressures, the dependence of a rate constant k_i on temperature is normally assumed to follow the Arrhenius equation [62, 72]

$$k_i = A \exp\left(\frac{-E_a}{RT}\right),$$

where A is a constant appropriate for the particular rate constant, E_a is the activation

energy (the minimum energy necessary for the reaction to occur), R is the gas constant, and T is temperature. Increasing temperatures therefore increases all rate constants. Also, all else being equal, the effect on a rate constant of changing the pressure from 1 atm to P atm is given by [71, 73]

$$\frac{k_P}{k_1} = \exp\left(\frac{-\Delta V (P - 1)}{RT}\right)$$

where k_1 and k_P are respectively the values of the rate constant associated with 1 atm and P atm, and ΔV is the molar volume change (or 'volume of activation') of the reaction, with all species in their standard states. Dissolution results in a reduction in mol/litre, i.e. a slight increase in litre/mol, and so ΔV is positive. Therefore the effect of increasing the pressure is to reduce the dissolution rate constant, and increase the precipitation rate constant, but overall these rate constants are still high, meaning that the dissolution of CO_2 can therefore happen extremely quickly in aquifer conditions also.

However, this rapid dissolution also requires good contact and mixing between the injected CO_2 and the resident water, but natural aquifer flows are often extremely slow. CO_2 injected into an aquifer can therefore take decades or longer to dissolve. Therefore, just like room condition models, it is common practice to model CO_2 dissolution in aquifer scenarios by assuming that the mass action law applies, and that there is instant local dissolution and equilibrium, with the overall rate of dissolution affected only by the rate of mixing. However, the way that this is done in practice is often questionable or confusing, with different definitions of the equilibrium constant in use. For example, one model and simulation of CO_2 storage in a deep North Sea aquifer that includes advection, dissolution of CO_2 and a rate-limited precipitation reaction [75], assumes that dissolution is locally instantaneous, and so simply sets local $[\text{CO}_2(\text{aq})]=K_1$. However, this implies either that the mass action law does not apply, or else one of the two species is measured dimensionally and the other dimensionlessly.

An alternative approach is to consider the thermodynamic equilibrium constant, defined as

$$K_1^* \equiv \frac{a_{\text{CO}_2(\text{aq})}}{a_{\text{CO}_2(\text{g})}}$$

where a , the (dimensionless) activity coefficient of a species, is the mole fraction of that species in a mixture ('effective concentration' for a solute, and 'effective partial pres-

Constant	Magnitude	Conditions	Source
K_1^+	0.0372 M atm ⁻¹	-	[73]
	0.0338 M atm ⁻¹	25°C	[77]
	0.034	-	[78]
	0.0339	25°C	[79]
	0.034	25°C	[80]

Table 1.1: Estimates of equilibrium constant K_1^+ .

sure' (fugacity) for a gas). Despite the fact that activities are dimensionless quantities, the activities are often replaced by the numerical values of the molalities, concentrations, or partial pressures [72] (e.g. [76]). Substituting concentration and partial pressure into this expression gives

$$K_1^+ \equiv \frac{[\text{CO}_2(\text{aq})]_{\text{eq}}}{(P_{\text{CO}_2})_{\text{eq}}},$$

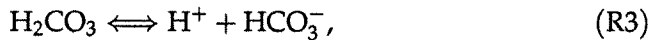
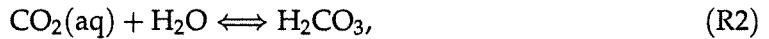
where P_{CO_2} is partial pressure of gaseous CO_2 (atm). K_1^+ has units M/atm, and this also assumes that the mass action law applies. When sources include reaction (R1), they rarely define which equilibrium constant is being used, or give units, but the value that is taken often implies that it is this definition of the equilibrium constant that has been used. Table 1.1 gives some examples of when this equilibrium constant has been used, with units quoted as given.

Alternatively, one source [81] combines the formulas for K_1^* and K_1^+ to give $K\Gamma P = \gamma C$, where K is the equilibrium constant, Γ is the gaseous CO_2 fugacity coefficient, P is partial pressure, γ is the aqueous CO_2 activity coefficient, and C is the aqueous concentration (mol/kg H_2O).

Given an injection of gaseous CO_2 into a system containing water, being able to quantify the amount that dissolves into the water, and the rate at which it does so, is very important, given the ubiquity of CO_2 and water. However, the ways in which this have been done can sometimes appear to be rather unsatisfactory. In Chapter 2 we will develop an alternative way of describing the rate at which CO_2 dissolves into water, and its concentration at equilibrium.

1.7.2 Reactions between dissolved CO₂ and water compounds

Once the injected CO₂ has dissolved into the water, there are a number of reactions that can happen within the water. The CO₂ can react with the water to form carbonic acid (R2), which can then split up – hydrogen ions dissociate from the carbonic acid (causing the pH to drop), and leave behind a bicarbonate ion (R3), and then a carbonate ion (R4):



The forward (respectively reverse) rate constants for these three reactions are denoted k_2 , k_3 and k_4 (resp. k_{-2} , k_{-3} and k_{-4}). These are the central key reactions between dissolved CO₂ and water compounds in both ocean acidification and carbon sequestration [44, 60, 82].

Some estimates of the rate constants for the hydration and dehydration reactions (R2), and their ratio, that are available in the literature are given in Table 1.2, with units given as stated in each reference. The ubiquity of carbon dioxide and water reacting together means that reaction (R2) has been studied over a long period, with the first attempts at kinetic data dating back to the second decade of the twentieth century [83], and the work of Vorländer and Strube [89]. There is therefore a relative abundance of rate information for this reaction. The agreement about rate constants k_2 and k_{-2} having units sec^{-1} implies that the mass action law is appropriate for reaction (R2), except that water is abundant and so does not affect any of the rates of reaction, i.e.

$$-\frac{d[\text{CO}_2(\text{aq})]}{dt} = \frac{d[\text{H}_2\text{CO}_3]}{dt} = k_2[\text{CO}_2(\text{aq})] - k_{-2}[\text{H}_2\text{CO}_3].$$

Table 1.3 gives some estimates for the rate constants and equilibrium constant for the third reaction. As this reaction is very fast, and significantly faster than reaction (R2), it is rather difficult to estimate kinetic data specifically for this reaction. Therefore models normally just assume this reaction to be instantaneous and always in equilibrium, or else just include a combined reaction (R2&3) (as below) (e.g. [5]) and assign all rate information to (R2) as the rate-limiting part of this process. Therefore, not much work

Constant	Magnitude	Conditions	Source
k_2	0.03 sec ⁻¹	25°C	[67]
	0.002 sec ⁻¹	0°C	[71]
	0.03 sec ⁻¹	25°	[83]
	0.062 sec ⁻¹	25°C, zero ionic strength	[84]
	0.037 ± 0.002 sec ⁻¹	25°C	[85]
	0.0437 sec ⁻¹	25°C, 0.5 ionic strength	[86]
	0.0040 sec ⁻¹	5°C, seawater	[87]
	0.0352 sec ⁻¹	25°C	[87]
k_{-2}	12 sec ⁻¹	25°C	[67]
	8.2 – 15.0	18°. Overview of 9 expts.	[83]
	20 sec ⁻¹	25°	[83]
	18 ± 7 sec ⁻¹	25°C	[85]
	19.2 sec ⁻¹	25°C, 0.5 ionic strength	[86]
	exp(30.15 – (8018)T ⁻¹) sec ⁻¹ (=25.6 sec ⁻¹ at T=298K)	Seawater, 15 – 32.5°C	[88]
	$K_2 = k_2/k_{-2}$	1/600	25°C

Table 1.2: Estimates of rate constants and equilibrium constant for reaction (R2).

Constant	Magnitude	Conditions	Source
k_3	1 × 10 ⁷ s ⁻¹	-	[85]
k_{-3}	5 × 10 ¹⁰ M ⁻¹ s ⁻¹	-	[85]
$K_3 = k_3/k_{-3}$	4.42 × 10 ⁻⁷	25°C	[77]
	1.72 × 10 ⁻⁴ M	-	[85]
	4.6 × 10 ⁻⁴ M	25°C, 0.5 ionic strength	[86]
	1.72 × 10 ⁻⁴ M	25°C, Zero ionic strength	[86]
	4.47 × 10 ⁻⁷	25°C, infinitely-dilute	[90]
	1.72 × 10 ⁻⁴	25°, low ionic strength	[91]
	3.15 × 10 ⁻⁴ M	0.2M ionic strength	[91]
	10 ^{^(1.707 × 10⁻⁴)} M ≈ 1 M	-	[92]

Table 1.3: Estimates of rate constants and equilibrium constant for reaction (R3).

Constant	Magnitude	Conditions	Source
k_4	59.44 sec^{-1}	-	[5]
	2.5 M sec^{-1}	-	[94]
k_{-4}	$5.0 \times 10^{10} \text{ kg mol}^{-1} \text{ sec}^{-1}$	-	[5]
	$5 \times 10^{10} \text{ M sec}^{-1}$	-	[94]
$K_4 = k_4/k_{-4}$	4.67×10^{-11}	25°C	[77]
	4.68×10^{-11}	25°C	[79]
	4.688×10^{-11}	25°C	[80]
	4.68×10^{-11}	25°C, infinitely-dilute	[90]
	$4.68 \times 10^{-11} \text{ M}$	25°C	[92]
	$4.5 \times 10^{-11} \text{ M}$	25°C	[94]
	$3.3 \times 10^{-11} \text{ M}$	10°C	[94]

Table 1.4: Estimates of rate constants and equilibrium constant for reaction (R4).

has been done actually estimating k_3 and k_{-3} , but has instead focussed on estimating k_2 , k_{-2} and K_3 . If k_3 and k_{-3} have units as stated, and K_3 has units M, this is all consistent with the mass action law for this reaction (as used, for example, in [5, 77, 92, 93]), i.e.

$$-\frac{d[\text{H}_2\text{CO}_3]}{dt} = \frac{d[\text{H}^+]}{dt} = \frac{d[\text{HCO}_3^-]}{dt} = k_3[\text{H}_2\text{CO}_3] - k_{-3}[\text{H}^+][\text{HCO}_3^-].$$

Table 1.4 gives some estimates of the rate constants and equilibrium constant for the fourth reaction. The units given by [94] for the three constants are inconsistent. If k_4 has units sec^{-1} , k_{-4} has units $\text{M}^{-1}\text{sec}^{-1}$, and K_4 has units M, this is consistent with the mass action law for this reaction (as used, for example, in [4, 77]), i.e.

$$-\frac{d[\text{HCO}_3^-]}{dt} = \frac{d[\text{H}^+]}{dt} = \frac{d[\text{CO}_3^{2-}]}{dt} = k_4[\text{HCO}_3^-] - k_{-4}[\text{H}^+][\text{CO}_3^{2-}].$$

Two of these reactions are often combined as follows:



Similarly to Section 1.7.1, the following expressions for the equilibrium constants for (R2&3) and (R4) can be derived by assuming they follow the mass action law (except that water is abundant):

$$K_{2\&3} = \frac{[\text{H}^+]_{\text{eq}}[\text{HCO}_3^-]_{\text{eq}}}{[\text{CO}_2(\text{aq})]_{\text{eq}}}, \quad K_4 = \frac{[\text{H}^+]_{\text{eq}}[\text{CO}_3^{2-}]_{\text{eq}}}{[\text{HCO}_3^-]_{\text{eq}}}. \quad (1.7.3)$$

The total CO_2 in the system comprising (R2&3) and (R4) is given by

$$\text{Tot}[\text{CO}_2] = [\text{CO}_2(\text{aq})] + [\text{HCO}_3^-] + [\text{CO}_3^{2-}]. \quad (1.7.4)$$

Substituting expressions for bicarbonate and carbonate from (1.7.3) into (1.7.4) and then re-arranging gives the following formulae for the concentrations of the different species at equilibrium, which are functions of the equilibrium pH, the total CO_2 in the system, and the equilibrium constants:

$$[\text{CO}_2(\text{aq})]_{\text{eq}} = \frac{[\text{H}^+]_{\text{eq}}^2}{[\text{H}^+]_{\text{eq}}^2 + [\text{H}^+]_{\text{eq}}K_{2\&3} + K_{2\&3}K_4} \text{Tot}[\text{CO}_2], \quad (1.7.5)$$

$$[\text{HCO}_3^-]_{\text{eq}} = \frac{[\text{H}^+]_{\text{eq}}K_{2\&3}}{[\text{H}^+]_{\text{eq}}^2 + [\text{H}^+]_{\text{eq}}K_{2\&3} + K_{2\&3}K_4} \text{Tot}[\text{CO}_2], \quad (1.7.6)$$

$$[\text{CO}_3^{2-}]_{\text{eq}} = \frac{K_{2\&3}K_4}{[\text{H}^+]_{\text{eq}}^2 + [\text{H}^+]_{\text{eq}}K_{2\&3} + K_{2\&3}K_4} \text{Tot}[\text{CO}_2]. \quad (1.7.7)$$

The equilibrium pH (which is affected by the initial pH, and the capacity of the system to buffer the pH), exerts a large influence on the extent to which the reactions happen, and which species is dominant when the system reaches equilibrium. A plot of these equilibrium concentrations against equilibrium pH is known as a Bjerrum plot. Figure 1.1 shows the variation in the equilibrium concentrations of these species with equilibrium pH when $\text{Tot}[\text{CO}_2] = 8.75 \times 10^{-4} \text{ M}$, $K_{2\&3} = 6 \times 10^{-7} \text{ M}$ and $K_4 = 6 \times 10^{-11} \text{ M}$. (This scenario will be modelled in Chapter 2.) Note that $K_4 = k_4/k_{-4}$, and

$$K_{2\&3} = \frac{[\text{H}^+]_{\text{eq}}[\text{HCO}_3^-]_{\text{eq}}}{[\text{CO}_2(\text{aq})]_{\text{eq}}} = \frac{[\text{H}_2\text{CO}_3]_{\text{eq}}}{[\text{CO}_2(\text{aq})]_{\text{eq}}} \frac{[\text{H}^+]_{\text{eq}}[\text{HCO}_3^-]_{\text{eq}}}{[\text{H}_2\text{CO}_3]_{\text{eq}}} = K_2K_3 = \frac{k_2k_3}{k_{-2}k_{-3}}.$$

In acidic conditions ($\text{pH} < 6$) $\text{CO}_2(\text{aq})$ dominates, in basic conditions ($\text{pH} > 10.5$) CO_3^{2-} dominates, and in between HCO_3^- dominates.

The chemical reactions between these dissolved species are therefore often modelled by establishing the equilibrium pH and the equilibrium constants (which may be varied with temperature and pressure), plus either the total CO_2 in the system or one of the three species' concentrations, and then reading off the equilibrium concentrations of the other species from the appropriate Bjerrum plot. This method therefore assumes that these reactions follow the mass action law, that they are well mixed, and that they are fast compared to the reactions between dissolved CO_2 and minerals.

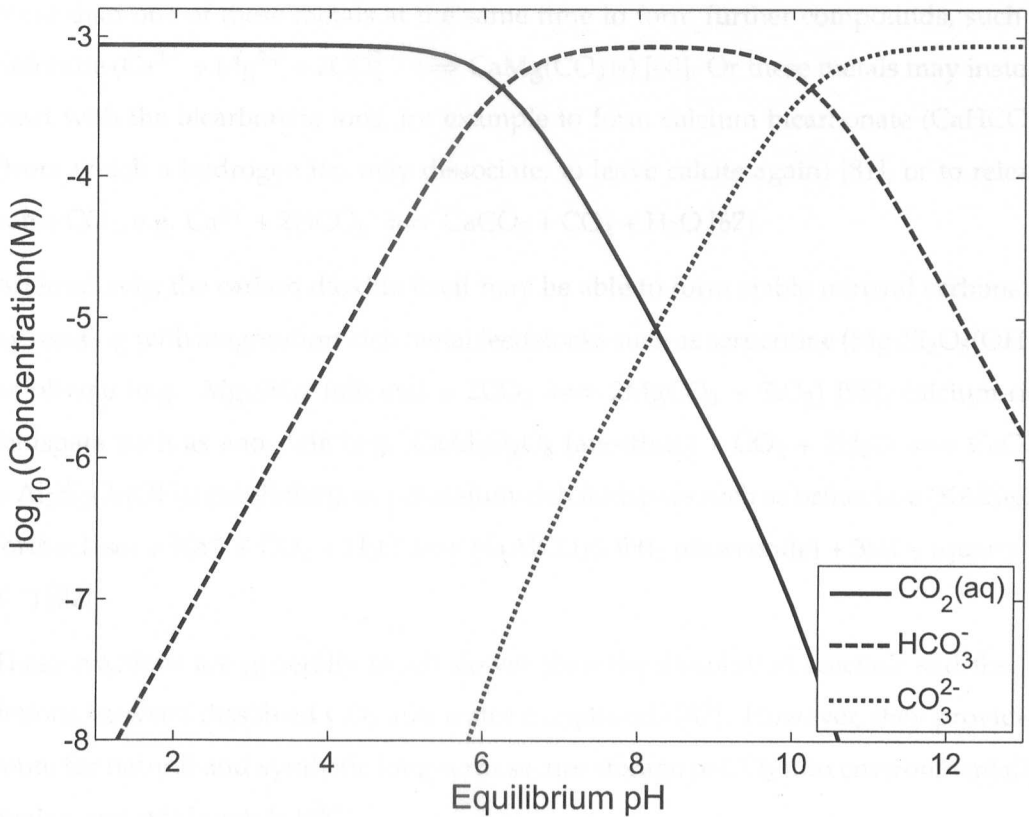


Figure 1.1: Example Bjerrum plot, using (1.7.5)-(1.7.7) and total $\text{CO}_2 = 8.75 \times 10^{-4} \text{ M}$.

This method also neglects any reactions not covered by (R2-4), although there are other reactions that may also happen. The solution contains water, hydrogen, and hydroxide ions (kept in balance through $\text{H}_2\text{O} \rightleftharpoons \text{H}^+ + \text{OH}^-$), and so some of the released hydrogen ions will combine with hydroxide ions to reform as water, which is one mechanism by which the pH can be buffered. Or, as an alternative to the carbonic acid route, $\text{CO}_2(\text{aq})$ can combine with OH^- ions, to form HCO_3^- directly [87], from which a hydrogen ion may dissociate.

1.7.3 Reactions between dissolved CO_2 and minerals

As there is a wide range of minerals within the seas and within different aquifers, so there is a wide range of reactions that can take place between the CO_2 , the dissolved species and these minerals. For example, the carbonate ions (CO_3^{2-}) may react directly with calcium, magnesium, iron, barium, or manganese, to form calcite, magnesium carbonate, siderite, witherite, or rhodocrosite, respectively. Carbonate may react with

more than one of these metals at the same time to form further compounds, such as dolomite ($\text{Ca}^{2+} + \text{Mg}^{2+} + 2\text{CO}_3^{2-} \rightleftharpoons \text{CaMg}(\text{CO}_3)_2$) [60]. Or these metals may instead react with the bicarbonate ions, for example to form calcium bicarbonate (CaHCO_3^+) (from which a hydrogen ion may dissociate, to leave calcite again) [81], or to release some CO_2 , e.g. $\text{Ca}^{2+} + 2\text{HCO}_3^- \rightleftharpoons \text{CaCO}_3 + \text{CO}_2 + \text{H}_2\text{O}$ [67].

Alternatively, the carbon dioxide itself may be able to form stable mineral carbonates by reacting with magnesium-rich metal feedstocks such as serpentine ($\text{Mg}_3\text{Si}_2\text{O}_5(\text{OH})_4$) or olivine (e.g. Mg_2SiO_4 (olivine) + $2\text{CO}_2 \rightleftharpoons 2\text{MgCO}_3 + \text{SiO}_2$) [95], calcium-rich feldspars such as anorthite (e.g. $\text{CaAl}_2\text{Si}_2\text{O}_8$ (anorthite) + $\text{CO}_2 + 2\text{H}_2\text{O} \rightleftharpoons \text{CaCO}_3 + \text{Al}_2\text{Si}_2\text{O}_5(\text{OH})_4$ (kaolinite)), or potassium-rich feldspars such as orthoclase (KAlSi_3O_8 (orthoclase) + $\text{Na}^+ + \text{CO}_2 + \text{H}_2\text{O} \rightleftharpoons \text{NaAlCO}_3(\text{OH})_2$ (dawsonite) + 3SiO_2 (quartz) + K^+) [82].

These reactions are generally much slower than the dissolution reaction and the reactions between dissolved CO_2 and water compounds [82]. However, they provide a route for natural and synthetic long-term secure storage of CO_2 into environmentally-benign and stable solids [95].

The reaction between carbonate ions and calcium, to form calcium carbonate,



is one of the most important mineralization reactions, because calcium is one of the more abundant metals in the sea and in saline aquifers (e.g. [63]), because calcium carbonate is a useful product (and so this process may be considered in an above-ground industrial process), and because it is this reaction that reflects the threat of ocean acidification to the survival of tiny marine organisms, as a reduction in the availability of carbonate impairs their ability to form biogenic calcium carbonate, their basic building block.

This reaction has been found to proceed at a rate proportional to the product of the concentrations in the forward, crystallization, direction [68], and so is also assumed to follow the mass action law in the reverse direction, i.e.

$$-\frac{d[\text{Ca}^{2+}]}{dt} = -\frac{d[\text{CO}_3^{2-}]}{dt} = \frac{d[\text{CaCO}_3]}{dt} = k_5[\text{Ca}^{2+}][\text{CO}_3^{2-}] - k_{-5}[\text{CaCO}_3].$$

The thermodynamic equilibrium constant, $K_5^* \equiv a_{\text{CaCO}_3} / a_{\text{Ca}^{2+}} a_{\text{CO}_3^{2-}}$, has been used for this reaction [90, 96], and this also implies that this reaction follows the mass action law.

Constant	Magnitude	Conditions	Source
k_5	$1.9 \times 10^{-2} \text{ mol cm}^{-2} \text{ s}^{-1}$	-	[76]
k_{-5}	$6.5 \times 10^{-11} \text{ mol cm}^{-2} \text{ s}^{-1}$	-	[76]
$K_5 = k_5/k_{-5}$	1590 M^{-1}		[97]
K_5^*	1674.94	-	[78]
	1659.59	25°C, infinitely-dilute	[90]
	$10^{(-1228.732 - 0.299444 T + 35512.75 T^{-1} + 485.818 \log T)}$	5-80°C	[73, 96]
	(= 1670.27 at $T=298\text{K}$)		

Table 1.5: Kinetic parameter estimates for reaction (R5).

Some estimates for the values (and units) of the kinetic parameters for this reaction are given in Table 1.5.

1.8 Aquifer-scale fluid mechanics of CCS

One route to understanding what happens to CO_2 injected into a saline aquifer is to consider the aquifer-scale fluid mechanics only, i.e. ignore the chemical reactions and the dissolution of CO_2 into the aquifer water, but treat the CO_2 and water as two immiscible fluids, and see how the CO_2 spreads out through the aquifer as a gravity current. Many different scenarios have been studied within this approach, including instantaneous or continuous injections, point or line injection sources, horizontal or sloping aquifer boundaries, an aquifer fluid with uniform permeability or an aquifer that contains local low-permeability layers, an aquifer with or without vertical fault lines, and injecting only CO_2 or injecting CO_2 with water.

However, aquifer-scale models of these CO_2 flows nearly always have a near-zero Reynolds number. For example, the flow of a fluid that has dynamic viscosity $\mu = 0.04 \text{ MPa}\cdot\text{s}$ and density $\rho = 1000 \text{ kg/m}^3$, through pore spaces with diameter $L = 1 \text{ mm}$, at a mean velocity of $U_0 = 1 \text{ m/day}$, has Reynolds number (defined as $\rho U_0 L / \mu$) 2.9×10^{-10} . Darcy's Law is therefore the normal starting place for modelling these slow, viscous pore-space flows. In three dimensions, this is expressed as:

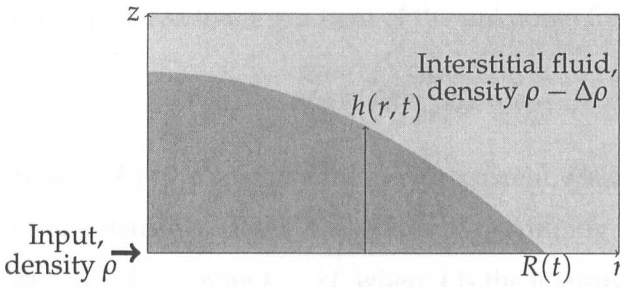


Figure 1.2: Gravity current intruding into a less dense fluid, from [49].

$$\mathbf{u} = \frac{-\mathbf{k}}{\mu} \cdot (\nabla p - \rho \mathbf{g}), \quad (1.8.1)$$

where \mathbf{u} is the velocity vector, \mathbf{k} is the permeability tensor, μ is the dynamic viscosity, ∇p is the pressure gradient, ρ is the density of the current, and \mathbf{g} is acceleration due to gravity. The minus sign in front of \mathbf{k} indicates that the current flows from high to low pressures. Faster flows are caused by a greater permeability, a smaller viscosity, or a greater pressure gradient.

From this starting point, thorough modelling of one of the most straightforward scenarios is provided in [49] – the point injection of a relatively heavy fluid of total volume $V = Qt^\alpha$, where t is time and Q and α are constants (so $\alpha = 0$ indicates a single instantaneous injection, and $\alpha = 1$ indicates a continuous injection), into the bottom of an axisymmetric, uniform, saturated, porous and permeable medium initially containing a slightly lighter fluid, immediately above a horizontal impermeable layer. (This is equivalent to the injection of a relatively light fluid into the top of a porous medium, immediately below a horizontal impermeable layer, which could be a typical CO_2 injection scenario.) This scenario is illustrated in Figure 1.2.

It is assumed that the injected fluid's horizontal velocities are greater than vertical velocities, and so the current is long and thin. This scenario therefore models a radial flow driven by a radial pressure gradient that seeks to make the injected fluid completely flat, and is thus a function of the weight of the fluid (above the weight of the resident water) and the steepness of the face of the spreading current. If $g' = g\Delta\rho/\rho$ is the reduced gravity, where $\Delta\rho$ is the difference between the densities of the injected fluid and the aquifer's ambient fluid, then with reduced gravity balancing the pressure gradient force (hydrostatic equilibrium), $\partial p/\partial z = -\rho g'$. The radial pressure gradient

driving the flow is related to the gradient of the unknown free surface by

$$\frac{\partial p}{\partial r} = \rho g' \frac{\partial h}{\partial r}, \quad (1.8.2)$$

where p is pressure, h is the height of the gravity current, r is distance from the injection point, and ρ is the density of the injected fluid. Substituting (1.8.2) into the horizontal component of (1.8.1) (assuming $\mathbf{k} = k\mathbf{I}$, where \mathbf{I} is the identity matrix), gives

$$u = \frac{-k}{\mu} \frac{\partial p}{\partial r}, \quad (1.8.3)$$

where u is the horizontal component of the velocity. The local continuity condition is

$$\phi \frac{\partial h}{\partial t} + \frac{1}{r} \frac{\partial}{\partial r} (r u h) = 0, \quad (1.8.4)$$

and substituting (1.8.2) into (1.8.3), and the result into (1.8.4) gives the following porous medium equation (a nonlinear diffusion equation) to describe the evolution of h :

$$\frac{\partial h}{\partial t} = \frac{\gamma}{r} \frac{\partial}{\partial r} \left(r h \frac{\partial h}{\partial r} \right) \quad 0 < r < R(t), \quad (1.8.5)$$

where $\gamma = k\rho g' / \phi\mu$, and has units m/s. This system is closed by giving the boundary condition $h[R(t), t] = 0$ (i.e. the height of the current at the nose is zero), and the following global continuity condition (given below in the corrected form given later by [58])

$$2\pi\phi \int_0^{R(t)} r h \, dr = Qt^\alpha. \quad (1.8.6)$$

This system is then solved by means of the following similarity solution [98]:

$$R(t) = \eta(\alpha)(\gamma Q/\phi)^{1/4} t^{(\alpha+1)/4}, \quad (1.8.7)$$

where η is a function of α only. This therefore describes how far an injected fluid will have spread from the injection point after a given time, and its rate of propagation – an instantaneous injection spreads like $t^{1/4}$, and a continuous injection spreads like $t^{1/2}$. It also gives the appropriate scaling to define its exact shape. A series of laboratory experiments were conducted to test this theoretical modelling, and there was found to be good agreement between the experimental data and theoretical predictions.

In an earlier work [48], a series of solutions were developed to model a series of more complex fluid flow scenarios, including instantaneous and continuous injections of

buoyant fluid into a shallow permeable layer, with fixed and variable permeabilities, above horizontal and sloping impermeable boundaries. Again, starting from (1.8.1), and combining this with conservation of mass $\nabla \cdot \mathbf{u} = 0$, local and global continuity conditions similar to (1.8.4) and (1.8.6), and boundary conditions suitable to each specific scenario, a series of similarity solutions were developed which give the shapes of the spread of the fluid as a function of time. A series of laboratory experiments using a Hele-Shaw cell were also performed to verify some of the theoretical predictions.

This modelling is appropriate for any fluid intruding below a less dense fluid or above a denser fluid. The behaviour of CO_2 specifically has been examined in a model of the movement of the interface between injected CO_2 and the surrounding water, as the CO_2 grows in volume and spreads laterally between two horizontal impermeable boundaries [99]. Injection is horizontal into the whole height of the water, and buoyancy causes the injected fluid to rise above the surrounding water. By allowing for miscibility and mass transfer between the two fluids, and the development of a drying front behind the main injection front, a series of similarity solutions were developed to model a series of injection scenarios, and found to compare well with numerical simulations of the flow dynamics of CO_2 injection.

The CO_2 currently being injected at Sleipner, North Sea, has been modelled [58] using the modelling for the axisymmetric flow of a buoyant fluid released into a porous medium below a horizontal boundary mentioned above [49]. This modelling is adjusted to reflect the fact that the Sleipner field is not uniform, but as the CO_2 rises buoyantly, it reaches a series of thin, low-impermeability layers, under which it pools and spreads horizontally, before breaking through. As above, this modelling predicts that the radii of the pools are proportional to the square root of time, and also predicts that the thickness close to the centres of the pools is nearly invariant. Seismic imaging shows that the highest layers of CO_2 appear to have started accumulating up to three years after October 1996 (when injection commenced), and their CO_2 input has increased with time. However, some of the lower pools appear to have shrunk in recent years, indicating that the leakage upwards has started overtaking the rate of influx from below.

Also based on the Sleipner injections, an attempt has been made to quantify the proportion of CO_2 trapped below a series of horizontal low-permeability layers in a saline

solution [100], to provide insight into whether an injected quantity of CO_2 would be mainly retained below its first layer of rock (and spread only laterally), or whether it would tend to ascend through the layers (as well as laterally). This was achieved by combining models of capillary retention with models of upward drainage. Allowances were made for the slope, permeability, porosity, and thickness of the horizontal layers. Calculations based on a typical example indicate that about 10-20% of the injected CO_2 that reaches a low-permeability boundary will remain trapped below it, with the rest draining vertically upwards.

Modelling the aquifer-scale fluid mechanics has been reasonably successful. For example, seismic imaging at Sleipner [58] shows there to be good agreement on the whole between the modelling and the imaging of the CO_2 pools. However, there are discrepancies, for example between the measured and estimated reservoir permeabilities. These discrepancies could be due to the limitations in the modelling that arise from considering only the fluid mechanics. The chemical reactions affect critical aquifer parameters such as density, viscosity, pH, porosity and permeability, and so omitting the reactive chemistry could produce inaccurate results. We now consider pore-scale models of water transport relevant to CCS.

1.9 Pore-scale water transport for CCS

If a stream of supercritical CO_2 is continuously injected into an aquifer, it forms a drop (a mass of CO_2 molecules) in the pore space. The drop is forced to spread out through the aquifer by further CO_2 being injected behind it. Rather than considering a stationary pore space and a moving drop, at the pore scale it can be easier to consider the alternative frame of reference of a stationary drop with the walls moving towards the drop dragging a stream of resident water with them. There may also be a groundwater flow that augments the pressure gradient flow on one side of the drop, and diminishes it the other side of the drop.

Suppose the pore is represented by a two-dimensional long thin straight channel of fixed width $2a$, parameterized by two independent spatial variables, length $-\infty < x^* < \infty$, and height $-a \leq y^* \leq a$, where $*$ denotes a dimensional variable. The front of the drop is stationary, and the origin is defined to be the centre of this front. The pore

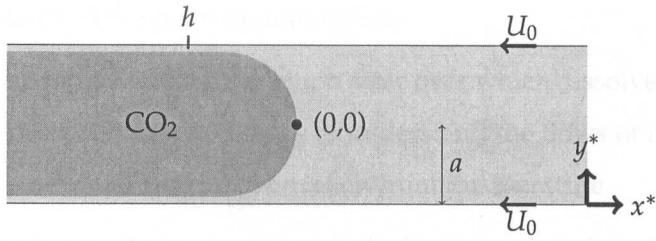


Figure 1.3: CO₂ drop in water-filled aquifer pore space, with thin film between CO₂ drop and wall.

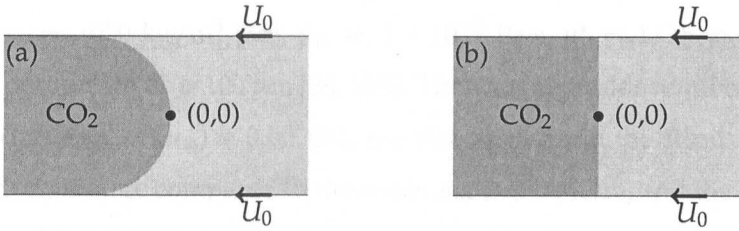


Figure 1.4: CO₂ drop in water-filled aquifer pore space, without thin films, and with (a) close to zero and (b) 90° contact angles between drop and wall.

walls move towards and past the drop at constant velocity $\mathbf{U} = (-U_0, 0)$.

Figure 1.3 shows the case when the water wets the pore walls preferentially to the CO₂, and so there is a thin film of water of width h between the CO₂ and the pore walls. The CO₂ forms a long drop in the channel, as described by Bretherton [101]. With a circular end to the drop, the distance between the drop and pore wall decreases in the direction of the flow, and the behaviour in the film is described by lubrication theory [102, 103]. With a large drop, the drop's length is many times the channel radius, and the ratio h/a is a function of the capillary number ($Ca \equiv \mu U_0 / \gamma$, where μ is the water's viscosity, and γ is surface tension) [104], given by $h \propto Ca^{2/3}$ as $Ca \rightarrow 0$ [101] (i.e. at low speeds). In this limit, the width of the thin film increases with the velocity of the walls. In this frame of reference (a stationary drop and travelling pore space and resident water), water leaks through the film, giving a non-zero net flux through the pore.

In the case when the CO₂ wets the pore walls preferentially to the water, the thin film disappears ($h = 0$). With the same frame of reference, there is no water leakage down the sides of the drop, and there is zero net flux of water through the pore. Figure 1.4 shows two such cases, when the contact angle between the drop and wall is (a) close to zero and (b) 90°. In these cases, the undissolved CO₂ is in contact with the moving pore walls, and this boundary comprises a moving contact-line problem [105–107], with a

shear-stress singularity at the point of intersection.

To make progress in understanding the length scale over which dissolved CO₂ stretches out in front of the drop, it is first necessary to understand the flows of the water which carries the CO₂. These water flows can be taken from the literature.

Let ρ_w be the water's density, μ_w be the water's dynamic viscosity, $p^*(x^*, y^*)$ denote pressure, and $\mathbf{u}^*(x^*, y^*) = (u^*, v^*)$ be the water velocity within the pore. The water is an incompressible viscous Newtonian fluid, and characteristic parameter values are as follows: $\rho_w = 1050 \text{ kg/m}^3$ [36], $\mu_w = 1 \times 10^{-3} \text{ Pa.s}$, $u^* = 1/15 \text{ m/day}$ [36], and suppose the pore width $2a$ is $100 \text{ }\mu\text{m}$ [36, 108]. Then the Reynolds number for the water flow (defined as $\rho_w u^* 2a / \mu_w$) is 0.000081, the viscous term in the steady state Navier-Stokes equations is large compared to the nonlinear inertia term, and the Navier-Stokes equations simplify to the Stokes flow equations (with no body forces):

$$\nabla \cdot \mathbf{u}^* = 0, \quad (1.9.1)$$

known as the continuity equation, and

$$\nabla p^* = \mu_w \nabla^2 \mathbf{u}^*, \quad (1.9.2)$$

known as the momentum equation.

1.9.1 Flows far in front of the CO₂ drop

Far in front of the CO₂ drop, with uni-directional flow in a long thin horizontal channel, $v^* = 0$, and the x^* and y^* components of equation (1.9.2) respectively give

$$\frac{\partial p^*}{\partial x^*} = \mu_w \frac{\partial^2 u^*}{\partial y^{*2}} \quad \text{and} \quad \frac{\partial p^*}{\partial y^*} = 0.$$

Therefore p^* is a function of x^* only. Integrating the first of these two equations twice with respect to y^* , and imposing the boundary conditions $u^* = -U_0$ on $y^* = \pm a$, gives

$$u^* = -U_0 + \frac{p_{x^*}^*}{2\mu_w} (y^{*2} - a^2), \quad (1.9.3)$$

where $p_{x^*}^* \equiv dp^*/dx^*$.

The flux through the channel is

$$Q = \int_{-a}^a u^* dy^* = -2aU_0 + \frac{p_{x^*}^*}{2\mu_w} \left[\frac{y^{*3}}{3} - y^* a^2 \right]_{y^*=-a}^{y^*=a} = -2aU_0 - \frac{2p_{x^*}^* a^3}{3\mu_w}.$$

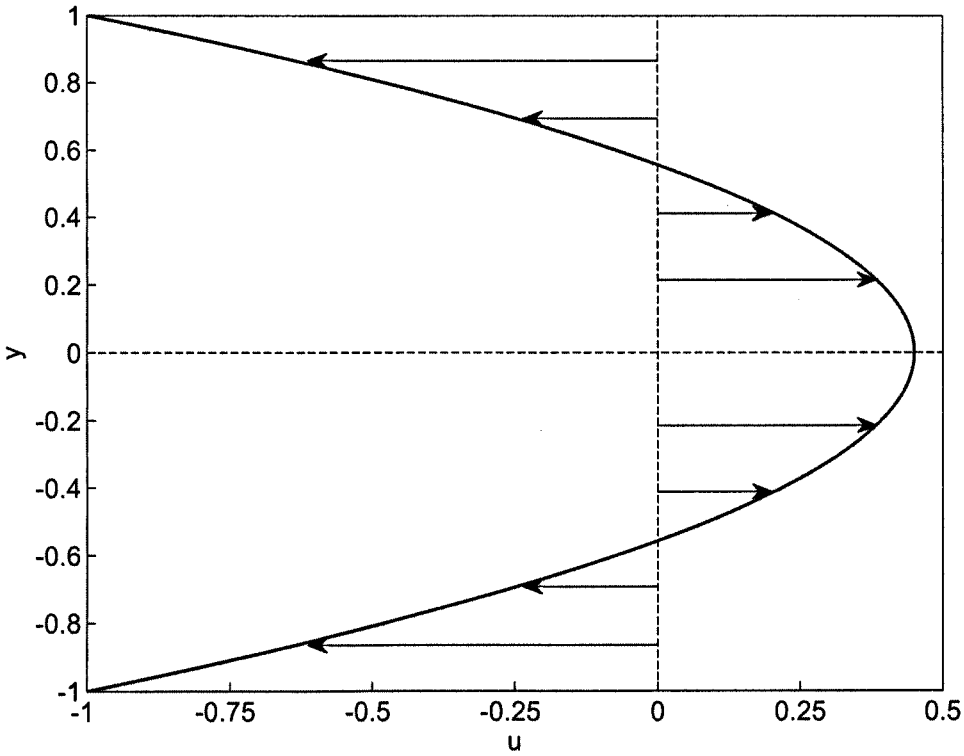


Figure 1.5: Example water flow field far in front of the CO₂ drop, using equation (1.9.4), $y \equiv y^*/a$, $u \equiv u^*/U_0$, and $h/a = 1/30$.

With the interface between the CO₂ drop and the water forming a boundary near $x^* = 0$, except for thin films of width h (e.g. Figure 1.3), the total flux through the two thin films between the CO₂ drop and the pore wall also equals $-2U_0h$. This gives $p_{x^*}^* = 3U_0(h-a)\mu_w/a^3$, and so the flow field equation (1.9.3) becomes

$$u^* = -U_0 + \frac{3U_0(h-a)}{2a^3}(y^{*2} - a^2) = -U_0 \left(1 + \frac{3}{2} \left(1 - \frac{h}{a} \right) \left(\frac{y^{*2}}{a^2} - 1 \right) \right). \quad (1.9.4)$$

Figure 1.5 gives an example flow field in dimensionless variables $y \equiv y^*/a$ and $u \equiv u^*/U_0$, for $h/a = 1/30$. The water's flow field is quadratic in y – by the sides of the channel it flows with the channel walls towards the end boundary, and in the centre of the channel it flows contrary to the channel walls and away from $x^* = 0$. This parabolic distribution is a Poiseuille velocity field with a return flow, as the boundary near $x^* = 0$ ensures the net flux through the channel is small. Increasing h/a increases the net flux through the channel, and reduces the strength of the reverse flow.

The case $h/a > 0$ in equation (1.9.4) is relevant to the non-zero flux scenario shown in Figure 1.3, and applying the limit $h/a \rightarrow 0$ to equation (1.9.4) (giving $u = -(3y^2 -$

1)/2), corresponds to the zero flux scenarios shown in Figure 1.4.

1.9.2 Flows immediately in front of the CO₂ drop, with no thin film

The long thin channel assumption does not hold in a region immediately in front of the drop, stretching from the front edge of the drop up to a distance in front of the drop approximately equal to the pore width. The particular case of no thin film, and a 90° contact angle between CO₂ drop and pore wall (illustrated by Figure 1.4(b)), with a non-wetting boundary, is perhaps the most straightforward to consider. The flows within a rectangular domain with no leakage have been considered by a number of authors, for example the flow at the end of a 2-d channel caused by a moving piston [109], or the flow in a channel with two stationary boundaries and two boundaries that move in opposite directions [110]. The piston problem enables a good first approximation to be obtained for the flows immediately in front of the drop.

The variables in the Stokes flow equations ((1.9.1) and (1.9.2)) are non-dimensionalised as follows:

$$x = \frac{x^*}{a}, \quad y = \frac{y^*}{a}, \quad u = \frac{u^*}{U_0}, \quad v = \frac{v^*}{U_0}, \quad P = \frac{p^* a}{\mu_w U_0},$$

and the dimensionless boundary conditions are as follows:

- Zero velocity perpendicular to, and zero stress tangential to, the surface of the drop (i.e. $u = 0$ and $v_x = 0$ on $x = 0$). (A zero stress condition is legitimate as the viscosity of supercritical CO₂ (~ 0.06 mPa.s [45]) is much less than the viscosity of the water (~ 1 mPa.s).) (1.9.5)

- In the frame of reference of a stationary drop, the walls move past at a constant velocity $(-U_0, 0)$, (i.e. $u = -1$ and $v = 0$ on $y = \pm 1$). (1.9.6)

- Far in front of the drop, substituting $h = 0$ into (1.9.4) gives $u \rightarrow (1 - 3y^2)/2$ and $v \rightarrow 0$ as $x \rightarrow \infty$. (1.9.7)

The flow of the water immediately in front of the drop, and its transition to the downstream profile, is described using a stream function $\psi(x, y)$, defined as follows (which ensures that conservation of mass (1.9.1) is satisfied):

$$\psi_y \equiv \frac{\partial \psi}{\partial y} = u, \quad \psi_x \equiv \frac{\partial \psi}{\partial x} = -v.$$

The momentum equation (1.9.2) gives

$$\frac{\partial P}{\partial x} = \frac{\partial^2 u}{\partial x^2} + \frac{\partial^2 u}{\partial y^2} = \psi_{yxx} + \psi_{yyy}, \quad (1.9.8)$$

$$\frac{\partial P}{\partial y} = \frac{\partial^2 v}{\partial x^2} + \frac{\partial^2 v}{\partial y^2} = -\psi_{xxx} - \psi_{xyy}. \quad (1.9.9)$$

Differentiating (1.9.8) with respect to y and (1.9.9) with respect to x , and equating, gives $\psi_{xxxx} + 2\psi_{xxyy} + \psi_{yyyy} = 0$, which is the 2-d biharmonic equation $\nabla^4 \psi = 0$. This equation has been investigated in the context of the bending of a clamped elastic rectangular plate at least since Mathieu [111], often using Fourier series. An alternative approach was initiated by Dougall [112], who deployed a generalization of eigenfunction expansions [113]. This approach was popularized 36 years later in 1940, by two papers published independently by Papkovich [114] and Fadle [115], and used subsequently in rectangular semi-infinite elastic strip problems (e.g. [116]), and Stokes flow fluid mechanics problems in rectangular domains (e.g. [117]). Later authors established existence, completeness, and convergence conditions for orthogonal Papkovich-Fadle eigenfunctions in elastic rectangular strips [118] and Stokes flow problems [119, 120].

Following Spence [117], Phillips [121], and Katopodes, Davis and Stone [109], we suppose ψ takes the following form,

$$\psi(x, y) = \frac{y}{2} - \frac{y^3}{2} + \sum_{n=-\infty}^{\infty} A_n Y_n(y) \exp(-m_n x), \quad (1.9.10)$$

where $Y_n(y)$, A_n and m_n are to be determined ($Y_n(y)$ are the orthogonal Papkovich-Fadle eigenfunctions, and A_n and m_n are constants with $A_n, \text{Re}(m_n) > 0$). Then ψ gives the correct downstream profile ((1.9.7) is satisfied). Applying the biharmonic equation to (1.9.10) and the boundary conditions above, to find the constants and the orthogonal Papkovich-Fadle eigenfunctions (details are given in Appendix 1.A at the end of this Chapter), gives

$$\psi(x, y) = \frac{y}{2} - \frac{y^3}{2} + \sum_{n \neq 0, n = -\infty}^{\infty} \frac{-1}{m_n \tan(m_n)} \left(\frac{\sin(m_n y)}{\sin(m_n)} - y \frac{\cos(m_n y)}{\cos(m_n)} \right) \exp(-m_n x), \quad (1.9.11)$$

where m_n are the roots of the transcendental equation $0 = \cos(m_n) \sin(m_n) - m_n$ with positive real part (also given in Appendix 1.A).

The same number of negative n 's as positive n 's must be taken to ensure that the complex parts of (1.9.11) cancel out. For the vast majority of points in the plane, ψ converges

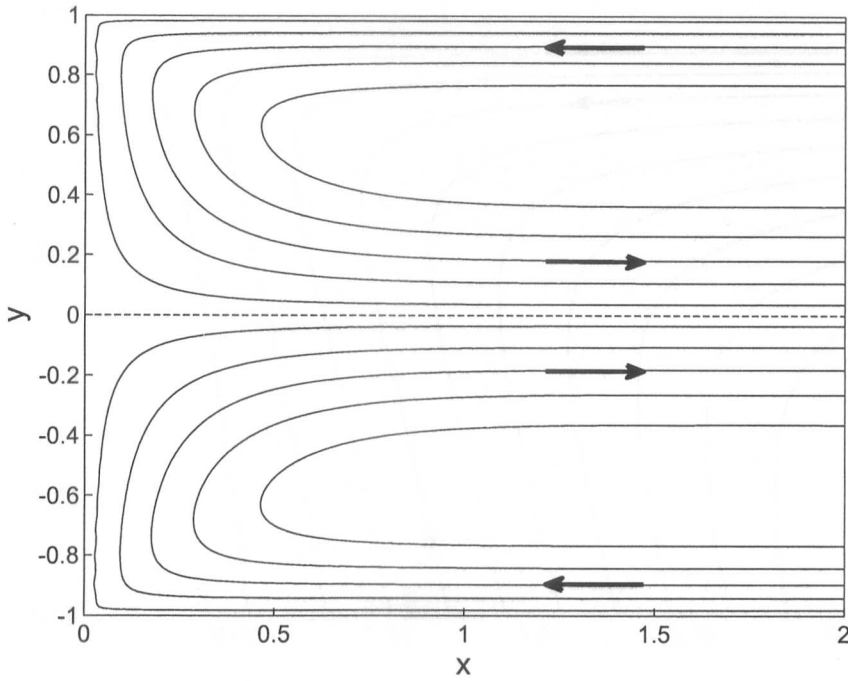


Figure 1.6: Water streamlines (1.9.11), with pore walls at $y = \pm 1$ travelling towards the stationary CO_2 drop at $x = 0$.

rapidly with increasing n . ψ is plotted in Figure 1.6, showing the streamlines for the flow in this zone as the water flows with the walls towards the end boundary, and against the walls at the centre of the channel, with $-20 \leq n \leq 20$, which is sufficient.

As Figure 1.6 illustrates, water is drawn towards the drop near the channel walls, then passes along the interface between drop and water, before flowing away from the drop. It can therefore collect CO_2 that dissolves from the drop into the water, and carry this CO_2 away from the drop. Understanding how far this dissolved CO_2 travels from the drop is of interest in understanding CCS.

Substituting $y = \pm 1$ into (1.9.11) gives the single points where $\psi = 0$, and these singularities mean that the solution does not converge as well near the corners. This can be seen by the slightly under-resolved streamlines near the corners in Figure 1.6. The flows of a viscous fluid near a sharp corner with no leakage can be much better represented by a stream function defined in polar σ -ordinates (r, θ) , where θ is the angle from the horizontal, and r is the distance from an origin comprising the point of contact between a plane (at $\theta = 0$), which is scraped at constant velocity U past another stationary plane positioned at angle $\theta = \alpha$ (the 'Taylor scraper' [122]). Dimensional analysis

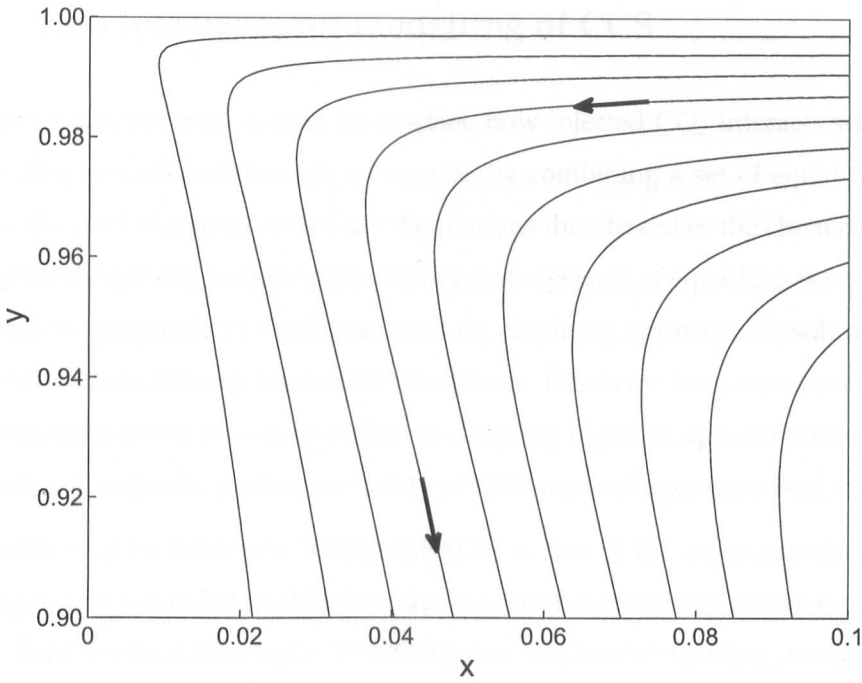


Figure 1.7: Top corner water streamlines ($\psi = rf(\theta)$ with $\alpha = \pi/2$ and $f(\theta)$ given by (1.9.12)), with pore walls at $y = \pm 1$ travelling towards the stationary CO_2 drop at $x = 0$.

shows that ψ (once scaled on U) must be of the form $\psi = rf(\theta)$, where $f(\theta)$ is to be determined. The corresponding radial and tangential velocities are:

$$\frac{1}{r} \frac{\partial \psi}{\partial \theta} = f'(\theta) \equiv u, \quad \frac{\partial \psi}{\partial r} = f(\theta) \equiv -v.$$

At $\theta = 0$, $u = 1$ and $v = 0$, and at $\theta = \alpha$, $u = 0$ and $v_r = 0$, and so the boundary conditions are $f'(0) = 1$, $f(0) = 0$, $f'(\alpha) = 0$, and $f(\alpha) = 0$. Applying the biharmonic equation $\nabla^4 \psi = 0$ gives $(f + 2f'' + f'''')/r^3 = 0$ [123], and this has solution $f(\theta) = c_1 \sin \theta + c_2 \cos \theta + c_3 \theta \sin \theta + c_4 \theta \cos \theta$, where c_1 to c_4 are constants determined by matching to the boundary conditions. This gives:

$$f(\theta) = \frac{\alpha(\theta - \alpha) \sin \theta - \theta \sin(\theta - \alpha) \sin \alpha}{\sin^2 \alpha - \alpha^2}. \quad (1.9.12)$$

(Note that this result contains a typo in Moffatt^e [124] – the fifth α in equation (2.1) should be a θ .) Substituting in $\alpha = \pi/2$, and using $r = \sqrt{x^2 + y^2}$ and $\theta = \tan^{-1}(y/x)$, gives the flow field at every point (x, y) , shown in Figure 1.7.

1.10 Reactive transport modelling of CCS

Reactive transport models seek to describe how injected CO_2 interacts with resident water, and spreads out through an aquifer, by combining a set of equations that describes the fluid transport with a set of equations that describes the chemical reactions. Understanding the behaviour produced by such systems of equations is very challenging, and the emphasis in the literature is on obtaining approximate solutions to particular situations through numerical simulation. This is far from easy, and as there are different approaches that can be taken to coupling together, approximating, and solving these two sets of equations, a variety of software packages have been constructed.

TOUGH2 (and its successor TOUGHREACT) is one of the more popular simulation packages, and was developed by introducing reactive chemistry into an existing multi-phase fluid and heat-flow code. TOUGH2 uses 'sequential iteration', which decouples and solves separately the reaction equations and the transport equations during a time step, but aims to arrive at a fully coupled solution at the end of each time step. The fluid transport solutions are based on spatial discretization by means of integral finite differences, and the chemical reaction solutions are obtained using a Newton-Raphson iterative finite difference method. Non-dissolved, precipitating and dissolving species may be modelled using either local equilibrium or kinetic laws, but aqueous chemical species must be modelling by assuming local equilibrium [81, 125]. A number of authors have used this package to simulate CO_2 injection.

For example, it has been used to form a conceptual model of the geology of the Colorado Plateau, Utah. The injection of 5m tonnes CO_2 /year for 30 years was simulated, to investigate how much of the CO_2 was permanently sequestered as a mineral, and how much leaked to the surface [126].

In a second example, TOUGH2 was used to simulate what might happen should CO_2 leak to the atmosphere in a variety of seepage scenarios and atmospheric conditions, by coupling together modelling of the vadose subsurface zone with modelling of the surface layer of the atmosphere [127]. The simulations indicate that the atmospheric concentration of CO_2 is likely to be diluted down to negligible concentrations fairly quickly, and the CO_2 can actually be returned to the subsurface by rainfall.

TOUGH2 was also used to simulate the injection of CO_2 into the Rio Vista natural gas

(methane) reservoir, California, to analyse the benefits of using carbon sequestration to achieve enhanced gas recovery (CSEGR) [128]. The large density and viscosity differences between CO_2 and CH_4 mean that CO_2 will tend to migrate downward relative to CH_4 , and there will be no extensive mixing between the two gases over the timescales of interest. Therefore, these simulations are based on relatively simple chemical reactions and ratios of the different species in different phases, but relatively complex fluid mechanics, including both advection and molecular diffusion for both the gas and liquid phases. The simulations show that the repressurization within the reservoir, caused by injecting CO_2 , means that CSEGR allows more than five times the mass of CH_4 to be recovered relative to that provided without CSEGR.

In contrast to this, one study into the interactions at Sleipner between injected CO_2 and the caprock uses complex models for the chemical reactions, but relatively straightforward models of the fluid mechanics (it is assumed that diffusion is the only mass transport mechanism at work in the cap rock) [129]. This study uses the software PHREEQC [130] to assess the amount of CO_2 permanently precipitated as carbonate minerals, and the impact on the porosity (and therefore permeability) of the caprock. A range of 15 minerals is included, including predominantly quartz, illite and kaolinite, and a kinetic rate law for the dissolution and precipitation of each mineral is specified, which is dependent on the reactive surface area, the temperature, the proton activity, the equilibrium constant, and the corresponding ion activity products. The diffusion into the cap rock is given by Fick's law for diffusion in sediments, $J = -D'_d \nabla(C)$, where J is the diffusional flux, D'_d is the effective diffusion coefficient, and C is concentration. It is concluded from the simulations that there is some initial carbonate dissolution, but the dominant long-term reaction is feldspar alteration. Also, diffusion into the cap rock is a slow process, and these reactions cause a slight decrease in the cap rock's porosity (and therefore permeability).

As interest in carbon sequestration has arisen only relatively recently, codes that have been developed for other purposes can be adapted to model CCS at the particular location they describe. For example, FEHMN (the Finite Element Heat Mass and Nuclide code) was developed to describe groundwater flow and radionuclide transport at Yucca Mountain, Nevada, in order to assess the safety of a potential radioactive waste repository located there [131]. In contrast to the finite differencing of TOUGH2,

FEHMN numerically solves the heat and mass transfer equations for multiphase flow in porous and permeable media using more powerful finite element methods [132]. Discretizing the governing partial differential equations onto a three-dimensional finite element mesh yields a system of nonlinear equations, and these are solved using a Newton-Raphson procedure.

There are many other packages that have been constructed to perform grid-based simulations of the pore-scale behaviour, in order to answer aquifer-scale questions, such as how far through the aquifer the CO₂ will spread out, and how much will dissolve into aquifer water. These include PFLOTRAN [133], CHILLER [134, 135], Hytec [136], and Geochemist's Workbench [137]. An alternative is to take a streamline-based approach to simulations [75]. A recent review of CO₂ modelling and simulation summarises 23 different simulators [138]. There are therefore many different ways that approximate numerical solutions have been found to proposed sets of transport and reaction partial differential equation models of carbon sequestration, and different methods have different strategies for deciding what to solve and what to approximate, and the approximations can be done in different ways.

Benchmarking the results from one software package (comparing them to the results from a different package), is therefore very difficult. The methods used by the different software programs are often extremely complicated, and require complicated programs, which can make independent testing of the programs very difficult. This also means that the programs effectively become black boxes where users may not understand how the programs work and to what situations they strictly apply, which makes it extremely easy to use them inappropriately, and to accept incorrect output. In addition, these problems are compounded by the fact that validating simulation results can be extremely difficult, due to the inaccessibility of deep saline aquifers. It can therefore be hard to assess how much trust can be placed in simulations of future events.

One part of the solution to these problems is to improve the understanding of the fundamental underpinning reaction and transport processes, so there is a better understanding of what can be expected to happen before the simulation programs are employed. One way this can be achieved is through an analytic investigation of the pore-scale behaviour of CO₂ dispersal within a saline aquifer.

1.11 Summary

There are two fundamental aspects to modelling what happens to CO_2 once it has dissolved into the oceans or been injected into a saline aquifer – the fluid mechanics and the chemical reactions. These two aspects both heavily affect each other, and errors in one aspect can rapidly feed back into the rest of the model. The most accurate reactive transport models therefore reflect the complexity of both the fluid flow and the chemical reactions. However, deriving and solving such models, either analytically or numerically, is extremely challenging, due to the wide range of temporal and spatial scales, the heterogeneity of the saline aquifer or ocean, and the difficulties with validating models. There is an urgent need to develop ways of making it easier to include both complex chemical reactions and complex fluid transport within reactive transport models.

Aquifer-scale CCS models containing detailed fluid mechanics, with either simplified geochemical reactions, or often no chemistry at all, can sometimes be solved analytically. Significant work has been carried out in understanding aquifer-scale average Darcy flows with no reactive chemistry. Smaller-scale (e.g. pore-scale) reactive transport models, which include both fluid mechanics and reactive chemistry, often have to be solved approximately and numerically for specific scenarios using complex simulation programs, due to the complexities of these models. These models often include either detailed geochemical fluid-rock interactions with complex mineralogies and reaction kinetics, coupled to simplified flow, or simplified chemistry with complex flow.

Complementing the models that have been studied extensively that contain just fluid mechanics, in Chapter 2 we investigate in detail just the main chemical reactions that happen as a result of CO_2 dissolution into water. Whenever chemical reactions are included in models, a local equilibrium is often assumed for reactions known to be ‘fast’, and equations from the kinetics are written down for reactions known to be ‘slow’. However, this gives concentrations which are functions of each other and the equilibrium constants, and it can be difficult to include more than a few ‘slow’ reactions. One way of improving reactive transport modelling is therefore to find simpler ways of describing the kinetics of the chemical reactions, by finding expressions for the concentrations which are functions of time and the initial conditions only.

The complexities of models that include both detailed reaction kinetics and detailed flow mean that attempts to understand reactive transport models in ways that apply to a wide range of CO₂ injection scenarios (rather than just particular individual scenarios), are rare. Therefore, in Chapter 3 we investigate what happens in a CCS scheme at the pore scale, using models that apply to a range of sequestration scenarios, and include both fluid mechanics and reactive chemistry. Once CO₂ has been injected into a pore, it dissolves from the ends of the drop into the resident water and is carried away, and the aim of the modelling is to establish the length scales over which the CO₂ that has dissolved from the drop into the water spreads out from the front of the drop, which the pressure gradient is causing to spread out horizontally.

Carrying out laboratory experiments, and understanding the results they produce, is also important in understanding what happens to CO₂ injected into a saline aquifer formation. In Chapter 4 we provide modelling for experiments which have recently been carried out at the University of Nottingham to investigate the changes in pH, and the concentrations of carbonic species and calcium ions, that occur in limestone saturated with water, as a result of gaseous CO₂ being bubbled up through the water/limestone mix, reacting as it travels. The modelling predictions are compared to the results from the experiments.

1.A The flow field ahead of a piston in a channel

From (1.9.10),

$$u = \psi_y = \frac{1}{2} - \frac{3y^2}{2} + \sum_{n=-\infty}^{\infty} A_n Y_{n,y}(y) \exp(-m_n x),$$

$$-v = \psi_x = \sum_{n=-\infty}^{\infty} A_n m_n Y_n(y) \exp(-m_n x),$$

and so ψ gives the correct downstream profile ((1.9.7) is satisfied). ($\text{Re}(m_n) > 0$ ensures that the terms in the summation disappear as $x \rightarrow \infty$. $m_n = 0$ is disallowed as it produces just the far field solution.)

Applying the biharmonic equation $\nabla^4 \psi = 0$ to (1.9.10) gives

$$\sum_{n=-\infty}^{\infty} A_n \left(m_n^4 Y_n + 2m_n^2 Y_{n,yy} + Y_{n,yyyy} \right) \exp(-m_n x) = 0.$$

If $m_n^4 Y_n + 2m_n^2 Y_{n,yy} + Y_{n,yyyy} = 0$ holds for all n , then this has solution

$$Y_n(y) = (c_1 + c_3 y) \sin(m_n y) + (c_2 + c_4 y) \cos(m_n y), \quad (1.11.1)$$

where c_1 to c_4 are constants. From (1.9.6), $v = 0$ on $y = \pm 1$, i.e. (as $m_n \neq 0$)

$$0 = (c_1 + c_3) \sin(m_n) + (c_2 + c_4) \cos(m_n), \quad (1.11.2)$$

$$\begin{aligned} \text{and } 0 &= (c_1 - c_3) \sin(-m_n) + (c_2 - c_4) \cos(-m_n) \\ &= (-c_1 + c_3) \sin(m_n) + (c_2 - c_4) \cos(m_n). \end{aligned} \quad (1.11.3)$$

From (1.11.1), $Y_{n,y}(y) = (c_3 - c_2 m_n - c_4 y m_n) \sin(m_n y) + (c_4 + c_1 m_n + c_3 y m_n) \cos(m_n y)$, and so $u = -1$ on $y = \pm 1$ gives

$$0 = (c_3 - c_2 m_n - c_4 m_n) \sin(m_n) + (c_4 + c_1 m_n + c_3 m_n) \cos(m_n), \quad (1.11.4)$$

$$\begin{aligned} \text{and } 0 &= (c_3 - c_2 m_n + c_4 m_n) \sin(-m_n) + (c_4 + c_1 m_n - c_3 m_n) \cos(-m_n) \\ &= (-c_3 + c_2 m_n - c_4 m_n) \sin(m_n) + (c_4 + c_1 m_n - c_3 m_n) \cos(m_n). \end{aligned} \quad (1.11.5)$$

Subtracting (1.11.5) from (1.11.4), and summing (1.11.2) and (1.11.3), gives

$$0 = (c_3 - c_2 m_n) \sin(m_n) + c_3 m_n \cos(m_n), \quad (1.11.6)$$

$$\text{and } 0 = c_3 \sin(m_n) + c_2 \cos(m_n). \quad (1.11.7)$$

Summing (1.11.4) and (1.11.5), and subtracting (1.11.3) from (1.11.2), gives

$$0 = -c_4 m_n \sin(m_n) + (c_4 + c_1 m_n) \cos(m_n), \quad (1.11.8)$$

$$\text{and } 0 = c_1 \sin(m_n) + c_4 \cos(m_n). \quad (1.11.9)$$

There are two potential sets of solutions, one with $c_2 = c_3 = 0$ and one with $c_1 = c_4 = 0$. If $\sin(m_n) = 0$, then $m_n = k\pi$ ($k \in \mathbb{Z} \setminus \{0\}$), and hence c_4 (from (1.11.9)), c_1 (from (1.11.8)), c_2 (from (1.11.3)) and c_3 (from (1.11.4)) all equal zero, which is the far field solution. Alternatively, $\sin(m_n) \neq 0$, and so from (1.11.7) and (1.11.9),

$$c_3 = \frac{-c_2 \cos(m_n)}{\sin(m_n)}, \quad c_1 = \frac{-c_4 \cos(m_n)}{\sin(m_n)},$$

and substituting these expressions into (1.11.4) and (1.11.5) gives

$$0 = (c_2 - c_4) \cos(m_n) \sin(m_n) + (c_2 + c_4) m_n, \quad (1.11.10)$$

$$0 = (c_2 + c_4) \cos(m_n) \sin(m_n) + (c_2 - c_4) m_n. \quad (1.11.11)$$

From (1.11.11), $(c_2 - c_4) = -(c_2 + c_4) \cos(m_n) \sin(m_n) / m_n$ (as $m_n \neq 0$), and substituting this expression into (1.11.10) gives

$$0 = \frac{-(c_2 + c_4) \cos^2(m_n) \sin^2(m_n)}{m_n} + (c_2 + c_4)m_n.$$

As $(c_2 + c_4) \neq 0$ (otherwise (1.11.11) gives $(c_2 - c_4) = 0$ also, and all four constants equal zero), this simplifies to the following transcendental equation for m_n :

$$0 = \cos(m_n) \sin(m_n) - m_n \quad (1.11.12)$$

Expressing (1.11.10) as $0 = c_2(\cos(m_n) \sin(m_n) + m_n) - c_4(\cos(m_n) \sin(m_n) - m_n)$ and substituting in (1.11.12) shows that c_2 , and hence c_3 , equal zero. The Papkovitch-Fadle eigenfunctions (1.11.1) can therefore be written

$$\begin{aligned} Y_n(y) &= -c_4 \frac{\cos(m_n) \sin(m_n y)}{\sin(m_n)} + c_4 y \cos(m_n y) \\ &= -c_4 \cos(m_n) \left(\frac{\sin(m_n y)}{\sin(m_n)} - y \frac{\cos(m_n y)}{\cos(m_n)} \right), \end{aligned}$$

and by writing $B_n = A_n c_4 \cos(m_n)$, ψ can be written

$$\psi(x, y) = \frac{y}{2} - \frac{y^3}{2} + \sum_{n \neq 0, n = -\infty}^{\infty} -B_n \left(\frac{\sin(m_n y)}{\sin(m_n)} - y \frac{\cos(m_n y)}{\cos(m_n)} \right) \exp(-m_n x).$$

The values of m_n are the roots of transcendental equation (1.11.12). This equation has a simple root $m_0 = 0$ (which is disallowed as $\text{Re}(m_n) > 0$), and infinitely-many complex quartets of roots $m_n, \bar{m}_n, -m_n$ and $-\bar{m}_n$ (where a bar denotes a complex conjugate). The values of m with a negative real part (without loss of generality assumed to be $-m_n$ and $-\bar{m}_n$) give an exponentially-growing solution (as $-x$ is negative) and so can be discounted. Using the rule that there is a conjugate pair of roots to (1.11.12) in each interval $(n + 1/8)\pi < \text{Re}(m_n) < (n + 1/4)\pi$ [121], the first 20 solutions with a positive complex part are found and given in Table 1.6.

Note that $m_{-n} = \bar{m}_n$, and so the complex parts of ψ cancel out when the same number of positive and negative values of n is used, e.g. $-20 \leq n \leq 20$. (For example, $\cos(m_n) + \cos(m_{-n}) = \cos(a_n + b_n i) + \cos(a_n - b_n i) = (\cos(a_n) \cosh(b_n) - i \sin(a_n) \sinh(b_n)) + (\cos(a_n) \cosh(b_n) + i \sin(a_n) \sinh(b_n)) = 2 \cos(a_n) \cosh(b_n)$.)

The sole remaining set of constants B_n are found by imposing an orthogonality condition and matching to the remaining boundary condition (1.9.5). With a velocity and

n	m_n	n	m_n
1	3.748838139078 + 1.384339142145i	11	35.307902530665 + 2.476402678710i
2	6.949979856990 + 1.676104942428i	12	38.451800004646 + 2.518899596647i
3	10.119258854116 + 1.858383839715i	13	41.595389718923 + 2.558067732979i
4	13.277273632746 + 1.991570820170i	14	44.738731042582 + 2.594390814285i
5	16.429870502544 + 2.096625735179i	15	47.881868801013 + 2.628254233801i
6	19.579408260032 + 2.183397558835i	16	51.024837506373 + 2.659970022509i
7	22.727035732178 + 2.257320224741i	17	54.167664185163 + 2.689794363883i
8	25.873384151411 + 2.321713978526i	18	57.310370319136 + 2.717940174489i
9	29.018831029547 + 2.378757559041i	19	60.452973208984 + 2.744586329988i
10	32.163616856643 + 2.429958323949i	20	63.595486952346 + 2.769884555900i

Table 1.6: First 20 solutions to $0 = \cos(m_n) \sin(m_n) - m_n$.

stress specified at $x = 0$ (known as the ‘canonical’ problem in [109]), and with $\cos(m_n)$ factored out of the Papkovich-Fadle eigenfunctions into the B_n , the remaining constants simplify to $B_n = \cot(m_n)/m_n$ [109], i.e.

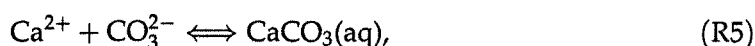
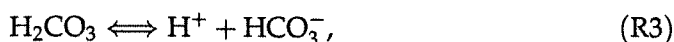
$$\psi(x, y) = \frac{y}{2} - \frac{y^3}{2} + \sum_{n \neq 0, n = -\infty}^{\infty} \frac{-1}{m_n \tan(m_n)} \left(\frac{\sin(m_n y)}{\sin(m_n)} - y \frac{\cos(m_n y)}{\cos(m_n)} \right) \exp(-m_n x).$$

The reactive chemistry of CO₂ dissolution in water

In this Chapter, the kinetics of the dissolution of CO₂ in water and subsequent chemical reactions are investigated. The principal chemical reactions that take place in ocean acidification and CO₂ dissolution into aquifer water in a CCS scheme are the same, and so this analysis helps provide an improved understanding of both of these two issues.

2.1 The chemical reactions

Suppose gaseous CO₂ is mixed with water, and the following reversible chemical reactions occur:



As described in the previous Chapter, gaseous carbon dioxide dissolves into the water (R1), reacting to form carbonic acid (R2). Hydrogen ions dissociate from the carbonic acid, to give bicarbonate (R3), and then a carbonate ion (R4). There are many mineralisation reactions that can and do occur. The formation of calcium carbonate is one of the more straightforward ones, and is very common. This reaction is therefore taken as a representative slower mineralisation reaction (R5). Some of this calcium carbonate precipitates out of the solution (R6). No further reactions with buffers that remove some of the hydrogen ions from the system are included; this removal will only drive the system of reactions further forward, and so result in more hydrogen being produced. The minimum quantity of hydrogen ions that is generated will therefore be obtained. It is assumed that the system is initially at equilibrium with all species at low concentrations compared to water, and is then subject to an instantaneous injection of gaseous carbon dioxide. The new equilibrium that the system reaches, the time scales over which this equilibrium is reached, and the behaviour of the different species as they go to their new equilibria, are investigated.

2.2 Mathematical modelling

2.2.1 Assumptions

From Section 1.7, each of the reactions (R1-5) individually follows the mass action law (with the additional assumption that water is abundant), and it is supposed that this also applies when the reactions are considered together as a single system of reactions. It is also assumed that the components are always well-mixed, and that the temperature, pressure, salinity, ionic strength, and particle surface area are constant and uniform, and any impact upon the rates of reaction caused by varying one or more of these factors can be captured by varying the rate constants appropriately. It is assumed that CO₂(aq) remains below carbon dioxide's solubility limit (without the need to impose a maximum value on its concentration), and that all the CaCO₃ that is formed in solution remains dissolved until its concentration reaches calcium carbonate's molar solubility limit S ; thereafter it precipitates instantaneously. It is also assumed that the reactions take place in a space that is spatially homogeneous (so any nucleation that occurs will also be homogeneous).

2.2.2 Full dimensional model

The kinetics of (R1-6) is therefore modelled by the following rate equations, where t is time (in sec), $[]$ denotes concentration (measured in mol/litre, or M), $[\text{CaCO}_3] = [\text{CaCO}_3(\text{aq})] + [\text{CaCO}_3(\text{s})]$, k_1 to k_5 and k_{-1} to k_{-5} are respectively the forward and reverse rate constants for the five reactions (R1-5), and $\mathcal{H}(\cdot)$ is the Heaviside step function ($\mathcal{H}(x) = 1$ if $x > 0$, $\mathcal{H}(x) = 0$ if $x < 0$):

$$\frac{d[\text{CO}_2(\text{g})]}{dt} = -k_1[\text{CO}_2(\text{g})] + k_{-1}[\text{CO}_2(\text{aq})], \quad (2.2.1a)$$

$$\frac{d[\text{CO}_2(\text{aq})]}{dt} = k_1[\text{CO}_2(\text{g})] - k_{-1}[\text{CO}_2(\text{aq})] - k_2[\text{CO}_2(\text{aq})] + k_{-2}[\text{H}_2\text{CO}_3], \quad (2.2.1b)$$

$$\frac{d[\text{H}_2\text{O}]}{dt} = -k_2[\text{CO}_2(\text{aq})] + k_{-2}[\text{H}_2\text{CO}_3], \quad (2.2.1c)$$

$$\frac{d[\text{H}_2\text{CO}_3]}{dt} = k_2[\text{CO}_2(\text{aq})] - k_{-2}[\text{H}_2\text{CO}_3] - k_3[\text{H}_2\text{CO}_3] + k_{-3}[\text{H}^+][\text{HCO}_3^-], \quad (2.2.1d)$$

$$\frac{d[\text{H}^+]}{dt} = k_3[\text{H}_2\text{CO}_3] - k_{-3}[\text{H}^+][\text{HCO}_3^-] + k_4[\text{HCO}_3^-] - k_{-4}[\text{H}^+][\text{CO}_3^{2-}], \quad (2.2.1e)$$

$$\frac{d[\text{HCO}_3^-]}{dt} = k_3[\text{H}_2\text{CO}_3] - k_{-3}[\text{H}^+][\text{HCO}_3^-] - k_4[\text{HCO}_3^-] + k_{-4}[\text{H}^+][\text{CO}_3^{2-}], \quad (2.2.1f)$$

$$\frac{d[\text{CO}_3^{2-}]}{dt} = k_4[\text{HCO}_3^-] - k_{-4}[\text{H}^+][\text{CO}_3^{2-}] - k_5[\text{Ca}^{2+}][\text{CO}_3^{2-}] + k_{-5}[\text{CaCO}_3(\text{aq})], \quad (2.2.1g)$$

$$\frac{d[\text{Ca}^{2+}]}{dt} = -k_5[\text{Ca}^{2+}][\text{CO}_3^{2-}] + k_{-5}[\text{CaCO}_3(\text{aq})], \quad (2.2.1h)$$

$$\frac{d[\text{CaCO}_3(\text{aq})]}{dt} = (k_5[\text{Ca}^{2+}][\text{CO}_3^{2-}] - k_{-5}[\text{CaCO}_3(\text{aq})]) \mathcal{H}(S - [\text{CaCO}_3]), \quad (2.2.1i)$$

$$\frac{d[\text{CaCO}_3(\text{s})]}{dt} = (k_5[\text{Ca}^{2+}][\text{CO}_3^{2-}] - k_{-5}[\text{CaCO}_3(\text{aq})]) \mathcal{H}([\text{CaCO}_3] - S). \quad (2.2.1j)$$

Equations (2.2.1) can be simplified by removing the explicit distinction between dissolved and precipitated CaCO₃, and by imposing mass conservation constraints consistent with the initial conditions. From (2.2.1i) and (2.2.1j),

$$\frac{d[\text{CaCO}_3]}{dt} = k_5[\text{Ca}^{2+}][\text{CO}_3^{2-}] - k_{-5}[\text{CaCO}_3(\text{aq})], \quad (2.2.2)$$

and so (2.2.1g), (2.2.1h) and (2.2.2) can alternatively be written as

$$\frac{d[\text{CO}_3^{2-}]}{dt} = k_4[\text{HCO}_3^-] - k_{-4}[\text{H}^+][\text{CO}_3^{2-}] - k_5[\text{Ca}^{2+}][\text{CO}_3^{2-}] + k_{-5} \min\{S, [\text{CaCO}_3]\}, \quad (2.2.3a)$$

$$\frac{d[\text{Ca}^{2+}]}{dt} = -\frac{d[\text{CaCO}_3]}{dt} = -k_5[\text{Ca}^{2+}][\text{CO}_3^{2-}] + k_{-5} \min\{S, [\text{CaCO}_3]\}. \quad (2.2.3b)$$

Therefore, equivalently to (2.2.1), the system comprises equations (2.2.1a)-(2.2.1f) and (2.2.3), and whenever a more detailed split between aqueous and solid CaCO₃ is required, this is given by

$$[\text{CaCO}_3(\text{aq})] = \min\{[\text{CaCO}_3], S\}, \quad [\text{CaCO}_3(\text{s})] = \max\{0, [\text{CaCO}_3] - S\}. \quad (2.2.4)$$

The four different elements within this system (C, O, H and Ca) must be conserved throughout the system's evolution (onwards from the time at which the extra CO₂(g) is injected), and so the system of nine equations has four constraints and five degrees of freedom. Noting that (2.2.1h-j) sum to zero, it follows that

$$[\text{Ca}^{2+}] + [\text{CaCO}_3] = [\text{Ca}^{2+}]_0 + [\text{CaCO}_3]_0,$$

(where subscript zero indicates an initial value), denoting conservation of calcium.

Similarly, conservation of carbon, hydrogen, and oxygen are respectively given by

$$\begin{aligned} & [\text{CO}_2(\text{g})] + [\text{CO}_2(\text{aq})] + [\text{H}_2\text{CO}_3] + [\text{HCO}_3^-] + [\text{CO}_3^{2-}] + [\text{CaCO}_3] \\ &= [\text{CO}_2(\text{g})]_0 + [\text{CO}_2(\text{aq})]_0 + [\text{H}_2\text{CO}_3]_0 + [\text{HCO}_3^-]_0 + [\text{CO}_3^{2-}]_0 + [\text{CaCO}_3]_0, \end{aligned}$$

$$2[\text{H}_2\text{O}] + 2[\text{H}_2\text{CO}_3] + [\text{H}^+] + [\text{HCO}_3^-] = 2[\text{H}_2\text{O}]_0 + 2[\text{H}_2\text{CO}_3]_0 + [\text{H}^+]_0 + [\text{HCO}_3^-]_0,$$

$$\begin{aligned} & 2[\text{CO}_2(\text{g})] + 2[\text{CO}_2(\text{aq})] + [\text{H}_2\text{O}] + 3[\text{H}_2\text{CO}_3] + 3[\text{HCO}_3^-] + 3[\text{CO}_3^{2-}] + 3[\text{CaCO}_3] \\ &= 2[\text{CO}_2(\text{g})]_0 + 2[\text{CO}_2(\text{aq})]_0 + [\text{H}_2\text{O}]_0 + 3[\text{H}_2\text{CO}_3]_0 + 3[\text{HCO}_3^-]_0 \\ & \quad + 3[\text{CO}_3^{2-}]_0 + 3[\text{CaCO}_3]_0. \end{aligned}$$

These four equations are re-arranged so that [CO₂(g)], [H⁺], [CaCO₃] (denoted X, Y and Z respectively) and [H₂O] are expressed as functions of the remaining five species and the initial concentrations. The system (2.2.1a)-(2.2.1f) and (2.2.3) therefore simplifies to the following system of five coupled ordinary differential equations,

$$\frac{d[\text{CO}_2(\text{aq})]}{dt} = k_1 X - k_{-1}[\text{CO}_2(\text{aq})] - k_2[\text{CO}_2(\text{aq})] + k_{-2}[\text{H}_2\text{CO}_3], \quad (2.2.5a)$$

$$\frac{d[\text{H}_2\text{CO}_3]}{dt} = k_2[\text{CO}_2(\text{aq})] - k_{-2}[\text{H}_2\text{CO}_3] - k_3[\text{H}_2\text{CO}_3] + k_{-3} Y [\text{HCO}_3^-], \quad (2.2.5b)$$

$$\frac{d[\text{HCO}_3^-]}{dt} = k_3[\text{H}_2\text{CO}_3] - k_{-3} Y [\text{HCO}_3^-] - k_4[\text{HCO}_3^-] + k_{-4} Y [\text{CO}_3^{2-}], \quad (2.2.5c)$$

$$\frac{d[\text{CO}_3^{2-}]}{dt} = k_4[\text{HCO}_3^-] - k_{-4} Y [\text{CO}_3^{2-}] - k_5[\text{CO}_3^{2-}][\text{Ca}^{2+}] + k_{-5} \min\{S, Z\}, \quad (2.2.5d)$$

$$\frac{d[\text{Ca}^{2+}]}{dt} = -k_5[\text{CO}_3^{2-}][\text{Ca}^{2+}] + k_{-5} \min\{S, Z\}, \quad (2.2.5e)$$

where

$$X \equiv [\text{CO}_2(\text{g})]_0 - [\text{CO}_2(\text{aq})] + [\text{CO}_2(\text{aq})]_0 - [\text{H}_2\text{CO}_3] + [\text{H}_2\text{CO}_3]_0 \\ - [\text{HCO}_3^-] + [\text{HCO}_3^-]_0 - [\text{CO}_3^{2-}] + [\text{CO}_3^{2-}]_0 + [\text{Ca}^{2+}] - [\text{Ca}^{2+}]_0, \quad (2.2.6a)$$

$$Y \equiv [\text{H}^+]_0 + [\text{HCO}_3^-] - [\text{HCO}_3^-]_0 + 2[\text{CO}_3^{2-}] - 2[\text{CO}_3^{2-}]_0 - 2[\text{Ca}^{2+}] + 2[\text{Ca}^{2+}]_0, \quad (2.2.6b)$$

$$Z \equiv [\text{CaCO}_3]_0 - [\text{Ca}^{2+}] + [\text{Ca}^{2+}]_0. \quad (2.2.6c)$$

This simplification reduces the number of parameters from 19 (the ten rate constants and nine initial concentrations) to 18.

2.2.3 Parameter estimates and initial conditions

Estimates of the rate constants for these reactions at standard temperature and pressure (25°C and 1 atm) are given in Table 2.1, based on the estimates in Chapter 1. The rate constants vary by at least nine orders of magnitude. Constants k_1 and k_{-1} are estimated based on $K_1 = 1$, and reaction (R1) being fast in a well-mixed scenario [139], and similar in speed to reaction (R3). Also, k_5 and k_{-5} are estimated based on reaction (R5) being relatively slow, and $K_5 \approx 2000 \text{ M}^{-1}$ at 25°C. As CaCO₃ dissociates to one molecule of Ca²⁺ and one molecule of CO₃²⁻, S (in M) is given by the square root of the solubility product constant, which for CaCO₃ in pure water at 25°C is 4.96×10^{-9} [62].

The Botucatu aquifer in Brazil has been well-characterised [63], and some of its shallower wells (e.g. Wells 56, 89 and 149), have conditions similar to standard temperature and pressure. Typical concentrations for this aquifer are $[\text{Ca}^{2+}]_0 = 10 \text{ mg/l} = 2.50 \times 10^{-4} \text{ M}$ (as calcium has atomic mass 40.078 g/mol), $[\text{HCO}_3^-]_0 = 20 \text{ mg/l} = 3.28 \times 10^{-4} \text{ M}$ (as bicarbonate has atomic mass 61.01 g/mol), and pH=6, i.e. $[\text{H}^+]_0 = 10^{-6} \text{ M}$, and so the behaviour of the system will be illustrated with these initial concentrations. From these three initial concentrations, the remaining species' initial concentrations are calculated using the fact that a reaction's equilibrium constant equals both its ratio of rate constants and its ratio of equilibrium concentrations. For example, for reaction (R4),

$$K_4 = \frac{k_4}{k_{-4}} = \frac{[\text{H}^+]_0[\text{CO}_3^{2-}]_0}{[\text{HCO}_3^-]_0}, \quad (2.2.7)$$

and so $[\text{CO}_3^{2-}]_0 = 1.97 \times 10^{-8} \text{ M}$. Similar calculations for the other four reactions give

Parameter	Magnitude	Source
k_1	$1 \times 10^{10} \text{ s}^{-1}$	[73]
k_{-1}	$1 \times 10^{10} \text{ s}^{-1}$	[73]
k_2	$6 \times 10^{-2} \text{ s}^{-1}$	[84]
k_{-2}	$2 \times 10^1 \text{ s}^{-1}$	[85]
k_3	$1 \times 10^7 \text{ s}^{-1}$	[85]
k_{-3}	$5 \times 10^{10} \text{ M}^{-1} \text{ s}^{-1}$	[85]
k_4	$3 \times 10^0 \text{ s}^{-1}$	[94]
k_{-4}	$5 \times 10^{10} \text{ M}^{-1} \text{ s}^{-1}$	[94]
k_5	$2 \times 10^0 \text{ M}^{-1} \text{ s}^{-1}$	[90]
k_{-5}	$1 \times 10^{-3} \text{ s}^{-1}$	[90]
S	$7 \times 10^{-5} \text{ M}$	[62]

Table 2.1: Parameter estimates at 25°C and 1 atm.

the remaining initial equilibrium concentrations (Table 2.2). Water's concentration does not deviate from its large pure value of 55.5 M (i.e. assume water has density 1000 g/l, and atomic mass 18.0106 g/mol). Note that $[\text{CO}_2(\text{aq})] + [\text{HCO}_3^-] + [\text{CO}_3^{2-}] = 8.75 \times 10^{-4} \text{ M}$, and the same values for K_2, K_3 and K_4 are being used as was used for the Bjerrum plot in Figure 1.1, and so that Bjerrum plot applies to this initial equilibrium scenario. The equilibrium concentrations required by the Bjerrum plot for a pH of 6 agree with the magnitudes given in Table 2.2.

The system is then perturbed by an instantaneous injection of CO₂(g) that increases [CO₂(g)] to 0.065 M, which will be sufficient to increase [CO₂(aq)] to its solubility limit at 25°C and 1 atm, found in Section 1.7.1 to be about 0.034 M. (Any more injected CO₂(g) will therefore remain undissolved, and will not affect any of the other species.) The time at which this injection happens is set to be $t = 0$, the conservation of mass constraints now apply, and we seek the evolution of the system to a new equilibrium.

Aquifer temperatures and pressures can be far above 25°C and 1 atm, and the initial concentrations can be rather different from the ones chosen here, but the results obtained here are extendable to a wider range of scenarios, as explained in Section 2.3.9 below.

Species	Initial equilibrium concentration	Species	Initial equilibrium concentration
[CO ₂ (g)]	5.47 × 10 ⁻⁴ M	[HCO ₃ ⁻]	3.28 × 10 ⁻⁴ M
[CO ₂ (aq)]	5.47 × 10 ⁻⁴ M	[CO ₃ ²⁻]	1.97 × 10 ⁻⁸ M
[H ₂ CO ₃]	1.64 × 10 ⁻⁶ M	[Ca ²⁺]	2.50 × 10 ⁻⁴ M
[H ⁺]	1.00 × 10 ⁻⁶ M	[CaCO ₃]	9.84 × 10 ⁻⁹ M

Table 2.2: Initial concentrations (before injection of extra CO₂(g)).

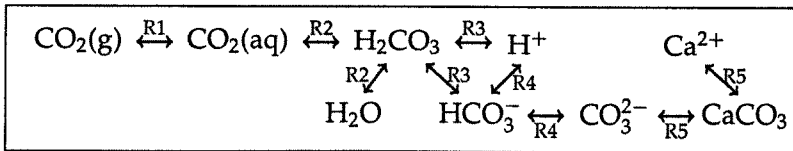


Figure 2.1: Reactive interactions between the different chemical species.

2.2.4 Predicted impact of CO₂(g) injection

Figure 2.1 shows the relationships between the different chemical species that occur as a result of the reactions listed in Section 2.1. If this were a simple chain of reactions, then all the species' concentrations would increase. However, the loop in the middle means that this will not be the case, and the overall effects of increasing CO₂(g) are not immediately obvious.

The ratio of a reaction's concentrations is constant for any equilibrium, so from (R1),

$$K_1 = \frac{k_1}{k_{-1}} = \frac{[\text{CO}_2(\text{aq})]_0}{[\text{CO}_2(\text{g})]_0} = \frac{[\text{CO}_2(\text{aq})]_\infty}{[\text{CO}_2(\text{g})]_\infty},$$

where a 0 subscript indicates an initial equilibrium value, and a ∞ subscript indicates a final equilibrium value. Therefore an increase in [CO₂(g)] (from [CO₂(g)]₀ to [CO₂(g)]_∞) must be balanced by an increase in [CO₂(aq)]. The expression for K₂ similarly indicates that there must be an increase in [H₂CO₃]. For reaction (R4),

$$K_4 = \frac{k_4}{k_{-4}} = \frac{[\text{H}^+]_0 [\text{CO}_3^{2-}]_0}{[\text{HCO}_3^-]_0} = \frac{[\text{H}^+]_\infty [\text{CO}_3^{2-}]_\infty}{[\text{HCO}_3^-]_\infty}.$$

[H⁺] is known to increase as a result of these reactions, and so [CO₃²⁻] must decrease, and [HCO₃⁻] must increase. From reaction (R5),

$$K_5 = \frac{k_5}{k_{-5}} = \frac{[\text{CaCO}_3]_0}{[\text{Ca}^{2+}]_0 [\text{CO}_3^{2-}]_0} = \frac{[\text{CaCO}_3]_\infty}{[\text{Ca}^{2+}]_\infty [\text{CO}_3^{2-}]_\infty}.$$

Therefore, a drop in [CO₃²⁻] must be balanced by an increase in [Ca²⁺], and a decrease in [CaCO₃]. Therefore, rather counter-intuitively, an increase in the amount of CO₂(g) results in a decrease in the amount of CaCO₃; some of the CaCO₃ already in the system breaks up, producing Ca²⁺. This agrees with the experience at Weyburn, Canada (Section 1.5), where injecting CO₂ with water dissolved calcium carbonate from the formation matrix, and increased the pore permeability. Therefore CO₂ cannot be sequestered as CaCO₃ through these reactions alone. Chapter 4 contains experimental evidence that agrees with this.

2.2.5 Dimensionless model

Six dimensionless variables are defined in Table 2.3 – B , D , F , G and H represent deviations of concentrations from initial values, and each is a function of a rescaled time variable \bar{t} . Table 2.4 defines 18 dimensionless parameters, denoted with Greek symbols, with the concentration of water (=55.5 M) and the rate constant k_2 chosen to be the arbitrary reference inverse concentration and time scale respectively. These parameters are evaluated using data in Tables 2.1 and 2.2 and [CO₂(g)]₀=0.065 M, and the resulting values, spanning 23 orders of magnitude, are given in Table 2.4. The parameters are expressed as the product of a corresponding $O(1)$ parameter (indicated by a hat) and a power of the parameter α . This is a precursor to taking the distinguished asymptotic limit $\alpha \rightarrow \infty$, with all hatted parameters remaining $O(1)$ in the limit.

Since the initial conditions (prior to CO₂ injection) have been chosen to satisfy the equilibrium equations (as in (2.2.7)), reactions (R2-5) yield the following identities:

$$\sigma \equiv \frac{\beta}{\delta}, \quad \omega \equiv \frac{\psi\delta}{\eta\mu}, \quad \phi \equiv \frac{\chi\eta\tau\lambda}{\mu\rho\kappa} \quad \text{and} \quad \theta \equiv \frac{\rho\kappa}{\tau\lambda}. \quad (2.2.8a-d)$$

Substituting the dimensionless variables, parameters and identities (2.2.8) into (2.2.5) yields the following dimensionless system of five equations, containing 14 independent parameters. The five variables all equal zero at $\bar{t} = 0$.

$$\frac{dB}{d\bar{t}} = \alpha - \gamma(B + D + F + G - H) - \nu(B + \beta) - B + \frac{\beta D}{\delta}, \quad (2.2.9a)$$

$$\frac{dD}{d\bar{t}} = B - \frac{\beta D}{\delta} - \psi(D + \delta) + \frac{\psi\delta}{\eta\mu}(F + \eta)(\mu + F + 2G - 2H), \quad (2.2.9b)$$

Variable	Definition
B	$([\text{CO}_2(\text{aq})] - [\text{CO}_2(\text{aq})]_0) / [\text{H}_2\text{O}]_0$
D	$([\text{H}_2\text{CO}_3] - [\text{H}_2\text{CO}_3]_0) / [\text{H}_2\text{O}]_0$
F	$([\text{HCO}_3^-] - [\text{HCO}_3^-]_0) / [\text{H}_2\text{O}]_0$
G	$([\text{CO}_3^{2-}] - [\text{CO}_3^{2-}]_0) / [\text{H}_2\text{O}]_0$
H	$([\text{Ca}^{2+}] - [\text{Ca}^{2+}]_0) / [\text{H}_2\text{O}]_0$
\bar{t}	$k_2 t$

Table 2.3: Dimensionless variables.

Parameter	Definition	Value at 25°C, 1 atm	Scaling
α	$[\text{CO}_2(\text{g})]_0 k_1 / [\text{H}_2\text{O}] k_2$	1.95×10^8	
β	$[\text{CO}_2(\text{aq})]_0 / [\text{H}_2\text{O}]$	9.85×10^{-6}	$\alpha^{-3/4} \hat{\beta}$
δ	$[\text{H}_2\text{CO}_3]_0 / [\text{H}_2\text{O}]$	2.95×10^{-8}	$\alpha^{-1} \hat{\delta}$
μ	$[\text{H}^+]_0 / [\text{H}_2\text{O}]$	1.80×10^{-8}	$\alpha^{-1} \hat{\mu}$
η	$[\text{HCO}_3^-]_0 / [\text{H}_2\text{O}]$	5.91×10^{-6}	$\alpha^{-3/4} \hat{\eta}$
θ	$[\text{CO}_3^{2-}]_0 / [\text{H}_2\text{O}]$	3.55×10^{-10}	
λ	$[\text{Ca}^{2+}]_0 / [\text{H}_2\text{O}]$	4.50×10^{-6}	$\alpha^{-3/4} \hat{\lambda}$
κ	$[\text{CaCO}_3]_0 / [\text{H}_2\text{O}]$	1.77×10^{-10}	$\alpha^{-5/4} \hat{\kappa}$
γ	k_1 / k_2	1.67×10^{11}	$\alpha^{3/2} \hat{\gamma}$
ν	k_{-1} / k_2	1.67×10^{11}	$\alpha^{3/2} \hat{\nu}$
σ	k_{-2} / k_2	3.33×10^2	
ψ	k_3 / k_2	1.67×10^8	$\alpha \hat{\psi}$
ω	$k_{-3} [\text{H}_2\text{O}] / k_2$	4.17×10^{13}	
χ	k_4 / k_2	5.00×10^1	$\alpha^{1/4} \hat{\chi}$
ϕ	$k_{-4} [\text{H}_2\text{O}] / k_2$	4.17×10^{13}	
τ	$k_5 [\text{H}_2\text{O}] / k_2$	1.67×10^3	$\alpha^{1/2} \hat{\tau}$
ρ	k_{-5} / k_2	1.67×10^{-2}	$\alpha^{-1/4} \hat{\rho}$
Σ	$S / [\text{H}_2\text{O}]$	1.27×10^{-6}	$\alpha^{-3/4} \hat{\Sigma}$

Table 2.4: Dimensionless parameters.

$$\frac{dF}{d\bar{t}} = \psi(D + \delta) + \left(\frac{-\psi\delta}{\eta\mu}(F + \eta) + \frac{\chi\eta}{\mu} \left(\frac{\tau\lambda}{\rho\kappa}G + 1 \right) \right) (\mu + F + 2G - 2H) - \chi(F + \eta), \quad (2.2.9c)$$

$$\frac{dG}{d\bar{t}} = \chi(F + \eta) - \frac{\chi\eta}{\mu} \left(\frac{\tau\lambda}{\rho\kappa}G + 1 \right) (\mu + F + 2G - 2H) - \tau \left(G + \frac{\rho\kappa}{\tau\lambda} \right) (H + \lambda) + \rho \min\{\Sigma, \kappa - H\}, \quad (2.2.9d)$$

$$\frac{dH}{d\bar{t}} = -\tau \left(G + \frac{\rho\kappa}{\tau\lambda} \right) (H + \lambda) + \rho \min\{\Sigma, \kappa - H\}. \quad (2.2.9e)$$

2.2.6 The evolution of the system to equilibrium

Numerical integration of (2.2.5), using one of Matlab's inbuilt programs for initial value ordinary differential equation problems (ode15s), and the parameter values given in Tables 2.1 and 2.2 (with $[\text{CO}_2(\text{g})]_0 = 0.065 \text{ M}$), yields results shown in Figure 2.2(a). (The evolution of calcium is given as the increase from its initial value.) The solutions produced agree with the predictions from Section 2.2.4 and [5, 12], that the injection of CO₂(g) leads to increases in [CO₂(aq)], [H₂CO₃], [H⁺], [HCO₃⁻], and [Ca²⁺], and decreases in [CO₃²⁻] and [CaCO₃]. The curve for the decrease in [CaCO₃] coincides exactly with the curve for the increase in [Ca²⁺] (as these are the only two species in the system containing the element calcium).

The new equilibrium concentrations are estimated to be $[\text{CO}_2(\text{aq})]_\infty \approx 3.305 \times 10^{-2} \text{ M}$, $[\text{HCO}_3^-]_\infty \approx 3.794 \times 10^{-4} \text{ M}$, and $[\text{CO}_3^{2-}]_\infty \approx 4.429 \times 10^{-10} \text{ M}$, which gives $\text{Tot}[\text{CO}_2] \approx 3.342 \times 10^{-2} \text{ M}$. Therefore, the Bjerrum plot in Figure 1.1 does not apply to this new equilibrium. A new Bjerrum is constructed for this new $\text{Tot}[\text{CO}_2]$ using equations (1.7.5)-(1.7.7) and the same values for $K_{2\&3}$ and K_4 (Figure 2.3). Also, $[\text{H}^+]_\infty \approx 5.1 \times 10^{-5} \text{ M}$ (i.e. the pH has dropped from 6 to 4.3), and this is shown with a vertical line in Figure 2.3. These equilibrium concentrations of CO₂(aq), HCO₃⁻ and CO₃²⁻ do indeed match the concentrations required by this Bjerrum plot for this equilibrium pH, which gives confidence that this modelling is accurate.

In Figure 2.2(b), the evolution of the system is plotted using dimensionless variables (2.2.9) with continuous lines, along with asymptotic approximations (dashed lines) that will be derived below. There is very close agreement between the simulations and the approximations. For each species J ($J=B, D, F, G, H$), the exponent

$$\Psi_J \equiv \frac{d \log |J|}{d \log \bar{t}} \quad (2.2.10)$$

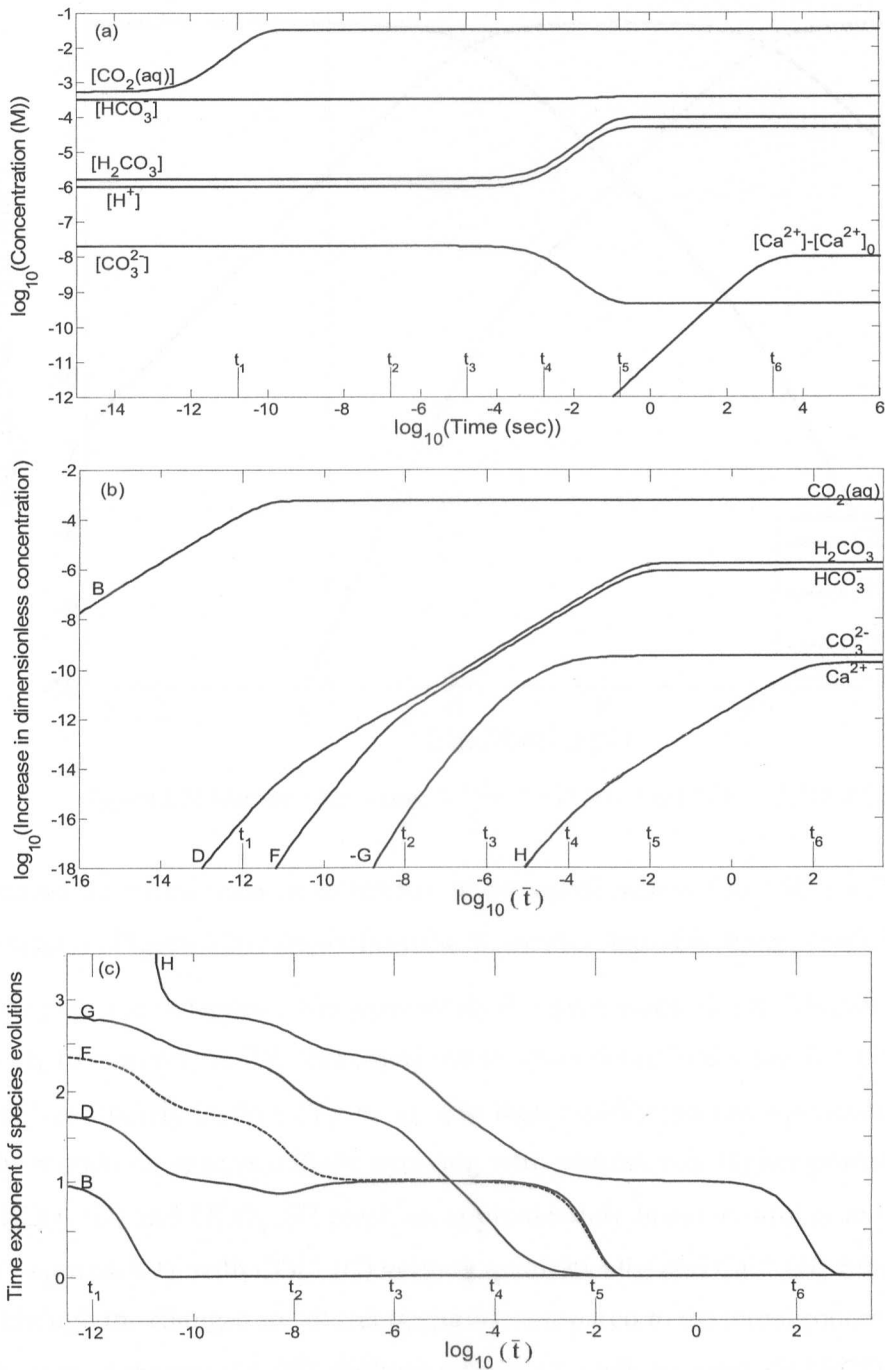


Figure 2.2: (a) Simulation results expressed in dimensional variables, satisfying (2.2.5); (b) Simulation of the dimensionless system (2.2.9) (continuous lines), with leading-order approximations derived below (dashed lines, where visible); (c) The time exponent Ψ_j of each species' evolution, in simulation of (2.2.9). In each graph, the vertical lines t_1 - t_6 indicate the six timescales: $\bar{t}_1 = \alpha^{-3/2}$, $\bar{t}_2 = \alpha^{-1}$, $\bar{t}_3 = \alpha^{-3/4}$, $\bar{t}_4 = \alpha^{-1/2}$, $\bar{t}_5 = \alpha^{-1/4}$, $\bar{t}_6 = \alpha^{1/4}$.

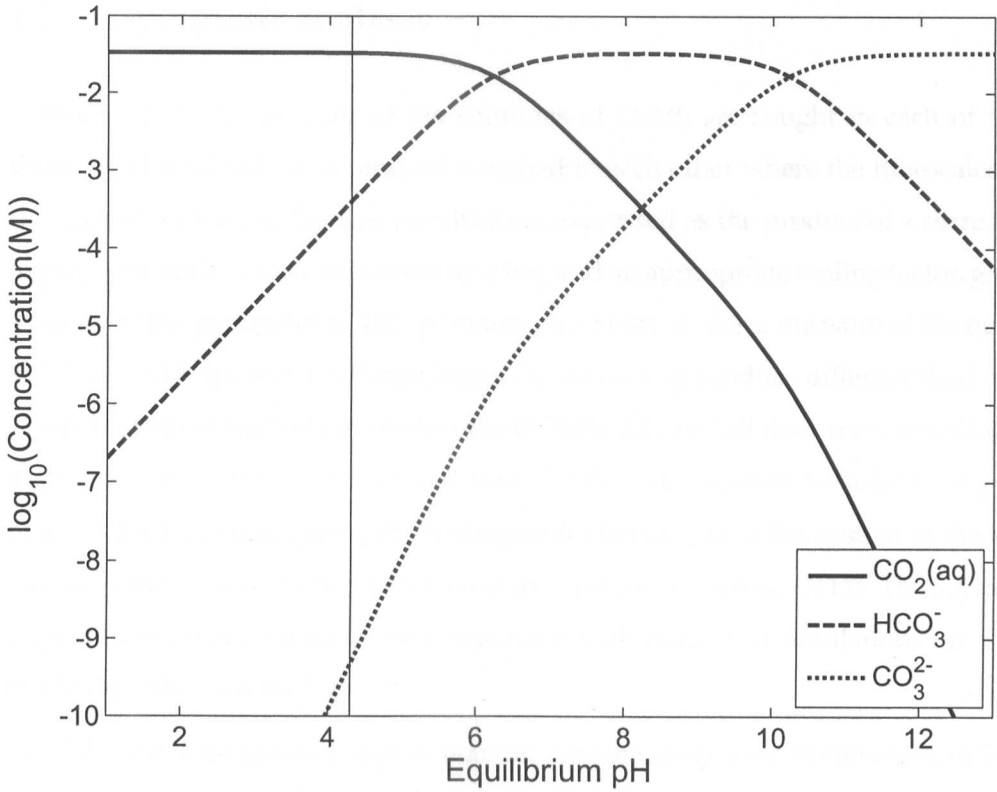


Figure 2.3: Bjerrum plot, using (1.7.5)-(1.7.7) and total $\text{CO}_2 = 3.342 \times 10^{-2}$ M.

provides a useful measure of the rate of change of each variable (as $J \propto t^{\Psi_J}$ when Ψ_J is constant). Figure 2.2(c) shows how the Ψ_J exhibit stepwise changes with time.

The plateaux in Figure 2.2(c) separate six different timescales in this system, indicated by t_1 to t_6 in Figure 2.2, and discussed in more detail in Section 2.3: (1) $\text{CO}_2(\text{aq})$ (B) evolves linearly in time ($\Psi_B \approx 1$), and then rapidly reaches equilibrium ($\Psi_B = 0$), the remaining species initially evolving with successively higher powers of time; (2) H_2CO_3 (D) and HCO_3^- (F) reach an approximately linear evolution in time (Ψ_D and Ψ_F approach 1), with CO_3^{2-} (G) varying quadratically, and Ca^{2+} (H) cubically in time, although the changes are all still negligible compared to the initial concentrations; (3,4) the rate of change of CO_3^{2-} declines rapidly (Ψ_G falls to zero); (5) H_2CO_3 , HCO_3^- and CO_3^{2-} (D , F and G) reach equilibrium while Ca^{2+} evolves linearly in time ($\Psi_H \approx 1$); (6) Ca^{2+} reaches equilibrium.

2.3 Asymptotic analysis

Asymptotic approximations of the solutions of (2.2.9) are sought in each of the six timescales identified above, and are matched to each other where the timescales overlap. In each timescale, the five variables are expressed as the product of a corresponding $O(1)$ variable, which is indicated by a hat, and an appropriate scaling factor, given as a power of the parameter α . This parameter is chosen as it is a measure of the quantity of injected CO₂(g), and a different initial condition will produce different final results. The hatted variables and parameters (from Table 2.4) and all their corresponding scaling factors of α are then substituted into (2.2.9), and the terms in successive powers of $\alpha^{-1/4}$ are balanced, giving the leading-order behaviour of the system in the distinguished limit $\alpha \rightarrow \infty$ (hatted parameters in Table 2.4 remaining $O(1)$). The asymptotic approximations are validated by comparison with numerical simulations for a large, but finite, value of α (Figure 2.2(b)).

The different leading-order approximations for each species are summarised in Section 2.3.7, and are combined into a single plot as the dashed lines overlying the continuous lines in Figure 2.2(b). There is uniformly close agreement between the simulations and these approximations. Wherever possible, they are constructed by summing the different timescales' approximations, and subtracting the intervening large-time limits, to give composite formulae.

2.3.1 Timescale 1: $\bar{t} = O(\alpha^{-3/2})$

Writing $B = \alpha^{-1/2}\hat{B}$, $D = \alpha^{-2}\hat{D}$, $F = \alpha^{-5/2}\hat{F}$, $G = \alpha^{-7/2}\hat{G}$, $H = \alpha^{-21/4}\hat{H}$ and $\bar{t} = \alpha^{-3/2}\hat{t}$ gives the following leading-order behaviour of (2.2.9) on this timescale as $\alpha \rightarrow \infty$:

$$\frac{d\hat{B}}{d\hat{t}} = 1 - (\hat{\gamma} + \hat{\nu})\hat{B}, \quad \frac{d\hat{D}}{d\hat{t}} = \hat{B}, \quad \frac{d\hat{F}}{d\hat{t}} = \hat{\psi}\hat{D}, \quad \frac{d\hat{G}}{d\hat{t}} = \frac{-\hat{\chi}\hat{\eta}}{\hat{\mu}}\hat{F}, \quad \frac{d\hat{H}}{d\hat{t}} = -\hat{\tau}\hat{G}\hat{\lambda}, \quad (2.3.1a-e)$$

with $\hat{B} = \hat{D} = \hat{F} = \hat{G} = \hat{H} = 0$ at $\hat{t} = 0$. \hat{B} equilibrates rapidly, with changes in the remaining variables slaved sequentially to this. Equations (2.3.1) have the solutions

$$\hat{B} = \frac{1}{\hat{\Omega}} (1 - \exp(-\hat{\Omega}\hat{t})), \quad (2.3.2a)$$

$$\hat{D} = \frac{1}{\hat{\Omega}} \left(\hat{t} + \frac{\exp(-\hat{\Omega}\hat{t}) - 1}{\hat{\Omega}} \right), \quad (2.3.2b)$$

$$\hat{F} = \frac{\hat{\psi}}{\hat{\Omega}} \left(\frac{\hat{t}^2}{2} - \frac{\hat{t}}{\hat{\Omega}} - \frac{\exp(-\hat{\Omega}\hat{t}) - 1}{\hat{\Omega}^2} \right), \quad (2.3.2c)$$

$$\hat{G} = \frac{-\hat{\chi}\hat{\eta}\hat{\psi}}{\hat{\Omega}\hat{\mu}} \left(\frac{\hat{t}^3}{6} - \frac{\hat{t}^2}{2\hat{\Omega}} + \frac{\hat{t}}{\hat{\Omega}^2} + \frac{\exp(-\hat{\Omega}\hat{t}) - 1}{\hat{\Omega}^3} \right), \quad (2.3.2d)$$

$$\hat{H} = \frac{\hat{\tau}\hat{\lambda}\hat{\chi}\hat{\eta}\hat{\psi}}{\hat{\Omega}\hat{\mu}} \left(\frac{\hat{t}^4}{24} - \frac{\hat{t}^3}{6\hat{\Omega}} + \frac{\hat{t}^2}{2\hat{\Omega}^2} - \frac{\hat{t}}{\hat{\Omega}^3} - \frac{\exp(-\hat{\Omega}\hat{t}) - 1}{\hat{\Omega}^4} \right), \quad (2.3.2e)$$

where $\hat{\Omega} \equiv \hat{\gamma} + \hat{\nu}$. The species evolve in successively higher powers of time, as expected from Figure 2.2(c). Examination of the neglected terms in (2.3.1) reveals that these approximations are valid until \hat{t} reaches $O(\alpha^{1/2})$, i.e. $\bar{t} = O(\alpha^{-1})$, at which time $\hat{B} = O(1)$, $\hat{D} = O(\alpha^{1/2})$, $\hat{F} = O(\alpha)$, $\hat{G} = O(\alpha^{3/2})$, and $\hat{H} = O(\alpha^2)$. The leading-order large-time limits of these variables, valid for $\alpha^{-3/2} \ll \bar{t} \ll \alpha^{-1}$ (i.e. between timescales t_1 and t_2), form the initial conditions for the next timescale. These limits are, in dimensionless unscaled variables,

$$B \approx \frac{\alpha}{\gamma + \nu}, \quad D \approx B\bar{t}, \quad F \approx \frac{\psi B \bar{t}^2}{2}, \quad G \approx \frac{-\chi\eta\psi B \bar{t}^3}{6\mu}, \quad H \approx \frac{\tau\lambda\chi\eta\psi B \bar{t}^4}{24\mu}. \quad (2.3.3a-e)$$

2.3.2 Timescale 2: $\bar{t} = O(\alpha^{-1})$

$O(1)$ variables are now defined using $B = \alpha^{-1/2}\hat{B}$, $D = \alpha^{-3/2}\hat{D}$, $F = \alpha^{-3/2}\hat{F}$, $G = \alpha^{-2}\hat{G}$, $H = \alpha^{-13/4}\hat{H}$ and $\bar{t} = \alpha^{-1}\hat{t}$, to yield the following leading-order reduction of (2.2.9):

$$0 = 1 - (\hat{\gamma} + \hat{\nu})\hat{B}, \quad \frac{d\hat{D}}{d\hat{t}} = \hat{B} - \hat{\psi}\hat{D} + \frac{\hat{\psi}\hat{\delta}}{\hat{\mu}}\hat{F}, \quad \frac{d\hat{F}}{d\hat{t}} = \hat{\psi}\hat{D} - \frac{\hat{\psi}\hat{\delta}}{\hat{\mu}}\hat{F}, \quad (2.3.4a-c)$$

$$\frac{d\hat{G}}{d\hat{t}} = \frac{-\hat{\chi}\hat{\eta}}{\hat{\mu}}\hat{F}, \quad \frac{d\hat{H}}{d\hat{t}} = -\hat{\tau}\hat{G}\hat{\lambda}. \quad (2.3.4d,e)$$

Therefore $\hat{B} = 1/(\hat{\gamma} + \hat{\nu})$. Also, $d(\hat{D} + \hat{F})/d\hat{t} = \hat{B}$, implying that $\hat{D} = \hat{B}\hat{t} - \hat{F}$ (the constant of integration is zero, from matching to (2.3.3)). Substituting this expression for \hat{D} into (2.3.4c) gives

$$\frac{d\hat{F}}{d\hat{t}} = \hat{\psi}\hat{B}\hat{t} - \hat{\psi} \left(1 + \frac{\hat{\delta}}{\hat{\mu}} \right) \hat{F},$$

which has solution

$$\hat{F} = c_1 \exp(-\hat{\Delta}\hat{t}) + \frac{\hat{\psi}\hat{B}\hat{t}}{\hat{\Delta}} - \frac{\hat{\psi}\hat{B}}{\hat{\Delta}^2},$$

where c_1 is a constant of integration and $\hat{\Delta} \equiv \hat{\psi} + \hat{\psi}\hat{\delta}/\hat{\mu}$. The Taylor series expansion of $\exp(-\hat{\Delta}\hat{t})$ about the point $\hat{t} = 0$ is $1 - \hat{\Delta}\hat{t} + \hat{\Delta}^2\hat{t}^2/2 + \dots$. Therefore, as $\hat{t} \rightarrow 0$, by

matching with (2.3.3c), this equation becomes

$$\frac{\hat{\psi}\hat{B}\hat{t}^2}{2} = c_1 \left(1 - \hat{\Delta}\hat{t} + \frac{\hat{\Delta}^2\hat{t}^2}{2} \right) + \frac{\hat{\psi}\hat{B}\hat{t}}{\hat{\Delta}} - \frac{\hat{\psi}\hat{B}}{\hat{\Delta}^2}.$$

This means that $c_1 = \hat{\psi}\hat{B}/\hat{\Delta}^2$, and so

$$\hat{F} = \hat{\psi}\hat{B} \left(\frac{\hat{t}}{\hat{\Delta}} + \frac{\exp(-\hat{\Delta}\hat{t}) - 1}{\hat{\Delta}^2} \right), \quad \hat{D} = \hat{B}\hat{t} - \hat{\psi}\hat{B} \left(\frac{\hat{t}}{\hat{\Delta}} + \frac{\exp(-\hat{\Delta}\hat{t}) - 1}{\hat{\Delta}^2} \right).$$

(For $\hat{t} \rightarrow 0$, substituting the three-term Taylor series expansion of $\exp(-\hat{\Delta}\hat{t})$ into this expression for \hat{D} gives $\hat{D} \approx \hat{B}\hat{t} - \hat{\psi}\hat{B}\hat{t}^2/2 \approx \hat{B}\hat{t}$, which matches (2.3.3b)). Likewise, substituting this expression for \hat{F} into (2.3.4d), integrating, finding the constant of integration by replacing $\exp(-\hat{\Delta}\hat{t})$ with a four-term Taylor series expansion and setting equal to (2.3.3d), and then repeating for \hat{H} , gives

$$\hat{G} = \frac{-\hat{\chi}\hat{\eta}\hat{\psi}\hat{B}}{\hat{\rho}} \left(\frac{\hat{t}^2}{2\hat{\Delta}} - \frac{\hat{t}}{\hat{\Delta}^2} - \frac{\exp(-\hat{\Delta}\hat{t}) - 1}{\hat{\Delta}^3} \right),$$

$$\hat{H} = \frac{\hat{\tau}\hat{\lambda}\hat{\chi}\hat{\eta}\hat{\psi}\hat{B}}{\hat{\rho}} \left(\frac{\hat{t}^3}{6\hat{\Delta}} - \frac{\hat{t}^2}{2\hat{\Delta}^2} + \frac{\hat{t}}{\hat{\Delta}^3} + \frac{\exp(-\hat{\Delta}\hat{t}) - 1}{\hat{\Delta}^4} \right).$$

Again, looking at the largest neglected terms in (2.3.4), these approximations are valid until \hat{t} reaches $O(\alpha^{1/4})$, at which time $\hat{B} = O(1)$, $\hat{D} = O(\alpha^{1/4})$, $\hat{F} = O(\alpha^{1/4})$, $\hat{G} = O(\alpha^{1/2})$, and $\hat{H} = O(\alpha^{3/4})$. The leading-order large-time limits of these variables, valid for $\alpha^{-1} \ll \bar{t} \ll \alpha^{-3/4}$ (i.e. between timescales t_2 and t_3), form the initial conditions for the next timescale. These limits are (2.3.3a) plus

$$D \approx \frac{B\bar{t}\delta}{\mu + \delta}, \quad F \approx \frac{B\bar{t}\mu}{\mu + \delta}, \quad G \approx \frac{-\chi\eta B\bar{t}^2}{2(\mu + \delta)}, \quad H \approx \frac{\tau\lambda\chi\eta B\bar{t}^3}{6(\mu + \delta)}, \quad (2.3.5a-d)$$

broadly consistent with the exponents $\Psi_B \approx 0$, $\Psi_D \approx 1$, $\Psi_F \approx 1$, $\Psi_G \approx 2$, and $\Psi_H \approx 3$ for $t_2 \ll \bar{t} \ll t_3$ in Figure 2.2(c).

2.3.3 Timescale 3: $\bar{t} = O(\alpha^{-3/4})$

On this timescale, $O(1)$ variables are defined using $B = \alpha^{-1/2}\hat{B}$, $D = \alpha^{-5/4}(\hat{D}_0 + \alpha^{-1/4}\hat{D}_1 + \dots)$, $F = \alpha^{-5/4}(\hat{F}_0 + \alpha^{-1/4}\hat{F}_1 + \dots)$, $G = \alpha^{-3/2}\hat{G}$, $H = \alpha^{-5/2}\hat{H}$ and $\bar{t} = \alpha^{-3/4}\hat{t}$, to yield the following reduction of (2.2.9):

$$\frac{d\hat{D}_0}{d\hat{t}} = \hat{B} - \hat{\psi} \left(\alpha^{1/4} \hat{D}_0 + \hat{D}_1 \right) + \frac{\hat{\psi}\hat{\delta}}{\hat{\eta}} \hat{F}_0 + \frac{\hat{\psi}\hat{\delta}}{\hat{\mu}} \left(\alpha^{1/4} \hat{F}_0 + \hat{F}_1 + 2\hat{G} \right) + O \left(\alpha^{-1/4} \right), \quad (2.3.6a)$$

$$\frac{d\hat{F}_0}{d\hat{t}} = \hat{\psi} \left(\alpha^{1/4} \hat{D}_0 + \hat{D}_1 \right) - \frac{\hat{\psi}\hat{\delta}}{\hat{\eta}} \hat{F}_0 - \frac{\hat{\psi}\hat{\delta}}{\hat{\mu}} \left(\alpha^{1/4} \hat{F}_0 + \hat{F}_1 + 2\hat{G} \right) + O \left(\alpha^{-1/4} \right), \quad (2.3.6b)$$

$$\frac{d\hat{G}}{d\hat{t}} = \frac{-\hat{\chi}\hat{\eta}\hat{\tau}\hat{\lambda}}{\hat{\rho}\hat{\kappa}} \hat{G} - \frac{\hat{\chi}\hat{\eta}}{\hat{\mu}} \hat{F}_0 + O \left(\alpha^{-1/4} \right), \quad (2.3.6c)$$

$$\frac{d\hat{H}}{d\hat{t}} = -\hat{\tau}\hat{G}\hat{\lambda} + O \left(\alpha^{-1} \right), \quad (2.3.6d)$$

with $\hat{B} = 1/(\hat{\gamma} + \nu)$ as in (2.3.4a). As the left hand sides of (2.3.6a,b) are $O(1)$, the $O(\alpha^{1/4})$ terms on the right hand sides must sum to zero, i.e.

$$-\hat{\psi}\hat{D}_0 + \frac{\hat{\psi}\hat{\delta}}{\hat{\mu}} \hat{F}_0 = 0. \quad (2.3.7)$$

In the limit $\alpha \rightarrow \infty$, the leading-order behaviour of (2.3.6) on this timescale is given by (2.3.6c,d) plus

$$\frac{d\hat{D}_0}{d\hat{t}} = \hat{B} - \hat{\psi}\hat{D}_1 + \frac{\hat{\psi}\hat{\delta}}{\hat{\eta}} \hat{F}_0 + \frac{\hat{\psi}\hat{\delta}}{\hat{\mu}} (\hat{F}_1 + 2\hat{G}), \quad (2.3.8a)$$

$$\frac{d\hat{F}_0}{d\hat{t}} = \hat{\psi}\hat{D}_1 - \frac{\hat{\psi}\hat{\delta}}{\hat{\eta}} \hat{F}_0 - \frac{\hat{\psi}\hat{\delta}}{\hat{\mu}} (\hat{F}_1 + 2\hat{G}). \quad (2.3.8b)$$

Therefore $d(\hat{D}_0 + \hat{F}_0)/d\hat{t} = \hat{B}$, implying $\hat{D}_0 = \hat{B}\hat{t} - \hat{F}_0$ (matching to (2.3.5a,b)). Substituting this into (2.3.7) gives the following leading order behaviour for D and F on this timescale:

$$\hat{D}_0 = \frac{\hat{B}\hat{t}\hat{\delta}}{\hat{\mu} + \hat{\delta}}, \quad \hat{F}_0 = \frac{\hat{B}\hat{t}\hat{\mu}}{\hat{\mu} + \hat{\delta}}. \quad (2.3.9a,b)$$

Substituting (2.3.9b) into (2.3.6c), and solving for \hat{G} gives

$$\hat{G} = \frac{\hat{\Lambda}^2 \hat{\Gamma}}{\hat{\chi}\hat{\eta}} \left(1 - \exp \left(\frac{-\hat{\chi}\hat{\eta}\hat{t}}{\hat{\Lambda}} \right) \right) - \hat{\Lambda}\hat{t},$$

where $\hat{\Gamma} \equiv \hat{B}/(\hat{\mu} + \hat{\delta})$ and $\hat{\Lambda} \equiv \hat{\rho}\hat{\kappa}/\hat{\tau}\hat{\lambda}$. \hat{H} is given by

$$\hat{H} = -\hat{\tau}\hat{\lambda} \frac{\hat{\Lambda}^2 \hat{\Gamma}}{\hat{\chi}\hat{\eta}} \left(\hat{t} + \frac{\hat{\Lambda}}{\hat{\chi}\hat{\eta}} \exp \left(\frac{-\hat{\chi}\hat{\eta}\hat{t}}{\hat{\Lambda}} \right) \right) + \hat{\tau}\hat{\lambda}\hat{\Lambda}\hat{t} \frac{\hat{t}^2}{2} + \frac{\hat{\tau}\hat{\lambda}\hat{\Lambda}^3 \hat{\Gamma}}{\hat{\chi}^2 \hat{\eta}^2}.$$

The constants of integration for \hat{G} and \hat{H} are deduced from matching to (2.3.5c,d). (Substituting the three-term Taylor series expansion of $\exp(-\hat{\chi}\hat{\eta}\hat{t}/\hat{\Lambda})$ about the point $\hat{t} = 0$ into these expressions for \hat{G} and \hat{H} gives (2.3.5c,d).)

The neglected terms in (2.3.6) indicate that these approximations are valid until \hat{t} reaches $O(\alpha^{1/4})$, at which point \hat{B} is $O(1)$, \hat{D} , \hat{F} and \hat{G} are $O(\alpha^{1/4})$, and \hat{H} is $O(\alpha^{1/2})$. The leading-order large-time limits of these variables, valid for $\alpha^{-3/4} \ll \bar{t} \ll \alpha^{-1/2}$ (i.e. between timescales t_3 and t_4), are given by (2.3.3a), (2.3.5a,b) and

$$G \approx \frac{-\rho\kappa B\bar{t}}{\tau\lambda(\mu + \delta)}, \quad H \approx \frac{\rho\kappa B\bar{t}^2}{2(\mu + \delta)}, \quad (2.3.10a,b)$$

consistent with $\Psi_G \approx 1$, $\Psi_H \approx 2$ in Figure 2.2(c) (although these exponents do not exhibit clear plateaux for $t_3 \ll \bar{t} \ll t_4$).

2.3.4 Timescale 4: $\bar{t} = O(\alpha^{-1/2})$

On the next timescale, $O(1)$ variables are defined using $B = \alpha^{-1/2}\hat{B}$, with $\hat{B} = 1/(\hat{\gamma} + \hat{\nu})$, $D = \alpha^{-1}(\hat{D}_0 + \alpha^{-1/4}\hat{D}_1 + \alpha^{-1/2}\hat{D}_2 + \dots)$, $F = \alpha^{-1}(\hat{F}_0 + \alpha^{-1/4}\hat{F}_1 + \alpha^{-1/2}\hat{F}_2 + \dots)$, $G = \alpha^{-5/4}(\hat{G}_0 + \alpha^{-1/4}\hat{G}_1 + \dots)$, $H = \alpha^{-2}\hat{H}$, and $\bar{t} = \alpha^{-1/2}\hat{t}$. Similarly to timescale 3, the resulting $O(\alpha^{1/2})$ terms in the ODEs for D and F must sum to zero, which gives (2.3.7), as must the $O(\alpha^{1/4})$ terms in the ODEs for D , F and G , which give

$$-\hat{\psi}\hat{D}_1 + \frac{\hat{\psi}\hat{\delta}}{\hat{\eta}\hat{\mu}}\hat{F}_0(\hat{\mu} + \hat{F}_0) + \frac{\hat{\psi}\hat{\delta}}{\hat{\mu}}(\hat{F}_1 + 2\hat{G}_0) = 0, \quad (2.3.11a)$$

$$\hat{\chi}\hat{\eta} - \frac{\hat{\chi}\hat{\eta}}{\hat{\mu}} \left(\frac{\hat{\tau}\hat{\lambda}}{\hat{\rho}\hat{\kappa}}\hat{G}_0 + 1 \right) (\hat{\mu} + \hat{F}_0) = 0. \quad (2.3.11b)$$

Then, in the limit $\alpha \rightarrow \infty$, the leading-order behaviour is given by

$$\frac{d\hat{D}_0}{d\hat{t}} = \hat{B} - \hat{\psi}\hat{D}_2 + \frac{\hat{\psi}\hat{\delta}}{\hat{\eta}\hat{\mu}} (2\hat{F}_0\hat{F}_1 + 2\hat{F}_0\hat{G}_0 + \hat{F}_1\hat{\mu} + \hat{\eta}(\hat{F}_2 + 2\hat{G}_1)), \quad (2.3.12a)$$

$$\frac{d\hat{F}_0}{d\hat{t}} = \hat{\psi}\hat{D}_2 - \frac{\hat{\psi}\hat{\delta}}{\hat{\eta}\hat{\mu}} (2\hat{F}_0\hat{F}_1 + 2\hat{F}_0\hat{G}_0 + \hat{F}_1\hat{\mu} + \hat{\eta}(\hat{F}_2 + 2\hat{G}_1)), \quad (2.3.12b)$$

$$\frac{d\hat{G}_0}{d\hat{t}} = \hat{\chi}\hat{F}_0 - \frac{\hat{\chi}\hat{\eta}}{\hat{\mu}} \left(\frac{\hat{\tau}\hat{\lambda}}{\hat{\rho}\hat{\kappa}}\hat{G}_0 + 1 \right) (\hat{F}_1 + 2\hat{G}_0) - \frac{\hat{\chi}\hat{\eta}\hat{\tau}\hat{\lambda}}{\hat{\mu}\hat{\rho}\hat{\kappa}}\hat{G}_1(\hat{\mu} + \hat{F}_0), \quad (2.3.12c)$$

$$\frac{d\hat{H}}{d\hat{t}} = -\hat{\tau}\hat{G}_0\hat{\lambda}. \quad (2.3.12d)$$

Therefore $d(\hat{D}_0 + \hat{F}_0)/d\hat{t} = \hat{B}$, and so $\hat{D}_0 = \hat{B}\hat{t} - \hat{F}_0$. This, together with (2.3.7), gives (2.3.9). Substituting (2.3.9b) into (2.3.11b), and simplifying, gives

$$\hat{G}_0 = \frac{-\hat{\rho}\hat{\kappa}\hat{B}\hat{t}}{\hat{\tau}\hat{\lambda}(\hat{\mu} + \hat{\delta} + \hat{B}\hat{t})}. \quad (2.3.13a)$$

To check that this solution for \hat{G} matches the small-time limit (2.3.10a), note that this expression differentiates to

$$\frac{d\hat{G}_0}{d\hat{t}} = \frac{-\hat{\rho}\hat{\kappa}\hat{B}(\hat{\mu} + \hat{\delta})}{\hat{\tau}\hat{\lambda}(\hat{\mu} + \hat{\delta} + \hat{B}\hat{t})^2},$$

and so the two-term Taylor series expansion of (2.3.13a) about the point $\hat{t} = 0$ is

$$G_0 = \frac{-\hat{\rho}\hat{\kappa}\hat{B}}{\hat{\tau}\hat{\lambda}} \left(0 + \frac{\hat{t}}{(\hat{\mu} + \hat{\delta})} \right),$$

which correctly matches (2.3.10a).

Substituting (2.3.13a) into (2.3.12d) gives

$$\frac{d\hat{H}}{d\hat{t}} = \frac{\hat{\rho}\hat{\kappa}\hat{B}\hat{t}}{\hat{\mu} + \hat{\delta} + \hat{B}\hat{t}}$$

and this has solution

$$\hat{H} = \hat{\rho}\hat{\kappa}\hat{t} - \frac{\hat{\rho}\hat{\kappa}(\hat{\mu} + \hat{\delta})}{\hat{B}} \ln(\hat{\mu} + \hat{\delta} + \hat{B}\hat{t}) + c_1,$$

where c_1 is a constant of integration. Noting that $\ln(\hat{\mu} + \hat{\delta} + \hat{B}\hat{t})$ differentiates to $B/(\hat{\mu} + \hat{\delta} + \hat{B}\hat{t})$, and then to $-B^2/(\hat{\mu} + \hat{\delta} + \hat{B}\hat{t})^2$, substituting the three-term Taylor series expansion of $\ln(\hat{\mu} + \hat{\delta} + \hat{B}\hat{t})$ about $\hat{t} = 0$ into this expression, and matching to (2.3.10b), gives

$$\frac{\hat{\rho}\hat{\kappa}\hat{B}\hat{t}^2}{2(\hat{\mu} + \hat{\delta})} + \dots = \hat{\rho}\hat{\kappa}\hat{t} - \frac{\hat{\rho}\hat{\kappa}(\hat{\mu} + \hat{\delta})}{\hat{B}} \left(\ln(\hat{\mu} + \hat{\delta}) + \frac{\hat{B}\hat{t}}{\hat{\mu} + \hat{\delta}} - \frac{\hat{B}^2\hat{t}^2}{2(\hat{\mu} + \hat{\delta})^2} + \dots \right) + c_1,$$

where the terms at the next order of the large-time limit (2.3.10b), and the terms at the next order of the Taylor series expansion of $\ln(\hat{\mu} + \hat{\delta} + \hat{B}\hat{t})$, are omitted. Therefore

$$c_1 = \frac{\hat{\rho}\hat{\kappa}(\hat{\mu} + \hat{\delta})}{\hat{B}} \ln(\hat{\mu} + \hat{\delta}),$$

and

$$\hat{H} = \hat{\rho}\hat{\kappa}\hat{t} - \frac{\hat{\rho}\hat{\kappa}(\hat{\mu} + \hat{\delta})}{\hat{B}} \ln \left(\frac{\hat{\mu} + \hat{\delta} + \hat{B}\hat{t}}{\hat{\mu} + \hat{\delta}} \right). \quad (2.3.13b)$$

These approximations are valid until \hat{t} reaches $O(\alpha^{1/4})$, at which point \hat{B} and \hat{G} are $O(1)$, and \hat{D} , \hat{F} and \hat{H} are $O(\alpha^{1/4})$. Noting that (2.3.13a) can be written

$$\hat{G}_0 = \frac{-\hat{\rho}\hat{\kappa}}{\hat{\tau}\hat{\lambda}} \left(1 + \frac{\hat{\mu} + \hat{\delta}}{\hat{B}\hat{t}} \right)^{-1}, \quad (2.3.14)$$

and that the sum of the infinite geometric series $\sum_{n=0}^{\infty} (-a)^n = (1+a)^{-1}$ if $|a| < 1$, then

$$\hat{G}_0 \approx \frac{-\hat{\rho}\hat{\kappa}}{\hat{\tau}\hat{\lambda}} \left(1 - \frac{\hat{\mu} + \hat{\delta}}{\hat{B}\hat{t}} + \dots \right) \text{ for } \hat{t} \gg O(1). \quad (2.3.15)$$

Therefore, the large-time limits of these variables, valid for $\alpha^{-1/2} \ll \bar{t} \ll \alpha^{-1/4}$ (i.e. between timescales t_4 and t_5), and consistent with $\Psi_G \approx 0$, $\Psi_H \approx 1$, are given by (2.3.3a), (2.3.5a,b), plus

$$G \approx \frac{-\rho\kappa}{\tau\lambda} + \frac{\rho\kappa(\mu + \delta)}{\tau\lambda B\bar{t}}, \quad H \approx \rho\kappa\bar{t}. \quad (2.3.16a,b)$$

2.3.5 Timescale 5: $\bar{t} = O(\alpha^{-1/4})$

On this timescale, $O(1)$ variables are defined using $B = \alpha^{-1/2}\hat{B}$, with $\hat{B} = 1/(\hat{\gamma} + \hat{\nu})$, $D = \alpha^{-3/4}(\hat{D}_0 + \alpha^{-1/4}\hat{D}_1 + \alpha^{-1/2}\hat{D}_2 + \alpha^{-3/4}\hat{D}_3 + \dots)$, $F = \alpha^{-3/4}(\hat{F}_0 + \alpha^{-1/4}\hat{F}_1 + \alpha^{-1/2}\hat{F}_2 + \alpha^{-3/4}\hat{F}_3 + \dots)$, $G = \alpha^{-5/4}(\hat{G}_0 + \alpha^{-1/4}\hat{G}_1 + \alpha^{-1/2}\hat{G}_2 + \alpha^{-3/4}\hat{G}_3 + \dots)$, $H = \alpha^{-7/4}\hat{H}$, and $\bar{t} = \alpha^{-1/4}\hat{t}$. The $O(\alpha^{3/4})$ terms in the ODEs for D , F and G give

$$-\hat{\psi}\hat{D}_0 + \frac{\hat{\psi}\hat{\delta}}{\hat{\eta}\hat{\mu}}(\hat{F}_0 + \hat{\eta})\hat{F}_0 = 0, \quad (2.3.17a)$$

$$-\frac{\hat{\chi}\hat{\eta}}{\hat{\mu}}\left(\frac{\hat{\tau}\hat{\lambda}}{\hat{\rho}\hat{\kappa}}\hat{G}_0 + 1\right)\hat{F}_0 = 0, \quad (2.3.17b)$$

the $O(\alpha^{1/2})$ terms give

$$-\hat{\psi}(\hat{D}_1 + \delta) + \frac{\hat{\psi}\hat{\delta}}{\hat{\eta}\hat{\mu}}((\hat{F}_0 + \hat{\eta})(\hat{\mu} + \hat{F}_1) + \hat{F}_1\hat{F}_0) = 0, \quad (2.3.18a)$$

$$\hat{\chi}(\hat{F}_0 + \hat{\eta}) - \frac{\hat{\chi}\hat{\eta}}{\hat{\mu}}\left(\frac{\hat{\tau}\hat{\lambda}}{\hat{\rho}\hat{\kappa}}\hat{G}_0 + 1\right)(\hat{\mu} + \hat{F}_1) - \frac{\hat{\chi}\hat{\eta}\hat{\tau}\hat{\lambda}}{\hat{\mu}\hat{\rho}\hat{\kappa}}\hat{G}_1\hat{F}_0 = 0, \quad (2.3.18b)$$

and the $O(\alpha^{1/4})$ terms give

$$-\hat{\psi}\hat{D}_2 + \frac{\hat{\psi}\hat{\delta}}{\hat{\eta}\hat{\mu}}((\hat{F}_0 + \hat{\eta})(\hat{F}_2 + 2\hat{G}_0) + \hat{F}_1(\hat{\mu} + \hat{F}_1) + \hat{F}_2\hat{F}_0) = 0, \quad (2.3.19a)$$

$$\hat{\chi}\hat{F}_1 - \frac{\hat{\chi}\hat{\eta}}{\hat{\mu}}\left(\frac{\hat{\tau}\hat{\lambda}}{\hat{\rho}\hat{\kappa}}\hat{G}_0 + 1\right)(\hat{F}_2 + 2\hat{G}_0) - \frac{\hat{\chi}\hat{\eta}\hat{\tau}\hat{\lambda}}{\hat{\mu}\hat{\rho}\hat{\kappa}}(\hat{G}_1(\hat{\mu} + \hat{F}_1) + \hat{G}_2\hat{F}_0) = 0. \quad (2.3.19b)$$

Then, the leading-order behaviour on this timescale is given by

$$\frac{d\hat{D}_0}{d\hat{t}} = \hat{B} - \frac{\hat{\beta}}{\hat{\delta}}\hat{D}_0 - \hat{\psi}\hat{D}_3 + \frac{\hat{\psi}\hat{\delta}}{\hat{\eta}\hat{\mu}}((\hat{F}_0 + \hat{\eta})(\hat{F}_3 + 2\hat{G}_1) + \hat{F}_1(\hat{F}_2 + 2\hat{G}_0) + \hat{F}_2(\hat{\mu} + \hat{F}_1) + \hat{F}_3\hat{F}_0),$$

$$\frac{d\hat{F}_0}{d\hat{t}} = \hat{\psi}\hat{D}_3 - \frac{\hat{\psi}\hat{\delta}}{\hat{\eta}\hat{\mu}}((\hat{F}_0 + \hat{\eta})(\hat{F}_3 + 2\hat{G}_1) + \hat{F}_1(\hat{F}_2 + 2\hat{G}_0) + \hat{F}_2(\hat{\mu} + \hat{F}_1) + \hat{F}_3\hat{F}_0),$$

$$\frac{d\hat{G}_0}{d\hat{t}} = \hat{\chi}\hat{F}_2 - \frac{\hat{\chi}\hat{\eta}}{\hat{\mu}}\left(\frac{\hat{\tau}\hat{\lambda}}{\hat{\rho}\hat{\kappa}}\hat{G}_0 + 1\right)(\hat{F}_3 + 2\hat{G}_1) - \frac{\hat{\chi}\hat{\eta}\hat{\tau}\hat{\lambda}}{\hat{\mu}\hat{\rho}\hat{\kappa}}(\hat{G}_1(\hat{F}_2 + 2\hat{G}_0) + \hat{G}_2(\hat{\mu} + \hat{F}_1) + \hat{G}_3\hat{F}_0),$$

$$\frac{d\hat{H}}{d\hat{t}} = -\hat{\tau}\hat{G}_0\hat{\lambda}. \quad (2.3.20a-d)$$

From (2.3.17a),

$$\hat{D}_0 = \frac{\delta}{\hat{\eta}\hat{\mu}} \hat{F}_0^2 + \frac{\delta}{\hat{\mu}} \hat{F}_0, \quad (2.3.21)$$

and differentiating with respect to \hat{t} gives

$$\frac{d\hat{D}_0}{d\hat{t}} = \frac{\delta}{\hat{\eta}\hat{\mu}} 2\hat{F}_0 \frac{d\hat{F}_0}{d\hat{t}} + \frac{\delta}{\hat{\mu}} \frac{d\hat{F}_0}{d\hat{t}}. \quad (2.3.22)$$

From (2.3.20a,b),

$$\frac{d\hat{D}_0}{d\hat{t}} + \frac{d\hat{F}_0}{d\hat{t}} = \hat{B} - \frac{\hat{\beta}}{\delta} \hat{D}_0, \quad (2.3.23)$$

and substituting (2.3.21) and (2.3.22) into this expression, and re-arranging, gives

$$\frac{d\hat{F}_0}{d\hat{t}} = \frac{\hat{B}\hat{\eta}\hat{\mu} - \hat{\beta}\hat{F}_0^2 - \hat{\beta}\hat{\eta}\hat{F}_0}{2\delta\hat{F}_0 + \delta\hat{\eta} + \hat{\mu}\hat{\eta}}, \quad (2.3.24)$$

and so \hat{F}_0 has the implicit solution

$$\hat{t} = \left(\frac{-\hat{\eta}\hat{\mu}}{2\hat{\beta}\hat{\Xi}} - \frac{\delta}{\hat{\beta}} \right) \ln \left(\frac{\hat{F}_0 + \hat{\eta}/2 - \hat{\Xi}}{\hat{\eta}/2 - \hat{\Xi}} \right) + \left(\frac{\hat{\eta}\hat{\mu}}{2\hat{\beta}\hat{\Xi}} - \frac{\delta}{\hat{\beta}} \right) \ln \left(\frac{\hat{F}_0 + \hat{\eta}/2 + \hat{\Xi}}{\hat{\eta}/2 + \hat{\Xi}} \right), \quad (2.3.25)$$

where $\hat{\Xi} \equiv \sqrt{\frac{\hat{\eta}^2}{4} + \frac{\hat{\beta}\hat{\eta}\hat{\mu}}{\delta}}$. From (2.3.17b), (2.3.18b) and (2.3.20d) respectively, the evolution of \hat{G} and \hat{H} is given by

$$\hat{G}_0 = \frac{-\hat{\rho}\hat{\kappa}}{\hat{\tau}\hat{\lambda}}, \quad \hat{G}_1 = \frac{\hat{\mu}\hat{\rho}\hat{\kappa}(\hat{F}_0 + \hat{\eta})}{\hat{\eta}\hat{\tau}\hat{\lambda}\hat{F}_0}, \quad \hat{H} = \hat{\rho}\hat{\kappa}\hat{t}. \quad (2.3.26a-c)$$

As $\hat{F}_0 \rightarrow 0$ as $\hat{t} \rightarrow 0$, the small-time limits of (2.3.24), (2.3.21) and (2.3.26b) are

$$\frac{d\hat{F}_0}{d\hat{t}} \approx \frac{\hat{B}\hat{\mu}}{\delta + \hat{\mu}}, \quad \hat{D}_0 \approx \frac{\delta\hat{F}_0}{\hat{\mu}}, \quad \hat{G}_1 \approx \frac{\hat{\mu}\hat{\rho}\hat{\kappa}}{\hat{\tau}\hat{\lambda}\hat{F}_0} \approx \frac{\hat{\rho}\hat{\kappa}(\hat{\mu} + \delta)}{\hat{\tau}\hat{\lambda}\hat{B}\hat{t}}, \quad (2.3.27a-c)$$

ensuring matching to (2.3.5a,b) and (2.3.16a). (The expression for \hat{G}_1 uses the result $\hat{F}_0 \approx \hat{B}\hat{\mu}\hat{t}/(\hat{\mu} + \delta)$ from (2.3.27a).)

From (2.3.24), \hat{F} rapidly equilibrates for $\hat{t} \gg 1$, and therefore also do \hat{D} and \hat{G} , and \hat{H} evolves linearly in time, consistent with Figure 2.2(c). The approximations above are valid until \hat{t} reaches $O(\alpha^{1/2})$, at which point \hat{B} , \hat{D} , \hat{F} and \hat{G} are $O(1)$, and \hat{H} is $O(\alpha^{1/2})$. The large-time limits for D and F , valid for $\alpha^{-1/4} \ll \hat{t} \ll \alpha^{1/4}$ (i.e. between timescales t_5 and t_6), are found by setting $d\hat{D}_0/d\hat{t} = 0$ and $d\hat{F}_0/d\hat{t} = 0$ in (2.3.23), to give

$$D \approx \frac{\delta}{\hat{\beta}} B, \quad (2.3.28a)$$

and substituting this expression into (2.3.21) and solving the quadratic in \hat{F}_0 , to give

$$F \approx \frac{-\eta}{2} + \sqrt{\frac{\eta^2}{4} + \frac{\eta\mu}{\beta}B}. \quad (2.3.28b)$$

The corresponding large-time limits of G and H are

$$G \approx \frac{-\rho\kappa}{\tau\lambda} + \frac{\mu\rho\kappa(F + \eta)}{\eta\tau\lambda F}, \quad H \approx \rho\kappa\bar{t}, \quad (2.3.28c,d)$$

(with F satisfying (2.3.28b)), consistent with $\Psi_B = \Psi_D = \Psi_F = \Psi_G = 0$ and $\Psi_H \approx 1$.

2.3.6 Timescale 6: $\bar{t} = O(\alpha^{1/4})$

On this final timescale, $O(1)$ variables are defined as $B = \alpha^{-1/2}\hat{B}$, with $\hat{B} = 1/(\hat{\gamma} + \hat{\nu})$, $D = \alpha^{-3/4}(\hat{D}_0 + \alpha^{-1/4}\hat{D}_1 + \alpha^{-1/2}\hat{D}_2 + \alpha^{-3/4}\hat{D}_3 + \dots)$, $F = \alpha^{-3/4}(\hat{F}_0 + \alpha^{-1/4}\hat{F}_1 + \alpha^{-1/2}\hat{F}_2 + \alpha^{-3/4}\hat{F}_3 + \dots)$, $G = \alpha^{-5/4}(\hat{G}_0 + \alpha^{-1/4}\hat{G}_1 + \alpha^{-1/2}\hat{G}_2 + \alpha^{-3/4}\hat{G}_3 + \dots)$, $H = \alpha^{-5/4}\hat{H}$, and $\bar{t} = \alpha^{1/4}\hat{t}$. Substituting these expansions into (2.2.9) gives identities (2.3.17), (2.3.18) and (2.3.19). Also, $O(1)$ balances for (2.2.9b-d) are given by

$$0 = \hat{B} - \frac{\hat{\beta}}{\hat{\delta}}\hat{D}_0 - \hat{\psi}\hat{D}_3 + \frac{\hat{\psi}\hat{\delta}}{\hat{\eta}\hat{\mu}} \left((\hat{F}_0 + \hat{\eta})(\hat{F}_3 + 2\hat{G}_1) + \hat{F}_1(\hat{F}_2 + 2\hat{G}_0) + \hat{F}_2(\hat{\mu} + \hat{F}_1) + \hat{F}_3\hat{F}_0 \right),$$

$$0 = \hat{\psi}\hat{D}_3 - \frac{\hat{\psi}\hat{\delta}}{\hat{\eta}\hat{\mu}} \left((\hat{F}_0 + \hat{\eta})(\hat{F}_3 + 2\hat{G}_1) + \hat{F}_1(\hat{F}_2 + 2\hat{G}_0) + \hat{F}_2(\hat{\mu} + \hat{F}_1) + \hat{F}_3\hat{F}_0 \right),$$

$$0 = \hat{\chi}\hat{F}_2 - \frac{\hat{\chi}\hat{\eta}}{\hat{\mu}} \left(\frac{\hat{\tau}\hat{\lambda}}{\hat{\rho}\hat{\kappa}}\hat{G}_0 + 1 \right) (\hat{F}_3 + 2\hat{G}_1) - \frac{\hat{\chi}\hat{\eta}\hat{\tau}\hat{\lambda}}{\hat{\mu}\hat{\rho}\hat{\kappa}} \left(\hat{G}_1(\hat{F}_2 + 2\hat{G}_0) + \hat{G}_2(\hat{\mu} + \hat{F}_1) + \hat{G}_3\hat{F}_0 \right).$$

Therefore, the solutions to D , F , and G on this timescale are given by (2.3.28a-c). Also, (2.2.9e) becomes

$$\frac{d\hat{H}}{d\hat{t}} = -\hat{\tau} \left(\hat{G}_0 + \alpha^{-1/4}\hat{G}_1 \right) \hat{\lambda} - \hat{\rho}\hat{H} + O(\alpha^{-1/2}), \quad (2.3.29)$$

and the solution to (2.3.29) that includes the first correction term for G and matches to (2.3.28d), is

$$\hat{H} = \left(\hat{\kappa} - \frac{\hat{\mu}\hat{\kappa}(\hat{F}_0 + \hat{\eta})}{\hat{\eta}\hat{F}_0} \right) (1 - \exp(-\hat{\rho}\hat{t})). \quad (2.3.30)$$

Thus for $\bar{t} \gg \alpha^{1/4}$, the large-time limits are (2.3.3a), (2.3.28a-c), and

$$H \approx \kappa - \frac{\mu\kappa(F + \eta)}{\eta F}, \quad (2.3.31)$$

(with F satisfying (2.3.28b)).

2.3.7 Plotted expressions

Each species' six evolution expressions, one from each of the six timescales, are matched together (or patched together where this is necessary to provide a good visual fit to the full simulations), and these combined expressions for the five species, given below, are plotted in Figure 2.2(b) with dashed lines. There is excellent agreement between these approximations and the simulations.

$$B = \frac{\alpha}{\Omega} (1 - \exp(-\Omega \bar{t})), \quad (2.3.32a)$$

where $\Omega \equiv \gamma + \nu$,

$$D = \begin{cases} \frac{\alpha}{\Omega} \left(\bar{t} + \frac{\exp(-\Omega \bar{t}) - 1}{\Omega} \right) - \psi B \left(\frac{\bar{t}}{\Delta} + \frac{\exp(-\Delta \bar{t}) - 1}{\Delta^2} \right) & \text{if } \bar{t} < \alpha^{-7/8}, \\ \frac{B \bar{t} \delta}{\mu + \delta} & \text{if } \alpha^{-7/8} < \bar{t} < \alpha^{-3/8}, \\ \frac{\delta}{\eta \mu} (F + \eta) F & \text{if } \alpha^{-3/8} < \bar{t} < \alpha^{-2/8}, \\ \frac{\delta}{\beta} B & \text{if } \alpha^{-2/8} < \bar{t}, \end{cases} \quad (2.3.32b)$$

where $\Delta \equiv \psi + \psi \delta / \mu$,

$$F = \begin{cases} \frac{\alpha \psi}{\Omega} \left(\frac{\bar{t}^2}{2} - \frac{\bar{t}}{\Omega} - \frac{\exp(-\Omega \bar{t}) - 1}{\Omega^2} \right) - \frac{\psi B \bar{t}^2}{2} + \psi B \left(\frac{\bar{t}}{\Delta} + \frac{\exp(-\Delta \bar{t}) - 1}{\Delta^2} \right) & \text{if } \bar{t} < \alpha^{-7/8}, \\ \frac{B \bar{t} \mu}{\mu + \delta} & \text{if } \alpha^{-7/8} < \bar{t} < \alpha^{-3/8}, \\ \tilde{F}(\bar{t}) & \text{if } \alpha^{-3/8} < \bar{t} < \alpha^{-2/8}, \\ \frac{-\eta}{2} + \sqrt{\frac{\eta^2}{4} + \frac{\eta \mu}{\beta} B} & \text{if } \alpha^{-2/8} < \bar{t}, \end{cases} \quad (2.3.32c)$$

where $\tilde{F}(\bar{t})$ is given implicitly by

$$\bar{t} = \left(\frac{-\eta \mu}{2\beta \Xi} - \frac{\delta}{\beta} \right) \ln \left(\frac{\tilde{F} + \frac{\eta}{2} - \Xi}{\frac{\eta}{2} - \Xi} \right) + \left(\frac{\eta \mu}{2\beta \Xi} - \frac{\delta}{\beta} \right) \ln \left(\frac{\tilde{F} + \frac{\eta}{2} + \Xi}{\frac{\eta}{2} + \Xi} \right),$$

$$\text{and } \Xi \equiv \sqrt{\frac{\eta^2}{4} + \frac{B\eta\mu}{\beta}},$$

$$G = \begin{cases} \begin{aligned} & \frac{-\alpha\chi\eta\psi}{\Omega\mu} \left(\frac{\bar{f}^3}{6} - \frac{\bar{f}^2}{2\Omega} + \frac{\bar{f}}{\Omega^2} + \frac{\exp(-\Omega\bar{f})-1}{\Omega^3} \right) + \frac{\chi\eta\psi B\bar{f}^3}{6\mu} \\ & - \frac{\chi\eta\psi B}{\mu} \left(\frac{\bar{f}^2}{2\Delta} - \frac{\bar{f}}{\Delta^2} - \frac{\exp(-\Delta\bar{f})-1}{\Delta^3} \right) + \frac{\chi\eta B\bar{f}^2}{2(\mu+\delta)} \\ & + \frac{\theta^2 B}{\chi\eta(\mu+\delta)} \left(1 - \exp\left(\frac{-\chi\eta\bar{f}}{\theta}\right) \right) - \frac{\theta B\bar{f}}{(\mu+\delta)} \end{aligned} & \text{if } \bar{f} < \alpha^{-5/8}, \\ \frac{-\theta B\bar{f}}{\mu+\delta+B\bar{f}} & \text{if } \alpha^{-5/8} < \bar{f} < \alpha^{-3/8}, \\ -\theta + \frac{\chi(F+\eta)}{\phi F} & \text{if } \alpha^{-3/8} < \bar{f}, \end{cases} \quad (2.3.32d)$$

$$H = \begin{cases} \begin{aligned} & \frac{\alpha\tau\lambda\chi\eta\psi}{\Omega\mu} \left(\frac{\bar{f}^4}{24} - \frac{\bar{f}^3}{6\Omega} + \frac{\bar{f}^2}{2\Omega^2} - \frac{\bar{f}}{\Omega^3} - \frac{\exp(-\Omega\bar{f})-1}{\Omega^4} \right) - \frac{\tau\lambda\chi\eta\psi B\bar{f}^4}{24\mu} \\ & + \frac{\tau\lambda\chi\eta\psi B}{\mu} \left(\frac{\bar{f}^3}{6\Delta} - \frac{\bar{f}^2}{2\Delta^2} + \frac{\bar{f}}{\Delta^3} + \frac{\exp(-\Delta\bar{f})-1}{\Delta^4} \right) - \frac{\tau\lambda\chi\eta B\bar{f}^3}{6(\mu+\delta)} \\ & - \tau\lambda \frac{\theta^2 B}{\chi\eta(\mu+\delta)} \left(\bar{f} + \frac{\theta}{\chi\eta} \exp\left(\frac{-\chi\eta\bar{f}}{\theta}\right) \right) + \frac{\tau\lambda\theta B\bar{f}^2}{2(\mu+\delta)} + \frac{\tau\lambda\theta^3 B}{\chi^2\eta^2(\mu+\delta)} \end{aligned} & \text{if } \bar{f} < \alpha^{-5/8}, \\ \rho\kappa\bar{f} - \frac{\rho\kappa(\mu+\delta)}{B} (\ln(\mu+\delta+B\bar{f}) - \ln(\mu+\delta)) & \text{if } \alpha^{-5/8} < \bar{f} < \alpha^{-3/8}, \\ \rho\kappa\bar{f} & \text{if } \alpha^{-3/8} < \bar{f} < \alpha^{-1/8}, \\ \left(\kappa - \frac{\mu\kappa(F+\eta)}{\eta F} \right) (1 - \exp(-\rho\bar{f})) & \text{if } \alpha^{-1/8} < \bar{f}, \end{cases} \quad (2.3.32e)$$

2.3.8 Equilibrium concentrations

The large-time limits of the leading-order approximations, given by (2.3.3a), (2.3.28a-c) and (2.3.31), give estimates of the concentrations at the new equilibrium, which in dimensional terms are:

$$[\text{CO}_2(\text{aq})]_{\infty} \approx [\text{CO}_2(\text{aq})]_0 + \frac{[\text{CO}_2(\text{g})]_0 K_1}{K_1 + 1}, \quad (2.3.33a)$$

$$[\text{H}_2\text{CO}_3]_{\infty} \approx [\text{H}_2\text{CO}_3]_0 + \frac{[\text{CO}_2(\text{g})]_0 K_1 K_2}{K_1 + 1}, \quad (2.3.33b)$$

$$[\text{HCO}_3^-]_{\infty} \approx \frac{[\text{HCO}_3^-]_0}{2} + \sqrt{\frac{[\text{HCO}_3^-]_0^2}{4} + \frac{[\text{CO}_2(\text{g})]_0 K_1 K_2 K_3}{K_1 + 1}}, \quad (2.3.33c)$$

$$[\text{CO}_3^{2-}]_{\infty} \approx \frac{K_4 [\text{HCO}_3^-]_{\infty}}{[\text{HCO}_3^-]_{\infty} - [\text{HCO}_3^-]_0}, \quad (2.3.33d)$$

$$[\text{Ca}^{2+}]_{\infty} \approx [\text{Ca}^{2+}]_0 + [\text{CaCO}_3]_0 - K_5 [\text{Ca}^{2+}]_0 [\text{CO}_3^{2-}]_{\infty}. \quad (2.3.33e)$$

These nontrivial algebraic relationships emerge from the systematic asymptotic analysis; their simplicity reflects the wide numerical range of dimensionless rate constants in Table 2.4. Equation (2.3.33a) shows that the proportion of injected CO₂(g) ([CO₂(g)]₀) that dissolves into the water is controlled only by carbon dioxide's dissolution constant K₁ – the further process of dissolved CO₂ being removed by reacting with water is less important. Furthermore, the ratio of dissolved:undissolved injected CO₂(g) is the ratio of the forwards and reverse rate constants for this reaction (R1). For example, if the rate constants are equal, then K₁ = 1, and half of the injected CO₂(g) will dissolve into the water.

From equation (2.3.33b), the proportion of injected and dissolved CO₂ that then reacts with the water to form carbonic acid is also simply the ratio of this reaction's rate constants, and from (2.3.33c), the proportion of extra carbonic acid that ends up as bicarbonate is governed by the carbonic acid dissociation constant. From (2.3.33d), the final quantity of carbonate ions is simply the product of the dissociation constant for bicarbonate and the ratio of the final bicarbonate concentration to the change in the bicarbonate concentration.

The concentrations of all the remaining species can be calculated using (2.3.33) and the conservation of mass constraints. From (2.3.33e) and (2.2.6c),

$$[\text{CaCO}_3]_{\infty} \approx K_5 [\text{Ca}^{2+}]_0 [\text{CO}_3^{2-}]_{\infty} = [\text{CaCO}_3]_0 \frac{[\text{CO}_3^{2-}]_{\infty}}{[\text{CO}_3^{2-}]_0},$$

as $K_5 [\text{Ca}^{2+}]_0 = [\text{CaCO}_3]_0 / [\text{CO}_3^{2-}]_0$. Therefore a decrease in [CO₃²⁻] (from [CO₃²⁻]₀ to [CO₃²⁻]_∞) must be accompanied by a decrease in [CaCO₃]. Therefore, the amount of CO₂ bound to calcium decreases as a result of these reactions. In this example, the concentration of calcium carbonate decreases to 2.2 × 10⁻¹⁰ M.

Also, substituting (2.3.32d,e) into (2.2.6b), and assuming K_4 , $K_4K_5[\text{Ca}^{2+}]_0$, $[\text{CO}_3^{2-}]_0$, and $[\text{CaCO}_3]_0$ are all negligible compared to $[\text{HCO}_3^-]_0$ (which is true for these parameter values with error $O(\alpha^{-1/4})$),

$$[\text{H}^+]_\infty \approx [\text{H}^+]_0 - \frac{[\text{HCO}_3^-]_0}{2} + \sqrt{\frac{[\text{HCO}_3^-]_0^2}{4} + \frac{[\text{CO}_2(\text{g})]_0 K_1 K_2 K_3}{K_1 + 1}},$$

which equals 5.1×10^{-5} M. Therefore, with no buffers (additional chemical reactions that absorb some of the extra hydrogen ions, limiting the drop in the pH), the pH has dropped from 6 to 4.3.

2.3.9 The six timescales

So far, the six timescales used to construct the asymptotic approximations have been defined as powers of α . Greater insight comes from examining the rate constants that appear in the solutions, such as the timescale $\hat{t} = O(1/(\hat{\gamma} + \hat{\nu}))$ implicit in (2.3.2a). The six timescales, expressed in terms of the original dimensional quantities, are given in Table 2.5, together with the corresponding values at 25°C and 1 atm.

In this well-mixed scenario, CO₂(aq) reaches equilibrium within $O(10^{-11}\text{s})$, H₂CO₃, HCO₃⁻ and CO₃²⁻ reach equilibrium within $O(10^{-2}\text{s})$, and Ca²⁺ reaches equilibrium in $O(10^3\text{s})$. Therefore, in practice, the rates of the first four reactions will be determined by the neglected transport and mixing processes, and may be assumed to be in local equilibrium as described by (2.3.32a-d). The reaction with calcium takes longer, and in practice will therefore be determined by the transport, mixing and reaction processes. In dimensional terms, its evolution in the well-mixed scenario is given by (2.3.30):

$$[\text{Ca}^{2+}] \approx [\text{Ca}^{2+}]_0 + ([\text{CaCO}_3]_0 - K_5[\text{Ca}^{2+}]_0[\text{CO}_3^{2-}]_\infty) (1 - \exp(-k_{-5}t)).$$

The results obtained above remain valid while the six timescales remain distinct, i.e.

$$\begin{aligned} \frac{1}{k_1 + k_{-1}} &\ll \frac{[\text{H}^+]_0}{k_3([\text{H}^+]_0 + [\text{H}_2\text{CO}_3]_0)} \ll \frac{[\text{CaCO}_3]_0}{k_4 K_5 [\text{HCO}_3^-]_0 [\text{Ca}^{2+}]_0} \\ &\ll \frac{[\text{H}_2\text{CO}_3]_0 + [\text{H}^+]_0}{k_2([\text{CO}_2(\text{aq})]_\infty - [\text{CO}_2(\text{aq})]_0)} \ll \frac{[\text{H}_2\text{CO}_3]_0}{k_2[\text{CO}_2(\text{aq})]_0} \ll \frac{1}{k_{-5}}. \end{aligned}$$

The validity of the model can therefore be assessed under different initial concentrations, and under different conditions (temperature, pressure, salinity, surface area, etc), via the impact on the rate constants, and will be valid provided this ordering is preserved.

Timescale	Dimensional expression	Value at 25°C & 1 atm (sec)
1	$\frac{1}{k_1 + k_{-1}}$	5.0×10^{-11}
2	$\frac{[\text{H}^+]_0}{k_3([\text{H}^+]_0 + [\text{H}_2\text{CO}_3]_0)}$	3.8×10^{-8}
3	$\frac{[\text{CaCO}_3]_0}{k_4 K_5 [\text{HCO}_3^-]_0 [\text{Ca}^{2+}]_0}$	2.0×10^{-5}
4	$\frac{[\text{H}_2\text{CO}_3]_0 + [\text{H}^+]_0}{k_2([\text{CO}_2(\text{aq})]_\infty - [\text{CO}_2(\text{aq})]_0)}$	1.4×10^{-3}
5	$\frac{[\text{H}_2\text{CO}_3]_0}{k_2[\text{CO}_2(\text{aq})]_0}$	5.0×10^{-2}
6	$\frac{1}{k_{-5}}$	1.0×10^3

Table 2.5: Summary of the six timescales

2.4 Summary

To investigate what happens to the chemical species dissolved in water following the injection of new CO₂, we have formulated a single model to describe the time dependence of all the concentrations by applying the mass action law to the complete set of principal reactions. This model includes no dependence of the concentrations on position, but assumes the solution is always well-mixed.

The solutions to this model were found numerically for a particular initial condition and set of parameter values, and these solutions match those required by the relevant Bjerrum plot. The method of matched asymptotic expansions was used to obtain expressions for the leading-order behaviours of the different species as they go to their new equilibrium over six different timescales, as functions of the initial condition of the system, the parameters, and time. These leading-order expressions all showed excellent agreement with the numerical solutions to the full model, due to the fact that the rate constants and initial concentrations vary over many orders of magnitude.

This model can be used to predict the impact on the chemical compositions of the oceans for a given quantity of new CO₂ dissolving in from the atmosphere. The pH

and the concentration of carbonate ions in the oceans have both been observed to decrease as a result of the additional CO₂, and this model agrees with those observations. This model predicts that the injection of extra CO₂ into the water causes some of the calcium carbonate already dissolved in the water to split up into its constituent elements, increasing the amount of dissolved calcium.

These results can also be used within reactive transport models of carbon sequestration. Such models would be able to include all these reactions by identifying the time scales over which the transport processes occur, and then, for the reactions faster than this, to specify the local equilibrium using the equilibrium expressions obtained by this asymptotic analysis, and for the reactions slower than this, by using the time-dependent evolution expressions obtained by this asymptotic analysis.

In the next Chapter we examine what happens within the pore-space of a saline aquifer, by inserting terms for advection and diffusion into these reaction equations. Rather than the temporal dependence of the concentrations that was examined in this Chapter, we consider the steady-state spatial dependence of the concentrations ahead of a spreading drop of CO₂.

Saline aquifer pore space distributions

When gaseous or supercritical CO_2 is injected into a saline aquifer, being lighter than the resident water, the mass of CO_2 molecules forms a drop in the pore space, and migrates upwards through the pore spaces until it reaches an impermeable layer, and then spreads out laterally underneath this overlying caprock. CO_2 dissolves from the ends of the drop into the water and is carried away from the drop, enabling more CO_2 to dissolve. The aim of this Chapter is to analyse what happens to this dissolved CO_2 using pore-scale models that include both fluid mechanics and reactive chemistry. The length scales ahead of an advancing CO_2 drop, over which the dissolved CO_2 and other species are affected, are investigated depending on the relative strengths of advection, diffusion and reaction, along with the concentrations of these different species over these length scales.

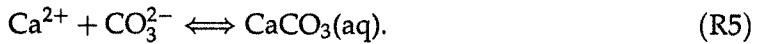
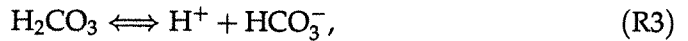
3.1 Model formulation

We suppose the pore is represented by a two-dimensional long thin straight channel of fixed width $2a$, parameterized by two independent spatial variables, length $-\infty < x^* < \infty$, and height $-a \leq y^* \leq a$, where $*$ denotes a dimensional variable. We work in a frame of reference in which the injected CO_2 is stationary, and the centre of the front of the drop is the origin. In this frame of reference, the walls move towards the drop with velocity $(-U_0, 0)$, dragging water with them. As illustrated in Figure 1.3, the water

wets the pore walls preferentially to the CO_2 , and so either side of the CO_2 drop is a thin film of water between the drop and the pore wall of width h , $h \ll a$. As discussed in Section 1.9, the ratio h/a is a function of the capillary number ($\text{Ca} \equiv \mu U_0/\gamma$, where μ is the water's viscosity, and γ is surface tension) [104], and hence U_0 , by $h \propto \text{Ca}^{2/3}$ as $\text{Ca} \rightarrow 0$ [101] (i.e. at low speeds). The end of the drop is semicircular.

Suppose that the water's concentration of dissolved CO_2 immediately next to the CO_2 drop is permanently in equilibrium with the concentration of gaseous (or supercritical) CO_2 in the drop, so that any dissolved CO_2 that is carried away by the water is then immediately replaced by CO_2 from the edge of the drop, which maintains its position in the channel. This equilibrium is specified by Henry's Law (see Section 1.7.1), where the Henry's Law constant depends on the aquifer conditions, such as temperature, pressure, and pH. From Chapter 1, the concentration of dissolved CO_2 is estimated to be at most ≈ 1 M.

If calcium is the aquifer's dominant metal, we suppose the following chemical reactions occur in the water, labelled (R2-5) (consistent with Chapters 1 and 2).



The water is an incompressible fluid, with velocity $\mathbf{u}^* = (u^*(x^*, y^*, t^*), v^*(x^*, y^*, t^*))$ in the channel, where t^* is time. Suppose the diffusion of the different chemical species in the water is governed by a single diffusion constant D_w , the mass action law applies to (R2-5), except that water is abundant relative to the dissolved species (and so it has constant concentration), and these reactions have forward and reverse rate constants k_2 to k_5 and k_{-2} to k_{-5} , respectively. Then the distributions of the chemical species in the pore's water are given by the following time-dependent advection-diffusion-reaction equations:

$$\begin{aligned}
 \frac{\partial[\text{CO}_2(\text{aq})]}{\partial t^*} + (\mathbf{u}^* \cdot \nabla^*)[\text{CO}_2(\text{aq})] &= D_w \nabla^{*2}[\text{CO}_2(\text{aq})] - k_2[\text{CO}_2(\text{aq})] + k_{-2}[\text{H}_2\text{CO}_3], \\
 \frac{\partial[\text{H}_2\text{CO}_3]}{\partial t^*} + (\mathbf{u}^* \cdot \nabla^*)[\text{H}_2\text{CO}_3] &= D_w \nabla^{*2}[\text{H}_2\text{CO}_3] + k_2[\text{CO}_2(\text{aq})] - k_{-2}[\text{H}_2\text{CO}_3] \\
 &\quad - k_3[\text{H}_2\text{CO}_3] + k_{-3}[\text{H}^+][\text{HCO}_3^-], \\
 \frac{\partial[\text{H}^+]}{\partial t^*} + (\mathbf{u}^* \cdot \nabla^*)[\text{H}^+] &= D_w \nabla^{*2}[\text{H}^+] + k_3[\text{H}_2\text{CO}_3] - k_{-3}[\text{H}^+][\text{HCO}_3^-] \\
 &\quad + k_4[\text{HCO}_3^-] - k_{-4}[\text{H}^+][\text{CO}_3^{2-}], \\
 \frac{\partial[\text{HCO}_3^-]}{\partial t^*} + (\mathbf{u}^* \cdot \nabla^*)[\text{HCO}_3^-] &= D_w \nabla^{*2}[\text{HCO}_3^-] + k_3[\text{H}_2\text{CO}_3] - k_{-3}[\text{H}^+][\text{HCO}_3^-] \\
 &\quad - k_4[\text{HCO}_3^-] + k_{-4}[\text{H}^+][\text{CO}_3^{2-}], \\
 \frac{\partial[\text{CO}_3^{2-}]}{\partial t^*} + (\mathbf{u}^* \cdot \nabla^*)[\text{CO}_3^{2-}] &= D_w \nabla^{*2}[\text{CO}_3^{2-}] + k_4[\text{HCO}_3^-] - k_{-4}[\text{H}^+][\text{CO}_3^{2-}] \\
 &\quad - k_5[\text{Ca}^{2+}][\text{CO}_3^{2-}] + k_{-5}[\text{CaCO}_3], \\
 \frac{\partial[\text{Ca}^{2+}]}{\partial t^*} + (\mathbf{u}^* \cdot \nabla^*)[\text{Ca}^{2+}] &= D_w \nabla^{*2}[\text{Ca}^{2+}] - k_5[\text{Ca}^{2+}][\text{CO}_3^{2-}] + k_{-5}[\text{CaCO}_3], \\
 \frac{\partial[\text{CaCO}_3]}{\partial t^*} + (\mathbf{u}^* \cdot \nabla^*)[\text{CaCO}_3] &= D_w \nabla^{*2}[\text{CaCO}_3] + k_5[\text{Ca}^{2+}][\text{CO}_3^{2-}] - k_{-5}[\text{CaCO}_3],
 \end{aligned}$$

where $\mathbf{u}^* \cdot \nabla^* = u^* \frac{\partial}{\partial x^*} + v^* \frac{\partial}{\partial y^*}$, $\nabla^{*2} = \frac{\partial^2}{\partial x^{*2}} + \frac{\partial^2}{\partial y^{*2}}$, and $[]$ denotes concentration (measured in mol/litre, or M). The boundary conditions are as follows.

On $y^* = \pm a$, each species has zero transverse flux, i.e.

$$\frac{\partial[\text{CO}_2(\text{aq})]}{\partial y^*} = \frac{\partial[\text{H}_2\text{CO}_3]}{\partial y^*} = \frac{\partial[\text{H}^+]}{\partial y^*} = \frac{\partial[\text{HCO}_3^-]}{\partial y^*} = \frac{\partial[\text{CO}_3^{2-}]}{\partial y^*} = \frac{\partial[\text{Ca}^{2+}]}{\partial y^*} = \frac{\partial[\text{CaCO}_3]}{\partial y^*} = 0.$$

(i.e. We suppose that no chemical species precipitates out of the water and into the channel wall, and that no CaCO_3 dissolves from the walls into the water.)

On the surface of the drop, the concentration of CO_2 is given by Henry's Law, and all other species have zero flux into the drop, i.e.

$$\begin{aligned}
 [\text{CO}_2(\text{aq})] &= k_H P_b = k_H RT[\text{CO}_2(\text{g})], \quad (\mathbf{n} \cdot \nabla^*)[\text{H}_2\text{CO}_3] = 0, \quad (\mathbf{n} \cdot \nabla^*)[\text{H}^+] = 0, \\
 (\mathbf{n} \cdot \nabla^*)[\text{HCO}_3^-] &= 0, \quad (\mathbf{n} \cdot \nabla^*)[\text{CO}_3^{2-}] = 0, \quad (\mathbf{n} \cdot \nabla^*)[\text{Ca}^{2+}] = 0, \quad (\mathbf{n} \cdot \nabla^*)[\text{CaCO}_3] = 0,
 \end{aligned}$$

by using the ideal gas law $P_b = nRT/V$, where P_b is the pressure of the CO_2 in the drop, n is number of mol, R is the gas constant, T is temperature, V is the drop's volume, $[\text{CO}_2(\text{g})] = n/V$ is concentration in the drop, k_H is the Henry's Law constant for these conditions, and \mathbf{n} is a unit normal vector from the surface into the CO_2 drop.

Far in front of the drop, we assume the concentrations are the same as they were in the

Boundary concentration	Magnitude	Boundary concentration	Magnitude
$[\text{CO}_2(\text{aq})]_{L^*}$	$5.47 \times 10^{-4} \text{ M}$	$[\text{HCO}_3^-]_{L^*}$	$3.28 \times 10^{-4} \text{ M}$
$[\text{H}_2\text{O}]_{L^*}$	$5.55 \times 10^1 \text{ M}$	$[\text{CO}_3^{2-}]_{L^*}$	$1.97 \times 10^{-8} \text{ M}$
$[\text{H}_2\text{CO}_3]_{L^*}$	$1.64 \times 10^{-6} \text{ M}$	$[\text{Ca}^{2+}]_{L^*}$	$2.50 \times 10^{-4} \text{ M}$
$[\text{H}^+]_{L^*}$	$1.00 \times 10^{-6} \text{ M}$	$[\text{CaCO}_3]_{L^*}$	$9.84 \times 10^{-9} \text{ M}$

Table 3.1: Boundary concentrations far in front of the drop.

whole of the pore space before the CO_2 was injected, denoted as:

$$\begin{aligned}
 [\text{CO}_2(\text{aq})] &= [\text{CO}_2(\text{aq})]_{L^*}, [\text{H}_2\text{CO}_3] = [\text{H}_2\text{CO}_3]_{L^*}, [\text{H}^+] = [\text{H}^+]_{L^*}, [\text{HCO}_3^-] = [\text{HCO}_3^-]_{L^*}, \\
 [\text{CO}_3^{2-}] &= [\text{CO}_3^{2-}]_{L^*}, [\text{Ca}^{2+}] = [\text{Ca}^{2+}]_{L^*}, [\text{CaCO}_3] = [\text{CaCO}_3]_{L^*},
 \end{aligned}$$

at $x^* = L^*$, where L^* is a large finite maximum value for x^* . At this boundary, we suppose conditions are the same as the initial condition in the temporal problem analysed in Chapter 2, i.e. $[\text{Ca}^{2+}]_{L^*} = 10 \text{ mg/l} = 2.50 \times 10^{-4} \text{ M}$, $[\text{HCO}_3^-]_{L^*} = 20 \text{ mg/l} = 3.28 \times 10^{-4} \text{ M}$, and $\text{pH}=6$, i.e. $[\text{H}^+]_{L^*} = 10^{-6} \text{ M}$. From these three initial concentrations, the remaining species' initial concentrations are calculated by substituting no advection, no diffusion and no time variation into the distribution equations above, and using the values of the rate constants given in Table 2.1. The resulting far boundary concentrations are given in Table 3.1, and (except for water) vary over four orders of magnitude.

3.2 Nondimensionalisation

Dimensionless variables are defined as follows:

$$\begin{aligned}
 t &= t^*k_2, \quad x = \frac{x^*}{a}, \quad y = \frac{y^*}{a}, \quad u = \frac{u^*}{U_0}, \quad v = \frac{v^*}{U_0}, \quad A = \frac{[\text{CO}_2(\text{g})]}{[\text{H}_2\text{O}]}, \quad B = \frac{[\text{CO}_2(\text{aq})]}{[\text{H}_2\text{O}]}, \\
 D &= \frac{[\text{H}_2\text{CO}_3]}{[\text{H}_2\text{O}]}, \quad E = \frac{[\text{H}^+]}{[\text{H}_2\text{O}]}, \quad F = \frac{[\text{HCO}_3^-]}{[\text{H}_2\text{O}]}, \quad G = \frac{[\text{CO}_3^{2-}]}{[\text{H}_2\text{O}]}, \quad H = \frac{[\text{Ca}^{2+}]}{[\text{H}_2\text{O}]}, \quad K = \frac{[\text{CaCO}_3]}{[\text{H}_2\text{O}]},
 \end{aligned}$$

and dimensionless parameters are defined as follows:

$$\begin{aligned}
 \sigma &= \frac{k_{-2}}{k_2}, \quad \psi = \frac{k_3}{k_2}, \quad \omega = \frac{k_{-3}[\text{H}_2\text{O}]}{k_2}, \quad \chi = \frac{k_4}{k_2}, \quad \phi = \frac{k_{-4}[\text{H}_2\text{O}]}{k_2}, \\
 \tau &= \frac{k_5[\text{H}_2\text{O}]}{k_2}, \quad \rho = \frac{k_{-5}}{k_2}, \quad \text{Pe} = \frac{aU_0}{D_w}, \quad \text{Da} = \frac{k_2a}{U_0},
 \end{aligned}$$

Parameter	Magnitude	Species	Magnitude
σ	3.33×10^2	B_L	9.84×10^{-6}
ψ	1.67×10^8	D_L	2.95×10^{-8}
ω	4.63×10^{13}	E_L	1.80×10^{-8}
χ	5.00×10^1	F_L	5.91×10^{-6}
ϕ	4.63×10^{13}	G_L	3.55×10^{-10}
τ	1.85×10^3	H_L	4.50×10^{-6}
ρ	1.67×10^{-2}	K_L	1.77×10^{-10}

Table 3.2: Dimensionless parameters and far boundary concentrations.

where Pe is the Péclet number (the ratio of advection to diffusion) and Da is a Damköhler number (the ratio of reaction to advection). Note that the product $PeDa = k_2 a^2 / D_w$ gives the ratio of reaction to diffusion, and is independent of U_0 . Using $[H_2O] = 55.5$ M and the rate constants as given in Table 2.1, the resulting dimensionless parameter values are given in Table 3.2. These ratios of rate constants vary over 15 orders of magnitude. Substituting these expressions into the distribution equations given above gives the following:

$$PeDa \frac{\partial B}{\partial t} + Pe(\mathbf{u} \cdot \nabla)B = \nabla^2 B + PeDa(-B + \sigma D), \quad (3.2.1)$$

$$PeDa \frac{\partial D}{\partial t} + Pe(\mathbf{u} \cdot \nabla)D = \nabla^2 D + PeDa(B - \sigma D - \psi D + \omega EF), \quad (3.2.2)$$

$$PeDa \frac{\partial E}{\partial t} + Pe(\mathbf{u} \cdot \nabla)E = \nabla^2 E + PeDa(\psi D - \omega EF + \chi F - \phi EG), \quad (3.2.3)$$

$$PeDa \frac{\partial F}{\partial t} + Pe(\mathbf{u} \cdot \nabla)F = \nabla^2 F + PeDa(\psi D - \omega EF - \chi F + \phi EG), \quad (3.2.4)$$

$$PeDa \frac{\partial G}{\partial t} + Pe(\mathbf{u} \cdot \nabla)G = \nabla^2 G + PeDa(\chi F - \phi EG - \tau GH + \rho K), \quad (3.2.5)$$

$$PeDa \frac{\partial H}{\partial t} + Pe(\mathbf{u} \cdot \nabla)H = \nabla^2 H + PeDa(-\tau GH + \rho K), \quad (3.2.6)$$

$$PeDa \frac{\partial K}{\partial t} + Pe(\mathbf{u} \cdot \nabla)K = \nabla^2 K + PeDa(\tau GH - \rho K), \quad (3.2.7)$$

where $\mathbf{u} \cdot \nabla = u \frac{\partial}{\partial x} + v \frac{\partial}{\partial y}$, $\nabla^2 = \frac{\partial^2}{\partial x^2} + \frac{\partial^2}{\partial y^2}$, and with boundary conditions as follows:

On $y = \pm 1$,

$$\frac{\partial B}{\partial y} = \frac{\partial D}{\partial y} = \frac{\partial E}{\partial y} = \frac{\partial F}{\partial y} = \frac{\partial G}{\partial y} = \frac{\partial H}{\partial y} = \frac{\partial K}{\partial y} = 0. \quad (3.2.8)$$

On the surface of the drop,

$$\begin{aligned} B = k_H RTA, (\mathbf{n} \cdot \nabla)D = 0, (\mathbf{n} \cdot \nabla)E = 0, (\mathbf{n} \cdot \nabla)F = 0, \\ (\mathbf{n} \cdot \nabla)G = 0, (\mathbf{n} \cdot \nabla)H = 0, (\mathbf{n} \cdot \nabla)K = 0, \end{aligned} \quad (3.2.9)$$

where \mathbf{n} is a unit normal vector from the surface into the CO_2 drop.

The far-field boundary condition is:

$$B = B_L, D = D_L, E = E_L, F = F_L, G = G_L, H = H_L, K = K_L, \quad (3.2.10)$$

at $x = L$, where $L \equiv L^*/a \gg 1$. The boundary concentrations given in Table 3.1 are scaled on $[\text{H}_2\text{O}]$ to give the dimensionless boundary concentrations given in Table 3.2.

3.3 Steady-state far-field model simplification

In the section of channel immediately in front of the drop, the "inner region", the water flow can be either parallel or perpendicular to the pore walls (or anything in between), whether or not there is a thin film between the CO_2 drop and the pore walls, and whatever the shape of the CO_2 drop. In Figure 1.6 for example, this inner region comprises the channel space up to about $x = 1$ ($x^* = a$).

In an outer far-field region beyond this space, the flow perpendicular to the walls is negligible compared to the flow parallel to the walls, and the flow field in the steady-state case is given by equation (1.9.4). If $\epsilon \equiv h/a$, this can be written in dimensionless variables as

$$u(y) = -\left(1 + \frac{3}{2}(1 - \epsilon)(y^2 - 1)\right), \quad v = 0. \quad (3.3.1)$$

The steady-state distributions of the dissolved chemical species in this far-field section of the pore are therefore given by the following steady-state advection-diffusion-reaction equations:

$$-\text{Pe} \left(1 + \frac{3}{2}(1 - \epsilon)(y^2 - 1) \right) B_x = B_{xx} + B_{yy} + \text{PeDa}(-B + \sigma D), \quad (3.3.2)$$

$$-\text{Pe} \left(1 + \frac{3}{2}(1 - \epsilon)(y^2 - 1) \right) D_x = D_{xx} + D_{yy} + \text{PeDa}(B - \sigma D - \psi D + \omega EF), \quad (3.3.3)$$

$$-\text{Pe} \left(1 + \frac{3}{2}(1 - \epsilon)(y^2 - 1) \right) E_x = E_{xx} + E_{yy} + \text{PeDa}(\psi D - \omega EF + \chi F - \phi EG), \quad (3.3.4)$$

$$-\text{Pe} \left(1 + \frac{3}{2}(1 - \epsilon)(y^2 - 1) \right) F_x = F_{xx} + F_{yy} + \text{PeDa}(\psi D - \omega EF - \chi F + \phi EG), \quad (3.3.5)$$

$$-\text{Pe} \left(1 + \frac{3}{2}(1 - \epsilon)(y^2 - 1) \right) G_x = G_{xx} + G_{yy} + \text{PeDa}(\chi F - \phi EG - \tau GH + \rho K), \quad (3.3.6)$$

$$-\text{Pe} \left(1 + \frac{3}{2}(1 - \epsilon)(y^2 - 1) \right) H_x = H_{xx} + H_{yy} + \text{PeDa}(-\tau GH + \rho K), \quad (3.3.7)$$

$$-\text{Pe} \left(1 + \frac{3}{2}(1 - \epsilon)(y^2 - 1) \right) K_x = K_{xx} + K_{yy} + \text{PeDa}(\tau GH - \rho K), \quad (3.3.8)$$

where B_x and B_{xx} denote the first and second partial derivatives of B with respect to x .

The boundary conditions on the pore walls are given by (3.2.8), and at $x = L$ by (3.2.10).

The concentration field at the outer limit of the inner region remains to be found, and this will provide a matching (inner) boundary condition for the outer region.

We now consider two simplifications to this model. In Section 3.4 we remove the reactive coupling between the species, and examine the steady-state far-field distribution (whatever the shape of the end of the drop) of a single dissolved chemical species with a model that includes a sink term proportional to the species' concentration, but no source terms from any other species, and accounting for the return flow (3.3.1). This simplified model comprises a single second order partial differential equation for the distribution of that species, and is relatively straightforward to examine analytically. It provides insight into the impact of advection on the distribution length scales, and indicates appropriate length scales to use in a more complex second simplification to the model that excludes advection but includes full reactive coupling between the different chemical species (Section 3.5).

3.4 Far-field distribution for a solute ahead of a moving drop in a pore

Let C be the far-field (dimensionless) concentration of a chemical species in a long thin channel, described by the following steady-state axial advection-diffusion-uptake equation:

$$- \text{Pe} \left(1 + \frac{3}{2}(1 - \epsilon)(y^2 - 1) \right) C_x = C_{xx} + C_{yy} - k \text{Pe} \text{Da} C, \quad (3.4.1)$$

where k is an $O(1)$ positive constant (if C is $\text{CO}_2(\text{aq})$ then $k = 1$, as in (3.3.2)), with boundary conditions $C_y = 0$ at $y = \pm 1$, $C = C_L$ at $x = L$ (i.e. C is known at a point a large finite distance ahead of the drop), and $C \rightarrow C_{II,\infty}(y)$ as $x \rightarrow 0$, for some $C_{II,\infty}$ (the concentration field at the outer limit of the inner region).

There is a strong stirring flow field, causing Taylor dispersion, and rather than a no-flux boundary condition, this model also includes a weak net flux through the channel; it is less than the velocity field by a factor of $O(\epsilon)$, where $\epsilon = h/a$, the ratio of film width to channel radius.

One distinguished limit we may consider is $\text{Pe} = O(1)$ and $\text{Da} = O(\epsilon^2)$ (so $\widehat{\text{Da}} \equiv \text{Da}/\epsilon^2$ is $O(1)$). This point in parameter space is chosen as it is the point from which the behaviour of the system at many other points of parameter space can be deduced. A long-wave approximation is then taken by supposing that lengths in the x direction vary over a long length scale $1/\epsilon$ (so $C = C(X, y)$ where $X \equiv x\epsilon$ is $O(1)$). Then (3.4.1) becomes

$$- \text{Pe} \epsilon \left(1 + \frac{3}{2}(1 - \epsilon)(y^2 - 1) \right) C_X = \epsilon^2 C_{XX} + C_{yy} - \epsilon^2 k \text{Pe} \widehat{\text{Da}} C, \quad (3.4.2)$$

with the same boundary conditions as (3.4.1), and $L \gg 1/\epsilon$.

C can be expanded in powers of ϵ as follows: $C = C_0 + \epsilon C_1 + \epsilon^2 C_2 + \dots$. Therefore, (3.4.2) implies that the leading-order component of transverse diffusion $C_{0,yy} = 0$, and as $C_y = 0$ on $y = \pm 1$, then $C_{0,y} = 0$ for all y , and C_0 is a function of X only. C_0 therefore gives the cross-sectional average at position x , and a condition is imposed such that deviations from this average (given by the smaller correction terms C_1, C_2, \dots) all integrate to zero across y .

The leading-order balance, at $O(\epsilon)$, is

$$-\text{Pe} \left(1 + \frac{3}{2}(y^2 - 1) \right) C_{0,X} = C_{1,yy}.$$

Integrating with respect to y gives

$$-\text{Pe} \left(\frac{y^3}{2} - \frac{y}{2} \right) C_{0,X} = C_{1,y} + c_1,$$

where c_1 is a constant of integration. The boundary conditions $C_{1,y} = 0$ at $y = \pm 1$ give $c_1 = 0$. Integrating again gives

$$-\text{Pe} \left(\frac{y^4}{8} - \frac{y^2}{4} \right) C_{0,X} = C_1 + c_2.$$

The constant c_2 is the value which gives $\int_{-1}^1 C_1 dy = 0$, so this becomes

$$C_1(x, y) = -\text{Pe} \left(\frac{y^4}{8} - \frac{y^2}{4} + \frac{7}{120} \right) C_{0,X}. \quad (3.4.3)$$

At $O(\epsilon^2)$, equation (3.4.2) is

$$-\text{Pe} \left(\left(1 + \frac{3}{2}(y^2 - 1) \right) C_{1,X} - \frac{3}{2}(y^2 - 1)C_{0,X} \right) = C_{0,XX} + C_{2,yy} - k \text{Pe} \widehat{\text{Da}} C_0.$$

Substituting in (3.4.3) gives

$$\frac{\text{Pe}^2}{240} (45y^6 - 105y^4 + 51y^2 - 7)C_{0,XX} + \text{Pe} \frac{3}{2}(y^2 - 1)C_{0,X} = C_{0,XX} + C_{2,yy} - k \text{Pe} \widehat{\text{Da}} C_0.$$

Integrating with respect to y between $y = -1$ and $y = 1$, and noting that $C_{2,y} = 0$ at $y = -1$ and $y = 1$, gives

$$0 = (1 + \alpha \text{Pe}^2) C_{0,XX} + \text{Pe} C_{0,X} - k \text{Pe} \widehat{\text{Da}} C_0, \quad (3.4.4)$$

where $\alpha = 2/105$. Thus, by employing a long-wave approximation and cross-sectionally averaging the concentrations transversally across the pore, the two-dimensional partial differential equation for the behaviour of the species, with terms for axial advection, axial and transverse diffusion, and uptake (equation (3.4.1)), has been turned into a one-dimensional ordinary differential equation for the leading-order behaviour of the species, where the four terms in this equation respectively denote axial diffusion, Taylor dispersion, advection, and uptake.

The general solution to (3.4.4) is $C_0(X) = c_3 \exp(\lambda_+ X) + c_4 \exp(\lambda_- X)$, where c_3 and c_4 are constants, and

$$\lambda_{\pm} = \frac{-\text{Pe} \pm \sqrt{\text{Pe}^2 + 4(1 + \alpha \text{Pe}^2)k \text{Pe} \widehat{\text{Da}}}}{2(1 + \alpha \text{Pe}^2)}.$$

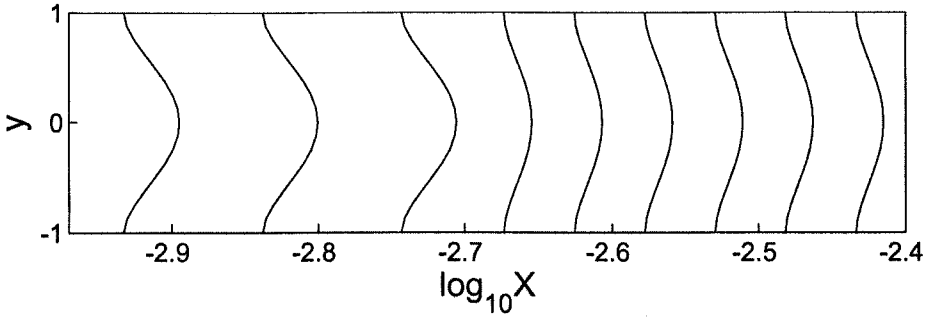


Figure 3.2: Example concentration field for $C = C_0 + \epsilon C_1$.

As $4(1 + \alpha Pe^2)kPe\widehat{Da}$ is positive, $\lambda_+ > 0$ and $\lambda_- < 0$, and so, to ensure the solutions are bounded in the far field, we set $c_3 = 0$. The leading-order solution is written as:

$$C_0(X) \approx c_4 \exp(-\lambda X), \quad \lambda = \frac{Pe + \sqrt{Pe^2 + 4(1 + \alpha Pe^2)kPe\widehat{Da}}}{2(1 + \alpha Pe^2)}. \quad (3.4.5)$$

(As the concentration field at the outer limit of the inner region, denoted $C_{II,\infty}$, is likely to be equal to a constant plus smaller-order correction terms that are functions of y , it should be expanded in powers of ϵ , and the leading-order constant term matched to c_4 .)

Thus in this model, the length scale over which the species spreads out from the drop is a function of the relative strengths of four effects, captured with the two dimensionless parameters Pe and Da through the parameter λ .

Figure 3.2 shows the impact of the flow on the concentration field in the channel. The lines give contours of equal concentrations given by $C = C_0 + \epsilon C_1$, where C_0 is given by (3.4.5) and C_1 by (3.4.3), when $Pe=0.03$, $Da=2.59$, $k=1$, $\epsilon = 1/30$, and $c_4=1$. Without the first correction term, these contours would be straight lines; the shape of the lines (the strength of their deviation away from straight lines) depends on Pe , Da , ϵ , and X .

Equation (3.4.5) for λ can be simplified in particular subsets of parameter space as follows. Equation (3.4.4) can be expressed as

$$0 = \left(\frac{1}{Pe} + \alpha Pe \right) \lambda^2 - \lambda - k\widehat{Da}. \quad (3.4.6)$$

The terms on the right hand side are labelled "Diff", "TD", "A", and "U" respectively, denoting diffusion, Taylor dispersion, advection, and uptake. At the distinguished limit in parameter space ($Pe = O(1)$, $Da = O(\epsilon^2)$, $\epsilon \rightarrow 0$), there is a balance between all four of these terms. Away from this point, there are balances between different subsets

of these terms. Figure 3.3 gives these dominant behaviours in different asymptotic parameter regimes, as derived below. (The region shaded grey (derived below) is not considered in this analysis as it gives the region where the long-wave approximation breaks down).

There are four regions in (Pe, Da) -space where there are two-way balances, and four boundary regions where there are three-way balances. The boundary regions are denoted with dashed lines in Figure 3.3. As expected, as Da gives the ratio of uptake to advection, uptake is important when \widehat{Da} is relatively large, and advection is important when \widehat{Da} is relatively small (with both important on the boundaries). Also, as Pe gives the ratio of Taylor dispersion to diffusion, TD is important when Pe is relatively large, and diffusion is important when Pe is relatively small (with both important on the boundaries).

When Pe is $O(1)$ and $\widehat{Da} \ll 1$ (i.e. $Da \ll \epsilon^2$), from (3.4.5),

$$\lambda \approx \frac{Pe}{1 + \alpha Pe^2},$$

and substituting this into (3.4.6) indicates a three-way balance between Diff, TD and A. For $Pe \gg 1$, $\lambda \approx 1/\alpha Pe$, and there is a balance between TD and A. For $Pe \ll 1$, $\lambda \approx Pe$, and there is a balance between Diff and A.

When Pe and \widehat{Da} are both $\ll 1$, and of comparable size, then

$$\lambda \approx \frac{Pe + \sqrt{Pe^2 + 4kPe\widehat{Da}}}{2},$$

and there is a three-way balance between Diff, A and U. For $\widehat{Da} \gg Pe$, $\lambda \approx \sqrt{kPe\widehat{Da}}$, and there is a balance between Diff and U. For $\widehat{Da} \ll Pe$, $\lambda \approx Pe$, and there is a balance between Diff and A.

When Pe is $O(1)$ and $1 \ll \widehat{Da} \ll 1/\epsilon^2$,

$$\lambda \approx \frac{\sqrt{(1 + \alpha Pe^2)kPe\widehat{Da}}}{1 + \alpha Pe^2} = \sqrt{\frac{kPe\widehat{Da}}{1 + \alpha Pe^2}},$$

and there is a three-way balance between Diff, U and TD. For $Pe \gg 1$, $\lambda \approx \sqrt{k\widehat{Da}/\alpha Pe}$, and there is a balance between TD and U. For $Pe \ll 1$, $\lambda \approx \sqrt{kPe\widehat{Da}}$, and there is a balance between Diff and U.

When $Pe \gg 1$, and $\widehat{Da} \approx 1/Pe$,

$$\lambda \approx \frac{Pe + \sqrt{Pe^2 + 4\alpha kPe^3\widehat{Da}}}{2\alpha Pe^2} = \frac{1 + \sqrt{1 + 4\alpha kPe\widehat{Da}}}{2\alpha Pe},$$

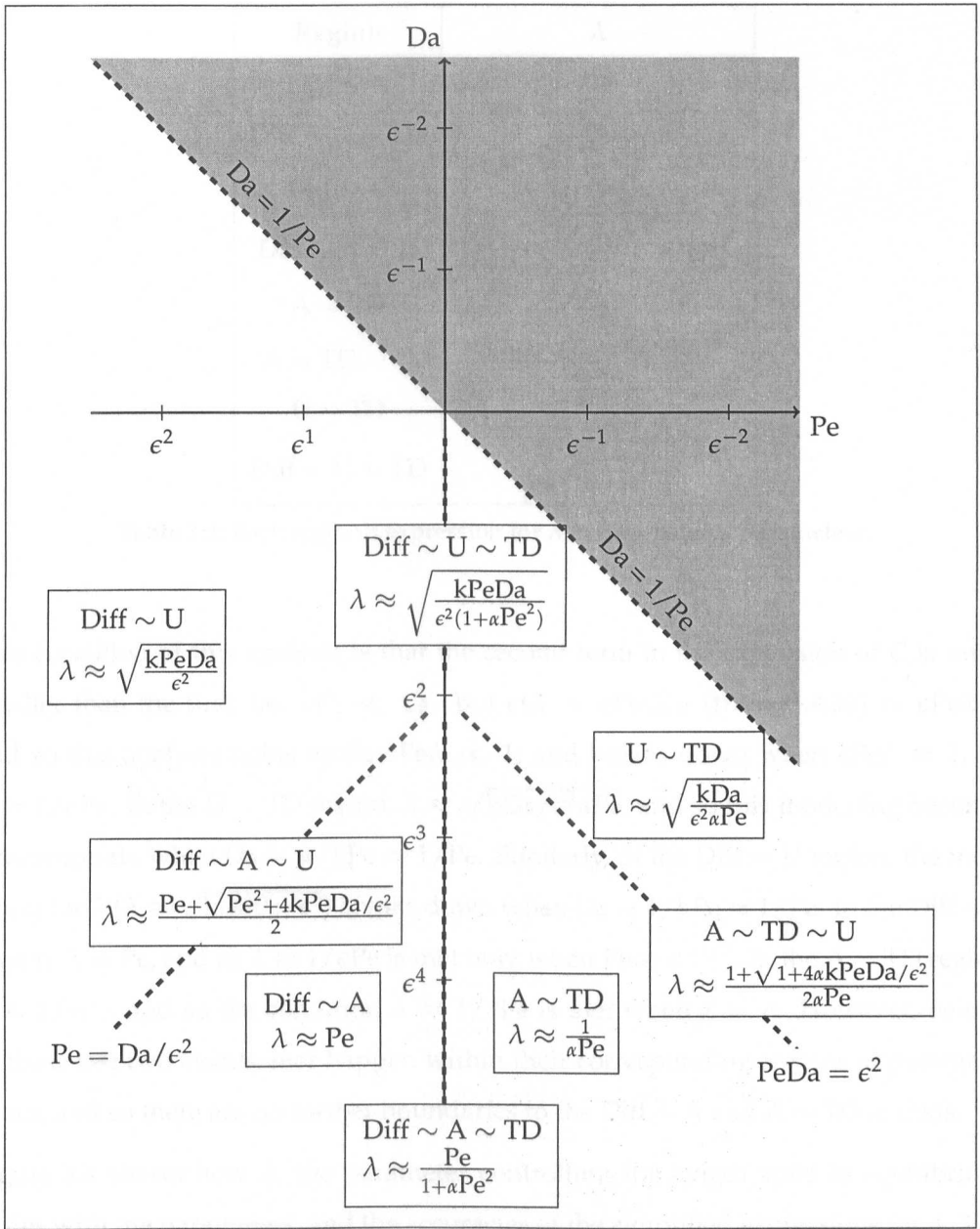


Figure 3.3: Asymptotic parameter regimes, showing dominant balances.

and there is a three-way balance between A , TD and U . For $Pe\widehat{Da} \ll 1$, $\lambda \approx 1/\alpha Pe$, and there is a balance between TD and A . For $Pe\widehat{Da} \gg 1$, $\lambda \approx \sqrt{4\alpha kPe\widehat{Da}}/2\alpha Pe = \sqrt{k\widehat{Da}/\alpha Pe}$, and there is a balance between TD and U .

Figure 3.3 illustrates how these limits provide complete coverage of parameter space around the organising centre $Pe = O(1)$, $\widehat{Da} = O(1)$. Table 3.3 gives the expression for λ in each region in the original dimensional parameters.

Region	λ
Diff \sim A	$\frac{aU_0}{D_w}$
Diff \sim A \sim TD	$\frac{aU_0 D_w}{D_w^2 + \alpha a^2 U_0^2}$
Diff \sim U	$\sqrt{\frac{kk_2 a^4}{D_w h^2}}$
Diff \sim A \sim U	$\frac{aU_0}{2D_w} + \sqrt{\left(\frac{aU_0}{2D_w}\right)^2 + \frac{kk_2 a^4}{D_w h^2}}$
A \sim TD	$\frac{D_w}{\alpha a U_0}$
A \sim TD \sim U	$\frac{D_w + D_w \sqrt{1 + 4\alpha k k_2 a^4 / D_w h^2}}{2\alpha a U_0}$
U \sim TD	$\sqrt{\frac{kk_2 a^2 D_w}{\alpha U_0^2 h^2}}$
Diff \sim U \sim TD	$\sqrt{\frac{kk_2 a^4 D_w}{h^2 (D_w^2 + \alpha a^2 U_0^2)}}$

Table 3.3: Each region's expression for λ in dimensional parameters.

One condition of this analysis is that the second term in the expansion of C is much smaller than the first, i.e. $\epsilon C_1 \ll C_0$. But $\epsilon C_1 \approx \epsilon \text{Pe} C_{0,X}$ (from (3.4.3)) $\approx \epsilon \text{Pe} \lambda C_0$, and so this analysis holds while $\epsilon \text{Pe} \lambda \ll 1$, and breaks down when $\epsilon \text{Pe} \lambda \approx 1$, i.e. $\lambda \approx 1/\epsilon \text{Pe}$. In the U \sim TD region, $\lambda \approx \sqrt{kDa/\epsilon^2 \alpha \text{Pe}}$, and so this modelling becomes inappropriate when $Da \approx \alpha/k\text{Pe} \approx 1/\text{Pe}$. Similarly, in the Diff \sim U region, the modelling for λ ($\lambda \approx \sqrt{kDa\text{Pe}/\epsilon^2}$) breaks down when $Da \approx 1/k\text{Pe} \approx 1/\text{Pe}$. In the Diff \sim A region, $\lambda \approx \text{Pe}$, and so $\lambda \approx 1/\epsilon \text{Pe}$ is met only when $\text{Pe} \approx \epsilon^{-1/2}$. In the A \sim TD region, $\lambda \approx 1/\alpha \text{Pe}$, and so the condition $\lambda \approx 1/\epsilon \text{Pe}$ is met when $\alpha = \epsilon$. However, neither of these last two events ever happen within their corresponding regions of parameter space, and so there are no further boundaries to the Diff \sim A and A \sim TD regions.

Figure 3.4 shows how λ , the parameter controlling the length scale to equilibrium, varies with the parameters, and the accuracies of the simplified expressions for λ . Two slices are taken through Figure 3.3: a horizontal slice at $Da = \epsilon^4$, for Figure 3.4(a), and a diagonal slice at $\text{Pe}Da = \epsilon^4$, for Figure 3.4(b). The full expression for λ (equation (3.4.5)) is plotted, along with the simplified expressions for λ in each region of parameter space (supposing that $k = 1$ and $\epsilon = 1/30$). (The simplified expressions are terminated just outside the regions to which they correspond.) The simplified expressions provide excellent agreement with the full expression through the majority of their regions, and where the agreement is not quite as excellent, the simplified expressions for λ in the three-way boundary regions (not plotted) do provide excellent agreement.

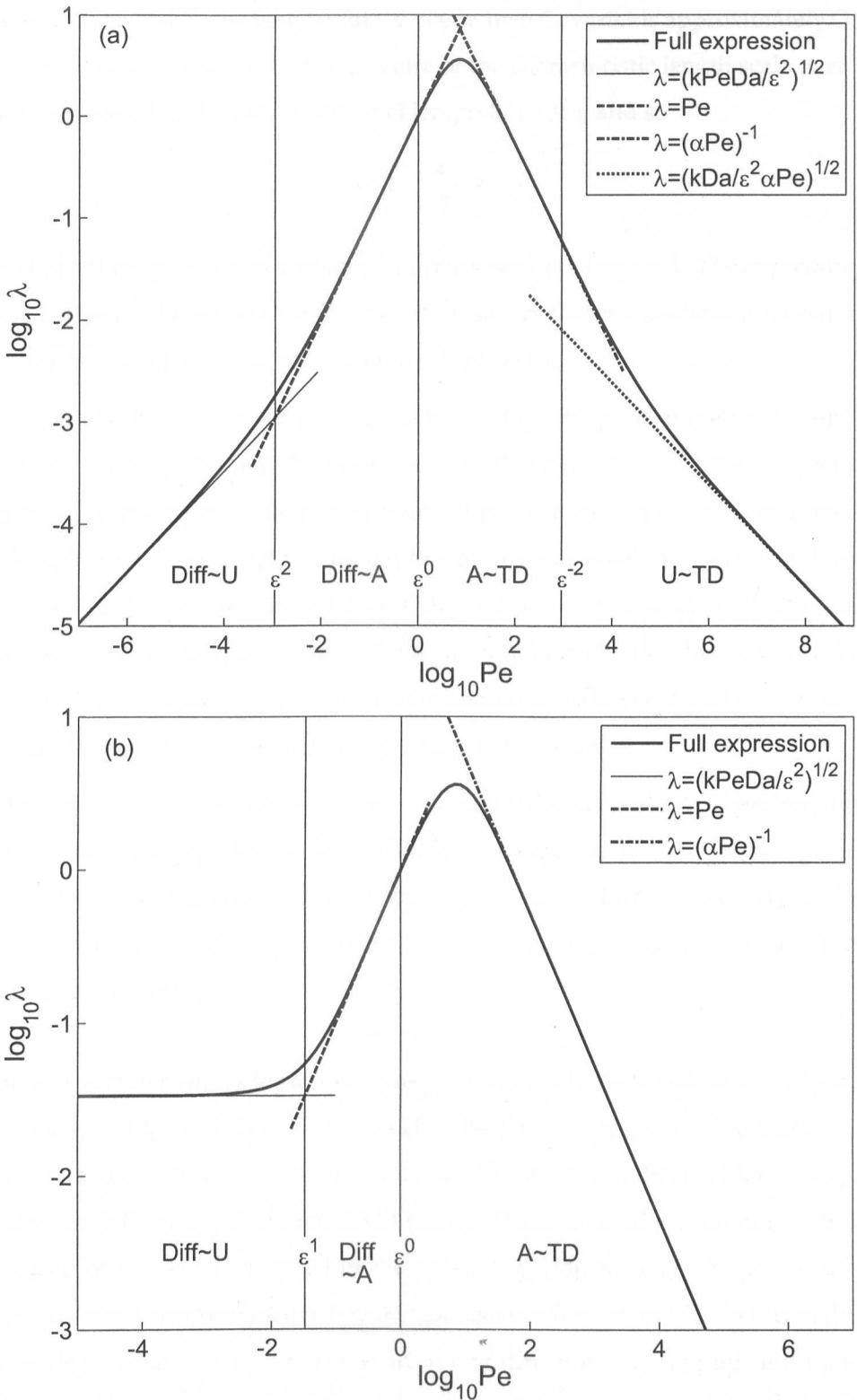


Figure 3.4: Full expression for λ (3.4.5), and its different approximations in different regions of parameter space, when $\epsilon = 1/30$, and (a) $Da = \epsilon^4$; (b) $PeDa = \epsilon^4$.

From equation (3.4.5), the length scale X over which C_0 varies is approximately $O(1/\lambda)$, or $x^* = Xa/\epsilon \approx a/\epsilon\lambda$. Let Λ be a measure of the characteristic length scale over which C varies, defined as the ratio of channel length to width, and so

$$\Lambda \equiv \frac{x^*}{a} \approx \frac{1}{\epsilon\lambda}.$$

The shortest length scale of variation Λ occurs with the largest λ . The expression for λ in the Diff~A~TD region ($\lambda \approx \text{Pe}/(1+\alpha\text{Pe}^2)$) shows that the maximum λ occurs when $\text{Pe} = \sqrt{1/\alpha} \approx 7$. (This is the maximum for λ while $\text{Da} < \epsilon^2$.)

Taking the limit $U_0 \rightarrow \infty$ corresponds to increasing the speed of the pore walls, or the spread of the drop through the pore space. In this case, $\text{Pe} \rightarrow \infty$, $\text{Da} \rightarrow 0$, and $\text{PeDa} = k_2 a^2 / D_w$ is constant. From Figure 3.4(b), this scenario minimises λ , and maximises the length scale of variation Λ . Taking this limit corresponds to travelling diagonally down and to the right in Figure 3.3, and, depending on the size of PeDa , the dominant processes will be either Taylor dispersion and uptake, or Taylor dispersion and advection. The Taylor dispersion produces an increased shearing of the advection flow, and increased overturning and mixing of the CO_2 in the water.

In the limit $U_0 \rightarrow 0$, then $\text{Pe} \rightarrow 0$, $\text{Da} \rightarrow \infty$, and PeDa is constant. Therefore diffusion balances chemical uptake. Taking this limit corresponds to travelling diagonally up and to the left in Figure 3.3. If capillary number $\text{Ca} = \mu U_0 / \gamma$, then $\epsilon \propto \text{Ca}^{2/3}$ at low speeds (when $\text{Ca} \ll 1$), and so ϵ is no longer constant, but varies with U_0 . Therefore Figure 3.4 does not apply.

Typical parameter values for a carbon sequestration scheme could be $a = 50 \mu\text{m}$, $U_0 = 0.1 \text{ m/day}$, and $D_w = 1.85 \times 10^{-9} \text{ m}^2/\text{s}$ [129, 140], in which case $\text{Pe} = aU_0/D_w = 0.031$. As $\text{Pe} \ll 1$, the limit $\text{Pe} \rightarrow 0$ is a sensible one to consider. In Section 3.5 we apply this limit to the fully coupled model (3.3.2)-(3.3.8). There is no advection in this limit, and the speed of the walls (or speed of the spreading drop through the pore space), can indeed be made arbitrarily small by taking a distance further and further from the point of injection (if the CO_2 is free to spread in any direction). Taking this limit gives the region of parameter space where axial diffusion balances reaction (or 'uptake' in Figure 3.3). Figure 3.3 provides a guide to the behaviour of the full system of seven coupled second order partial differential equations, and in this case, it predicts $\Lambda \approx 1/\sqrt{\text{PeDa}}$.

3.5 Coupled chemical distributions when axial diffusion balances reaction

To gain further insight into the complete steady-state far field model (3.3.2)-(3.3.8), and the comparative distributions of the different species in front of the drop, we now consider the region of parameter space where axial diffusion balances reaction, and there is no advection, determined by taking the idealised limit $Pe \rightarrow 0$. In this region, Figure 3.3 indicates that lengths in the x direction vary over a length scale of approximate magnitude $1/\sqrt{PeDa}$ (which is a ratio of diffusion to reaction), so $X \equiv x\sqrt{PeDa}$ is $O(1)$. The equations describing the steady-state behaviour of the seven species dissolved in the water are therefore, from (3.3.2)-(3.3.8)

$$\begin{aligned}
 0 &= B_{XX} - B + \sigma D, \\
 0 &= D_{XX} + B - \sigma D - \psi D + \omega EF, \\
 0 &= E_{XX} + \psi D - \omega EF + \chi F - \phi EG, \\
 0 &= F_{XX} + \psi D - \omega EF - \chi F + \phi EG, \\
 0 &= G_{XX} + \chi F - \phi EG - \tau GH + \rho K, \\
 0 &= H_{XX} - \tau GH + \rho K, \\
 0 &= K_{XX} + \tau GH - \rho K,
 \end{aligned}$$

with boundary conditions

$$B = B_L, D = D_L, E = E_L, F = F_L, G = G_L, H = H_L, K = K_L \text{ at } x = L, \quad (3.5.1)$$

(as given in Table 3.2), where L is the large finite maximum value for X . As $Pe, U_0 \rightarrow 0$, then Ca, ϵ and $h \rightarrow 0$ also. For simplicity, supposing there is a 90° contact angle between drop and pore wall (Figure 1.4(b) rather than 1.4(a)), then the inner boundary conditions can therefore simply be applied at $X = 0$, i.e. (3.2.9) becomes

$$B = k_H RTA, D_X = E_X = F_X = G_X = H_X = K_X = 0 \text{ at } X = 0. \quad (3.5.2)$$

The value of B at $X = 0$ indicates how much CO_2 has dissolved, and will be specified ($\equiv B_0$). If the walls are actually moving very slowly ($0 < Pe, h \ll 1$), or contact angle $\neq 90^\circ$, the solution must be found in this outer region by matching to the concentration field at the outer limit of an inner region. When this is done, applying the limit $Pe \rightarrow 0$

to this solution, or taking the leading-order solution when Pe is very small, will give the solutions to be found below with the $X = 0$ boundary condition.

A new set of variables, which give the perturbations in the species' concentrations from the far field equilibrium, are defined as:

$$\begin{aligned} b &= B - B_L, \quad d = D - D_L, \quad e = E - E_L, \quad f = F - F_L, \\ g &= G - G_L, \quad h = H - H_L, \quad k = K - K_L. \end{aligned}$$

Substituting these expressions into the equations above, and omitting the far field equilibrium combinations of terms that sum to zero (i.e. $B_L = \sigma D_L$, $\psi D_L = \omega E_L F_L$, $\chi F_L = \phi E_L G_L$, $\rho K_L = \tau G_L H_L$), gives:

$$0 = b_{XX} - b + \sigma d, \quad (3.5.3)$$

$$0 = d_{XX} + b - (\sigma + \psi)d + \omega(E_L f + e F_L + e f), \quad (3.5.4)$$

$$0 = e_{XX} + \psi d - \omega(E_L f + e F_L + e f) + \chi f - \phi(E_L g + e G_L + e g), \quad (3.5.5)$$

$$0 = f_{XX} + \psi d - \omega(E_L f + e F_L + e f) - \chi f + \phi(E_L g + e G_L + e g), \quad (3.5.6)$$

$$0 = g_{XX} + \chi f - \phi(G_L e + g E_L + g e) - \tau(G_L h + g H_L + g h) + \rho k, \quad (3.5.7)$$

$$0 = h_{XX} - \tau(G_L h + g H_L + g h) + \rho k, \quad (3.5.8)$$

$$0 = k_{XX} + \tau(G_L h + g H_L + g h) - \rho k, \quad (3.5.9)$$

with $b = B_0 - B_L$ and $d_X = e_X = f_X = g_X = h_X = k_X = 0$ at $X = 0$, and $b = d = e = f = g = h = k = 0$ at $X = L$. These two sets of boundary conditions can be re-written equivalently as:

$$b = B_0 - B_L, \quad d_X = e_X = f_X = (e - f - 2g + 2h)_X = (h + k)_X = k_X = 0 \text{ at } X = 0, \quad (3.5.10a-g)$$

$$b + d + f + g - h = d = e = f = e - f - 2g + 2h = h + k = k = 0 \text{ at } X = L. \quad (3.5.11a-g)$$

From summing (3.5.8) and (3.5.9), $(h + k)_{XX} = 0$. Integrating once, and using boundary condition (3.5.10f) to give the constant of integration, gives $(h + k)_X = 0$. Integrating again and using (3.5.11f) gives $h + k = 0$. Similarly, (3.5.5)-(3.5.6)-2(3.5.7)+2(3.5.8), with (3.5.10e) and (3.5.11e), gives $e - f - 2g + 2h = 0$. Also, (3.5.3)+(3.5.4)+(3.5.6)+(3.5.7)-(3.5.8) gives $(b + d + f + g - h)_{XX} = 0$. Integrating once gives $(b + d + f + g - h)_X = b_{X0}$, where b_{X0} is an unknown constant. Integrating again and applying (3.5.11a) gives $b + d + f + g - h = b_{X0}(X - L)$. Therefore $k = -h$, $e = b_{X0}(X - L) - b - d + g - h$ and

$f = b_{X0}(X - L) - b - d - g + h$, and the 14th-order system of seven coupled second-order equations (3.5.3)-(3.5.9) thus simplifies to the following 8th-order system of four coupled second-order nonlinear equations.

$$0 = b_{XX} - b + \sigma d,$$

$$0 = d_{XX} + b - (\sigma + \psi)d + \omega E_L(b_{X0}(X - L) - b - d - g + h) + \omega F_L(b_{X0}(X - L) - b - d + g - h) + \omega(b_{X0}(X - L) - b - d + g - h)(b_{X0}(X - L) - b - d - g + h),$$

$$0 = g_{XX} + \chi(b_{X0}(X - L) - b - d - g + h) - \phi(G_L + g)(b_{X0}(X - L) - b - d + g - h) - \phi E_L g - \tau(G_L h + g H_L + gh) - \rho h,$$

$$0 = h_{XX} - \tau(G_L h + g H_L + gh) - \rho h.$$

The unused boundary conditions containing e , f or k terms are adapted by substituting in the expressions for e , f and k . Substituting $k = -h$ into (3.5.10g) gives $h_X = 0$. Differentiating the expressions for e and f , substituting them into (3.5.10c,d), and noting that $d_X = h_X = 0$, gives $g_X = 0$ and $b_X = b_{X0}$. Similarly, at $X = L$, $h = d = 0$, and (3.5.11c,d) give $b = g = 0$. This 8th-order system that also contains the unknown b_{X0} therefore has the following nine boundary conditions:

$$b = B_0 - B_L, \quad b_X = b_{X0}, \quad d_X = g_X = h_X = 0 \quad \text{at } X = 0,$$

$$\text{and } b = d = g = h = 0 \quad \text{at } X = L.$$

The system of equations is thus nonautonomous. The solution depends on the domain size L , and as this can be chosen to be anything up to ∞ , there is no limit to how far from the injection point the concentrations of the chemical species are affected, given infinite time. This is the case with this idealised limit $Pe \rightarrow 0$. In the previous Section it was found that taking the limit $Pe \rightarrow \infty$, with fixed $PeDa$, also gives an infinite length scale of variation.

To gain insight into this complete model, for reasons of mathematical convenience, we consider the case $b_{X0} = 0$, and discard the boundary condition on b_X at $X = 0$. This has the advantage of making the system of equations autonomous, and eliminates the dependence on domain size L . We investigate the distributions of the chemical species in the water ahead of the drop in this case. To reflect the fact that it is 8th-order,

nonlinear, and contains the full set of reaction terms, this model is labelled "8NF":

$$\text{Model } \left\{ \begin{array}{l} 0 = b_{XX} - b + \sigma d, \\ 0 = d_{XX} + b - (\sigma + \psi)d + \omega E_L(-b - d - g + h) + \omega F_L(-b - d + g - h) \\ \quad + \omega((b + d)^2 - (g - h)^2), \\ \text{8NF} \left\{ \begin{array}{l} 0 = g_{XX} + \chi(-b - d - g + h) - \phi(G_L + g)(-b - d + g - h) - \phi g E_L \\ \quad - \tau(G_L h + g H_L + gh) - \rho h, \\ 0 = h_{XX} - \tau(G_L h + g H_L + gh) - \rho h, \end{array} \right. \end{array} \right.$$

with boundary conditions

$$b = B_0 - B_L, d_X = g_X = h_X = 0 \text{ at } X = 0, b = d = g = h = 0 \text{ at } X = L. \quad (3.5.12)$$

The amount of injected CO₂ can be chosen to be sufficiently small (i.e. $0 < B_0 - B_L \ll B_L$) that the quadratic perturbation terms (e.g. gh) are negligible compared to the linear perturbation terms. In this case, the system can be approximated by removing the quadratic perturbation terms, and hence all the nonlinearity in the system, giving the following linear 8th-order system of four coupled second-order equations:

$$\text{Model } \left\{ \begin{array}{l} 0 = b_{XX} - b + \sigma d, \\ 0 = d_{XX} + b - (\sigma + \psi)d - \omega E_L(b + d + g - h) - \omega F_L(b + d - g + h), \\ \text{8LF} \left\{ \begin{array}{l} 0 = g_{XX} - \chi(b + d + g - h) + \phi G_L(b + d - g + h) - \phi g E_L \\ \quad - \tau(G_L h + g H_L) - \rho h, \\ 0 = h_{XX} - \tau(G_L h + g H_L) - \rho h, \end{array} \right. \end{array} \right.$$

with boundary conditions (3.5.12).

Model 8NF is a challenging system of equations that we were unable to solve numerically using Matlab's inbuilt solver for boundary value ordinary differential equation problems (bvp4c). Two Newton-Raphson programs were therefore constructed to find numerically the solution to 8NF for a given B_0 : one that uses central differences to estimate the second derivatives; and one that uses Chebyshev polynomials. The details of these two methods are given in Appendix 3.A at the end of this Chapter. In what follows, the solution to 8LF is found analytically and asymptotically (Section 3.5.1), and then this is used to verify that the Newton-Raphson methods are working correctly (Section 3.5.2). The solutions for larger amplitudes are then found (Sections 3.5.3 and 3.5.4), which require the nonlinear version of this model.

3.5.1 Small amplitude approximation: Model 8LF

Model 8LF can be expressed as the product of a linear operator and a vector of perturbations:

$$\begin{pmatrix} d_X^2 - 1 & \sigma & 0 & 0 \\ \{1 - \omega E_L & \{d_X^2 - (\sigma + \psi) & \omega(-E_L + F_L) & \omega(E_L - F_L) \\ -\omega F_L\} & -\omega(E_L + F_L)\} & & \\ -\chi + \phi G_L & -\chi + \phi G_L & \{d_X^2 - \chi - \phi G_L & \{\chi + \phi G_L \\ -\phi E_L - \tau H_L\} & -\tau G_L - \rho\} \\ 0 & 0 & -\tau H_L & d_X^2 - \tau G_L - \rho \end{pmatrix} \begin{pmatrix} b \\ d \\ g \\ h \end{pmatrix} = 0. \quad (3.5.13)$$

There is one solution to this system of four coupled second order equations that matches boundary conditions (3.5.12), and this solution is a linear combination of eight exponentials. It takes the form

$$\begin{pmatrix} b \\ d \\ g \\ h \end{pmatrix} = \sum_{p=1}^8 c_p \begin{pmatrix} Z_{p,b} \\ Z_{p,d} \\ Z_{p,g} \\ Z_{p,h} \end{pmatrix} \exp(-\lambda_p X), \quad (3.5.14)$$

where c_p are constants determined by the boundary conditions, and λ_p are constants which control the length scales over which the perturbations grow or decay. These expressions are substituted into (3.5.13), which only holds true if the terms for each p separately sum to zero. This gives the eigenvalue problem

$$\begin{pmatrix} 1 & -\sigma & 0 & 0 \\ \{-1 + \omega E_L & \{\sigma + \psi + & \omega(E_L - F_L) & \omega(-E_L + F_L) \\ +\omega F_L\} & \omega(E_L + F_L)\} & & \\ \chi - \phi G_L & \chi - \phi G_L & \{\chi + \phi G_L + & \{-\chi - \phi G_L \\ \phi E_L + \tau H_L\} & +\tau G_L + \rho\} \\ 0 & 0 & \tau H_L & \tau G_L + \rho \end{pmatrix} \mathbf{Z}_p = \lambda_p^2 \mathbf{Z}_p,$$

where $\mathbf{Z}_p = (Z_{p,b}, Z_{p,d}, Z_{p,g}, Z_{p,h})$, for $p = 1, \dots, 8$. The four eigenvalues λ_p^2 and corresponding eigenvectors \mathbf{Z}_p are found numerically, using the parameter values given in Table 3.2. It is found that $\lambda_p^2 > 0$ for all p . The four negative square roots of λ_p^2 are

p	1	2	3	4
λ_p^2	4.4069×10^8	8.3966×10^5	2.0675×10^2	1.6670×10^{-2}
$Z_{p,b}$	7.5639×10^{-7}	2.0903×10^{-4}	8.5093×10^{-1}	-7.0317×10^{-1}
$Z_{p,d}$	-1.0000×10^0	-5.2654×10^{-1}	-5.2524×10^{-1}	-2.0743×10^{-3}
$Z_{p,g}$	3.7152×10^{-5}	-8.5015×10^{-1}	6.2646×10^{-3}	1.9481×10^{-4}
$Z_{p,h}$	7.0116×10^{-16}	-8.4211×10^{-9}	2.5203×10^{-7}	7.1102×10^{-1}
c_p	-2.9911×10^{-13}	9.5133×10^{-14}	8.2534×10^{-10}	-3.2573×10^{-14}

Table 3.4: Solution to 8LF when $b_0 = 7 \times 10^{-10}$.

allocated to λ_5 to λ_8 . These produce an exponentially growing solution in (3.5.14) (taking the limit $L \rightarrow \infty$), and so c_5 to c_8 must equal zero. The positive square roots (λ_1 to λ_4) and Z_1 to Z_4 are used to find the constants c_1 to c_4 as follows. From (3.5.14), on the boundary $X = 0$,

$$\begin{pmatrix} b \\ d_X \\ g_X \\ h_X \end{pmatrix} = \begin{pmatrix} Z_{1,b} & Z_{2,b} & Z_{3,b} & Z_{4,b} \\ -\lambda_1 Z_{1,d} & -\lambda_2 Z_{2,d} & -\lambda_3 Z_{3,d} & -\lambda_4 Z_{4,d} \\ -\lambda_1 Z_{1,g} & -\lambda_2 Z_{2,g} & -\lambda_3 Z_{3,g} & -\lambda_4 Z_{4,g} \\ -\lambda_1 Z_{1,h} & -\lambda_2 Z_{2,h} & -\lambda_3 Z_{3,h} & -\lambda_4 Z_{4,h} \end{pmatrix} \begin{pmatrix} c_1 \\ c_2 \\ c_3 \\ c_4 \end{pmatrix}.$$

Now, $B_L = 9.844298 \times 10^{-6}$, and so $B_0 = 9.845 \times 10^{-6}$ is chosen as this results in a small, but positive, value of b at $X = 0$ ($\equiv b_0 = 7.0 \times 10^{-10}$). Substituting in this value for b , the remaining bubble tip boundary conditions from (3.5.12) ($d_X = g_X = h_X = 0$), and pre-multiplying both sides of this equation by the inverse of the matrix on the right hand side, gives the four constants. The solution for this b_0 is given in Table 3.4, and these solutions are plotted in Figure 3.5.

In Figure 3.5(a), the log of the absolute values b , d , g and h are plotted against $\log X$. b remains positive, and h remains negative, over the whole of X , but d and g change sign round about $X = 1$, leading to singularities in these log plots. These two species overshoot their target of zero very slightly, but smoothly, as shown in a linear plot in Figure 3.5(b). There are four length scales in the problem, of $O(1/\lambda_p)$, which range over five orders of magnitude for X , and these length scales are also indicated in Figure 3.5(a).

The two length scales $O(1/\lambda_1)$ and $O(1/\lambda_2)$ provide extremely short boundary layers within which there are actually no noticeable changes in the sizes of the perturbations

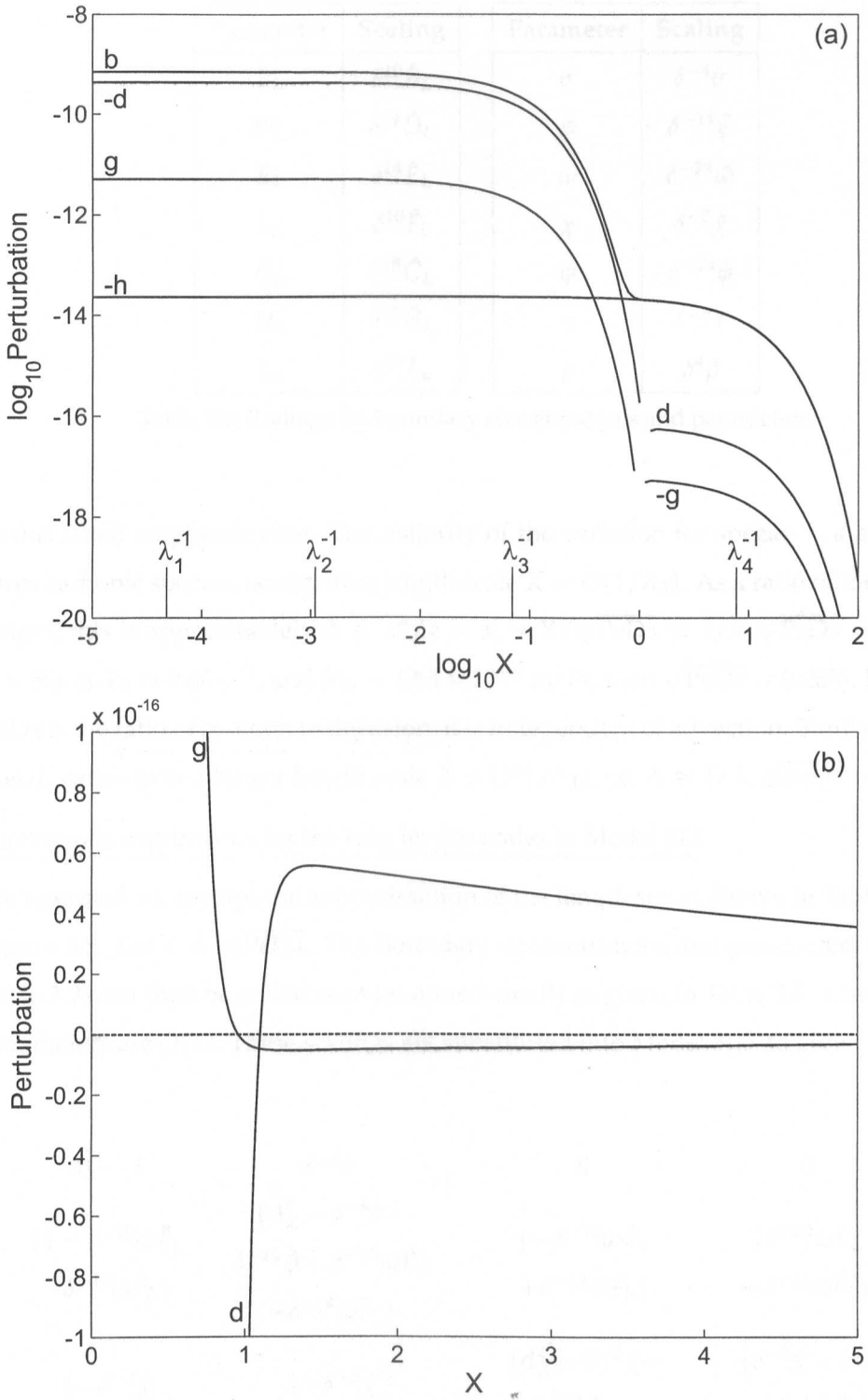


Figure 3.5: Solution to 8LF when $b_0 = 7 \times 10^{-10}$: (a) Using logarithmic axes (the gaps in the plots are when $d = 0$ and $g = 0$), and (b) using linear axes, to show overshooting for d and g .

Parameter	Scaling	Parameter	Scaling
B_L	$\delta^{10}\hat{B}_L$	σ	$\delta^{-4}\hat{\sigma}$
D_L	$\delta^{14}\hat{D}_L$	ψ	$\delta^{-14}\hat{\psi}$
E_L	$\delta^{14}\hat{E}_L$	ω	$\delta^{-24}\hat{\omega}$
F_L	$\delta^{10}\hat{F}_L$	χ	$\delta^{-2}\hat{\chi}$
G_L	$\delta^{18}\hat{G}_L$	ϕ	$\delta^{-24}\hat{\phi}$
H_L	$\delta^{10}\hat{H}_L$	τ	$\delta^{-6}\hat{\tau}$
I_∞	$\delta^{18}\hat{I}_\infty$	ρ	$\delta^4\hat{\rho}$

Table 3.5: Scalings for boundary concentrations and parameters.

in this small amplitude case. The majority of the variation for species b , d and g , the three carbonic species, occurs over length scale $X = O(1/\lambda_3)$. As a ratio of the channel height, this is approximately $\Lambda \equiv x^*/a = x = X/\sqrt{\text{PeDa}} \approx 1/\lambda_3\sqrt{\text{PeDa}} = 0.24$. (If $a = 50\mu\text{m}$, $k_2 = 0.06\text{ s}^{-1}$, and $D_w = 1.85 \times 10^{-9}\text{ m}^2/\text{s}$, then $\sqrt{\text{PeDa}} = 0.285$). Note that PeDa is the ratio of reaction to diffusion; it is independent of advection. Similarly, h , the metal, varies over a longer length scale $X = O(1/\lambda_4)$, i.e. $\Lambda \approx 1/\lambda_4\sqrt{\text{PeDa}} = 27.20$.

Asymptotic expressions for the four length scales in Model 8LF

We now seek an asymptotic approximation of the length scales shown in Table 3.4 and Figure 3.5. Let $\delta \equiv \sqrt{\text{PeDa}}$. The boundary concentrations and parameters (given in Table 3.2) can then be scaled on δ (assumed small) as given in Table 3.5, where hatted parameters are $O(1)$. These scalings are substituted into Model 8LF, to give:

$$\begin{pmatrix}
 d_X^2 - 1 & \delta^{-4}\hat{\sigma} & 0 & 0 \\
 \{1 - \delta^{-10}\hat{\omega}\hat{E}_L - \delta^{-14}\hat{\omega}\hat{F}_L\} & \{d_X^2 - \delta^{-4}\hat{\sigma} - \delta^{-14}\hat{\psi} - \delta^{-10}\hat{\omega}\hat{E}_L - \delta^{-14}\hat{\omega}\hat{F}_L\} & \{-\delta^{-10}\hat{\omega}\hat{E}_L + \delta^{-14}\hat{\omega}\hat{F}_L\} & \{\delta^{-10}\hat{\omega}\hat{E}_L - \delta^{-14}\hat{\omega}\hat{F}_L\} \\
 \{-\delta^{-2}\hat{\chi} + \delta^{-6}\hat{\phi}\hat{G}_L\} & \{-\delta^{-2}\hat{\chi} + \delta^{-6}\hat{\phi}\hat{G}_L\} & \{d_X^2 - \delta^{-2}\hat{\chi} - \delta^{-6}\hat{\phi}\hat{G}_L - \delta^{-10}\hat{\phi}\hat{E}_L - \delta^4\hat{\tau}\hat{H}_L\} & \{\delta^{-2}\hat{\chi} - \delta^4\hat{\rho} + \delta^{-6}\hat{\phi}\hat{G}_L - \delta^{12}\hat{\tau}\hat{G}_L\} \\
 0 & 0 & -\delta^4\hat{\tau}\hat{H}_L & \{d_X^2 - \delta^4\hat{\rho} - \delta^{12}\hat{\tau}\hat{G}_L\}
 \end{pmatrix}
 \begin{pmatrix}
 b \\
 d \\
 g \\
 h
 \end{pmatrix}
 = \mathbf{0}.$$

Taking the limit $\delta \rightarrow 0$, and assuming all hatted quantities remain $O(1)$, gives, to leading order,

$$\begin{pmatrix} d_X^2 - 1 & \delta^{-4}\hat{\sigma} & 0 & 0 \\ -\delta^{-14}\hat{\omega}\hat{F}_L & d_X^2 - \delta^{-14}(\hat{\psi} + \hat{\omega}\hat{F}_L) & \delta^{-14}\hat{\omega}\hat{F}_L & -\delta^{-14}\hat{\omega}\hat{F}_L \\ \delta^{-6}\hat{\phi}\hat{G}_L & \delta^{-6}\hat{\phi}\hat{G}_L & d_X^2 - \delta^{-10}\hat{\phi}\hat{E}_L & \delta^{-6}\hat{\phi}\hat{G}_L \\ 0 & 0 & -\delta^4\hat{\tau}\hat{H}_L & d_X^2 - \delta^4\hat{\rho} \end{pmatrix} \begin{pmatrix} b \\ d \\ g \\ h \end{pmatrix} = 0,$$

or, substituting in (3.5.14),

$$\begin{pmatrix} \lambda_p^2 - 1 & \delta^{-4}\hat{\sigma} & 0 & 0 \\ -\delta^{-14}\hat{\omega}\hat{F}_L & \lambda_p^2 - \delta^{-14}(\hat{\psi} + \hat{\omega}\hat{F}_L) & \delta^{-14}\hat{\omega}\hat{F}_L & -\delta^{-14}\hat{\omega}\hat{F}_L \\ \delta^{-6}\hat{\phi}\hat{G}_L & \delta^{-6}\hat{\phi}\hat{G}_L & \lambda_p^2 - \delta^{-10}\hat{\phi}\hat{E}_L & \delta^{-6}\hat{\phi}\hat{G}_L \\ 0 & 0 & -\delta^4\hat{\tau}\hat{H}_L & \lambda_p^2 - \delta^4\hat{\rho} \end{pmatrix} \begin{pmatrix} Z_{p,b} \\ Z_{p,d} \\ Z_{p,g} \\ Z_{p,h} \end{pmatrix} = 0.$$

This is the eigenvalue problem

$$\begin{pmatrix} 1 & -\delta^{-4}\hat{\sigma} & 0 & 0 \\ \delta^{-14}\hat{\omega}\hat{F}_L & \delta^{-14}(\hat{\psi} + \hat{\omega}\hat{F}_L) & -\delta^{-14}\hat{\omega}\hat{F}_L & \delta^{-14}\hat{\omega}\hat{F}_L \\ -\delta^{-6}\hat{\phi}\hat{G}_L & -\delta^{-6}\hat{\phi}\hat{G}_L & \delta^{-10}\hat{\phi}\hat{E}_L & -\delta^{-6}\hat{\phi}\hat{G}_L \\ 0 & 0 & \delta^4\hat{\tau}\hat{H}_L & \delta^4\hat{\rho} \end{pmatrix} \mathbf{Z}_p = \lambda_p^2 \mathbf{Z}_p. \quad (3.5.15)$$

The eigenvalues λ_p^2 are the roots of the characteristic equation $\det(\mathbf{A} - \lambda_p^2 \mathbf{I}_4) = 0$, where \mathbf{A} is the matrix on the left hand side of (3.5.15), and \mathbf{I}_4 is the 4×4 identity matrix, i.e.

$$\begin{aligned} 0 &= \lambda_p^8 + \lambda_p^6 \left(-\delta^{-14}(\hat{\psi} + \hat{\omega}\hat{F}_L) - \delta^{-10}\hat{\phi}\hat{E}_L - 1 - \delta^4\hat{\rho} \right) \\ &+ \lambda_p^4 \left(\delta^{-24}\hat{\phi}\hat{E}_L(\hat{\psi} + \hat{\omega}\hat{F}_L) - \delta^{-20}\hat{\phi}\hat{G}_L\hat{\omega}\hat{F}_L + \delta^{-18}\hat{\sigma}\hat{\omega}\hat{F}_L + \delta^{-14}(\hat{\psi} + \hat{\omega}\hat{F}_L) \right. \\ &\quad \left. + \delta^{-10}\hat{\rho}(\hat{\psi} + \hat{\omega}\hat{F}_L) + \delta^{-10}\hat{\phi}\hat{E}_L + \delta^{-6}\hat{\phi}\hat{E}_L\hat{\rho} + \delta^{-2}\hat{\tau}\hat{H}_L\hat{\phi}\hat{G}_L + \delta^4\hat{\rho} \right) \\ &+ \lambda_p^2 \left(-\delta^{-28}\hat{\sigma}\hat{\omega}\hat{F}_L\hat{\phi}\hat{E}_L + \delta^{-24}\hat{\sigma}\hat{\omega}\hat{F}_L\hat{\phi}\hat{G}_L - \delta^{-24}\hat{\phi}\hat{E}_L(\hat{\psi} + \hat{\omega}\hat{F}_L) + \delta^{-20}\hat{\phi}\hat{G}_L\hat{\omega}\hat{F}_L \right. \\ &\quad - \delta^{-20}\hat{\phi}\hat{E}_L\hat{\rho}(\hat{\psi} + \hat{\omega}\hat{F}_L) + \delta^{-16}\hat{\phi}\hat{G}_L\hat{\omega}\hat{F}_L\hat{\rho} - \delta^{-16}\hat{\phi}\hat{G}_L\hat{\tau}\hat{H}_L\hat{\psi} \\ &\quad \left. - \delta^{-14}\hat{\sigma}\hat{\omega}\hat{F}_L\hat{\rho} - \delta^{-10}\hat{\rho}(\hat{\psi} + \hat{\omega}\hat{F}_L) - \delta^{-6}\hat{\phi}\hat{E}_L\hat{\rho} - \delta^{-2}\hat{\tau}\hat{H}_L\hat{\phi}\hat{G}_L \right) \\ &+ \delta^{-24}\hat{\sigma}\hat{\omega}\hat{F}_L\hat{\phi}\hat{E}_L\hat{\rho} - \delta^{-20}\hat{\sigma}\hat{\omega}\hat{F}_L\hat{\phi}\hat{G}_L\hat{\rho} + \delta^{-20}\hat{\phi}\hat{E}_L(\hat{\psi} + \hat{\omega}\hat{F}_L)\hat{\rho} - \delta^{-16}\hat{\phi}\hat{G}_L\hat{\omega}\hat{F}_L\hat{\rho} \\ &\quad + \delta^{-16}\hat{\phi}\hat{G}_L\hat{\tau}\hat{H}_L\hat{\psi} \\ &\approx \lambda_p^8 - \lambda_p^6 \delta^{-14}(\hat{\psi} + \hat{\omega}\hat{F}_L) + \lambda_p^4 \delta^{-24}\hat{\phi}\hat{E}_L(\hat{\psi} + \hat{\omega}\hat{F}_L) - \lambda_p^2 \delta^{-28}\hat{\sigma}\hat{\omega}\hat{F}_L\hat{\phi}\hat{E}_L \\ &\quad + \delta^{-24}\hat{\sigma}\hat{\omega}\hat{F}_L\hat{\phi}\hat{E}_L\hat{\rho}, \end{aligned} \quad (3.5.16)$$

Eigenvalue	Asymptotic formula	Asymptotic value
λ_1^2	$\psi + \omega F_L$	4.3985×10^8
λ_2^2	ϕE_L	8.3333×10^5
λ_3^2	$\sigma \omega F_L / (\psi + \omega F_L)$	2.0703×10^2
λ_4^2	ρ	1.6667×10^{-2}

Table 3.6: Asymptotic values of λ_p^2 .

taking the leading-order coefficient of each term.

There are only four values of λ_p^2 which give a leading-order balance between at least two terms on the right hand side of this equation. The first of these eigenvalues is $\lambda_1^2 \approx \delta^{-14}(\hat{\psi} + \hat{\omega}\hat{F}_L)$, which gives a dominant balance between the first and second terms in (3.5.16). The second is $\lambda_2^2 \approx \delta^{-10}\hat{\phi}\hat{E}_L$, which gives a dominant balance between the second and third terms; the third is $\lambda_3^2 \approx \delta^{-4}\hat{\sigma}\hat{\omega}\hat{F}_L/(\hat{\psi} + \hat{\omega}\hat{F}_L)$, which gives a dominant balance between the third and fourth terms; the fourth eigenvalue is $\lambda_4^2 \approx \delta^4\hat{\rho}$, which gives a dominant balance between the fourth and fifth terms in (3.5.16). These formulae are given in Table 3.6, along with the evaluation of these formulas. Comparison with the exact values found numerically (Table 3.4) shows excellent agreement.

Far field simplification for Model 8LF

We now seek an asymptotic approximation of the species' far field behaviour. In the far field, Figure 3.5(a) indicates that the three carbonic species b , d and g are slaved to h , and are prevented from continuing their rapid decreases by the slower decline of h . The graph indicates that b and h are $O(10^{-14})$, d is $O(10^{-16})$, g is $O(10^{-18})$, and X is $O(10^1)$ in this region, and so these variables can be scaled on δ (assumed small) as $b = \delta^{25}\hat{b}$, $d = \delta^{29}\hat{d}$, $g = \delta^{33}\hat{g}$, $h = \delta^{25}\hat{h}$, and $X = \delta^{-2}\hat{X}$, where hatted variables are $O(1)$. Substituting these scalings, and the parameter scalings given in Table 3.5, into Model 8LF gives:

$$0 = -\hat{b} + \hat{\sigma}\hat{d} + \delta^4\hat{b}_{\hat{X}\hat{X}}, \quad (3.5.17)$$

$$0 = -\hat{\omega}\hat{F}_L(\hat{b} + \hat{h}) - \delta^4(\hat{\psi}\hat{d} + \hat{\omega}\hat{E}_L(\hat{b} - \hat{h}) + \hat{\omega}\hat{F}_L\hat{d}) + O(\delta^8), \quad (3.5.18)$$

$$0 = \hat{\phi}\hat{G}_L(\hat{b} + \hat{h}) + \delta^4(\hat{\chi}(-\hat{b} + \hat{h}) + \hat{\phi}\hat{G}_L\hat{d} - \hat{\phi}\hat{E}_L\hat{g}) + O(\delta^8), \quad (3.5.19)$$

$$0 = \hat{h}_{\hat{X}\hat{X}} - \hat{\rho}\hat{h} - \delta^8\hat{\tau}(\hat{G}_L\hat{h} + \hat{H}_L\hat{g}). \quad (3.5.20)$$

The four variables can be expanded in powers of δ^4 , e.g. $\hat{b} = \hat{b}_0 + \delta^4 \hat{b}_1 + \dots$ In the asymptotic limit $\delta \rightarrow 0$, the leading order terms on the right hand sides must sum to zero, and so $\hat{b}_0 = \hat{\sigma} \hat{d}_0$, $\hat{b}_0 = -\hat{h}_0$, and $\hat{h}_{0,XX} = \hat{\rho} \hat{h}_0$. At the next order, equations (3.5.18) and (3.5.19) give

$$0 = -\hat{\omega} \hat{F}_L(\hat{b}_1 + \hat{h}_1) - \hat{\psi} \hat{d}_0 - \hat{\omega} \hat{E}_L(\hat{b}_0 - \hat{h}_0) - \hat{\omega} \hat{F}_L \hat{d}_0, \quad (3.5.21)$$

$$\text{and } 0 = \hat{\phi} \hat{G}_L(\hat{b}_1 + \hat{h}_1) + \hat{\chi}(-\hat{b}_0 + \hat{h}_0) + \hat{\phi} \hat{G}_L \hat{d}_0 - \hat{\phi} \hat{E}_L \hat{g}_0. \quad (3.5.22)$$

Multiplying (3.5.21) by $\hat{\phi} \hat{G}_L$, (3.5.22) by $\hat{\omega} \hat{F}_L$, and summing, gives:

$$\begin{aligned} 0 &= -\hat{\phi} \hat{G}_L(\hat{\psi} \hat{d}_0 + \hat{\omega} \hat{E}_L(\hat{b}_0 - \hat{h}_0)) + \hat{\omega} \hat{F}_L(-\hat{\chi}(\hat{b}_0 - \hat{h}_0) - \hat{\phi} \hat{E}_L \hat{g}_0) \\ &= \hat{\phi} \hat{G}_L(\hat{\psi} \hat{h}_0 / \hat{\sigma} + 2\hat{\omega} \hat{E}_L \hat{h}_0) + \hat{\omega} \hat{F}_L(2\hat{\chi} \hat{h}_0 - \hat{\phi} \hat{E}_L \hat{g}_0). \end{aligned}$$

This expression is simplified by replacing $\hat{\chi} \hat{F}_L$ with $\hat{\phi} \hat{E}_L \hat{G}_L$, $\hat{\omega} \hat{F}_L \hat{E}_L$ with $\hat{\psi} \hat{D}_L$, solving for g , and replacing $\hat{\sigma} \hat{D}_L$ with \hat{B}_L . This gives the expression for g in this system:

$$b = -h, \quad (3.5.23)$$

$$d = -h/\sigma, \quad (3.5.24)$$

$$g = (1/B_L + 4/F_L)G_L h, \quad (3.5.25)$$

$$h = h_{\lambda_3} \exp(-\sqrt{\rho}X), \quad (3.5.26)$$

where h_{λ_3} is the value of h at the outer limit of the λ_3 length scale. When (3.5.23)-(3.5.26) are plotted (taking $h_{\lambda_3} = h_0$, the value of h at $X = 0$) against the solutions given in Table 3.4 and plotted in Figure 3.5, the plots for (3.5.23) and (3.5.26) coincide with the lines for b and h from the point at which these two species meet, and the plots for (3.5.24) and (3.5.25) coincide with the lines for d and g onwards from the points at which they change sign.

3.5.2 Model 8NF

Two Newton-Raphson programs are constructed to solve Model 8NF, the model appropriate for larger amplitude perturbations (see Appendix 3.A). One uses central differences to estimate the second derivatives, and one uses Chebyshev polynomials. To verify that the two Newton-Raphson methods work correctly, the solutions they find to Model 8LF (with the same parameter values and value for b_0 as in Section 3.5.1) are

compared to the known solution found in Section 3.5.1 (details are given in Appendix 3.A.4). The solutions they produce are generally within 1% of the known solution. For each species, the Chebyshev errors are mostly lower than the central difference errors, and the Chebyshev method needs only an all-zeros initial guess, while the central differences method requires a reasonably accurate initial guess.

As the Chebyshev method is found to be more robust than the central differences method, it is used to solve 8NF at this small amplitude. The Chebyshev solutions to 8LF and 8NF are indistinguishable, which indicates that $b_0 = 7.0 \times 10^{-10}$ is indeed sufficiently small for the linear model to be a good approximation to the nonlinear model. The value of b_0 is slightly increased, to 8.0×10^{-10} , and the solution to 8NF found for this new b_0 by continuation (using the converged solution to the first b_0 to provide the initial guess for the value of each species at each collocation point). This process is repeated, continuing along b_0 , with the increment by which b_0 increases growing bigger or smaller depending on how easily the previous solution was found. As b_0 changes, the distributions of the four species across X also change. Figures 3.6-9 show the converged solutions predicted by the Chebyshev method. The Chebyshev method can only find solutions to Model 8NF when b_0 is less than 4.4×10^{-8} (or B is 0.44% above the pre-injection level). These are the continuous lines in Figures 3.6-9. Above this level, the Chebyshev method predicts solutions that do not satisfy the boundary condition $g_X = 0$ at $X = 0$. These 'solutions' are shown with dashed lines in Figures 3.6-9. As $d = D - D_L$, the most negative that d can be is $-D_L (= -2.95 \times 10^{-8})$, otherwise this gives a negative D , and the solutions that fail to satisfy g 's no flux boundary condition also give values for which D is negative. There are two likely reasons why the method is unable to find solutions that satisfy g 's boundary condition: first, because of a lack of resolution (the Chebyshev method dictates the locations of the X -axis discretisation points, and these are forced to be very sparse at this end of a logarithmic scale, even though 5000 collocation points were taken in total); and second, because of the assumption $b_{X0} = 0$, which may lead to unphysical results.

The solutions to 8NF which do satisfy g 's boundary condition all show uniform values for b , d , g and h when $X < 10^{-3}$, and the length scales over which equilibrium is reached remain the same. An alternative model is now sought for which solutions can be found for higher amplitudes, while continuing to assume $b_{X0} = 0$.

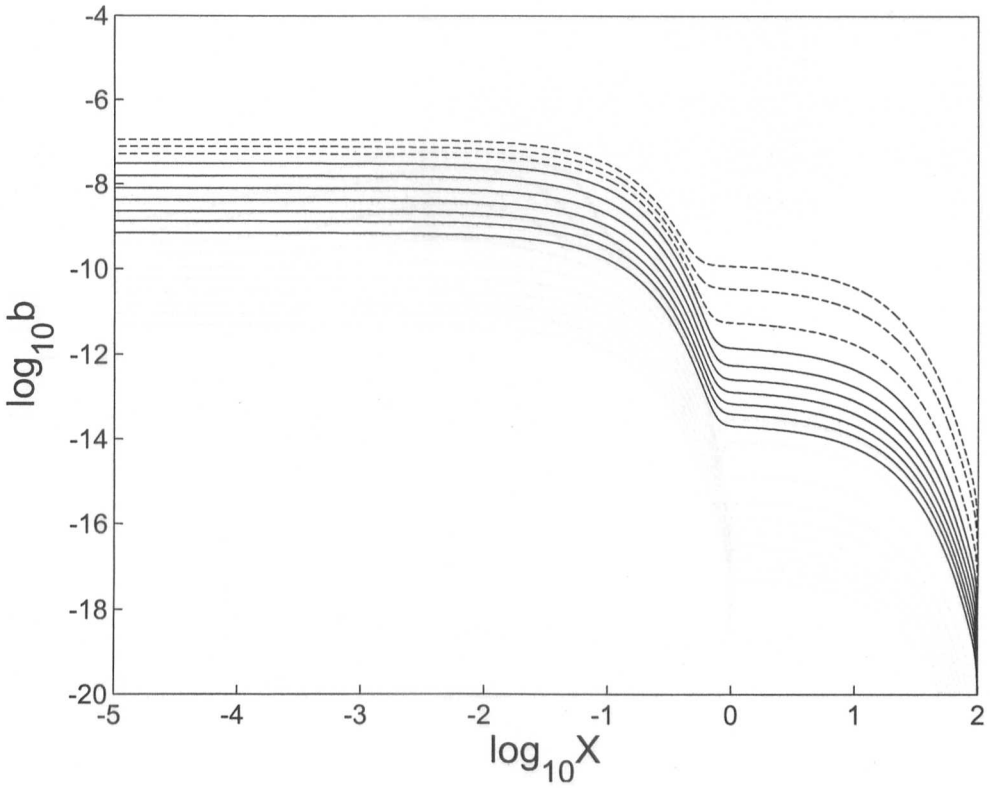


Figure 3.6: Model 8NF: Distributions of b as the value of b at $X = 0$ is increased.

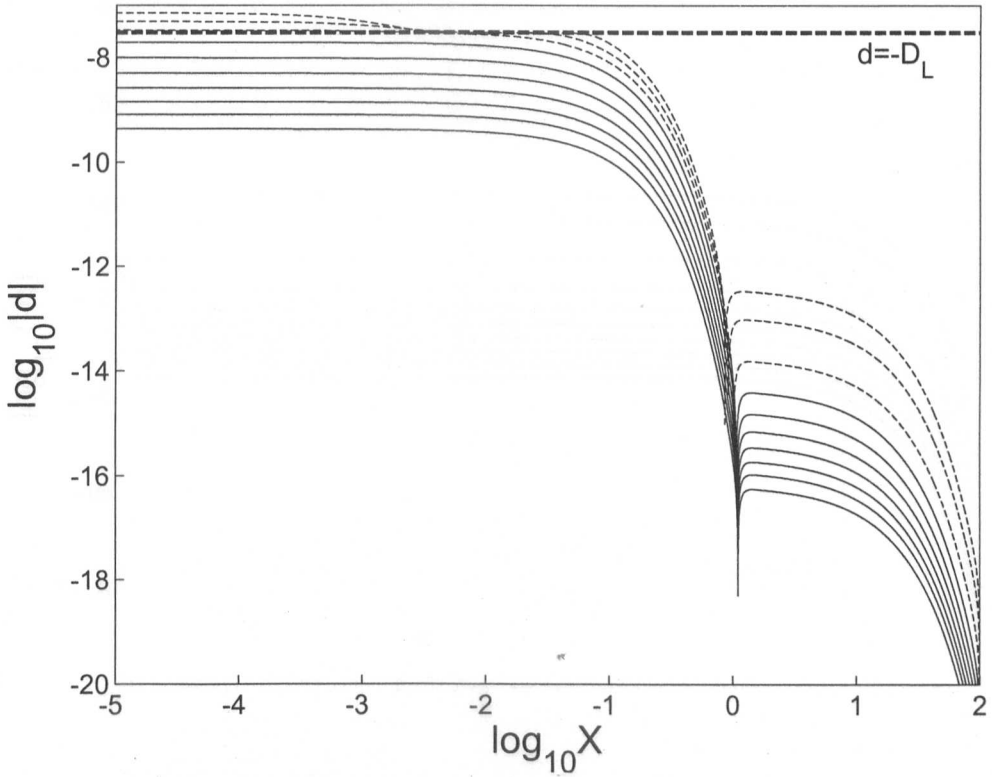


Figure 3.7: Model 8NF: Distributions of d as the value of b at $X = 0$ is increased.

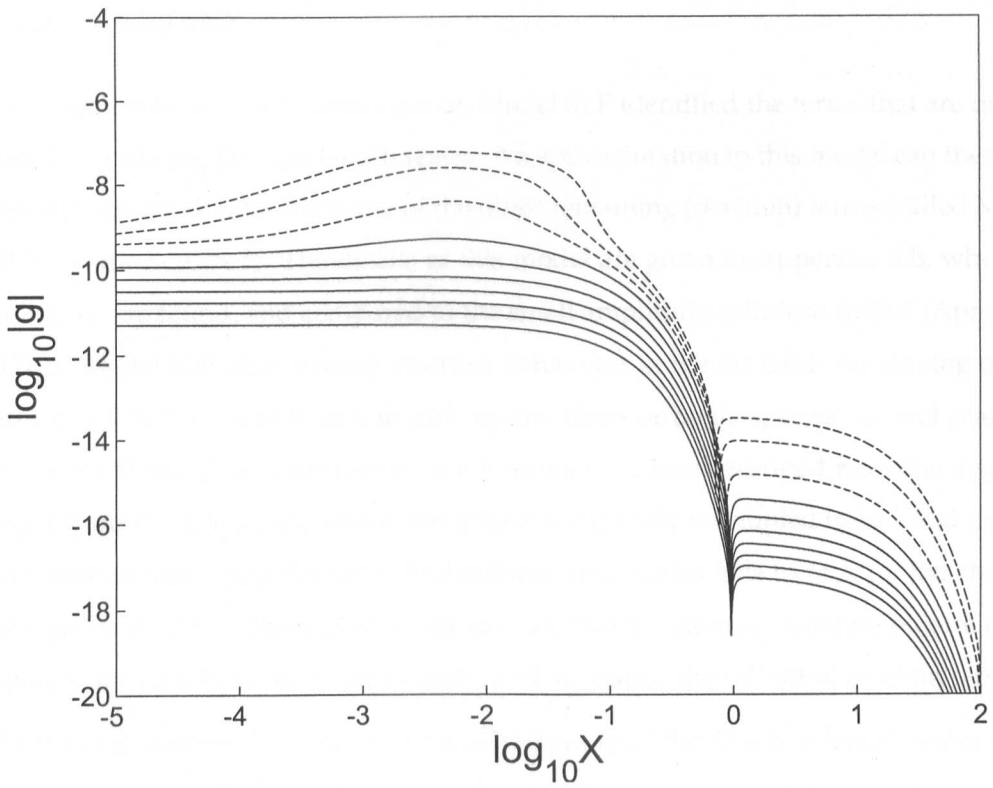


Figure 3.8: Model 8NF: Distributions of g as the value of b at $X = 0$ is increased.

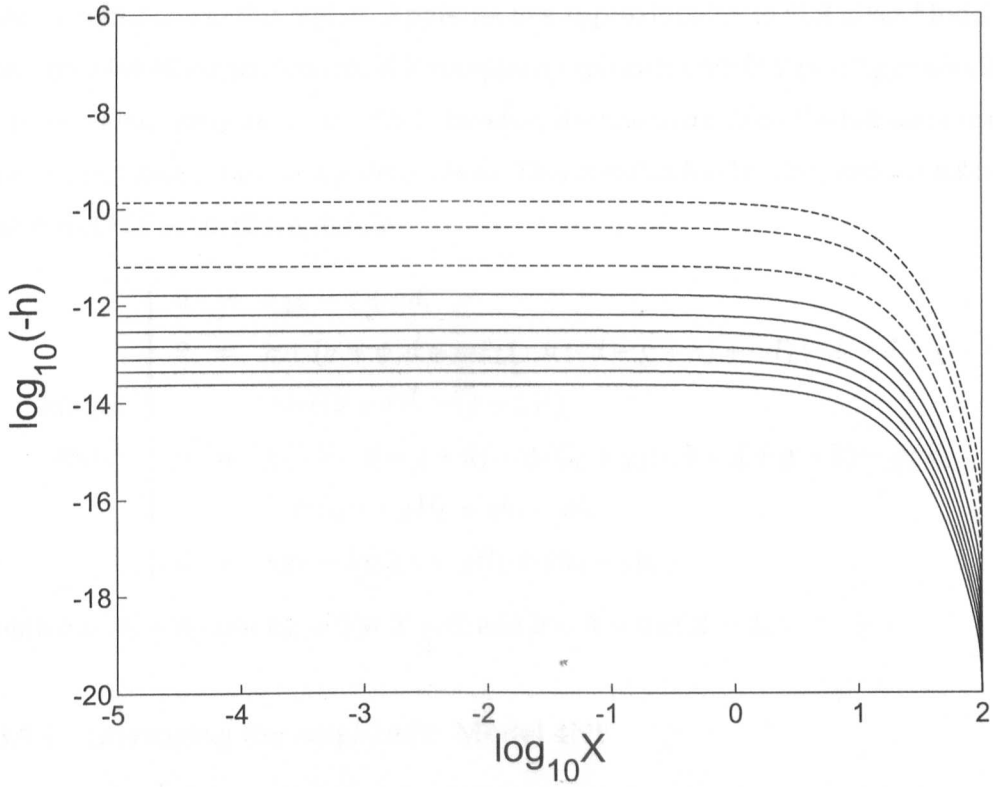


Figure 3.9: Model 8NF: Distributions of h as the value of b at $X = 0$ is increased.

3.5.3 Model 4NF

The asymptotic analysis carried out on Model 8LF identified the terms that are important in producing the four length scales. An approximation to this model can therefore be obtained by eliminating some of the other remaining (reaction) terms (called Model 8LR, 'R' for Reduced). The details of this model are given in Appendix 3.B, where its solutions are found, and compared to the small amplitude solutions to 8LF (Appendix 3.B.2). Model 8LR shows some incorrect behaviour in the far field: the slaving of b , d and g to h is lost, as 8LR fails to pick up the three carbonic species' second plateaux in the far field. This is because all the h terms have been dropped from the d_{XX} and g_{XX} equations in 8LR, and so b , d and g have completely decoupled from h and are free to continue their steep declines. The reduced model also fails to pick up the changes of sign for d and g . These differences indicate that to retain an accurate picture of the species' far field behaviour, the models need to contain the full set of reaction terms.

As the four species all show uniform behaviour over the first two length scales ($X = O(10^{-4.3})$ and $O(10^{-3.0})$), eliminating the d and g derivatives makes no difference to the distributions in this region. Applying this approximation to 8LR gives Model 4LR, and the plotted expressions for 4LR completely coincide with 8LR (see Appendix 3.B.3). The best alternative model to 8NF is therefore the one that retains the full set of reaction terms, and drops the d and g derivatives. This is called Model 4NF, and is identical to 8NF and 8LF at small amplitude.

$$\text{Model 4NF} \left\{ \begin{array}{l} 0 = b_{XX} - b + \sigma d, \\ 0 = b - (\sigma + \psi)d + \omega E_L(-b - d - g + h) + \omega F_L(-b - d + g - h) \\ \quad + \omega((b + d)^2 - (g - h)^2), \\ 0 = \chi(-b - d - g + h) - \phi(G_L + g)(-b - d + g - h) - \phi g E_L \\ \quad - \tau(G_L h + g H_L + gh) - \rho h, \\ 0 = h_{XX} - \tau(G_L h + g H_L + gh) - \rho h, \end{array} \right.$$

with $b = B_0 - B_L$ and $h_X = 0$ at $X = 0$, and $b = h = 0$ at $X = L$.

3.5.4 Increasing the amplitude: Model 4NF

Using the Chebyshev method to solve Model 4NF, by starting again at $b_0 = 7 \times 10^{-10}$ and then continuing along b_0 as before, gives the distributions given in Figures 3.10-

13. Solutions are given up to the point at which the Chebyshev solution to d develops a discontinuity (caused by dropping d_{XX}) just as d begins to deviate from its plateau; this takes place when $b_0 \approx 1 \times 10^{-5}$ (i.e. B at the bubble tip is about twice its pre-injection level). From Section 1.7.1, the maximum solubility for CO_2 is likely to be about 1 M, and so a maximum value for B at the bubble tip is $\approx 1 \text{ M} / 55.5 \text{ M} = 0.018$. Therefore the original target maximum size for b_0 was $b_0 = B - B_L \approx 0.018 - 9.84 \times 10^{-6} \approx 0.018$, a substantially greater value.

Behaviour close to the CO_2 drop

Figure 3.11 shows that d quickly reduces to its minimum as b_0 increases. (g has a minimum $= -G_L = -3.55 \times 10^{-10}$, but g is only negative when $X > 1$.) When d hits its minimum, g is forced to be approximately equal to b in this region (and so experiences a rapid jump up to b), for the following reason: Suppose X is $O(10^{-2})$ in this region, b is $O(10^{-6})$, d is $O(10^{-8})$, and $g \gg h$. Then leading-order balances to 4NF can only be obtained if g is also $O(10^{-6})$. Suppose also that h is $O(10^{-8})$, so these variables can be scaled on δ as $b = \delta^{10}\hat{b}$, $d = \delta^{14}\hat{d}$, $g = \delta^{10}\hat{g}$, $h = \delta^{14}\hat{h}$, and $X = \delta^4\hat{X}$, where hatted variables are $O(1)$. Substituting these scalings, and the scalings for the boundary concentrations and parameters given in Table 3.5, into Model 4NF gives:

$$0 = \hat{b}_{\hat{X}\hat{X}} + \delta^8(-\hat{b} + \partial\hat{d}), \quad (3.5.27)$$

$$0 = \hat{\omega}\hat{F}_L(-\hat{b} + \hat{g}) + \hat{\omega}(\hat{b}^2 - \hat{g}^2) + \delta^4(-\hat{\psi}\hat{d} - \hat{\omega}\hat{E}_L(\hat{b} + \hat{g}) - \hat{\omega}\hat{F}_L(\hat{d} + \hat{h}) + 2\hat{\omega}(\hat{b}\hat{d} + \hat{g}\hat{h})) + O(\delta^8), \quad (3.5.28)$$

$$0 = \hat{\phi}\hat{g}(\hat{b} - \hat{g}) - \delta^4\hat{\phi}\hat{g}(\hat{E}_L - \hat{d} - \hat{h}) + O(\delta^6), \quad (3.5.29)$$

$$0 = \hat{h}_{\hat{X}\hat{X}} - \delta^8\hat{\tau}\hat{g}\hat{H}_L + O(\delta^{18}). \quad (3.5.30)$$

The four variables can be expanded in powers of δ^4 as before, and in the asymptotic limit $\delta \rightarrow 0$, the leading-order terms on the right hand sides of (3.5.28) and (3.5.29) must sum to zero, i.e. $0 = \hat{\omega}\hat{F}_L(-\hat{b}_0 + \hat{g}_0) + \hat{\omega}\hat{b}_0^2 - \hat{\omega}\hat{g}_0^2 = \hat{\omega}(\hat{b}_0 - \hat{g}_0)(-\hat{F}_L + \hat{b}_0 + \hat{g}_0)$, and $0 = \hat{\phi}\hat{g}_0(\hat{b}_0 - \hat{g}_0)$. The second equation has solution $\hat{b}_0 = \hat{g}_0$, and this also satisfies the first equation.

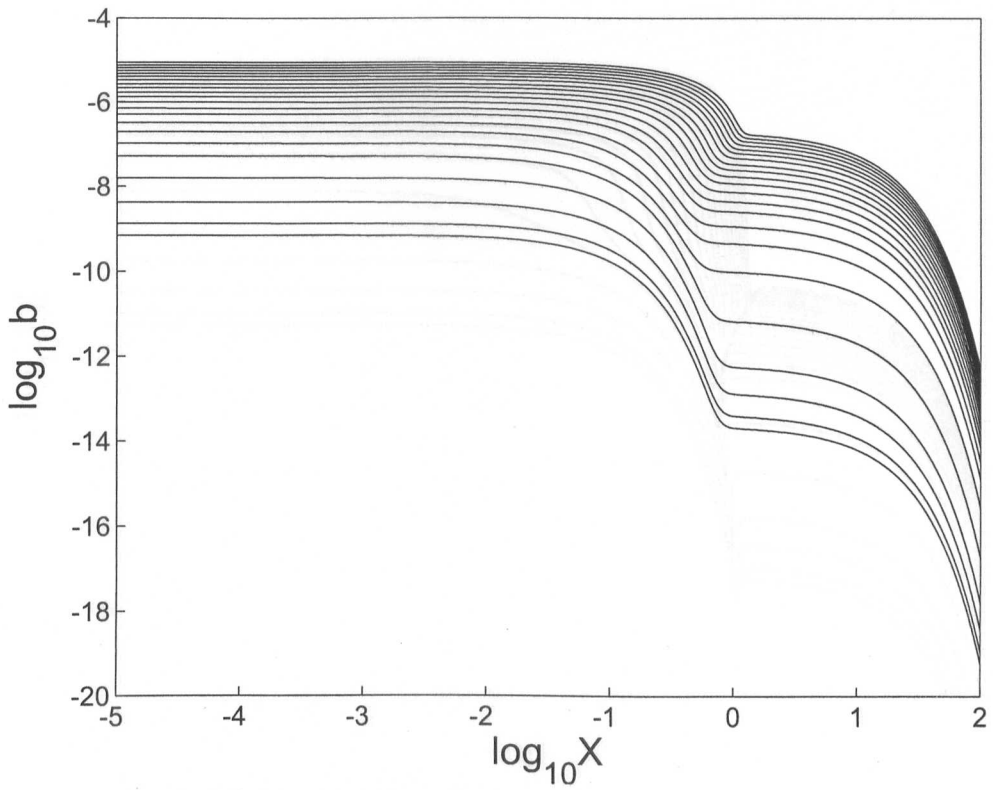


Figure 3.10: Model 4NF: Distributions of b as the value of b at $X = 0$ is increased.

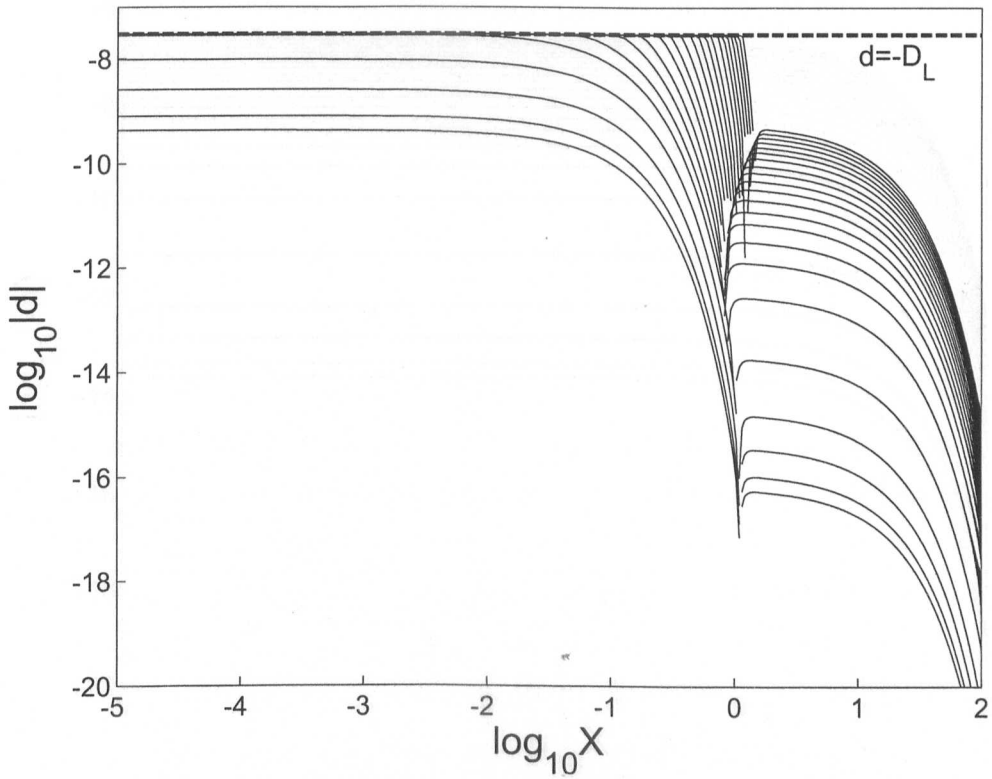


Figure 3.11: Model 4NF: Distributions of d as the value of b at $X = 0$ is increased.

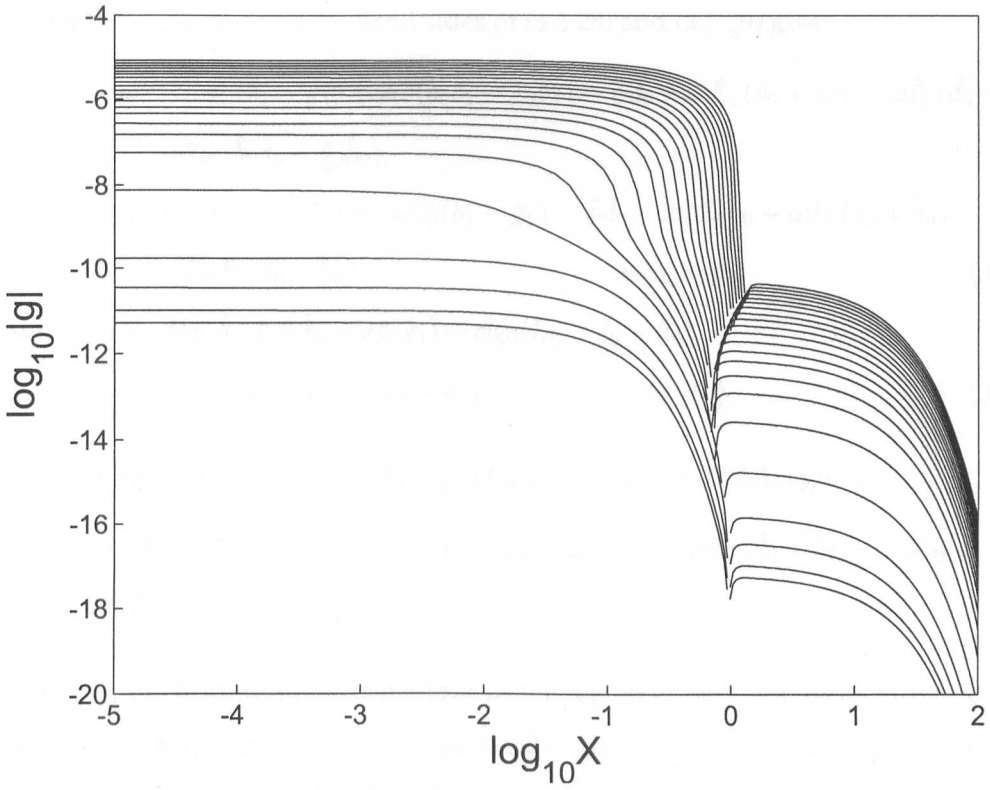


Figure 3.12: Model 4NF: Distributions of g as the value of b at $X = 0$ is increased.

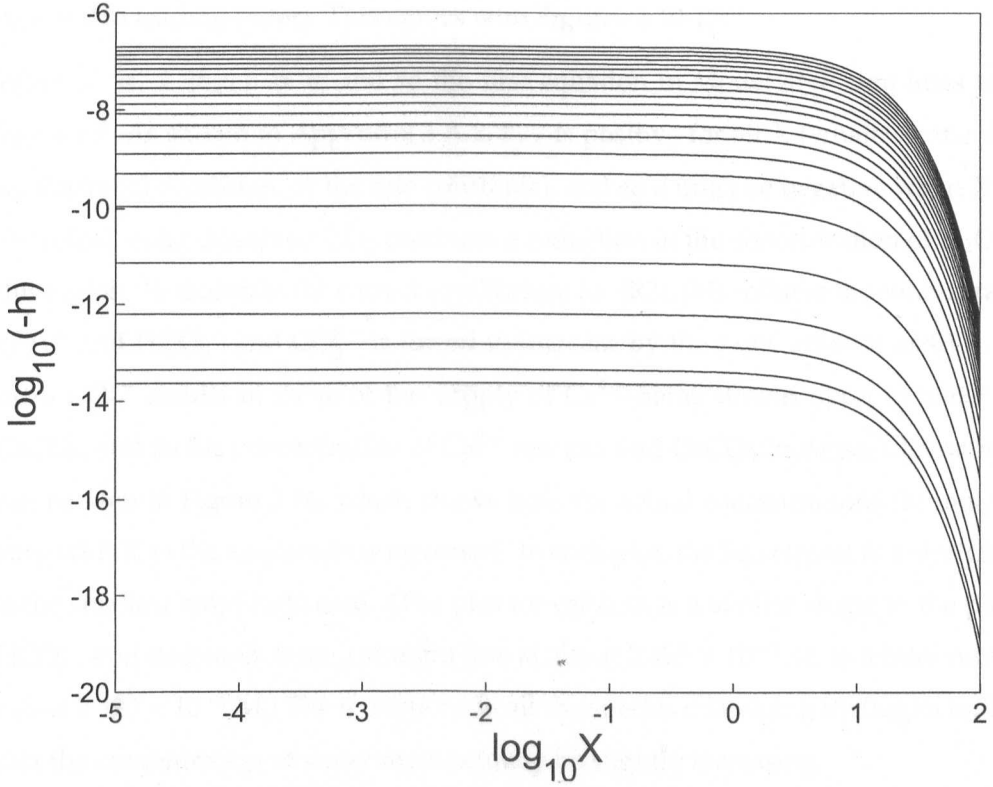


Figure 3.13: Model 4NF: Distributions of h as the value of b at $X = 0$ is increased.

The $O(\delta^4)$ terms on the right hand sides of (3.5.28) and (3.5.29) give:

$$\begin{aligned}
 0 &= -\hat{\omega}\hat{F}_L(\hat{b}_1 - \hat{g}_1) + 2\hat{\omega}(\hat{b}_0\hat{b}_1 - \hat{g}_0\hat{g}_1) - \hat{\psi}\hat{d}_0 - \hat{\omega}\hat{E}_L(\hat{b}_0 + \hat{g}_0) - \hat{\omega}\hat{F}_L(\hat{d}_0 + \hat{h}_0) \\
 &\quad + 2\hat{\omega}(\hat{b}_0\hat{d}_0 + \hat{g}_0\hat{h}_0), \\
 &= -\hat{\omega}\hat{F}_L(\hat{b}_1 - \hat{g}_1) + 2\hat{\omega}\hat{b}_0(\hat{b}_1 - \hat{g}_1) - \hat{\psi}\hat{d}_0 - 2\hat{\omega}\hat{E}_L\hat{b}_0 - \hat{\omega}\hat{F}_L(\hat{d}_0 + \hat{h}_0) \\
 &\quad + 2\hat{\omega}\hat{b}_0(\hat{d}_0 + \hat{h}_0) \qquad \qquad \qquad \text{as } \hat{b}_0 = \hat{g}_0, \tag{3.5.31}
 \end{aligned}$$

$$\begin{aligned}
 \text{and } 0 &= \hat{\phi}(\hat{g}_0\hat{b}_1 + \hat{g}_1\hat{b}_0 - 2\hat{g}_0\hat{g}_1) - \hat{\phi}\hat{g}_0(\hat{E}_L - \hat{d}_0 - \hat{h}_0) \\
 &= (\hat{b}_1 - \hat{g}_1) - (\hat{E}_L - \hat{d}_0 - \hat{h}_0) \qquad \qquad \text{as } \hat{b}_0 = \hat{g}_0. \tag{3.5.32}
 \end{aligned}$$

Substituting an expression for $(\hat{b}_1 - \hat{g}_1)$ from (3.5.32) into (3.5.31) gives

$$\begin{aligned}
 0 &= (-\hat{\omega}\hat{F}_L + 2\hat{\omega}\hat{b}_0)(\hat{E}_L - \hat{d}_0 - \hat{h}_0) - \hat{\psi}\hat{d}_0 - 2\hat{\omega}\hat{E}_L\hat{b}_0 - \hat{\omega}\hat{F}_L(\hat{d}_0 + \hat{h}_0) + 2\hat{\omega}\hat{b}_0(\hat{d}_0 + \hat{h}_0) \\
 &= -\hat{\omega}\hat{E}_L\hat{F}_L - \hat{\psi}\hat{d}_0.
 \end{aligned}$$

Therefore, the leading-order behaviour in the region close to the drop is: $b = g = b_0$, the value of b specified at $X = 0$ (as (3.5.27) gives $b_{XX} = 0$ to leading order); $d = -\omega E_L F_L / \psi = -D_L$, i.e. $D = 0$; and $h = h_0$, the value of h at $X = 0$ (as (3.5.30) gives $h_{XX} = 0$ to leading order). This agrees with Figures 3.10-13.

When $X \ll 1$, $|b_{XX}| \gg b$, and so the first equation in Model 4NF simplifies to $0 = b_{XX} + \sigma d$. As shown in Appendix 3.A.2, b_{XX} is positive for all X (whatever the size of b_0 , the initial condition, or the rate constants), and so d must be negative when $X \ll 1$. Therefore, extra dissolved CO_2 produces a reduction in the concentration of H_2CO_3 in this region. To maintain the correct equilibrium for (R3), this reduces the concentrations of H^+ and HCO_3^- , and CO_3^{2-} is forced to increase by the same amount as CO_2 . This extra CO_3^{2-} results in some of the supply of Ca^{2+} being drawn upon to make extra CaCO_3 , and so the concentration of Ca^{2+} reduces and CaCO_3 increases. These results can be seen in Figure 3.14, which shows how the actual concentrations (in mol/litre) vary with X as the amplitude is increased. In each plot, the line closest to a straight line is the smallest amplitude case. (The plot for calcium is a similar shape to the plot for HCO_3^- , and decreases from a straight line at about 2.495×10^{-4} M, to a minimum just below 2.390×10^{-4} M.) The reductions in all the species containing hydrogen indicates that the concentration of water must actually be slightly increasing.

In Figure 3.14, the concentrations of H^+ and HCO_3^- go slightly negative, and the dashed lines on all six plots correspond to these cases. These are the two species (e and f) that

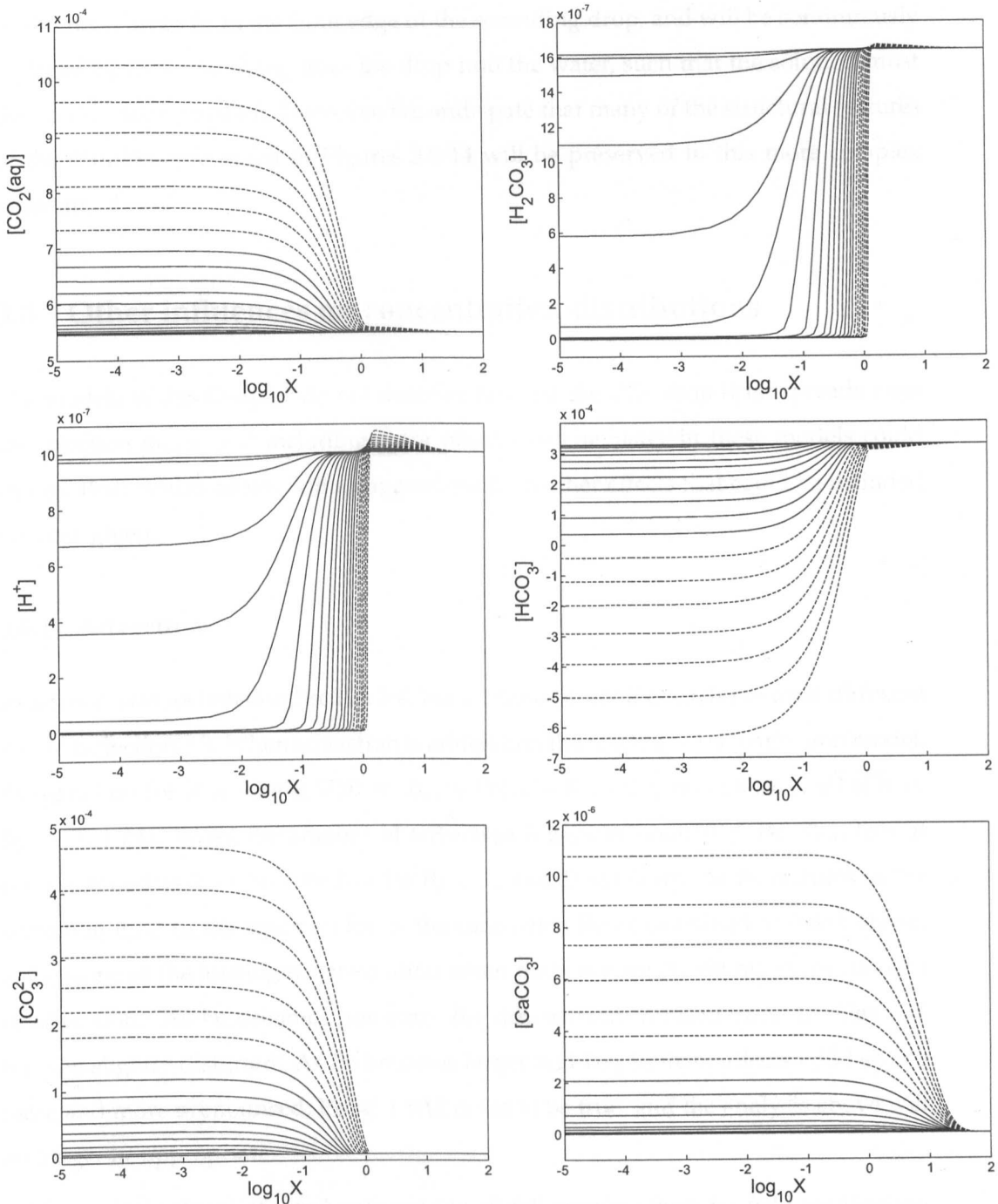


Figure 3.14: Model 4NF: Distributions of the different chemical species as the value of $\text{CO}_2(\text{aq})$ at the edge of the drop is increased. In each plot, the line closest to a straight line is the smallest amplitude case.

were eliminated from the 14th-order problem (3.5.3)-(3.5.9) by replacing them with expressions involving b_{X0} . These numerical results therefore show that $b_{X0} = 0$ is an inappropriate simplification to this model for these magnitudes. CO_2 will continu-

ously travel away from the front edge of the spreading drop, and will be continuously replaced by CO₂ dissolving from the drop into the water, such that the solution must depend on domain size L . However, we anticipate that many of the structural features of the solutions presented in Figures 3.5-14 will be preserved in this more complex problem.

3.6 Other influences on concentration distributions

The models in this Chapter do not describe how far the CO₂ drop itself spreads from the injection point, and including extra physics or chemistry in these models could change their results again. Some suggestions for further effects that could be included are now given.

3.6.1 Advection

Advection was included in Section 3.4, but excluded from the reaction–axial diffusion model in Section 3.5. When advection is added into the reaction–axial diffusion model, the equation for B is $-\text{Pe}(\mathbf{u} \cdot \nabla)B = B_{xx} + \text{PeDa}(-B + \sigma D)$, or $-\text{Pe} u B_x / \sqrt{\text{PeDa}} = B_{xx} - B + \sigma D$. When the amount of advection is zero or small, $0 \leq \text{Pe} \ll 1$, then B can be expanded as $B = B_0 + \text{Pe}B_1 + \text{Pe}^2B_2 + \dots$, and D similarly. As Pe features in the advection term in the equation for B , the case when $\text{Pe}=0$, examined in detail above, is the same as the leading-order solution when there is a small, but non-zero, amount of advection. As Pe becomes non-zero, the downstream concentration profiles will become slightly distorted. As Pe becomes larger and larger, these effects will become more and more pronounced, $\text{Pe} \ll 1$ will cease to be true, and the analysis above will no longer be appropriate.

In the analysis above, the carbonic species all fall towards their far field equilibrium concentrations within a short distance from the drop. In this region, advection in the y direction will be no less important than in the x direction, and so if advection were to be included in the model, this would need to take the form of the two-dimensional flow discussed in Section 1.9.2, rather than the simpler one-dimensional Poiseuille flow of Section 1.9.1.

3.6.2 Density-driven convection

The differences in densities between the undissolved CO₂ and the resident water are sufficient to produce a spreading horizontal gravity current if the lighter CO₂ remains above the heavier water without mixing into it [50, 51]. Alternatively, if the lighter CO₂ is pushed into the heavier water, the density differences may produce Rayleigh-Taylor fingering instabilities, as discussed in Section 1.4. When these become sufficiently large to overcome inertia, the heavier of the two fluids migrates downwards and sideways, leading to the formation of fingering with overturning and rolling flows. Overturning can also occur in the water when CO₂ dissolves into the water adjacent to it, increasing its density compared to the water without dissolved CO₂, or if CO₂ is injected below water, and starts rising above it.

This density-driven convection flow in a carbon sequestration scenario is analogous to temperature-driven Rayleigh-Benard convection [141]. The strength of conduction to convection in a temperature-driven flow is given by the Rayleigh number, and instability arises and so turbulent mixing occurs when the Rayleigh number is greater than some critical value. Density-driven convection is known to be likely and play an important role in a carbon sequestration scenario, as small density differences are sufficient to create density-driven convection. (For example, the driving force from a density difference of 1 kg/m³ relative to a reference density of 1000 kg/m³ is equivalent to the driving force from a hydraulic gradient caused by just a 1 m decrease in the hydraulic head over a lateral distance of 1 km [142].) This is supported by experimental [143, 144], analytical [141, 145], and numerical simulation [146] evidence.

3.6.3 Alternative pore space structure

The pore spaces within an aquifer are not straight horizontal separate 2-d channels, but curved and tortuous 3-d tubes, with many connections between the different pores. Advection and density-driven convection are likely to be increased if the pore turns downwards, or reduced if it turns upwards.

3.6.4 Variable thin film width

The size of the gap between the drop of CO_2 and the pore walls may not be the same all the way round the drop, and as CO_2 is lighter than the aquifer water, the size of this gap between the bottom of the drop and the lower pore wall may well be fairly large, increasing the advective flow. This can lead to increased dissolution and mixing.

3.6.5 Additional chemical reactions

There are more chemical reactions that could be included in the model. Including extra species for the dissolved CO_2 to react with, for example, can lead to more CO_2 being predicted to dissolve into the water. If the CO_2 or other dissolved species form compounds by reacting with the resident minerals, these may precipitate out of the solution, depositing solids on to the pore walls, reducing the permeability of the pore space, and making it harder for the CO_2 to travel away from the injection point.

3.6.6 Alternative parameter values or initial conditions

The steady state distributions may well be different when the initial chemical composition of the water is different, or changes in the temperature, pressure, pH, salinity, or other conditions mean that the rate constants are different. The robustness of the species' distributions to changes in the input parameters can be assessed using Monte Carlo simulation. Different values for the rate constants and the initial composition of the system would first be drawn at random from appropriate distributions. (Appropriate log-normal distributions are the ideal distributions from which to sample, as this gives a wide range of possible positive values.) These values would then be used to find the dimensionless parameters, the far-field equilibrium concentrations, and the steady state solutions to the small amplitude linear approximation, and then the Newton-Raphson techniques can be applied as above. Critical measures of the outcome, such as distance to equilibrium, can then be found.

3.6.7 Ionic charge

Hydrogen, bicarbonate, carbonate and calcium are charged particles, and so will all be attracted to or repelled away from each other. The size of the electrical force exerted by one ion on another is given by Coulomb's law $F = q_1q_2/4\pi\epsilon x^{*2}$ [72], where q_1 and q_2 are the sizes of the two ions' charges, x^* is the distance between the ions, and ϵ is the permittivity of the medium. This can be estimated by $\epsilon = \epsilon_0\epsilon_r$, where ϵ_0 is permittivity in a vacuum ($8.85 \times 10^{-12} \text{ C}^2\text{J}^{-1}\text{m}^{-1}$) and ϵ_r is the relative permittivity of the medium (or 'dielectric constant'), $\epsilon_r = 78$ for water at 25°C and 55 for water at 100°C . The size of the charge on an ion is the number of electrons it has lost or gained (one for hydrogen and bicarbonate and two for carbonate and calcium) multiplied by the charge carried by a single electron $\approx -1.602 \times 10^{-19} \text{ C}$.

If a packet of aquifer water of volume $(10 \mu\text{m})^3$ is saturated with dissolved CO_2 , and thus is 10 kg/m^3 denser than the surrounding water, then its extra weight above the surrounding water is $9.81 \times 10^{-14} \text{ N}$. From Coulomb's law, the charge force between a hydrogen cation and a carbonate anion, for example, is this size when the distance between the two ions is $x^* \approx 7.8 \times 10^{-9} \text{ m}$, and 1% of this size when $x^* \approx 7.8 \times 10^{-8} \text{ m}$. Charge forces are important over very short length scales, but less important at the longer length scales over which conduction and convection effects occur.

3.7 Conclusions

Injected CO_2 forms a spreading drop in an aquifer's pore space, dissolves from the tip of the drop into the resident water and spreads away from the tip of the drop, causing changes in the chemical composition of the water in front of the drop as it reacts with the other species in the water.

In Section 3.4 we analysed a model for the steady state far field distribution of any single species dissolving from a spreading drop into a long thin channel filled with water, accounting for advection, Taylor dispersion, diffusion, and a chemical sink. The model included a weak net flux through the channel, less than the flow by a factor of $O(\epsilon)$, where ϵ is the ratio of film width (between drop and pore walls) to channel radius. For fixed ϵ , the length scale over which the dissolved species spreads out is minimised if the Péclet number is $O(1)$ (i.e. advection and diffusion are equally important), and

increases as the Péclet number increases, due to Taylor dispersion.

If minimising the distance through an aquifer pore over which CO₂ spreads out is desirable, this model therefore suggests that the CO₂ should be injected in such a way as to make the speed of spread of the CO₂ drop through the pore space as close as possible to the speed at which the CO₂ that dissolves from the drop into the water in the pore space will diffuse through the water, and to err on the side of a slower spread of CO₂ through the pore space. The speed at which the CO₂ drop spreads through a given pore space can be controlled, for example, by changing the speed and pressure at which it is injected, whether it is injected together with water, and whether the CO₂ is free to spread in all directions.

In Section 3.5 we examined the case when the speed of the spread of the drop through the pore space (measured by the Péclet number) is small, as this is one of the more straightforward cases to consider when coupling between the different chemical species is included. This gives a model that includes axial diffusion and full chemical reaction. This model indicates that the length scale over which the dissolved species spreads out increases as the Péclet number decreases. To examine the effects on the concentrations of the different dissolved species in the vicinity of the drop, we considered a number of simplified versions of the model, including one which produces a finite maximum distance that the dissolved CO₂ will spread out in front of the spreading drop. When solutions could be found to this model, they indicate that the concentrations of the dissolved carbonic species largely revert to their far field equilibrium concentrations within a distance in front of the drop approximately equal to the channel radius. The effect on the metal's concentration is much smaller, and occurs over a longer distance in front of the drop, and this causes a few small changes in the carbonic species' concentrations over this longer length scale. Carbonic acid, hydrogen and calcium all experience drops in their concentrations in the region next to the CO₂ drop, with the carbonic acid dropping to virtually zero.

The simplifications that were included in the model included setting the flux of CO₂ from the tip of the drop into the water (" b_{X0} ") equal to zero, supposing there is no thin film between CO₂ drop and pore wall, that there is a 90° contact angle between drop and wall (so no "inner region" in the pore space), and that the interface between drop and water is flat. The concentration fields should be examined in models that do not

make these simplifications, and we anticipate that many of the features that were found in our solutions will be preserved when these complexities are included. There are also other features that could be included in the modelling to improve its realism, including a non-zero speed for the spreading of the drop, density-driven convection, alternative pore space structures, additional chemical reactions, and alternative parameter values and initial conditions in the aquifer (due to different temperature, pressure, mineralogy, and pH).

3.A Two Newton-Raphson schemes for Models 8NF and 4NF

3.A.1 Introduction

Two Newton-Raphson schemes are constructed to solve Models 8NF and 4NF. Model 8NF is as follows. (4NF is the same, except that the d and g derivatives and boundary conditions are removed.)

$$\text{Model 8NF} \left\{ \begin{array}{l} 0 = b_{XX} - b + \sigma d, \\ 0 = d_{XX} + b - (\sigma + \psi)d + \omega E_L(-b - d - g + h) + \omega F_L(-b - d + g - h) \\ \quad + \omega((b + d)^2 - (g - h)^2), \\ 0 = g_{XX} + \chi(-b - d - g + h) - \phi(G_L + g)(-b - d + g - h) - \phi g E_L \\ \quad - \tau(G_L h + g H_L + gh) - \rho h, \\ 0 = h_{XX} - \tau(G_L h + g H_L + gh) - \rho h, \end{array} \right.$$

with $b = B_0 - B_L$ and $d_X = g_X = h_X = 0$ at $X = 0$, and $b = d = g = h = 0$ at $X = L$.

As described below, the X -axis is discretised into $N + 1$ collocation points, labelled x_n , $n = 0, \dots, N$, and the values of the four species at $X = x_n$ are labelled b_n , d_n , g_n , and h_n . Two Newton-Raphson methods are used to seek solutions to the following system of $4(N - 1)$ equations, to give the values of the four species at the $N - 1$ internal nodes, providing solutions that satisfy 8NF at each node:

$$0 = b_{XX,n} - b_n + \sigma d_n, \quad (3.7.1)$$

$$0 = d_{XX,n} + b_n - (\sigma + \psi)d_n + \omega E_L(-b_n - d_n - g_n + h_n) + \omega F_L(-b_n - d_n + g_n - h_n) + \omega(-b_n - d_n + g_n - h_n)(-b_n - d_n - g_n + h_n), \quad (3.7.2)$$

$$0 = g_{XX,n} + \chi(-b_n - d_n - g_n + h_n) - \phi G_L(-b_n - d_n + g_n - h_n) - \phi E_L g_n - \phi g(-b_n - d_n + g_n - h_n) - \tau(G_L h_n + g_n H_L + g_n h_n) - \rho h_n, \quad (3.7.3)$$

$$0 = h_{XX,n} - \tau(G_L h_n + g_n H_L + g_n h_n) - \rho h_n, \quad (3.7.4)$$

for $n = 1, \dots, N - 1$, with boundary conditions $b_0 = B_0 - B_L$ (specified), $d_0 = d_1$, $g_0 = g_1$, $h_0 = h_1$ and $b_N = d_N = g_N = h_N = 0$.

The differences between the two Newton-Raphson methods lie in the ways the X-axis is discretised, and the ways the second derivatives in (3.7.1)-(3.7.4) are estimated.

3.A.2 Scheme 1: Central differences

The eigenmode analysis of Model 8LF shows that the species vary between $X = 10^{-5}$ and $X = 10^2$, and so this is the chosen domain. The $N + 1$ nodes within this domain are chosen to be uniform in $\log X$, and an initial guess for the value of each species at each node that will satisfy equations (3.7.1)-(3.7.4) is taken from the algebraic solutions to either Model 8LR or 4LR (see Appendix 3.B), and labelled $b_{n,1}$, $d_{n,1}$, $g_{n,1}$ and $h_{n,1}$.

Given three nonlinearly-separated adjacent values of X (x_{n-1} , x_n and x_{n+1}), and corresponding known estimates of b (b_{n-1} , b_n and b_{n+1}), the central difference estimate of b_{XX} at x_n can be found as follows. Let $L_1 = x_n - x_{n-1}$ and $L_2 = x_{n+1} - x_n$, such that $0 < L_1 < L_2 \ll 1$. Then b_{n-1} can be written as $b(x - L_1)$, and b_{n+1} can be written as $b(x + L_2)$. Since b and all its derivatives are single-valued, finite and continuous across X , by Taylor's theorem

$$\begin{aligned} b(x - L_1) &= b(x) - L_1 b_X(x) + \frac{L_1^2}{2} b_{XX}(x) - \frac{L_1^3}{6} b_{XXX}(x) + \dots, \\ b(x + L_2) &= b(x) + L_2 b_X(x) + \frac{L_2^2}{2} b_{XX}(x) + \frac{L_2^3}{6} b_{XXX}(x) + \dots, \end{aligned}$$

and so

$$\begin{aligned} b(x - L_1) + b(x + L_1) &= 2b(x) - (L_1 - L_2)b_X(x) + \frac{1}{2}(L_1^2 + L_2^2)b_{XX}(x) + O(L_1^3) + O(L_2^3), \\ b(x - L_1) - b(x + L_1) &= -(L_1 + L_2)b_X(x) + \frac{1}{2}(L_1^2 - L_2^2)b_{XX}(x) + O(L_1^3) + O(L_2^3). \end{aligned}$$

Since $L_1, L_2 \ll 1$, the third order powers of L_1 and L_2 are negligible compared to the second and lower order powers, and so dropping all the terms greater than second order in L_1 or L_2 gives two equations for $b_X(x)$ and $b_{XX}(x)$ in terms of $b(x - L_1)$, $b(x)$, $b(x + L_2)$, L_1 and L_2 . Solving gives the following central difference estimate for the second derivative, which is accurate within $O(L_2^3)$.

$$b_{XX,n} = \frac{(L_1 + L_2)(b_{n-1} - 2b_n + b_{n+1}) - (L_1 - L_2)(b_{n-1} - b_{n+1})}{\{(L_1 + L_2)(L_1^2 + L_2^2) - (L_1 - L_2)(L_1^2 - L_2^2)\}/2}. \quad (3.7.5)$$

The numerator can be re-written $(L_1 + L_2)\{(b_{n-1} - b_n) - (b_n - b_{n+1})\} - (L_1 - L_2)(b_{n-1} - b_n + b_n - b_{n+1}) = 2L_2(b_{n-1} - b_n) - 2L_1(b_n - b_{n+1})$. As b decreases monotonically across X , both halves of this expression are positive. As $L_2 > L_1$, and the difference between L_1 and L_2 is more than the difference between the two differences of successive values of b , the numerator is positive. Also, as $(L_1 + L_2)(L_1^2 + L_2^2) > (L_1 - L_2)(L_1^2 - L_2^2) > 0$, the denominator is also always positive, and so b_{XX} is positive for all X .

Expression (3.7.5), similar expressions for $d_{XX,n}$, $g_{XX,n}$ and $h_{XX,n}$, the initial guesses $b_{n,1}$, $d_{n,1}$, $g_{n,1}$ and $h_{n,1}$, and the boundary conditions, are used to estimate the second derivatives at each point x_n . This enables the right hand sides of equations (3.7.1)-(3.7.4), written $y = (\text{Ex}_{1,n,1}, \text{Ex}_{2,n,1}, \text{Ex}_{3,n,1}, \text{Ex}_{4,n,1})$ to be evaluated at each node x_n , $n = 1, \dots, N - 1$.

A second set of estimates for the solution (labelled $b_{n,2}$, $d_{n,2}$, $g_{n,2}$ and $h_{n,2}$) is then found by adjusting the initial estimates towards the actual solution at the $N - 1$ internal X -axis points using the Newton-Raphson formula

$$\begin{pmatrix} b_{n,2} \\ d_{n,2} \\ g_{n,2} \\ h_{n,2} \end{pmatrix} = \begin{pmatrix} b_{n,1} \\ d_{n,1} \\ g_{n,1} \\ h_{n,1} \end{pmatrix} - J^{-1}(\mathbf{y}) \cdot \mathbf{y}, \quad (3.7.6)$$

for $n = 1, \dots, N - 1$. J is the Jacobian of (3.7.1)-(3.7.4), containing the derivative of each expression with respect to each unknown, constructed as:

$$J(\mathbf{y}) = \begin{pmatrix} \frac{\partial \text{Ex1}}{\partial b_1} \Big|_1 & \frac{\partial \text{Ex1}}{\partial d_1} \Big|_1 & \frac{\partial \text{Ex1}}{\partial g_1} \Big|_1 & \frac{\partial \text{Ex1}}{\partial h_1} \Big|_1 & \frac{\partial \text{Ex1}}{\partial b_{N-1}} \Big|_1 & \frac{\partial \text{Ex1}}{\partial d_{N-1}} \Big|_1 & \frac{\partial \text{Ex1}}{\partial g_{N-1}} \Big|_1 & \frac{\partial \text{Ex1}}{\partial h_{N-1}} \Big|_1 \\ \frac{\partial \text{Ex2}}{\partial b_1} \Big|_1 & \frac{\partial \text{Ex2}}{\partial d_1} \Big|_1 & \frac{\partial \text{Ex2}}{\partial g_1} \Big|_1 & \frac{\partial \text{Ex2}}{\partial h_1} \Big|_1 & \dots & \frac{\partial \text{Ex2}}{\partial b_{N-1}} \Big|_1 & \frac{\partial \text{Ex2}}{\partial d_{N-1}} \Big|_1 & \frac{\partial \text{Ex2}}{\partial g_{N-1}} \Big|_1 & \frac{\partial \text{Ex2}}{\partial h_{N-1}} \Big|_1 \\ \frac{\partial \text{Ex3}}{\partial b_1} \Big|_1 & \frac{\partial \text{Ex3}}{\partial d_1} \Big|_1 & \frac{\partial \text{Ex3}}{\partial g_1} \Big|_1 & \frac{\partial \text{Ex3}}{\partial h_1} \Big|_1 & \frac{\partial \text{Ex3}}{\partial b_{N-1}} \Big|_1 & \frac{\partial \text{Ex3}}{\partial d_{N-1}} \Big|_1 & \frac{\partial \text{Ex3}}{\partial g_{N-1}} \Big|_1 & \frac{\partial \text{Ex3}}{\partial h_{N-1}} \Big|_1 \\ \frac{\partial \text{Ex4}}{\partial b_1} \Big|_1 & \frac{\partial \text{Ex4}}{\partial d_1} \Big|_1 & \frac{\partial \text{Ex4}}{\partial g_1} \Big|_1 & \frac{\partial \text{Ex4}}{\partial h_1} \Big|_1 & \frac{\partial \text{Ex4}}{\partial b_{N-1}} \Big|_1 & \frac{\partial \text{Ex4}}{\partial d_{N-1}} \Big|_1 & \frac{\partial \text{Ex4}}{\partial g_{N-1}} \Big|_1 & \frac{\partial \text{Ex4}}{\partial h_{N-1}} \Big|_1 \\ \dots & \dots \\ \frac{\partial \text{Ex1}}{\partial b_1} \Big|_{N-1} & \frac{\partial \text{Ex1}}{\partial d_1} \Big|_{N-1} & \frac{\partial \text{Ex1}}{\partial g_1} \Big|_{N-1} & \frac{\partial \text{Ex1}}{\partial h_1} \Big|_{N-1} & \frac{\partial \text{Ex1}}{\partial b_{N-1}} \Big|_{N-1} & \frac{\partial \text{Ex1}}{\partial d_{N-1}} \Big|_{N-1} & \frac{\partial \text{Ex1}}{\partial g_{N-1}} \Big|_{N-1} & \frac{\partial \text{Ex1}}{\partial h_{N-1}} \Big|_{N-1} \\ \frac{\partial \text{Ex2}}{\partial b_1} \Big|_{N-1} & \frac{\partial \text{Ex2}}{\partial d_1} \Big|_{N-1} & \frac{\partial \text{Ex2}}{\partial g_1} \Big|_{N-1} & \frac{\partial \text{Ex2}}{\partial h_1} \Big|_{N-1} & \dots & \frac{\partial \text{Ex2}}{\partial b_{N-1}} \Big|_{N-1} & \frac{\partial \text{Ex2}}{\partial d_{N-1}} \Big|_{N-1} & \frac{\partial \text{Ex2}}{\partial g_{N-1}} \Big|_{N-1} & \frac{\partial \text{Ex2}}{\partial h_{N-1}} \Big|_{N-1} \\ \frac{\partial \text{Ex3}}{\partial b_1} \Big|_{N-1} & \frac{\partial \text{Ex3}}{\partial d_1} \Big|_{N-1} & \frac{\partial \text{Ex3}}{\partial g_1} \Big|_{N-1} & \frac{\partial \text{Ex3}}{\partial h_1} \Big|_{N-1} & \frac{\partial \text{Ex3}}{\partial b_{N-1}} \Big|_{N-1} & \frac{\partial \text{Ex3}}{\partial d_{N-1}} \Big|_{N-1} & \frac{\partial \text{Ex3}}{\partial g_{N-1}} \Big|_{N-1} & \frac{\partial \text{Ex3}}{\partial h_{N-1}} \Big|_{N-1} \\ \frac{\partial \text{Ex4}}{\partial b_1} \Big|_{N-1} & \frac{\partial \text{Ex4}}{\partial d_1} \Big|_{N-1} & \frac{\partial \text{Ex4}}{\partial g_1} \Big|_{N-1} & \frac{\partial \text{Ex4}}{\partial h_1} \Big|_{N-1} & \frac{\partial \text{Ex4}}{\partial b_{N-1}} \Big|_{N-1} & \frac{\partial \text{Ex4}}{\partial d_{N-1}} \Big|_{N-1} & \frac{\partial \text{Ex4}}{\partial g_{N-1}} \Big|_{N-1} & \frac{\partial \text{Ex4}}{\partial h_{N-1}} \Big|_{N-1} \end{pmatrix}.$$

For example, the top left entry in this matrix is found by substituting $n = 1$ into Ex1, and then differentiating with respect to b_1 , to give $-2(L_1 + L_2) / \{(L_1 + L_2)(L_1^2 + L_2^2) - (L_1 - L_2)(L_1^2 - L_2^2)\} - 1$. All the elements in J are zero except for the elements in the main diagonal of 4×4 blocks, and the first 4×4 blocks above and below this main diagonal.

A third set of estimates is obtained by repeating the process to adjust the second set of estimates, and this process is continued until the iterations converge on the correct solution to (3.7.1)-(3.7.4) for this B_0 . The iterations are said to have converged when the maximum of all the $4(N - 1)$ increments is smaller than a specified value.

3.A.3 Scheme 2: Chebyshev polynomials

With the Chebyshev spectral method, the X -axis is discretised into $N + 1$ Chebyshev collocation points, defined as $x_n^C = \cos(n\pi/N)$, $n = 0, \dots, N$. These points are the projections onto the x -axis of equally-spaced points on a unit semicircle [147]. Thus they range $-1 \leq x_n^C \leq 1$, and have the characteristic that there are many points near the two boundaries, and fewer points nearer the middle of the domain. They are converted to the actual X -axis range $0 \leq x_n \leq L$ using $x_n = (1 + x_n^C)L/2$, where L is the finite maximum value for X . With $L = 100$, it is necessary to take $N = 5000$ in order to be able to obtain solutions down to $X = 10^{-5}$, as $(1 + \cos(4999\pi/5000))100/2 \approx 10^{-5}$.

As an initial guess, each species is estimated to be zero at each x_n^C (except at the bubble tip boundary, where $b_0 = B_0 - B_L$). The second derivative of each species at each point x_n^C is then estimated using the $(N + 1) \times (N + 1)$ Chebyshev differentiation matrix D_N ,

whose $(i, j)^{th}$ entry is defined as follows [147]

$$(D_N)_{ij} = \begin{cases} (2N^2 + 1)/6 & i = j = 0, \\ -(2N^2 + 1)/6 & i = j = N, \\ -x_i^C/2(1 - (x_i^C)^2) & i = j = 1, \dots, N - 1, \\ c_i(-1)^{i+j}/c_j(x_i^C - x_j^C) & i \neq j; i, j = 0, \dots, N; \end{cases} \quad c_i = \begin{cases} 2 & i = 0 \text{ or } N \\ 1 & \text{otherwise.} \end{cases}$$

For each of the $N + 1$ collocation points, this matrix assigns a (non-zero) weight to all the $N + 1$ points. Multiplying D_N^2 by the $4(N + 1)$ vector of estimates of the species at the $N + 1$ collocation points gives a $4(N + 1)$ -vector of estimates of the second derivatives of the four species at the $(N + 1)$ collocation points.

The Newton-Raphson formula (3.7.6) is then used to find a second set of estimates of the values of the species at the collocation points, and this process is repeated. Once the solution has converged, and the value of each species at the $N + 1$ points is known, the unique polynomial in X of degree $\leq N$ that satisfies these points is found, to facilitate easy interpolation at any point on the X -axis.

3.A.4 Validation of the two Newton-Raphson methods

To check that the two Newton-Raphson methods work correctly, the solutions to Model 8LF are found using these two numerical methods, and compared to the known (sum of exponentials) solution described in Section 3.5.1. The solution is first found to 8LF using the Chebyshev method with $B_0 = 9.845 \times 10^{-6}$, an initial guess of zero at each point for each species each time, and $N = 20$. The absolute difference between the converged Chebyshev estimate of the perturbation and the known exact value is found for each of the four species at a random sample of 1000 points across X (this is possible despite $N = 20$ as the Chebyshev method produces a polynomial solution), and the maximum of these 4000 values found. This error is called the "infinity norm" error, i.e. Infinity norm = max over 4000 points across X of |Chebyshev estimate - known value|. This is then repeated (with initial guesses of zero each time), with N increasing from 20 to 120, and Figure 3.15 shows how the size of the infinity norm varies with N . As expected, there is an approximately linear decrease in $\log(\text{Infinity norm})$ with N , i.e. exponential decrease of the infinity norm with N , up to about $N = 100$,

after which the error is constant. This is the level of spectral accuracy, and is the size of the computer's rounding error. The central difference method cannot find the correct solution without a fairly accurate initial guess, which is provided by the solution to Model 4LR or 8LR (see Appendix 3.B).

Both schemes successfully converge on the known solution (each time in one step as this is a linear problem). Figure 3.16 shows the percentage errors across X in these two solutions, defined as

$$\text{Error} = \left| \frac{\text{Newton-Raphson value} - \text{Eigenanalysis value}}{\text{Eigenanalysis value}} \right|. \quad (3.7.7)$$

For each species, the Chebyshev errors are generally lower than the central difference errors, and all the errors are generally below 1%, except for at the overshoots and in the far field, where the perturbations are all very small. Both the central difference and Chebyshev methods have converged on the solution correctly, but the Chebyshev method is more robust – it requires a less accurate initial guess, and has a more accurate solution.

3.B Other pore space models

3.B.1 Model 8LR

The first term on the right hand side of equation (3.5.16) corresponds to the four d_X^2 terms in the matrix in (3.5.13), and the second term in (3.5.16) corresponds to the d_X^2 terms in the first, third and fourth rows of (3.5.13), and the $-(\psi + \omega F_L)$ terms in the R2C2 (second row, second column) term. The third term corresponds to the d_X^2 terms in the first and fourth rows of (3.5.13), the $-(\psi + \omega F_L)$ terms in R2C2, and the $-\phi E$ term in R3C3. The fourth term corresponds to σ in R1C2, $-\omega F_L$ in R2C1, $-\phi E_L$ in R3C3, and d_X^2 in R4C4. The fifth term in (3.5.16) corresponds to σ in R1C2, $-\omega F_L$ in R2C1, $-\phi E_L$ in R3C3, and $-\rho$ in R4C4.

Model 8LF can therefore be simplified as follows. The terms corresponding to the four eigenvalues, as outlined in the paragraph above, are retained. The equation for g_{XX} additionally requires term(s) that provide a link to b and d in order to match to a no flux boundary condition on $X = 0$. From (3.5.13), the options are $-\chi b$, $\phi G_L b$, $-\chi d$, and $\phi G_L d$. Each of the two ϕG_L terms is significantly larger than the corresponding χ term,

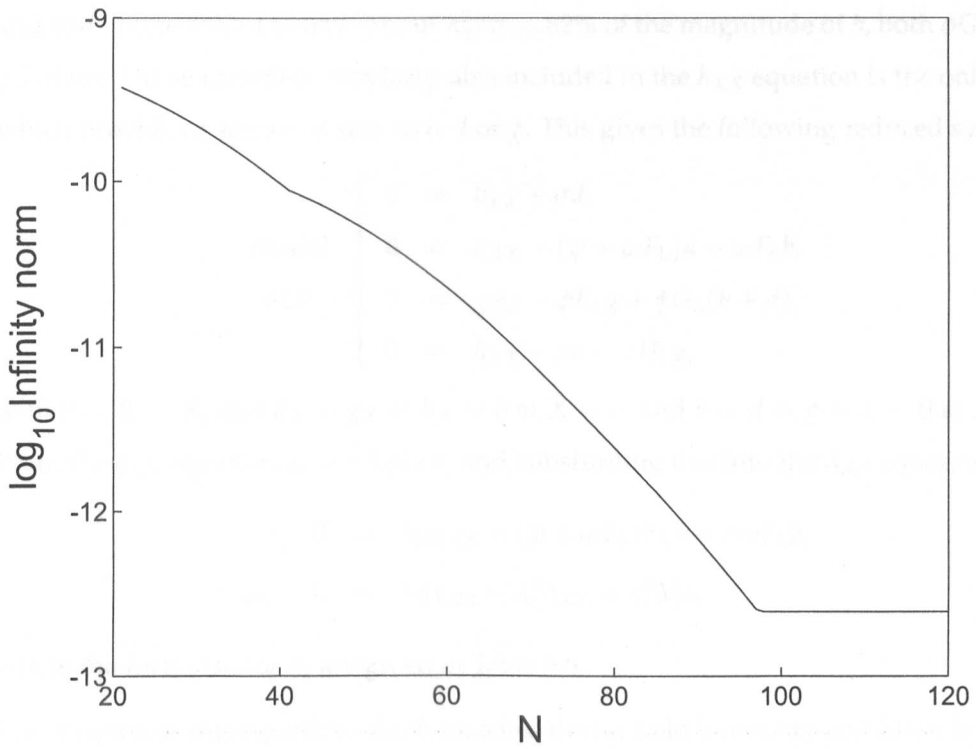


Figure 3.15: Model 8LF solved with Chebyshev: Infinity norm error against N .

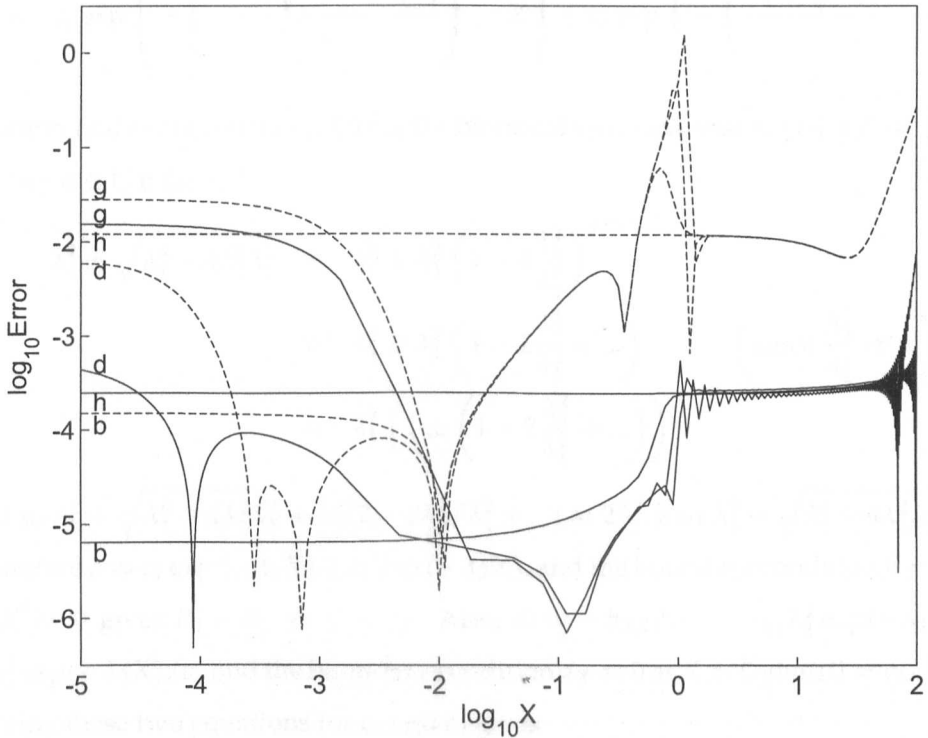


Figure 3.16: Pointwise errors in solutions to 8LF, defined by (3.7.7), using Chebyshev method (continuous lines) and central difference method (dashed lines).

and as d will be found to have about $\lambda_3^2/\sigma = 62\%$ of the magnitude of b , both $\phi G_L b$ and $\phi G_L d$ need to be included. Similarly, also included in the h_{XX} equation is the only term which provides a source or sink to b , d or g . This gives the following reduced system.

$$\text{Model } \begin{cases} 0 = b_{XX} + \sigma d, \\ 0 = d_{XX} - (\psi + \omega F_L)d - \omega F_L b, \\ \text{8LR} \begin{cases} 0 = g_{XX} - \phi E_L g + \phi G_L(b + d), \\ 0 = h_{XX} - \rho h - \tau H_L g, \end{cases} \end{cases}$$

with $b = B_0 - B_L$ and $d_X = g_X = h_X = 0$ at $X = 0$, and $b = d = g = h = 0$ at $X = L$. From the b_{XX} equation, $d = -b_{XX}/\sigma$, and substituting this into the d_{XX} equation gives

$$\begin{aligned} 0 &= b_{XXXX} - (\psi + \omega F_L)b_{XX} + \sigma \omega F_L b, \\ \text{or, } 0 &= b_{XXXX} - \lambda_1^2 b_{XX} + \lambda_1^2 \lambda_3^2 b, \end{aligned}$$

where the formulae for λ_i are given in Table 3.6.

The solution to this equation which matches the far field boundary condition is

$$b = c_1 \exp\left(-\left(\frac{\lambda_1^2 + \sqrt{\lambda_1^4 - 4\lambda_1^2 \lambda_3^2}}{2}\right)^{1/2} X\right) + c_2 \exp\left(-\left(\frac{\lambda_1^2 - \sqrt{\lambda_1^4 - 4\lambda_1^2 \lambda_3^2}}{2}\right)^{1/2} X\right),$$

where c_1 and c_2 are constants. Using the binomial series expansion $(1+x)^n = \sum_{k=0}^{\infty} {}^n C_k x^k$ for any $n \in \mathbb{C}$ if $|x| < 1$,

$$\begin{aligned} \lambda_1^2 \pm \sqrt{\lambda_1^4 - 4\lambda_1^2 \lambda_3^2} &= \lambda_1^2 \pm \lambda_1^2 \left(1 - 4\frac{\lambda_3^2}{\lambda_1^2}\right)^{1/2} \\ &\approx \lambda_1^2 \pm \lambda_1^2 \left(1 - 2\frac{\lambda_3^2}{\lambda_1^2} + \dots\right) \quad \left(\text{since } \frac{\lambda_3^2}{\lambda_1^2} \ll 1\right) \\ &= \lambda_1^2 \left(1 \pm \left(1 - 2\frac{\lambda_3^2}{\lambda_1^2} + \dots\right)\right), \end{aligned}$$

and so $\lambda_1^2 + \sqrt{\lambda_1^4 - 4\lambda_1^2 \lambda_3^2} = \lambda_1^2(2 - 2\lambda_3^2/\lambda_1^2 + \dots) \approx 2\lambda_1^2$, and $\lambda_1^2 - \sqrt{\lambda_1^4 - 4\lambda_1^2 \lambda_3^2} \approx 2\lambda_3^2$.

Therefore $b \approx c_1 \exp(-\lambda_1 X) + c_2 \exp(-\lambda_3 X)$, and the boundary condition $b = B_0 - B_L$ at $X = 0$ gives $B_0 - B_L = c_1 + c_2$. Also, $d = -b_{XX}/\sigma = -c_1 \lambda_1^2 \exp(-\lambda_1 X)/\sigma - c_2 \lambda_3^2 \exp(-\lambda_3 X)/\sigma$, and the boundary condition $d_X = 0$ at $X = 0$ gives $0 = c_1 \lambda_1^3 + c_2 \lambda_3^3$.

Solving these two equations for c_1 and c_2 gives

$$\begin{aligned} b &= \frac{B_0 - B_L}{\lambda_3^3 - \lambda_1^3} (\lambda_3^3 \exp(-\lambda_1 X) - \lambda_1^3 \exp(-\lambda_3 X)), \\ d &= \frac{-(B_0 - B_L)\lambda_1^2 \lambda_3^2}{\sigma(\lambda_3^3 - \lambda_1^3)} (\lambda_3 \exp(-\lambda_1 X) - \lambda_1 \exp(-\lambda_3 X)). \end{aligned}$$

The distributions of these two species are governed by two length scales. There is a very thin boundary layer over a length scale of magnitude $O(1/\lambda_1)$, and then the second longer length scale, of magnitude $O(1/\lambda_3)$, controls the distance over which equilibrium is reached. The solution to g that matches the boundary conditions is then:

$$g = \frac{\phi G_L(B_0 - B_L)}{\lambda_3^3 - \lambda_1^3} \left(\frac{\lambda_3^3(1 - \lambda_1^2/\sigma)}{\lambda_2^2 - \lambda_1^2} \exp(-\lambda_1 X) - \frac{\lambda_1^3(1 - \lambda_3^2/\sigma)}{\lambda_2^2 - \lambda_3^2} \exp(-\lambda_3 X) - \left[\frac{\lambda_1 \lambda_3^3(1 - \lambda_1^2/\sigma)}{\lambda_2^2 - \lambda_1^2} - \frac{\lambda_3 \lambda_1^3(1 - \lambda_3^2/\sigma)}{\lambda_2^2 - \lambda_3^2} \right] \frac{\exp(-\lambda_2 X)}{\lambda_2} \right).$$

The distribution of g is thus controlled by three length scales – there are two boundary layers, of magnitudes $O(1/\lambda_1)$ and $O(1/\lambda_2)$, and equilibrium is reached over the longest of these three length scales, which, as for b and d , is $O(1/\lambda_3)$. The solution to h that matches the boundary conditions is then:

$$h = \frac{\tau H_L \phi G_L(B_0 - B_L)}{\lambda_3^3 - \lambda_1^3} \left(\frac{\lambda_3^3(1 - \lambda_1^2/\sigma)}{(\lambda_2^2 - \lambda_1^2)(\lambda_1^2 - \lambda_4^2)} \exp(-\lambda_1 X) - \frac{\lambda_1^3(1 - \lambda_3^2/\sigma)}{(\lambda_2^2 - \lambda_3^2)(\lambda_3^2 - \lambda_4^2)} \exp(-\lambda_3 X) - \left[\frac{\lambda_1 \lambda_3^3(1 - \lambda_1^2/\sigma)}{\lambda_2^2 - \lambda_1^2} - \frac{\lambda_3 \lambda_1^3(1 - \lambda_3^2/\sigma)}{\lambda_2^2 - \lambda_3^2} \right] \frac{\exp(-\lambda_2 X)}{\lambda_2(\lambda_4^2 - \lambda_2^2)} - \left[\frac{\lambda_1 \lambda_3^3(1 - \lambda_1^2/\sigma)}{(\lambda_2^2 - \lambda_1^2)(\lambda_1^2 - \lambda_4^2)} - \frac{\lambda_3 \lambda_1^3(1 - \lambda_3^2/\sigma)}{(\lambda_2^2 - \lambda_3^2)(\lambda_3^2 - \lambda_4^2)} - \frac{\lambda_1 \lambda_3^3(1 - \lambda_1^2/\sigma)}{(\lambda_2^2 - \lambda_1^2)(\lambda_4^2 - \lambda_2^2)} + \frac{\lambda_3 \lambda_1^3(1 - \lambda_3^2/\sigma)}{(\lambda_2^2 - \lambda_3^2)(\lambda_4^2 - \lambda_2^2)} \right] \frac{\exp(-\lambda_4 X)}{\lambda_4} \right).$$

Species h has three boundary layers, of magnitude $O(1/\lambda_1)$, $O(1/\lambda_2)$ and $O(1/\lambda_3)$, and equilibrium is reached over a length scale $O(1/\lambda_4)$. This set of approximations is tested in Appendix 3.B.2.

3.B.2 Comparison of 8LF and 8LR

Figure 3.17 shows the solutions to 8LF (from Section 3.5.1) and 8LR (from Appendix 3.B.1). As before, $B_0 = 9.845 \times 10^{-6}$ is chosen. The two lines for each species are completely coincident near the bubble tip (to visible accuracy), and each species' reduced model has the correct equilibrium length scales. However, 8LR has failed to pick up the three carbonic species' second plateaux in the far field, continuing straight down instead. This is because all the h terms have been dropped from the d_{XX} and g_{XX} equations in 8LR, and so b , d and g have completely decoupled from h and are free to continue their steep declines. Correcting this discrepancy by restoring the h terms back into these equations would also restore the difficulty in solving the systems without

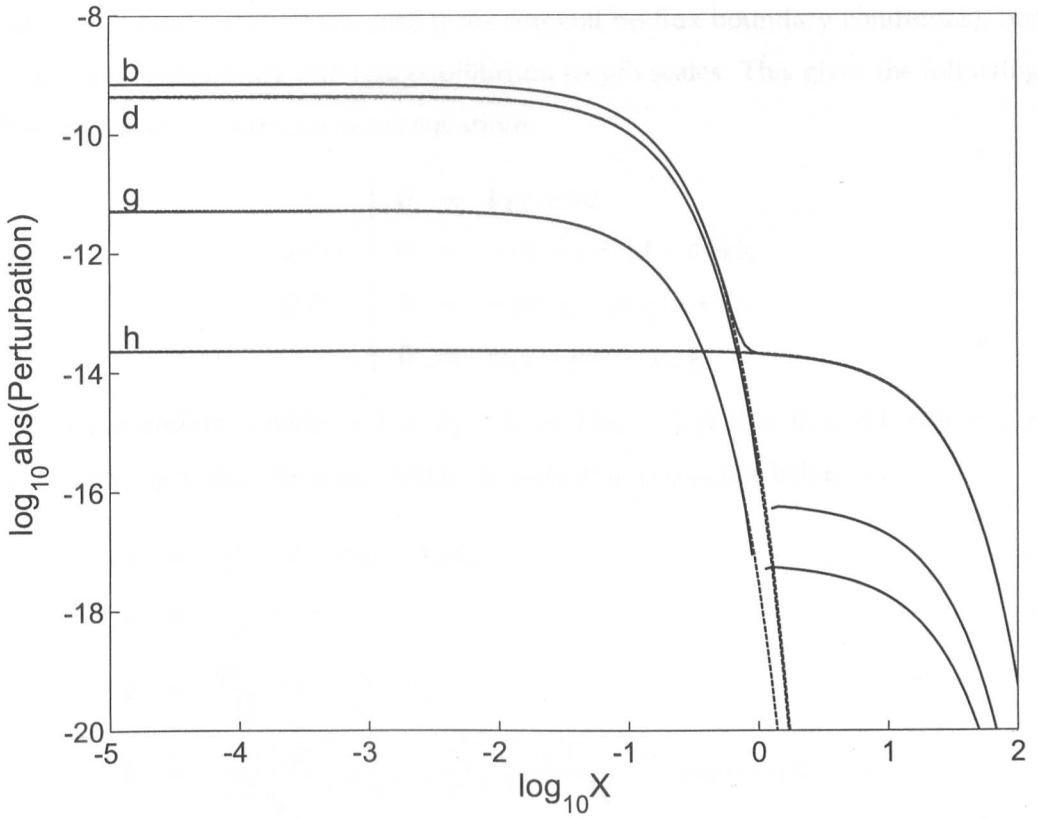


Figure 3.17: Linear perturbation models: 8LF (continuous lines) and 8LR (dashed lines).

resorting to an eigenanalysis as was used for 8LF. The reduced model has also failed to pick up the overshoots for d and g that are in the full model. These differences indicate that to retain an accurate picture of the species' far field behaviour, the full set of reaction terms should be retained.

3.B.3 Model 4LR

The two length scales $O(1/\lambda_1)$ and $O(1/\lambda_2)$ provide extremely short boundary layers within which there is actually no noticeable change in the sizes of the perturbations in this small amplitude case. If knowing the fine detail of the behaviour of the four species near the bubble-tip is less important, the 8th-order model may therefore be reduced to a 4th-order model by eliminating the derivatives that result in terms in the model involving λ_1 and λ_2 . As h has its own lengthscale and b_{XX} must be kept (otherwise this leaves $0 = \sigma d$), the derivatives d_{XX} and g_{XX} are therefore removed. Removing these two terms will therefore give approximations which are slightly less accurate

near $X = 0$ (and do not quite match the original no-flux boundary conditions), but do not have significantly different equilibrium length scales. This gives the following 4th-order system of reduced linear equations:

$$\text{Model 4LR} \quad \begin{cases} 0 = b_{XX} + \sigma d, \\ 0 = -(\psi + \omega_{FL})d - \omega_{FL}b, \\ 0 = -\phi E_L g + \phi G_L(b + d), \\ 0 = h_{XX} - \rho h - \tau H_L g, \end{cases}$$

with four boundary conditions $b = B_0 - B_L$ and $h_X = 0$ at $X = 0$, and $b = h = 0$ at $x = L$. These give the following (much-simplified) approximate behaviour:

$$\begin{aligned} b &= (B_0 - B_L) \exp(-\lambda_3 X), \\ d &= \frac{-\lambda_3^2}{\sigma} b, \\ g &= \frac{\phi G_L}{\lambda_2^2} \left(1 - \frac{\lambda_3^2}{\sigma}\right) b, \\ h &= \frac{\tau H_L \phi G_L}{\lambda_2^2 (\lambda_4^2 - \lambda_3^2)} \left(1 - \frac{\lambda_3^2}{\sigma}\right) \left(\frac{\lambda_3 (B_0 - B_L)}{\lambda_4} \exp(-\lambda_4 X) - b\right). \end{aligned}$$

When these expressions are plotted, they coincide completely with the expressions for Model 8LR. Therefore, using Model 4NF in Section 3.5.3 is justified. (Also, despite the far field failings, 4LR and 8LR provide sufficiently good initial guesses for the central differences Newton-Raphson method of solving 8NF and 4NF.)

CO₂ rising through saturated limestone

The aim of this Chapter is to provide modelling for some experiments which have recently been carried out at the University of Nottingham. These experiments involve injecting gaseous carbon dioxide into different media, and measuring its speed of ascent, rate of dissolution, and the changes in the chemical composition of the water and limestone through which it flows. They simulate what could happen within a saline aquifer after injection of CO₂.

Miss Yang Wei, of the School of Geography, University of Nottingham, has performed some experiments in order to investigate the changes in pH, the concentrations of carbonic species and calcium ions, and electrical conductivity, that occur in limestone saturated with water, as a result of CO₂(g) being bubbled up through the water/limestone mixture, reacting as it travels.

After describing the experiments and the initial condition of the system, some mathematical modelling is performed to predict the chemical changes in the limestone, and these modelling predictions are compared to the results from the experiments.

4.1 Experimental set-up

Figure 4.1 illustrates the experimental apparatus. A column of ground limestone (at least 99% CaCO₃, 96% of the particles of diameter 300-850 μm, density 1480 kg/m³) 0.7m high was placed in a cylindrical tube of diameter 0.2m. To saturate the limestone,

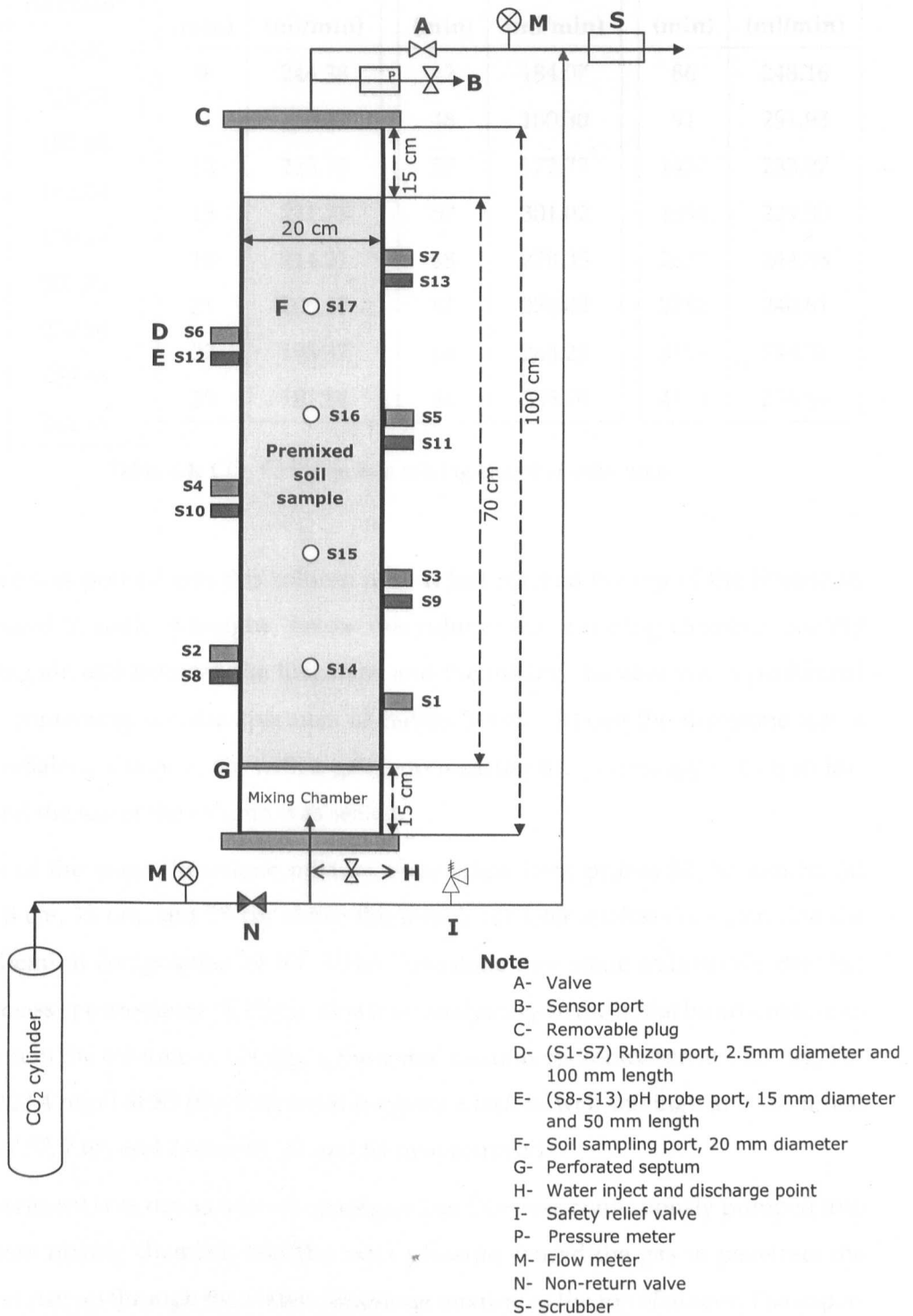


Figure 4.1: Experimental set-up (courtesy of Yang Wei, University of Nottingham).

Time (min)	Flow rate (ml/min)						
0	301.02	9	244.38	42	184.07	86	248.16
1	225.53	11	233.07	48	180.30	91	251.93
2	187.84	13	225.53	57	172.77	1437	233.07
3	165.24	15	221.75	57	301.02	1694	229.30
4	150.19	18	214.21	58	278.35	2637	244.38
4	301.02	21	206.68	61	270.80	2752	240.61
6	270.80	27	195.37	68	263.25	3177	244.38
7	259.48	35	187.84	81	255.70	4158	236.84
8	248.16						

Table 4.1: CO₂ flow rate into mixing chamber with time.

tap water was poured into this column until it just reached the top of the limestone, and allowed to settle overnight. Below this column was a mixing chamber, initially containing air, and between the limestone and the mixing chamber was a perforated septum, containing circular apertures of radius 3 mm. Above the limestone was a region initially containing air, with a gauge to measure the percentage of CO₂ in this space, and the top of the column was sealed.

Samples of the water/limestone mixture were taken from probes S1, S3 and S5 (at heights 5 cm, 15 cm, and 25 cm above the mesh), for later analysis to determine the initial chemical composition of the water/limestone mix using inductively coupled plasma mass spectrometry (ICPMS). This later analysis gave the initial bicarbonate concentration in the column as 174 mg/l, the initial calcium concentration as 75.9 mg/l at S3 and 127.4 mg/l at S5 (the difference suggests a lack of well-mixing), and the initial pH was 7.57, 7.68, and 7.60 at S1, S3 and S5 (respectively).

The experiment was run as follows: pure gaseous CO₂ was continuously pumped into the bottom mixing chamber, and the extra pressure caused the gas to penetrate the mesh and rise up through the water/limestone mixture to the top chamber. The experiment was run for about 96 hours, and the pH, the flow rate of CO₂ into the bottom mixing chamber, and the percentage of CO₂ in the top chamber, were measured at various time intervals. Samples of the water/limestone mixture were also collected at

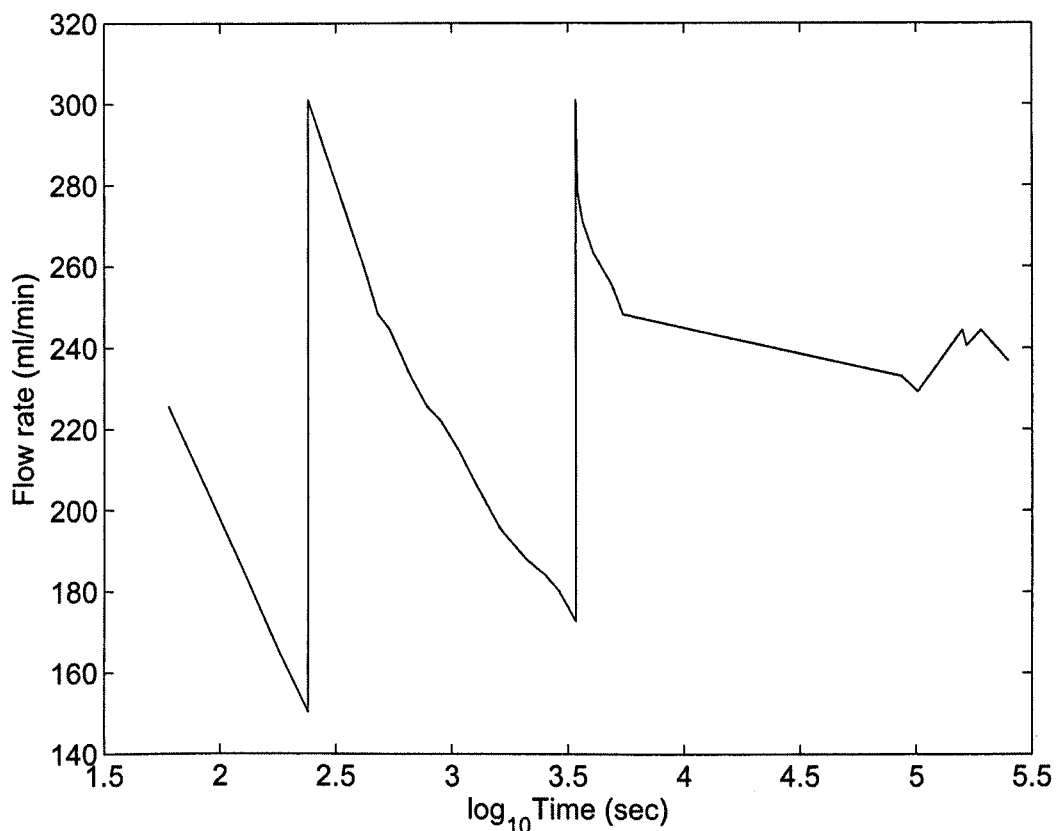


Figure 4.2: CO₂ flow rate into mixing chamber with time.

particular times. The room temperature was 17.9 °C, and the pressure from the gas cylinder to push CO₂(g) into the mixing chamber was about 2.0 bar.

Table 4.1 and Figure 4.2 give the CO₂ flow rate into the bottom mixing chamber against time. The flow rate reduced as the pressure difference between the CO₂ cylinder and the mixing chamber reduced, and when the flow rate reduced to about 150 ml/min, the gauge was opened wider to increase the flow rate up to about 300 ml/min. This happened on 4 and 57 minutes (hence the jumps in flow rate at these two times).

4.2 Experimental data

Table 4.2 gives the measured gas composition of the top chamber with time, percent-wise. Some of the rows sum to more or less than 100% due to equipment error and the failure to measure argon (0.9% of air). Table 4.3 gives the observed pH with time, at S1, S3 and S5, and Table 4.4 gives the concentration of dissolved Ca²⁺ in the water

Time (min)	CO ₂ (%)	O ₂ (%)	N ₂ (%)	Time (min)	CO ₂ (%)	O ₂ (%)	N ₂ (%)	Time (min)	CO ₂ (%)	O ₂ (%)	N ₂ (%)
0	0.0	20.2	79.5	35	27.0	15.0	58.0	113	95.3	1.0	3.6
4	0.1	20.2	79.5	41	48.0	11.4	40.7	122	96.5	0.8	2.6
8	0.3	20.2	79.4	45	54.1	9.9	35.8	139	97.8	0.6	1.4
10	0.5	20.1	79.2	51	59.7	8.5	31.6	162	97.4	0.5	2.1
12	1.0	20.1	78.8	58	69.3	6.8	23.9	180	98.9	0.5	0.3
15	4.5	18.9	74.2	66	78.7	5.1	16.4	213	98.6	0.3	0.9
23	5.6	19.3	74.9	74	84.6	3.9	11.6	255	99.6	0.4	0.0
25	7.4	18.8	73.6	84	89.2	2.4	8.3	1181	99.4	0.6	0.0
27	7.4	18.9	73.6	93	91.1	1.9	7.2	1475	99.9	0.8	0.0
32	15.5	17.0	68.2	103	94.1	1.2	4.5	2885	97.6	0.8	1.1

Table 4.2: Gas composition in top chamber with time.

with time (these concentrations exclude solid calcium). The results in this Table come from the samples of the limestone taken at various times, and later analysed using inductively coupled plasma mass spectrometry. The values in these Tables are plotted in Figures 4.3-5 below along with the modelling predictions that will be derived below.

During the course of the experiment, bubbles could not be seen in the water/limestone mixture; it was completely still, with no bubbling or churning at the interface with the gas in the top chamber. This suggests that the CO₂ bubbles dissolved into the water extremely quickly. Even though the experiment was run (i.e. CO₂ was pumped in) for over 96 hours, the vast majority of the changes appear to have come within the first 3 hours, with the pH and Ca then reaching a plateau despite the additional CO₂.

After the experiment ended, a few channels could be seen in the limestone adjacent to the edge of the container, which were believed to have been formed by the rising CO₂. They measured just a few mm in diameter, and were tilted slightly away from vertical.

4.3 Mathematical modelling

In the water/limestone mix, suppose that following the dissolution of CO₂ from the bubbles into the water (R1), the dissolved CO₂ can react with the water (R2) and the

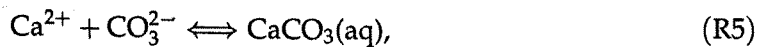
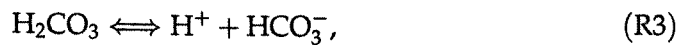
Time (min)	pH			Time (min)	pH			Time (min)	pH		
	S1	S3	S5		S1	S3	S5		S1	S3	S5
0	7.57	7.68	7.60	41	6.56	6.72	6.86	206	6.13	6.43	6.25
6	7.28	7.38	7.25	46	6.63	6.78	6.97	236	6.28	6.39	6.30
11	6.30	7.38	7.40	51	6.63	6.82	7.12	241	6.08	6.38	6.24
16	6.29	7.41	7.12	56	6.70	6.84	6.88	271	6.03	6.43	6.10
21	6.42	7.38	7.15	61	6.60	6.75	6.63	331	6.16	6.57	6.24
26	6.69	7.32	7.10	100	6.71	6.40	6.52	1236	6.19	6.24	6.27
31	6.49	6.85	7.05	177	6.20	6.25	6.51	1531	6.18	6.36	6.16
36	6.55	6.72	6.75	186	6.20	6.45	6.33	2961	6.16	6.18	6.12

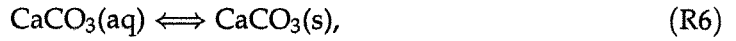
Table 4.3: Observed pH with time.

Time (min)	[Ca ²⁺] (mg/l)		Time (min)	[Ca ²⁺] (mg/l)		Time (min)	[Ca ²⁺] (mg/l)	
	S3	S5		S3	S5		S3	S5
0	75.90	127.40	1440	281.90	289.80	4390	299.10	381.80
10	83.05	144.80	1720	285.20	294.10	5545	-	505.40
45	81.67	158.70	2770	294.30	270.80	5550	303.40	-
70	89.67	192.60	3190	299.80	362.40	5770	305.30	-
100	94.30	291.40	4170	303.50	317.20			

Table 4.4: Calcium concentration with time.

different compounds in the water, including carbonic acid, hydrogen, bicarbonate, carbonate, calcium, and calcium carbonate (R2-5), and the calcium carbonate can precipitate out of the solution back onto the solid medium (R6). As the CO₂(g) in the mixture dissolves into the water extremely quickly, suppose also that none of the mixture's CO₂(g) can interact with the top chamber, but only its dissolved CO₂ (R7), i.e.





where TC stands for 'top chamber'. Assume that CO₂(aq) remains below carbon dioxide's solubility limit, and that all the CaCO₃ that is formed in solution remains dissolved until its concentration reaches calcium carbonate's molar solubility limit S ; thereafter it precipitates instantaneously (R6). Suppose that the water/limestone mixture is well-mixed, with negligible advection and diffusion compared to reaction, so the other reactions (R1-5) and (R7) each individually follows the mass action law, with forward and reverse rate constants $k_1, k_2, k_3, k_4, k_5, k_7$ and $k_{-1}, k_{-2}, k_{-3}, k_{-4}, k_{-5}, k_{-7}$ respectively, with the additional assumption that water is abundant (compared to the species dissolved in the water). Suppose that the temperature, pressure, salinity, ionic strength, and particle surface area are constant and uniform.

As we suppose that the water/limestone mixture is well-mixed, and so the concentrations may vary temporally but not spatially, we consider the changes in the species' concentrations in the whole mixture with time. If there is a continuous injection of CO₂(g) from time 0 to time t_1 , the rate equations for this system are therefore:

$$\frac{d[\text{CO}_2(\text{g})_{\text{mix}}]}{dt} = Q\mathcal{H}(t_1 - t) - k_1[\text{CO}_2(\text{g})_{\text{mix}}] + k_{-1}[\text{CO}_2(\text{aq})], \quad (4.3.1a)$$

$$\begin{aligned} \frac{d[\text{CO}_2(\text{aq})]}{dt} &= k_1[\text{CO}_2(\text{g})_{\text{mix}}] - k_{-1}[\text{CO}_2(\text{aq})] - k_2[\text{CO}_2(\text{aq})] + k_{-2}[\text{H}_2\text{CO}_3] \\ &\quad - k_7[\text{CO}_2(\text{aq})] + k_{-7}[\text{CO}_2(\text{g})_{\text{TC}}], \end{aligned} \quad (4.3.1b)$$

$$\frac{d[\text{H}_2\text{O}]}{dt} = -k_2[\text{CO}_2(\text{aq})] + k_{-2}[\text{H}_2\text{CO}_3], \quad (4.3.1c)$$

$$\frac{d[\text{H}_2\text{CO}_3]}{dt} = k_2[\text{CO}_2(\text{aq})] - k_{-2}[\text{H}_2\text{CO}_3] - k_3[\text{H}_2\text{CO}_3] + k_{-3}[\text{H}^+][\text{HCO}_3^-], \quad (4.3.1d)$$

$$\frac{d[\text{H}^+]}{dt} = k_3[\text{H}_2\text{CO}_3] - k_{-3}[\text{H}^+][\text{HCO}_3^-] + k_4[\text{HCO}_3^-] - k_{-4}[\text{H}^+][\text{CO}_3^{2-}], \quad (4.3.1e)$$

$$\frac{d[\text{HCO}_3^-]}{dt} = k_3[\text{H}_2\text{CO}_3] - k_{-3}[\text{H}^+][\text{HCO}_3^-] - k_4[\text{HCO}_3^-] + k_{-4}[\text{H}^+][\text{CO}_3^{2-}], \quad (4.3.1f)$$

$$\begin{aligned} \frac{d[\text{CO}_3^{2-}]}{dt} &= k_4[\text{HCO}_3^-] - k_{-4}[\text{H}^+][\text{CO}_3^{2-}] - k_5[\text{Ca}^{2+}][\text{CO}_3^{2-}] + k_{-5}[\text{CaCO}_3(\text{aq})], \\ &\quad \cdot \end{aligned} \quad (4.3.1g)$$

$$\frac{d[\text{Ca}^{2+}]}{dt} = -k_5[\text{Ca}^{2+}][\text{CO}_3^{2-}] + k_{-5}[\text{CaCO}_3(\text{aq})], \quad (4.3.1h)$$

$$\frac{d[\text{CaCO}_3]}{dt} = k_5[\text{Ca}^{2+}][\text{CO}_3^{2-}] - k_{-5}[\text{CaCO}_3(\text{aq})], \quad (4.3.1i)$$

$$\frac{d[\text{CO}_2(\text{g})_{\text{TC}}]}{dt} = k_7[\text{CO}_2(\text{aq})] - k_{-7}[\text{CO}_2(\text{g})_{\text{TC}}]. \quad (4.3.1j)$$

where t is time (in sec), $[]$ denotes concentration (in M), Q is CO₂(g) inflow rate in M/s, $\mathcal{H}(\cdot)$ is the Heaviside step function ($\mathcal{H}(x) = 1$ if $x > 0$, $\mathcal{H}(x) = 0$ if $x < 0$), and the expression for CaCO₃ is combined from the expressions for CaCO₃(aq) and CaCO₃(s) as in (2.2.1i), (2.2.1j) and (2.2.2).

Multiplying (4.3.1i) by V_{TC} and (4.3.1b) by V_{mix} , the volumes of the top chamber and water/limestone mixture respectively, and summing, gives

$$V_{TC} \frac{d[\text{CO}_2(\text{g})_{TC}]}{dt} + V_{mix} \frac{d[\text{CO}_2(\text{aq})]}{dt} = (V_{TC} - V_{mix})(k_7[\text{CO}_2(\text{aq})] - k_{-7}[\text{CO}_2(\text{g})_{TC}]) + V_{mix}(k_1[\text{CO}_2(\text{g})_{mix}] - k_{-1}[\text{CO}_2(\text{aq})] - k_2[\text{CO}_2(\text{aq})] + k_{-2}[\text{H}_2\text{CO}_3]). \quad (4.3.2)$$

Suppose that $[\text{CO}_2(\text{aq})]$ is permanently in equilibrium with $[\text{CO}_2(\text{g})_{TC}]$ (i.e. reaction (R7) is much faster than any other reaction). According to Henry's Law (see Section 1.7.1), the equilibrium between CO₂(aq) and CO₂(g)_{TC} is given by $S = k_H P$, where S is the solubility of the gas in the liquid (i.e. $[\text{CO}_2(\text{aq})]$), P is the partial pressure of the gas in the top chamber (atm), and k_H is the Henry's law constant (in M/atm). P can be replaced with nRT/V , from the ideal gas law, where n is number of mol, R is the gas constant, T is temperature, and V is volume. Noting that n/V is $[\text{CO}_2(\text{g})_{TC}]$, (4.3.1) and Henry's Law give

$$\frac{k_{-7}}{k_7} = \frac{[\text{CO}_2(\text{aq})]}{[\text{CO}_2(\text{g})_{TC}]} = k_H RT. \quad (4.3.3)$$

Substituting expressions for $[\text{CO}_2(\text{g})_{TC}]$ and $[\text{CO}_2(\text{aq})]$ from (4.3.3) into (4.3.2), and dividing through by V_{mix} , gives the following replacements for (4.3.1b) and (4.3.1j):

$$\left(\frac{V_{TC}}{V_{mix}} \frac{1}{k_H RT} + 1 \right) \frac{d[\text{CO}_2(\text{aq})]}{dt} = \left(\frac{V_{TC}}{V_{mix}} + k_H RT \right) \frac{d[\text{CO}_2(\text{g})_{TC}]}{dt} = k_1[\text{CO}_2(\text{g})_{mix}] - k_{-1}[\text{CO}_2(\text{aq})] - k_2[\text{CO}_2(\text{aq})] + k_{-2}[\text{H}_2\text{CO}_3]. \quad (4.3.4)$$

The rate of change of CO₂(aq) does depend on the relative volumes of the water/limestone mixture and the top chamber, as this affects how many CO₂ molecules are available to react in the water, and this model reflects that fact. $k_H = 0.04155$ M/atm for CO₂ in water at $T = 291$ K (from equations (1.7.1) and (1.7.2)), and $R = 0.082$ atm K⁻¹ M⁻¹, and so $k_H RT = 0.991$ (hence 'CO₂ distributes itself approximately equally between its gas phase and aqueous phase' [73] (see Section 1.7.1)). Therefore, when the two volumes are equal, the CO₂ molecules are split approximately equally between the water

Species	Concentration	Species	Concentration
[CO ₂ (g)]	1.19×10^{-4} M	[HCO ₃ ⁻]	2.85×10^{-3} M
[CO ₂ (aq)]	1.19×10^{-4} M	[CO ₃ ²⁻]	6.81×10^{-6} M
[H ₂ CO ₃]	3.58×10^{-7} M	[Ca ²⁺]	3.17×10^{-3} M
[H ⁺]	2.51×10^{-8} M	[CaCO ₃]	4.33×10^{-5} M

Table 4.5: Initial equilibrium condition at S5.

and the top chamber, and under this model, the rate of change of CO₂(aq) would correctly be half of what it would be if $V_{TC} = 0$. Also, if the top chamber were the whole atmosphere, this model would give the rate of change of CO₂(aq) as effectively zero.

The portion of the water/limestone mixture that is available to hold dissolved CO₂ is the portion that is water, and large beds of randomly-packed uniform spheres have an average void fraction of about 39% [148]. Therefore, from Figure 4.1, as the two cylindrical volumes have equal cross-sectional area, the volume ratio can be estimated as

$$\frac{V_{TC}}{V_{mix}} = \frac{0.15}{0.70 \times 0.39} = 0.55.$$

The initial condition at S5 was pH=7.6, [HCO₃⁻]=174 mg/l, and [Ca²⁺]=127 mg/l. Noting that calcium has atomic mass 40.078 g/mol, bicarbonate has atomic mass 61.01 g/mol, and using the rate constants given in Table 2.1 and equilibrium expressions such as (2.2.7), gives the initial equilibrium condition given in Table 4.5. Water has constant concentration of about 55.5 M.

Suppose the rate of flow of CO₂(g) into the mixing chamber is a constant 240 ml/min = 4×10^{-6} m³/sec (roughly the mean flux in Figure 4.2). From the ideal gas law, with a pressure of 2.0 bar and temperature of 291 K, this volume is 3.3×10^{-4} mol/sec. Using a void fraction of 39%, the water in the whole water/limestone mixture has a volume of 8.6 litre, and so $Q \approx 3.8 \times 10^{-5}$ M/sec.

4.4 Comparison of mathematical modelling with experimental data

Using the initial condition given in Table 4.5, $t_1 = 250,000$ sec (the time for which CO₂ was injected, according to Table 4.1), $Q = 3.8 \times 10^{-5}$ M/sec, the values of the rate constants given in Table 2.1, $V_{TC}/V_{mix} = 0.55$, and $k_H RT = 0.991$, the results from the model comprising equations (4.3.1a,c-i) and (4.3.4) are found using numerical integration.

Figure 4.3 gives the change in hydrogen concentration as predicted by the model, and the measured values given in Table 4.3 (except for the observed values at Time=0). The observed rate of pH fall is broadly in line with the model prediction. However, the model predicts that the pH decreases all the time that gaseous CO₂ is pumped in, and then stops changing, but the observations indicate that a plateau is reached much before t_1 . This suggests that either there is a buffer within the water/limestone mix that is preventing the pH from decreasing further, which needs to be included in the model, or perhaps later observations of pH would indeed have shown further decreases (for example, the line for S3 looks far from flat). An attempt was made to limit the model's increase in $[H^+]$ by introducing a pH buffer: including the reaction $CaCO_3 + H^+ \rightleftharpoons CaHCO_3^+$, adjusting the rate formulas for CaCO₃ and H⁺, and including a new one for CaHCO₃⁺. However, this made no noticeable difference to the plots in Figure 4.3.

With density 1.2 g/l and atomic mass 29 g/mol, air has total concentration 0.041 mol/l. With a volume of 4.712 l, the top chamber therefore contained 0.195 mol of air at the start of the experiment. This 0.195 mol of O₂ and N₂ comprised only about 2.4% of the air in the top chamber at the end, according to Table 4.2, so the top chamber contained 8.1 mol at the end in total, of which 7.9 mol is CO₂ (or $[CO_2(g)_{TC}] = 1.68$ M). Similar calculations give $[CO_2(g)_{TC}]$ at each time point, and these are plotted along with the model predictions in Figure 4.4. The observed changes happen at a faster rate than the model predicts. This is despite the model assuming the water/limestone mix is a permanently well-mixed chamber, but the mixture was observed to be completely still during the experiment! The rate constants for reactions (R2) and (R3) may need to be adjusted.

The concentrations of dissolved calcium given in Table 4.4 are turned from mg/l to

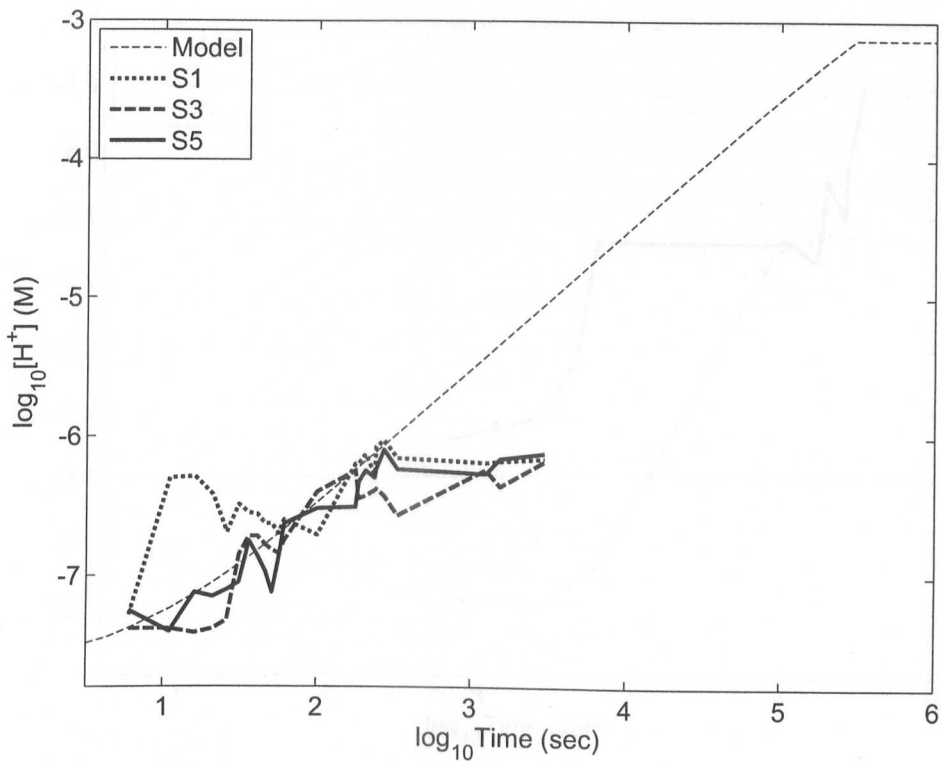


Figure 4.3: Hydrogen concentration with time: Table 4.3 data and model prediction.

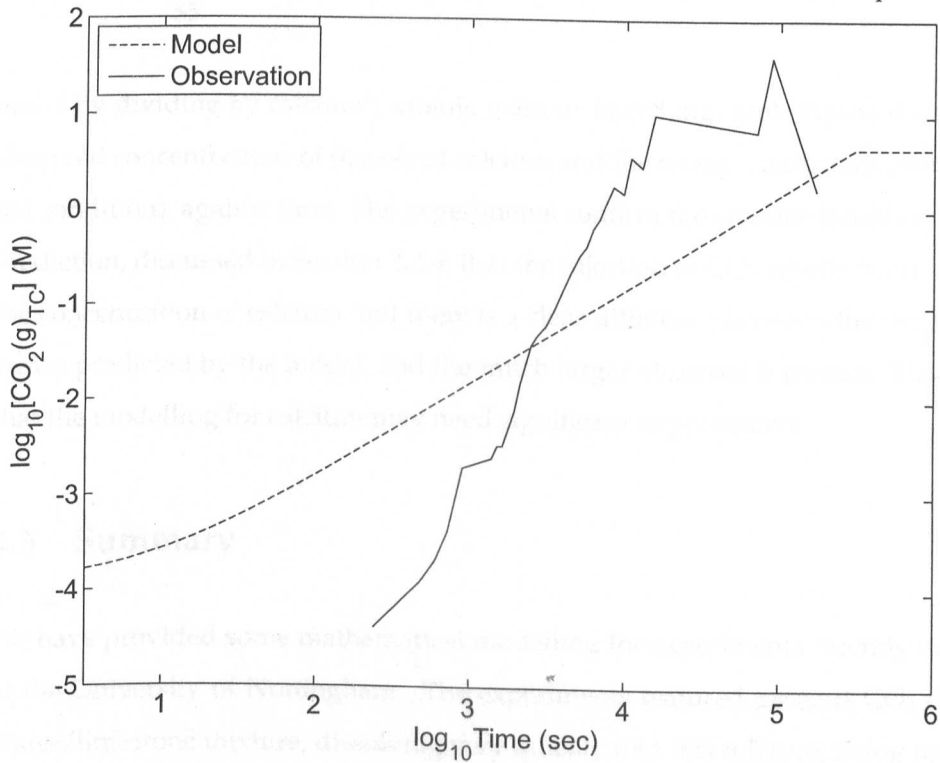


Figure 4.4: Top chamber CO₂(g) with time: Table 4.2 data and model prediction.

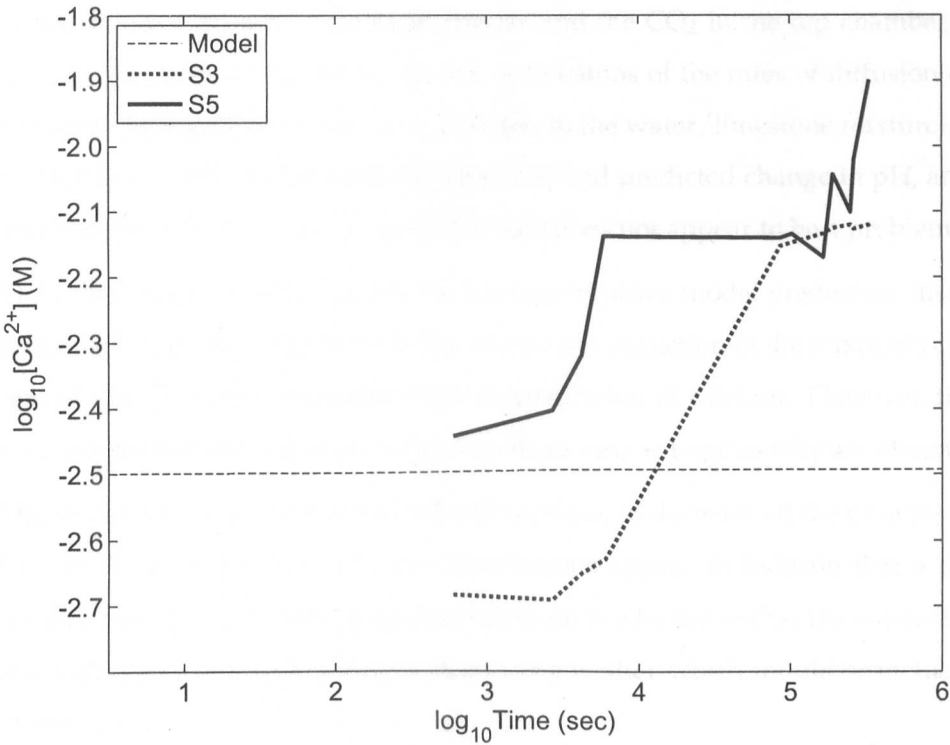


Figure 4.5: Calcium concentration with time: Table 4.4 data and model prediction for S5.

mol/l by dividing by calcium's atomic mass of 40,078 mg/mol. Figure 4.5 shows the observed concentrations of dissolved calcium and the model predictions (with S5's initial condition), against time. The experiments confirm the counter-intuitive modelling prediction, discussed in Section 2.2.4, that the injection of CO₂ results in an increase in the concentration of calcium, but there is a clear difference between the very slight increase predicted by the model, and the much larger observed increases. This suggests that the modelling for calcium may need significant improvement.

4.5 Summary

We have provided some mathematical modelling for experiments recently carried out at the University of Nottingham. The experiments featured gaseous CO₂ entering a water/limestone mixture, dissolving very quickly into this mixture, rising up through the mixture while reacting with the water and species dissolved in the water, before entering a top chamber. Our model gives the temporal changes of the concentrations

of the different dissolved chemical species and the CO₂ in the top chamber, as functions of the chemical reactions, but not as functions of the rates of diffusion or rate of transport through the medium (i.e. position in the water/limestone mixture). There is no significant time lag between the observed and predicted change in pH, and so this assumption of the mixture being well-mixed does not appear to be a problem.

The experimental results confirm the counter-intuitive model prediction, discussed in Section 2.2.4, that the injection of CO₂ results in a reduction in the mixture's concentration of CaCO₃, and an increase in the concentration of calcium. However, the model does not predict these changes to be anywhere near as large as they are observed to be.

The model also predicts that the pH will continue to decrease all the time that gaseous CO₂ is being pumped in, but the observations appear to indicate that a plateau is reached fairly quickly. This suggests that there is a buffer within the water/limestone mix that is preventing the pH from decreasing further, which should be included in the model.

Conclusions

The dissolution of CO_2 in water, and reaction with water, is a very important natural and industrial process. There are many challenges to successfully modelling CO_2 dissolution in water, including the large number of reaction and transport processes that can occur, and the extremely wide range of temporal, spatial, and concentration scales. Also, saline aquifers are extremely heterogeneous environments, and model validation is difficult. One part of the solution to these problems is to improve the understanding of the fundamental underpinning reaction and transport processes, so that there is a better understanding of what can be expected to happen. This requires the formulation of a series of smaller sub-problems, with careful rationalisations, which can be understood and analysed in detail. We consider a series of such sub-problems.

In Chapter 2 we formulated a single model for the time dependence of what happens to the concentrations of the key chemical species dissolved in water, following the injection of extra gaseous CO_2 . This model includes no dependence of the concentrations on position, but assumes everything is always well-mixed. The results from this model can be used to help predict the long-term impact on the atmosphere and oceans of the additional CO_2 , once everything is well-mixed and equilibrium is reached. In the literature the mass action law is taken as being an accurate way of describing each of the individual principal chemical reactions that occur as a result of CO_2 dissolving into water, and the model is formulated by applying this law to the complete set of principal reactions.

The solutions to this model (the distributions of the different dissolved species with time) can be found numerically for any initial condition and set of parameter values.

The method of matched asymptotic expansions was used to obtain expressions for the leading-order behaviour of the different species as they go to their new equilibria over six different timescales, following the injection of extra gaseous CO_2 , as functions of the initial condition of the system, the parameters, and time. Leading-order expressions which give the new equilibrium of the system as functions of the initial condition and the parameters were also obtained. These leading-order expressions all show excellent agreement with the numerical solutions to the model, which is because the rate constants and initial concentrations vary over many orders of magnitude. Due to the ubiquity of CO_2 reacting with water, what happens when this reaction takes place has been studied for over a century, but, to the best of our knowledge, this asymptotic approach has not been seen in the literature, and it is also unusual to see so many reactions handled at once in an analytic approach. This analysis therefore produces new evolution and equilibrium expressions that should be of practical utility, and which complement computational models that are used widely in geophysics and geochemistry.

Up to half of all the anthropogenic CO_2 emissions to the atmosphere end up dissolving into the oceans, rivers and lakes, and this model predicts the impact on the chemical compositions of these ecosystems (including the change in pH and availability of carbonate ions), for a given quantity of new CO_2 . The model predicts that hydrogen increases and carbonate ions decrease (which matches what has been observed), and the new equilibrium concentrations it predicts agree with the Bjerrum plot corresponding to the new equilibrium. Rather counterintuitively, this model also predicts that there is a decrease in the concentration of dissolved calcium carbonate as a result of the additional CO_2 ; some of the calcium carbonate already dissolved in the water is caused to split up into its constituent elements by the injection of extra CO_2 . This increases the amount of dissolved calcium.

These results can also be used within models of carbon sequestration. Reactive transport models of CO_2 dissolution and convection that include both complex modelling of the chemical reactions and complex modelling of the chemical transport are currently rare. Such models would be able to include all these reactions by identifying the time scales over which the transport processes occur, and then, for the reactions faster than this, to specify the local equilibrium using the equilibrium expressions ob-

tained by this asymptotic analysis, and for the reactions slower than this, by using the time-dependent evolution expressions obtained by this asymptotic analysis.

In Chapter 3 we considered the pore-scale behaviour of CO_2 injected into a saline aquifer. Injected CO_2 forms a spreading drop in an aquifer's pore space. Being lighter than the resident water, the CO_2 migrates upwards through the pore spaces until it reaches an impermeable layer, and then spreads out laterally underneath this overlying caprock. CO_2 dissolves from the ends of the drop into the water and is transported away from the drop, enabling more CO_2 to dissolve, and causing changes in the chemical composition of the water in front of the drop as it reacts with the other species in the water. The whole of this problem includes many complex interactions, and we investigated two particular subsets in detail.

First of all we analysed a two-dimensional partial differential equation model for the far field steady-state distribution of any single species released from a spreading drop into a long thin pore filled with water, accounting for advection, Taylor dispersion, diffusion, and a chemical sink. The model included a weak net flux through the channel, less than the flow by a factor of $O(\epsilon)$, where ϵ is the ratio of film width to channel radius. A long-wave approximation was employed, and the concentrations were averaged across the channel cross-section, and this turned the model into a one-dimensional ordinary differential equation model for the leading-order behaviour of the species. This provided the length scale over which the species reaches equilibrium, and the distribution of the species to that equilibrium. The equilibrium length scale is dependent on the relative strengths of advection, diffusion and reaction, measured through the dimensionless Péclet and Damköhler numbers (the ratios of advection to diffusion and reaction to advection, respectively), valid when $\text{Da} < 1/\text{Pe}$. There were found to be different dominant balances between different subsets of the four effects in different regions of Pe - Da parameter space, enabling the expression for the length scale to be simplified in these different cases.

For a fixed ratio of film width (between drop and pore walls) to channel radius, the length scale over which the dissolved species spreads out is minimised if the Péclet number is $O(1)$ (i.e. advection and diffusion are equally important), and increases as the Péclet number increases, due to Taylor dispersion. If minimising the distance through an aquifer pore over which CO_2 spreads out is desirable, this model therefore

suggests that the CO_2 should be injected in such a way as to make the speed of spread of the CO_2 drop through the pore space as close as possible to the speed at which the CO_2 that dissolves from the drop into the water in the pore space will diffuse through the water. The speed at which the CO_2 drop spreads through a given pore space can be controlled, for example, by changing the speed and pressure at which it is injected, whether it is injected together with water, and whether the CO_2 is free to spread in all directions.

The second pore-scale model we examined comprised one of these cases with full reactive coupling between the different chemical species. We considered the case when the speed of the spread of the drop through the pore space (measured by the Péclet number) is small, as this is one of the more straightforward cases to consider when reactive coupling is included. This gave a model that includes axial diffusion and fully coupled chemical reaction. To examine the effects on the concentrations of the different dissolved species in the vicinity of the drop, we considered a number of simplified versions of the model, including one which produces a finite maximum distance for the dissolved CO_2 to spread out in front of the spreading drop. The solutions indicated that the dissolved carbonic species largely revert to their far field equilibrium concentrations within a distance in front of the drop approximately equal to the channel radius. The effect on the calcium's concentration is much smaller, and occurs over a longer distance in front of the drop. Carbonic acid, hydrogen and calcium all experience drops in their concentrations in the region next to the CO_2 drop, with the carbonic acid dropping to virtually zero.

The simplifications that were included in the model included setting the flux of CO_2 from the tip of the drop into the water equal to zero, and the interface between drop and water to be flat. The next steps with these submodels would be to examine whether the predictions outlined in the paragraph above still hold true for models that do not make some of these simplifications. We anticipate that many of the features that were found in our solutions will be preserved when these complexities are included. Other features such as density-driven convection, alternative pore space structures, additional chemical reactions, and alternative parameter values and initial conditions in the aquifer, could also be included in these submodels of CCS. The dependence of the concentration distributions on time could also be examined.

Finally, we adapted the model formulated in Chapter 2 that describes the temporal behaviour of species dissolved in water, following an injection of extra CO_2 , to make it applicable to experiments recently carried out at the University of Nottingham. The experiments featured gaseous CO_2 entering a water/limestone mixture, dissolving very quickly into this mixture, rising up through the mixture, while reacting with the water and species dissolved in the water, before entering a top chamber. The model included no dependence of concentrations on position in the water/limestone mixture (so this solution was always well-mixed), and was adapted to model this situation by including an expression for the behaviour of the CO_2 in the top chamber, and by making the behaviour of dissolved CO_2 dependant on the volumes of the water/limestone mixture and the top chamber. The rate of change of dissolved CO_2 will depend on these relative volumes, as this affects how many CO_2 molecules are available to react in the water.

Similarly to the original temporal model, this model predicts that the injection of CO_2 results in a reduction in the mixture's concentration of CaCO_3 , and an increase in the concentration of calcium, and the experimental results confirm these model predictions. However, the observed changes are much bigger than the model predicts. The model also predicts that the pH will continue to decrease throughout the 96 hours that gaseous CO_2 was pumped in, but the observations indicate that a plateau was reached after just a few hours. There is therefore probably a buffer within the water/limestone mix that is preventing the pH from decreasing further. There is therefore clear room for improvement in this modelling.

References

- [1] M.J. Mitchell, O.E. Jensen, K.A. Cliffe, and M.M. Maroto-Valer. A model of carbon dioxide dissolution and mineral carbonation kinetics. *Proceedings of the Royal Society of London Series A*, 466:1265–1290, 2010.
- [2] J.H. Christensen, B. Hewitson, A. Busuioc, A. Chen, X. Gao, R. Held, R. Jones, R.K. Kolli, W.K. Kwon, R. Laprise, et al. *Climate change 2007: The physical science basis. Contribution of working group I to the fourth assessment report of the Intergovernmental Panel on Climate Change*. Summary for policymakers, pp.2,10,14. Available free online at <www.ipcc.ch/publications_and_data/ar4/wg1/en/contents.html>.
- [3] R. Lal. Carbon sequestration. *Philosophical Transactions of the Royal Society of London, Series B: Biological Sciences*, 363(5677):815–830, 2008.
- [4] F.J. Millero. Thermodynamics of the carbon dioxide system in the oceans. *Geochimica et Cosmochimica Acta*, 59(4):661–677, 1995.
- [5] K.G. Schulz, U. Riebesell, B. Rost, S. Thoms, and R.E. Zeebe. Determination of the rate constants for the carbon dioxide to bicarbonate inter-conversion in pH-buffered seawater systems. *Marine chemistry*, 100(1-2):53–65, 2006. ISSN 0304-4203.
- [6] R.A. Feely, C.L. Sabine, K. Lee, W. Berelson, J. Kleypas, V.J. Fabry, and F.J. Millero. Impact of anthropogenic CO₂ on the CaCO₃ system in the oceans. *Science*, 305(5682):362–366, 2004.
- [7] R. Rosa and B. Seibel. Synergistic effects of climate-related variables suggest future physiological impairment in a top oceanic predator. *Proceedings of the National Academy of Sciences of the U.S.A.*, 105(52):20776–20780, 2008.

REFERENCES

- [8] R. Bibby, S. Widdicombe, H. Parry, J. Spicer, and R. Pipe. Effects of ocean acidification on the immune response of the blue mussel *mytilus edulis*. *Aquatic Biology*, 2:67–74, 2008.
- [9] D.L. Dixon, P.L. Munday, and G.P. Jones. Ocean acidification disrupts the innate ability of fish to detect predator olfactory cues. *Ecology letters*, 13(1):68–75, 2010.
- [10] S.D. Simpson, P.L. Munday, M.L. Wittenrich, R. Manassa, D.L. Dixon, M. Gagliano, and H.Y. Yan. Ocean acidification erodes crucial auditory behaviour in a marine fish. *Biology Letters*, (Yet to appear in print):, 2011.
- [11] K.C. Hester, E.T. Peltzer, W.J. Kirkwood, and P.G. Brewer. Unanticipated consequences of ocean acidification: A noisier ocean at lower pH. *Geophysical Research Letters*, 35(19):L19601, 2008.
- [12] J.C. Orr, V.J. Fabry, O. Aumont, L. Bopp, S.C. Doney, R.A. Feely, A. Gnanadesikan, N. Gruber, A. Ishida, F. Joos, et al. Anthropogenic ocean acidification over the twenty-first century and its impact on calcifying organisms. *Nature*, 437(7059): 681–686, 2005.
- [13] J.M. Hall-Spencer, R. Rodolfo-Metalpa, S. Martin, E. Ransome, M. Fine, S.M. Turner, S.J. Rowley, D. Tedesco, and M.C. Buia. Volcanic carbon dioxide vents show ecosystem effects of ocean acidification. *Nature*, 454(7200):96–99, 2008. ISSN 0028-0836.
- [14] D. J. C. MacKay. *Sustainable Energy - without the hot air*. pp.6-8. Cambridge: UIT Cambridge Ltd, 2009. Available free online at <www.withouthotair.com>.
- [15] B. Metz, O.R. Davidson, P.R. Bosch, R. Dave, and L.A. Meyer. *Climate change 2007: Mitigation. Contribution of working group III to the fourth assessment report of the Intergovernmental Panel on Climate Change*. Cambridge University Press, Cambridge, pp.104,253. Available free online at <www.ipcc.ch/publications_and_data/ar4/wg3/en/contents.html>.
- [16] Energy Information Administration, U.S. Government. *International Energy Outlook 2009*. Chapter 5 - Electricity, 2009. Available free online at <www.eia.doe.gov/oiaf/ieo/index.html>.

REFERENCES

- [17] World Energy Council. *Survey of Energy Resources 2010*. WEC, 2010. Available free online at <www.worldenergy.org/publications/>.
- [18] S. Wiel, N. Martin, M. Levine, and L. Price. The role of building energy efficiency in managing atmospheric carbon dioxide. *Environmental Science & Policy*, 1(1): 27–38, 1998.
- [19] D. Pearce. The role of carbon taxes in adjusting to global warming. *The Economic Journal*, 101(407):938–948, 1991.
- [20] K.A. Beauchemin, S.M. McGinn, and H.V. Petit. Methane abatement strategies for cattle: Lipid supplementation of diets. *Canadian Journal of Animal Science*, 87(3):431–440, 2007.
- [21] J.H. Martin. Glacial-interglacial CO₂ change: The iron hypothesis. *Paleoceanography*, 5(1):1–13, 1990.
- [22] V. Smetacek and S.W.A. Naqvi. The next generation of iron fertilization experiments in the Southern Ocean. *Philosophical Transactions of the Royal Society A: Mathematical, Physical and Engineering Sciences*, 366(1882):3947–3967, 2008.
- [23] K.Z. House, C.F. Harvey, M.J. Aziz, and D.P. Schrag. The energy penalty of post-combustion CO₂ capture & storage and its implications for retrofitting the US installed base. *Energy & Environmental Science*, 2(2):193–205, 2009.
- [24] P. Linga, R. Kumar, and P. Englezos. The clathrate hydrate process for post and pre-combustion capture of carbon dioxide. *Journal of Hazardous Materials*, 149(3): 625–629, 2007.
- [25] B.J.P. Buhre, L.K. Elliott, C.D. Sheng, R.P. Gupta, and T.F. Wall. Oxy-fuel combustion technology for coal-fired power generation. *Progress in Energy and Combustion Science*, 31(4):283–307, 2005.
- [26] P. Cho, T. Mattisson, and A. Lyngfelt. Comparison of iron-, nickel-, copper- and manganese-based oxygen carriers for chemical-looping combustion. *Fuel*, 83(9): 1215–1225, 2004.
- [27] Z.X. Zhang, G.X. Wang, P. Massarotto, and V. Rudolph. Optimization of pipeline

REFERENCES

- transport for CO₂ sequestration. *Energy Conversion and Management*, 47(6):702–715, 2006.
- [28] A. Aspelund, M.J. Mølnvik, and G. De Koeijer. Ship transport of CO₂: Technical solutions and analysis of costs, energy utilization, exergy efficiency and CO₂ emissions. *Chemical Engineering Research and Design*, 84(9):847–855, 2006.
- [29] T.A. Torp and J. Gale. Demonstrating storage of CO₂ in geological reservoirs: the Sleipner and SACS projects. *Energy*, 29(9-10):1361–1369, 2004.
- [30] L.D.D. Harvey. Impact of deep-ocean carbon sequestration on atmospheric CO₂ and on surface-water chemistry. *Geophysical Research Letters*, 30(5):1237, 2003.
- [31] J.M. Nordbotten, M.A. Celia, and S. Bachu. Injection and storage of CO₂ in deep saline aquifers: Analytical solution for CO₂ plume evolution during injection. *Transport in Porous Media*, 58(3):339–360, 2005.
- [32] K.Z. House, D.P. Schrag, C.F. Harvey, and K.S. Lackner. Permanent carbon dioxide storage in deep-sea sediments. *Proceedings of the National Academy of Sciences*, 103(33):12291–12295, 2006.
- [33] S.H. Stevens, V.A. Kuuskraa, J. Gale, and D. Beecy. CO₂ injection and sequestration in depleted oil and gas fields and deep coal seams: worldwide potential and costs. *Environmental Geosciences*, 8(3):200–209, 2001.
- [34] A.C. Aycaguer, M. Lev-On, and A.M. Winer. Reducing carbon dioxide emissions with enhanced oil recovery projects: A life cycle assessment approach. *Energy and Fuels*, 15(2):303–308, 2001.
- [35] C.M. Oldenburg, S.H. Stevens, and S.M. Benson. Economic feasibility of carbon sequestration with enhanced gas recovery (CSEGR). *Energy*, 29(9-10):1413–1422, 2004.
- [36] R. Qi, T.C. LaForce, and M.J. Blunt. Design of carbon dioxide storage in aquifers. *International Journal of Greenhouse Gas Control*, 3(2):195–205, 2009.
- [37] H. Hassanzadeh, M. Pooladi-Darvish, and D.W. Keith. Accelerating CO₂ dissolution in saline aquifers for geological storage - mechanistic and sensitivity studies. *Energy & Fuels*, 23(6):3328–3336, 2009.

REFERENCES

- [38] M. Packer. Algal capture of carbon dioxide; biomass generation as a tool for greenhouse gas mitigation with reference to New Zealand energy strategy and policy. *Energy Policy*, 37(9):3428–3437, 2009.
- [39] D.J. Nowak and D.E. Crane. Carbon storage and sequestration by urban trees in the USA. *Environmental Pollution*, 116(3):381–389, 2002.
- [40] T.J. Lavery, B. Roudnew, P. Gill, J. Seymour, L. Seuront, G. Johnson, J.G. Mitchell, and V. Smetacek. Iron defecation by sperm whales stimulates carbon export in the Southern Ocean. *Proceedings of the Royal Society B: Biological Sciences*, volume (number):page–page, 2010.
- [41] W.J.J. Huijgen, G.J. Witkamp, R.N.J. Comans, et al. Mineral CO₂ sequestration by steel slag carbonation. *Environmental Science and Technology*, 39(24):9676–9682, 2005.
- [42] International Energy Agency. *Responding to urgent energy challenges - IEA calls for greater investment in the oil sector and for CCS to be made eligible to receive revenues generated by the CDM*. IEA press release number 08(07), 2008. Available online at <www.iea.org/press/allpress.asp>.
- [43] International Energy Agency. *Energy Technology Perspectives 2008*. Fact sheet – The BLUE scenario, 2008. Available free online at <www.iea.org/techno/etp/index.asp>.
- [44] B. Metz, O. Davidson, H. de Coninck, M. Loos, and L. Meyer. *IPCC special report on carbon dioxide capture and storage*. Chapter 5: Underground geological storage. Cambridge: Cambridge University Press, 2005. Available free online at <www.ipcc.ch/publications_and_data/publications_and_data_reports.shtml>.
- [45] K.K. Liong, P.A. Wells, and N.R. Foster. Diffusion of fatty acid esters in supercritical carbon dioxide. *Industrial & Engineering Chemistry Research*, 31(1):390–399, 1992.
- [46] S. Hill. Channeling in packed columns. *Chemical Engineering Science*, 1(6):247–253, 1952.
- [47] D.L. Youngs. Numerical simulation of turbulent mixing by Rayleigh-Taylor instability. *Physica D: Nonlinear Phenomena*, 12(1-3):32–44, 1984.

REFERENCES

- [48] H.E. Huppert and A.W. Woods. Gravity-driven flows in porous layers. *Journal of Fluid Mechanics*, 292:55–70, 1995.
- [49] S. Lyle, H.E. Huppert, M. Hallworth, M. Bickle, and A. Chadwick. Axisymmetric gravity currents in a porous medium. *Journal of Fluid Mechanics*, 543:293–302, 2005.
- [50] H.E. Huppert. Propagation of two-dimensional and axisymmetric viscous gravity currents over a rigid horizontal surface. *Journal of Fluid Mechanics*, 121(1): 43–58, 1982.
- [51] J.A. Neufeld and H.E. Huppert. Modelling carbon dioxide sequestration in layered strata. *Journal of Fluid Mechanics*, 625:353–370, 2009.
- [52] S. Shackley and C. Gough (eds). *Carbon capture and its storage - An integrated assessment*. Chapter 2. Aldershot: Ashgate Publishing Ltd, 2006.
- [53] H. Tazieff. Mechanisms of the Nyos carbon dioxide disaster and of so-called phreatic steam eruptions. *Journal of Volcanology and Geothermal Research*, 39(2-3): 109–116, 1989.
- [54] P.J. Baxter, M. Kapila, and D. Mfonfu. Lake Nyos disaster, Cameroon, 1986: the medical effects of large scale emission of carbon dioxide? *British Medical Journal*, 298(6685):1437–1441, 1989.
- [55] D.M. Evans. Denver area earthquakes and the Rocky Mountain Arsenal disposal well. *Mt. Geol.:(United States)*, 3(1):23–26, 1966.
- [56] British Geological Survey, CRE Group Ltd, RWE Aktiengesellschaft, TNO Institute of Applied Geoscience, BRGM, IKU Petroleum Research, Statoil, and University of Sunderland. *The underground disposal of carbon dioxide: Final report of Joule II project no. CT92-0031*. Research funded in part by The Commission of the European Communities in the framework of the Joule Programme, ISBN 085272280X. February 1996.
- [57] S. Emberley, I. Hutcheon, M. Shevalier, K. Durocher, W.D. Gunter, and E.H. Perkins. Geochemical monitoring of fluid-rock interaction and CO₂ storage at the Weyburn CO₂-injection enhanced oil recovery site, Saskatchewan, Canada. *Energy*, 29(9-10):1393–1401, 2004.

REFERENCES

- [58] M. Bickle, A. Chadwick, H. Huppert, M. Hallworth, and S. Lyle. Modelling carbon dioxide accumulation at Sleipner: Implications for underground carbon storage. *Earth and Planetary Science Letters*, 255(1-2):164–176, 2007.
- [59] J.P. Kaszuba, D.R. Janecky, and M.G. Snow. Carbon dioxide reaction processes in a model brine aquifer at 200 C and 200 bars: implications for geologic sequestration of carbon. *Applied Geochemistry*, 18(7):1065–1080, 2003.
- [60] M.L. Druckenmiller and M.M. Maroto-Valer. Carbon sequestration using brine of adjusted pH to form mineral carbonates. *Fuel Processing Technology*, 86(14-15): 1599–1614, 2005.
- [61] P.B. Stewart and P.K. Munjal. Solubility of carbon dioxide in pure water, synthetic sea water, and synthetic sea water concentrates at -5° to 25°C and 10- to 45-atm. pressure. *Journal of Chemical and Engineering data*, 15(1):67–71, 1970. ISSN 0021-9568.
- [62] N. J. Tro. *Chemistry, a molecular approach*. pp.154-155,533,587,747-748. New Jersey: Pearson Prentice-Hall, 2008.
- [63] S.X. Meng and J.B. Maynard. Use of statistical analysis to formulate conceptual models of geochemical behavior: water chemical data from the Botucatu aquifer in Sao Paulo state, Brazil. *Journal of Hydrology*, 250(1-4):78–97, 2001.
- [64] R. Wiebe. The binary system carbon dioxide-water under pressure. *Chemical Reviews*, 29(3):475–481, 1941. ISSN 0009-2665.
- [65] R. Wiebe and V.L. Gaddy. The solubility of carbon dioxide in water at various temperatures from 12 to 40° and at pressures to 500 atmospheres. Critical Phenomena. *Journal of the American Chemical Society*, 62(4):815–817, 1940. ISSN 0002-7863.
- [66] C.L. Yaws. *The Yaws handbook of properties for environmental and green engineering*. Chapter 11, Henry's Law constant for gases in water - Organic compounds. Gulf Publishing Company, Houston, Texas, 2008.
- [67] W. Dreybrodt, J. Lauckner, L. Zaihua, U. Svensson, and D. Buhmann. The kinetics of the reaction $\text{CO}_2 + \text{H}_2\text{O} \rightarrow \text{H}^+ + \text{HCO}_3^-$ as one of the rate limiting steps

REFERENCES

- for the dissolution of calcite in the system $\text{H}_2\text{O}-\text{CO}_2-\text{CaCO}_3$. *Geochimica et Cosmochimica Acta*, 60(18):3375–3381, 1996. ISSN 0016-7037.
- [68] G.H. Nancollas and M.M. Reddy. The crystallization of calcium carbonate: II. Calcite growth mechanism. *Journal of Colloid and Interface Science*, 37(4):824–830, 1971. ISSN 0021-9797.
- [69] S. Bishnoi and G.T. Rochelle. Absorption of carbon dioxide into aqueous piperazine: reaction kinetics, mass transfer and solubility. *Chemical engineering science*, 55(22):5531–5543, 2000. ISSN 0009-2509.
- [70] K. B. Krauskopf. *Introduction to Geochemistry*. 2nd edn, p.2. Tokyo: McGraw-Hill Kogakusha, Ltd, 1979.
- [71] A. C. Lasaga. *Kinetic theory in the Earth sciences*. pp.5,47,181. New Jersey: Princeton University Press, 1998.
- [72] P. Atkins and J. de Paula. *Atkins' physical chemistry*. 8th edition, pp.205,796,807,986. Oxford: Oxford University Press, 2006.
- [73] W. Stumm and J.J. Morgan. *Aquatic chemistry - chemical equilibria and rates in natural waters*. pp.46-49,54,76,981. New York: John Wiley, 1996.
- [74] J.F. Harper. Bubble rise in a liquid with a surfactant gas, in particular carbon dioxide. *Journal of Fluid Mechanics*, 581:157–165, 2007.
- [75] E.I. Obi and M.J. Blunt. Streamline-based simulation of carbon dioxide storage in a North Sea aquifer. *Water Resources Research*, 42(3):W03414, 2006.
- [76] L. Chou, R.M. Garrels, and R. Wollast. Comparative study of the kinetics and mechanisms of dissolution of carbonate minerals. *Chemical Geology*, 78(3-4):269–282, 1989. ISSN 0009-2541.
- [77] C.B. Andersen. Understanding carbonate equilibria by measuring alkalinity in experimental and natural systems. *Journal of Geoscience Education*, 50(4):389–403, 2002.
- [78] D. Langmuir. *Aqueous environmental geochemistry*. p.48. New Jersey: Prentice-Hall, 1997.

REFERENCES

- [79] O.S. Pokrovsky and J. Schott. Processes at the magnesium-bearing carbonates/solution interface. II. kinetics and mechanism of magnesite dissolution. *Geochimica et cosmochimica acta*, 63(6):881–897, 1999. ISSN 0016-7037.
- [80] E. Busenberg and L.N. Plummer. A comparative study of the dissolution and crystal growth kinetics of calcite and aragonite. *Studies in Diagenesis*, 1578:139–168, 1986.
- [81] T. Xu, J.A. Apps, and K. Pruess. Numerical simulation of CO₂ disposal by mineral trapping in deep aquifers. *Applied Geochemistry*, 19(6):917–936, 2004.
- [82] K. Ghesmat, H. Hassanzadeh, and J. Abedi. The impact of geochemistry on convective mixing in a gravitationally unstable diffusive boundary layer in porous media: CO₂ storage in saline aquifers. *Journal of Fluid Mechanics*, pages 1–33, 2011. ISSN 1469-7645.
- [83] D.M. Kern. The hydration of carbon dioxide. *Journal of Chemical Education*, 37(1): 14–23, 1960. ISSN 0021-9584.
- [84] G.M. Bond, J. Stringer, D.K. Brandvold, F.A. Simsek, M.G. Medina, and G. Ege-land. Development of integrated system for biomimetic CO₂ sequestration using the enzyme carbonic anhydrase. *Energy and Fuels*, 15(2):309–316, 2001.
- [85] Y. Pocker and D.W. Bjorkquist. Stopped-flow studies of carbon dioxide hydration and bicarbonate dehydration in H₂O and D₂O acid-base and metal ion catalysis. *Journal of the American Chemical Society*, 99(20):6537–6543, 1977.
- [86] R. van Eldik and D.A. Palmer. Effects of pressure on the kinetics of the dehydration of carbonic acid and the hydrolysis of CO₂ in aqueous solution. *Journal of Solution Chemistry*, 11(5):339–346, 1982. ISSN 0095-9782.
- [87] K.S. Johnson. Carbon dioxide hydration and dehydration kinetics in seawater. *Limnology and Oceanography*, 27(5):849–855, 1982. ISSN 0024-3590.
- [88] A.L. Soli and R.H. Byrne. CO₂ system hydration and dehydration kinetics and the equilibrium CO₂/H₂CO₃ ratio in aqueous NaCl solution. *Marine chemistry*, 78(2-3):65–73, 2002. ISSN 0304-4203.

REFERENCES

- [89] D. Vorländer and W. Strube. Die Einwirkung von Kohlensäure auf Alkalien und alkalische Erden, eine Zeitreaktion. *Berichte der deutschen chemischen Gesellschaft*, 46(1):172–181, 1913. ISSN 1099-0682.
- [90] J. Drever. *The geochemistry of natural waters*. 3rd edn, pp.42,44. New Jersey: Prentice-Hall, 2002.
- [91] C. Ho and J.M. Sturtevant. The kinetics of the hydration of carbon dioxide at 25°. *Journal of Biological Chemistry*, 238(10):3499–3501, 1963. ISSN 0021-9258.
- [92] G. Kaufmann and W. Dreybrodt. Calcite dissolution kinetics in the system $\text{CaCO}_3\text{-H}_2\text{O-CO}_2$ at high undersaturation. *Geochimica et Cosmochimica Acta*, 71(6):1398–1410, 2007.
- [93] J.M. Smith, S.W. Davison, and G.F. Payne. Development of a strategy to control the dissolved concentrations of oxygen and carbon dioxide at constant shear in a plant cell bioreactor. *Biotechnology and bioengineering*, 35(11):1088–1101, 1990.
- [94] P. Warneck. *Chemistry of the natural atmosphere*. Table 8-3 (p.395). San Diego: Academic Press, Inc., 1988.
- [95] M.M. Maroto-Valer, D.J. Fauth, M.E. Kuchta, Y. Zhang, and J.M. Andresen. Activation of magnesium rich minerals as carbonation feedstock materials for CO_2 sequestration. *Fuel Processing Technology*, 86(14-15):1627–1645, 2005.
- [96] L.N. Plummer and E. Busenberg. The solubilities of calcite, aragonite and vaterite in $\text{CO}_2\text{-H}_2\text{O}$ solutions between 0 and 90 C, and an evaluation of the aqueous model for the system $\text{CaCO}_3\text{-CO}_2\text{-H}_2\text{O}$. *Geochimica et Cosmochimica Acta*, 46(6):1011–1040, 1982.
- [97] M.M. Reddy and G.H. Nancollas. The crystallization of calcium carbonate: I. Isotopic exchange and kinetics. *Journal of colloid and interface science*, 36(2):166–172, 1971. ISSN 0021-9797.
- [98] G.I. Barenblatt. *Scaling*. Cambridge University Press, 2003.
- [99] J.M. Nordbotten and M.A. Celia. Similarity solutions for fluid injection into confined aquifers. *Journal of Fluid Mechanics*, 561:307–327, 2006.

REFERENCES

- [100] A. Farcas and A.W. Woods. The effect of drainage on the capillary retention of CO₂ in a layered permeable rock. *Journal of Fluid Mechanics*, 618:349–359, 2009.
- [101] F.P. Bretherton. The motion of long bubbles in tubes. *Journal of Fluid Mechanics*, 10(02):166–188, 1961.
- [102] O. Reynolds. On the theory of lubrication and its application to Mr. Beauchamp Tower's experiments. *Phil. Trans. Roy. Soc*, 177(pt 1):157–234, 1886.
- [103] W.F. Cope. The hydrodynamical theory of film lubrication. *Proceedings of the Royal Society of London. Series A. Mathematical and Physical Sciences*, 197(1049):201–217, 1949.
- [104] L.W. Schwartz, H.M. Princen, and A.D. Kiss. On the motion of bubbles in capillary tubes. *Journal of Fluid Mechanics*, 172(259):259–275, 1986.
- [105] Y.D. Shikhmurzaev. The moving contact line on a smooth solid surface. *International Journal of Multiphase Flow*, 19(4):589–610, 1993.
- [106] Y.D. Shikhmurzaev. Moving contact lines in liquid/liquid/solid systems. *Journal of Fluid Mechanics*, 334(1):211–249, 1997.
- [107] E.B. Dussan. On the spreading of liquids on solid surfaces: static and dynamic contact lines. *Annual Review of Fluid Mechanics*, 11(1):371–400, 1979.
- [108] J. Bloomfield, D. Gooddy, M. Bright, and P. Williams. Pore-throat size distributions in Permo-Triassic sandstones from the United Kingdom and some implications for contaminant hydrogeology. *Hydrogeology Journal*, 9(3):219–230, 2001.
- [109] F.V. Katopodes, A.M.J. Davis, and H.A. Stone. Piston flow in a two-dimensional channel. *Physics of Fluids*, 12:1240–1243, 2000.
- [110] F. Gurcan, P.H. Gaskell, M.D. Savage, and M.C.T. Wilson. Eddy genesis and transformation of Stokes flow in a double-lid driven cavity. *Proceedings of the Institution of Mechanical Engineers, Part C: Journal of Mechanical Engineering Science*, 217(3):353–364, 2003.
- [111] E. Mathieu. Mémoire sur l'équation aux différences partielles du quatrième ordre $\Delta\Delta u=0$, et sur l'équilibre d'élasticité d'un corps solide. *Journal de Mathématiques Pures et Appliquées, ser.2*, 14:378–421, 1869.

REFERENCES

- [112] J. Dougall. An analytical theory of the equilibrium of an isotropic elastic plate. *Transactions of the Royal Society of Edinburgh*, 41(1):129–228, 1904.
- [113] V.V. Meleshko. Biharmonic problem in a rectangle. *Applied Scientific Research*, 58(1):217–249, 1998.
- [114] P.F. Papkovich. Über eine Form der Lösung des biharmonischen Problems für das Rechteck. *C. R. Doklady Akademii Nauk SSSR*, 27:334–338, 1940. (English abstract in *Mathematical Reviews*, 2:332, 1941).
- [115] J. Fadle. Die Selbstspannungs-Eigenwertfunktionen der quadratischen Scheibe. *Ing. Archiv.*, 11:125–148, 1940.
- [116] R.C.T. Smith. The bending of a semi-infinite strip. *Australian Journal of Scientific Research, Ser. A*, 5:227–237, 1952.
- [117] D.A. Spence. A class of biharmonic end-strip problems arising in elasticity and Stokes flow. *IMA Journal of Applied Mathematics*, 30(2):107–139, 1983.
- [118] R.D. Gregory. The traction boundary value problem for the elastostatic semi-infinite strip; existence of solution, and completeness of the Papkovich-Fadle eigenfunctions. *Journal of Elasticity*, 10(3):295–327, 1980.
- [119] D.D. Joseph. The convergence of biorthogonal series for biharmonic and Stokes flow edge problems: Part I. *SIAM Journal on Applied Mathematics*, 33(2):337–347, 1977.
- [120] D.D. Joseph and L. Sturges. The convergence of biorthogonal series for biharmonic and Stokes flow edge problems: Part II. *SIAM Journal on Applied Mathematics*, 34(1):7–26, 1978.
- [121] T.N. Phillips. Singular matched eigenfunction expansions for Stokes flow around a corner. *IMA Journal of Applied Mathematics*, 42(1):13–26, 1989.
- [122] G.I. Taylor. On scraping viscous fluid from a plane surface. *The Scientific Papers of Sir Geoffrey Ingram Taylor*, vol. IV (ed. G.K. Batchelor):410–413. Cambridge University Press, 1971.
- [123] G.K. Batchelor. *An introduction to fluid dynamics*. p.225. Cambridge University Press, 2002.

REFERENCES

- [124] H.K. Moffatt. Viscous and resistive eddies near a sharp corner. *Journal of Fluid Mechanics*, 18(01):1–18, 1964.
- [125] T. Xu, E. Sonnenthal, N. Spycher, and K. Pruess. TOUGHREACT - A simulation program for non-isothermal multiphase reactive geochemical transport in variably saturated geologic media: Applications to geothermal injectivity and CO₂ geological sequestration. *Computers & Geosciences*, 32(2):145–165, 2006.
- [126] S.P. White, R.G. Allis, J. Moore, T. Chidsey, C. Morgan, W. Gwynn, and M. Adams. Simulation of reactive transport of injected CO₂ on the Colorado Plateau, Utah, USA. *Chemical Geology*, 217(3-4):387–405, 2005.
- [127] C.M. Oldenburg and A.J.A. Unger. Coupled vadose zone and atmospheric surface-layer transport of carbon dioxide from geologic carbon sequestration sites. *Vadose Zone Journal*, 3(3):848–857, 2004.
- [128] C.M. Oldenburg, K. Pruess, and S.M. Benson. Process modeling of CO₂ injection into natural gas reservoirs for carbon sequestration and enhanced gas recovery. *Energy and Fuels*, 15(2):293–298, 2001.
- [129] I. Gaus, M. Azaroual, and I. Czernichowski-Lauriol. Reactive transport modelling of the impact of CO₂ injection on the clayey cap rock at Sleipner (North Sea). *Chemical Geology*, 217(3-4):319–337, 2005.
- [130] D.L. Parkhurst and C.A.J. Appelo. *User's guide to PHREEQC (version 2) - a computer program for speciation, batch-reaction, one-dimensional transport, and inverse geochemical calculations*. U.S. Geological Survey. Water-Resources Investigations Report 99-4259, 1999.
- [131] G. Zvoloski, Z. Dash, and S. Kelkar. *FEHMN 1.0: Finite element heat and mass transfer code*. Los Alamos National Laboratory Technical Report LA-12062-MS, 1991.
- [132] J.B. Czarnecki, C.C. Faunt, C.W. Gable, and G.A. Zvoloski. On the development of a three-dimensional finite-element groundwater flow model of the saturated zone, Yucca Mountain, Nevada. Technical report, Geological Survey, Lakewood, CO (United States), 1996.

REFERENCES

- [133] R.T. Mills, C. Lu, P.C. Lichtner, and G.E. Hammond. Simulating subsurface flow and transport on ultrascale computers using PFLOTTRAN. *Journal of Physics: Conference Series*, 78:012051, 2007.
- [134] M.H. Reed. Calculation of multicomponent chemical equilibria and reaction processes in systems involving minerals, gases and an aqueous phase. *Geochimica et Cosmochimica Acta*, 46:513–528, 1982.
- [135] M.H. Reed and N.F. Spycher. *User's guide for CHILLER: a program for computing water-rock reactions, boiling, mixing and other reaction processes in aqueous-mineral-gas systems and minplot guide, third ed.* Department of Geological Sciences, University of Oregon, Corvallis, Oregon, 1998.
- [136] V. Lagneau, A. Pipart, and H. Catalette. Reactive transport modelling of CO₂ sequestration in deep saline aquifers. *Oil and Gas Science and Technology-Revue de l'IFP-Institut Francais du Petrole*, 60(2):231–248, 2005. ISSN 1294-4475.
- [137] C.M. Bethke. *The Geochemist's Workbench Version 4.0: A User's Guide*. University of Illinois, Urbana, IL, 2002.
- [138] X. Jiang. A review of physical modelling and numerical simulation of long-term geological storage of CO₂. *Applied Energy*, 88:3557–3566, 2011.
- [139] C. A. Rochelle, I. Czernichowski-Lauriol, and A. E. Milodowski. *The impact of chemical reactions on CO₂ storage in geological formations: a brief review*. In: S.J. Baines and R.H. Worden (eds): Geological storage of carbon dioxide, p.89. London: Geological Society, Special Publications 233, 87-106, 2004.
- [140] F. Takemura and A. Yabe. Rising speed and dissolution rate of a carbon dioxide bubble in slightly contaminated water. *Journal of Fluid Mechanics*, 378:319–334, 1999.
- [141] X. Xu, S. Chen, and D. Zhang. Convective stability analysis of the long-term storage of carbon dioxide in deep saline aquifers. *Advances in water resources*, 29(3):397–407, 2006. ISSN 0309-1708.
- [142] C.T. Simmons. Variable density groundwater flow: From current challenges to future possibilities. *Hydrogeology Journal*, 13(1):116–119, 2005. ISSN 1431-2174.

REFERENCES

- [143] J.A. Neufeld, M.A. Hesse, A. Riaz, M.A. Hallworth, H.A. Tchelepi, and H.E. Huppert. Convective dissolution of carbon dioxide in saline aquifers. *Geophysical Research Letters*, 37:L22404, 2010.
- [144] S. Backhaus, K. Turitsyn, and R.E. Ecke. Convective instability and mass transport of diffusion layers in a Hele-Shaw geometry. *Physical Review Letters*, 106(10):104501, 2011.
- [145] S. Rapaka, S. Chen, R.J. Pawar, P.H. Stauffer, and D. Zhang. Non-modal growth of perturbations in density-driven convection in porous media. *Journal of Fluid Mechanics*, 609(-1):285–303, 2008.
- [146] R. Farajzadeh, H. Salimi, P.L.J. Zitha, and H. Bruining. Numerical simulation of density-driven natural convection in porous media with application for CO₂ injection projects. *International Journal of Heat and Mass Transfer*, 50(25-26):5054–5064, 2007.
- [147] L.N. Trefethen. *Spectral methods in MATLAB*. ch. 5-7. Society for Industrial Mathematics, 2000. ISBN 0898714656.
- [148] R.F. Benenati and C.B. Brosilow. Void fraction distribution in beds of spheres. *AIChE Journal*, 8(3):359–361, 1962.